Optical Fiber Sensor Technologies for Efficient and Economical Oil Recovery

Final Technical Report

Reporting Period Start Date: 1 October 1998
Reporting Period End Date: 31 March 2003

Principal Investigator: Anbo Wang

Principal Report Authors: Kristie L. Cooper, Gary R. Pickrell, Anbo Wang

Report Issued: June 2003

DOE Award Number: DE-FT26-98BC15167

Submitted by: Center for Photonics Technology
Bradley Department of Electrical and Computer Engineering
Virginia Polytechnic Institute & State University
Blacksburg, VA 24061-0111

CPT
CENTER FOR PHOTONICS TECHNOLOGY

Disclaimer:

Abstract

Efficient recovery of petroleum reserves from existing oil wells has been proven to be difficult due to the lack of robust instrumentation that can accurately and reliably monitor processes in the downhole environment. Commercially available sensors for measurement of pressure, temperature, and fluid flow exhibit shortened lifetimes in the harsh downhole conditions, which are characterized by high pressures (up to 20 kpsi), temperatures up to 250°C, and exposure to chemically reactive fluids. Development of robust sensors that deliver continuous, real-time data on reservoir performance and petroleum flow pathways will facilitate application of advanced recovery technologies, including horizontal and multi-lateral wells.

This is the final report for the four-year program "Optical Fiber Sensor Technologies for Efficient and Economical Oil Recovery", funded by the National Petroleum Technology Office of the U.S. Department of Energy, and performed by the Center for Photonics Technology of the Bradley Department of Electrical and Computer Engineering at Virginia Tech from October 1, 1999 to March 31, 2003. The main objective of this research program was to develop cost-effective, reliable optical fiber sensor instrumentation for real-time monitoring of various key parameters crucial to efficient and economical oil production.

During the program, optical fiber sensors were demonstrated for the measurement of temperature, pressure, flow, and acoustic waves, including three successful field tests in the Chevron/Texaco oil fields in Coalinga, California, and at the world-class oil flow simulation facilities in Tulsa, Oklahoma. Research efforts included the design and fabrication of sensor probes, development of signal processing algorithms, construction of test systems, development and testing of strategies for the protection of optical fibers and sensors in the downhole environment, development of remote monitoring capabilities allowing real-time monitoring of the field test data from virtually anywhere in the world, and development of novel data processing techniques. Comprehensive testing was performed to systematically evaluate the performance of the fiber optic sensor systems in both lab and field environments.

Table of Contents

List of Figures

List of Tables

Executive Summary

This report summarizes the successful achievements during the four and a half-year program "Optical Fiber Sensor Technologies for Efficient and Economical Oil Recovery", funded by the National Petroleum Technology Office of the U.S. Department of Energy, and performed by the Center for Photonics Technology (CPT) of the Bradley Department of Electrical and Computer Engineering at Virginia Tech. The objective was the development and demonstration of cost-effective, reliable optical fiber sensors for the measurement of temperature, pressure, flow, and acoustic waves in downhole environments. Sensors were successfully demonstrated for the measurement of all four target parameters, including three successful field tests in the Chevron/Texaco oil fields in Coalinga, California and at the world class oil flow loop facility in Tulsa, Oklahoma.

In the first program year, solid research progress was made in specification of the technical requirements, design and fabrication of the SCIIB sensor probes, development of the sensor systems, development of DSP-based signal processing techniques, and construction of the test systems.

During the second year, research efforts were directed towards improvement of the fabrication processes for SCIIB sensors, evaluation and improvement of the performance of the SCIIB optoelectronic signal conditioning system, and development and testing of strategies for the protection of optical fibers and sensors in the downhole environment.

Building upon the demonstrated success in the first two years, the sensor system performance was improved dramatically during the third year:

- By selecting suitable materials for the glass tube and optical fiber, the cross-sensitivity of the pressure and temperature sensors was minimized.
- A metal foil based sensor packaging technique was developed for both mechanical protection and a waterproof isolation medium.
- Most of the important noise sources in the SCIIB signal demodulation system were analyzed and identified by both theoretical analysis and experiment. Several compensating structures were designed which improved the system stability.
- To satisfy the strict performance requirements for the pressure and temperature sensors, a spectrometer based white light signal demodulation system was developed. By using a novel data processing method invented at CPT, the stability of this system is better than 0.5psi with a 6000psi dynamic range. The resolution of the white light system has been shown to be 0.03nm corresponding to 0.03 psi for the pressure sensor system.
- During the first field test, the sensor was successfully deployed using Chevron's hydraulic deployment method into a test well in Coalinga, California, the remote data access through internet was realized allowing real-time data monitoring from virtually anywhere in the world and the long-term stability of the sensor head in downhole environment verified.

During the fourth year, research efforts were focused on the development and evaluation of the fiber optic flow sensor system, flow sensor field testing in Tulsa, OK and the second, more extensive, field testing of the pressure and temperature sensors in Coalinga, CA.

- The feasibility of a self-compensating fiber optic flow sensor based on a cantilever beam and interferometer for real-time flow rate measurements in the fluid filled pipes of oil field was clearly demonstrated.
- Prototype flow sensors were fabricated based on the fabrication experience of hundreds of test sensors.
- A lab-scale flow testing system was constructed and used for prototype sensor evaluation.
- Field-testing was performed in both the indoor and outdoor flow testing facility at the University of Tulsa, OK.
- Testing of a white light pressure and temperature sensor system continued in the oil fields of the Chevron/Texaco Company in Coalinga CA

1.0 Introduction

This is the final report for the Virginia Tech Center for Photonics Technology (VTCPT) research project "Optical Fiber Sensor Technologies for Efficient and Economical Oil Recovery." The main objective for this four and one-half year program has been the development and demonstration of cost-effective, reliable optical fiber sensors for the measurement of temperature, pressure, flow, and acoustic waves in downhole environments for use in oil recovery.

The sensors developed under this program are based on the Self-Calibrated Interferometric/Intensity-Based (SCIIB) and white light interferometer fiber optic sensor configurations invented at the Center for Photonics Technology. The SCIIB design measures displacement (elongation or contraction) of a small Fabry-Perot interferometer cavity constructed in an optical fiber. The Fabry-Perot assembly is typically cylindrical, and generally has dimensions on the order of 0.1 mm in diameter and 5 mm long. By proper mechanical design of the assembly, physical parameters such as pressure, temperature, flow, and acoustic waves can be made to induce a displacement in the Fabry-Perot assembly, which may then be measured by the SCIIB system. In the SCIIB configuration, the Fabry-Perot assembly is designed so that the output of the cavity over the sensor's dynamic range is limited to the quasi-linear region of the interference signal output of the cavity. In this way, interpretation of the nonlinear output of typical interferometers is avoided, simplifying the signal processing.

The SCIIB system uses optical filtering to process the optical signal output so that two signals are produced: one which contains information about the cavity displacement, and another that contains information regarding undesired effects in the first signal, such as fluctuations in the optical source power, or changes in optical fiber loss. The second signal is used as a reference to eliminate these undesired effects, and provide self-calibration functions in the sensor.

In the third year of the program a new white light interferometry-based signal demodulation system was developed. Both the SCIIB system and the white light system have their own specific advantages. The white light system was developed to provide extremely high resolution measurements at moderate frequencies. The SCIIB system provides very high frequency response high resolution measurements. The white light system was employed in the field tests for pressure, temperature and flow measurement.

This report describes in detail the development of the automated sensor fabrication system; two separate instrumentation systems – SCIIB and white light; temperature, pressure, flow and acoustic sensors; sensor packaging methods; and results of the successful field testing in Tulsa, OK and Coalinga, CA.

2.0 Background

Data published by the U.S. Department of Energy [1] indicate that approximately two-thirds of the oil discovered in the U.S. remains in the ground after the primary, secondary and tertiary recovery operations have been completed. This is largely due to the limited availability of information concerning reservoirs, well operation and well-to-well interrelations. Real-time, on-line measurement and monitoring of some key physical parameters as well as their temporal and spatial variations in reservoirs and wells is therefore vitally important. Significant improvements in the capability, cost-effectiveness and reliability of instrumentation for oil recovery can lead to reductions in development cost, lower operating costs and higher recovery factors.

Real-time monitoring of temperature in wells is important in the monitoring and management of steam floods in heavy oil reservoirs, detecting inflows in horizontal wells, and in optimizing the performance of electrical submersible and progressive cavity pumps. Continuous reliable downhole pressure measurements from wells will provide key data that will permit better, faster reservoir characterization and improved forecasting of reservoir capability, thereby permitting operators to optimize the economic recovery of reserves. Measurement of oil flow at various critical locations in a reservoir would provide important information about reservoir architecture, geometrical dimensions, zonal performance, and well-to-well interactions, and further contribute to reservoir optimization and reserves recovery. Acoustic wave detection would provide 4D geophysical data, sand influx data, hydrate or wax detection, and completion/infrastructure monitoring. This would provide an excellent view of reservoir depletion as well as permit the optimization of production infrastructure.

Although the measurement of these physical parameters is highly desirable in the oil industry, the hostile environment involved in wells and reservoirs, the strict technical requirements on measurements, and the unavailability of reliable sensors has unfortunately made obtaining the needed data impractical. Some of the major measurement difficulties include 1) remote operation, 2) immunity to electromagnetic interference (EMI), 3) high temperature and pressure environments, 4) strict requirements on measurement resolution and accuracy, 5) small size, and 6) multi-year reliability. Moreover, due to the increasing application of offshore drilling and horizontal wells, some of the measurement difficulties described above are further increased. These combined difficulties render conventional electrical and electronic sensors and measurement devices very difficult to apply and incapable of meeting the current and future oil industry's needs. This situation suggests that innovative sensors be developed to support the industrial efforts for more efficient and economical oil recovery, which benefits the entire nation.

Optical fiber-based sensing instrumentation has been demonstrated to be especially attractive for the measurement of a wide variety of physical and chemical parameters because of such inherent advantages as 1) an immunity to EMI, 2) avoidance of ground loops, 3) capability to

respond to a wide variety of measurands, 4) avoidance of electric sparks, 5) resistance to harsh environments, 6) remote operation, 7) capability of multiplexing, and 8) ease of integration into large-scale fiber networking and communication systems. Because of these inherent advantages, fiber sensors are attractive to the oil industry.

Most of the fiber sensors developed to date may be classified into two groups: interferometers in which optical phase is affected, and intensity-based devices in which optical intensity is modulated. In general, interferometric sensors have the advantages of ultra-high resolution, accuracy and configurational versatility. However, they have the disadvantages of relative measurement, costly signal processing and low frequency response. In contrast, the intensity-based devices have the advantages of simple signal demodulation, absolute measurement, and high frequency response. Because of the advantages of these two types of fiber sensors, tremendous efforts have been made to combine the two sensor types into a single sensor design to obtain all the major advantages at the same time. Due to significant difficulties encountered by the researchers, however, limited progress was made.

The Center for Photonics Technology at Virginia Tech developed an optical fiber-based sensor technology, the Self-Calibrated Interferometric/Intensity-Based (SCIIB) fiber sensor [2]. To our knowledge, this was the first time to successfully realize the combination of fiber interferometry and intensity-modulated sensing in a single sensor element. In addition to the generic advantages of optical fiber sensors, the new technology has also been shown to have all the distinct advantages of interferometric and intensity-based sensors, while their disadvantages are eliminated or significantly minimized.

The purpose of this four and a half -year program was to expand the basic breakthrough fiber optics telemetry technology to develop cost-effective, reliable fiber sensors optimized for downhole applications in the oil industry, to meet the increasing needs for innovative sensors that allow significant improvement in oil recovery. The program involved active participation from Chevron and the University of Tulsa.

3.0 Specification of Technical Requirements

In the first year of this program, CPT personnel worked closely with the engineers from Baker Hughes and Chevron to specify the technical requirements for the downhole measurements. The specifications for sensor performance shown in Table 3-1 were adopted based on input from Baker Hughes and used as guidelines for sensor design and fabrication.

Table 3-1. Initial sensor specifications.

Sensor	Specification	Value
Temperature	range	-40 to +200°C
	accuracy	± 1.0°C
	resolution	0.01°C
	pressure	To 20,000 psia
Pressure	ranges	0 to 5,000 psia 0 to 10,000 psia 0 to 16,000 psia 0 to 20,000 psia
	accuracy	± 0.03% F.S.
	resolution	0.01 psia
	temperature	-55 to +250°C
Flow	range	0 to 100,000 barrels/day
	accuracy	10% F.S.
	resolution	0.1% F.S.
	temperature	0 to 177°C
	pressure	0 to 16,000 psia

4.0 SCIIB Sensor System Overview

The self-calibrated interferometric/intensity-based (SCIIB) fiber optic sensor successfully combines the advantages of both the interferometric and the intensity-based fiber sensors in a single system. Through proper sensor design, the SCIIB technology can provide absolute measurement of various parameters with the full self-compensation capability for source power fluctuation and changes in fiber loss. Starting with a review of fiber optic Fabry-Perot sensing techniques, this chapter presents the SCIIB system configuration, followed by a detailed discussion of the unique signal processing method and the results of the preliminary sensor performance testing.

4.1 Principle of Operation

The basic SCIIB configuration is shown in Figure 4.1. The light from a broadband optical source is launched into a two-by-two fiber coupler and propagates along the optical fiber to the sensor head. For the multimode SCIIB system (which is suitable for short distance application), the light source is an 850nm LED. In the single mode system, a 1310nm SLED is used. As shown in the inset of Figure 4.1, the input fiber and a reflector are thermally fused to a hollow glass tube with a predetermined air gap separation. By thermally fusing the glass capillary tube to the glass fibers, the use of organic adhesives such as epoxy is avoided, eliminating the temperature limits, temperature-dependent mechanical properties and hysteresis of those adhesives. The incident light is first partially reflected at the endface of the input fiber (R1 in Figure 4.1). The remainder of the light propagates across the air gap to the reflector surface where a second reflection (R2) is generated. The two reflections travel

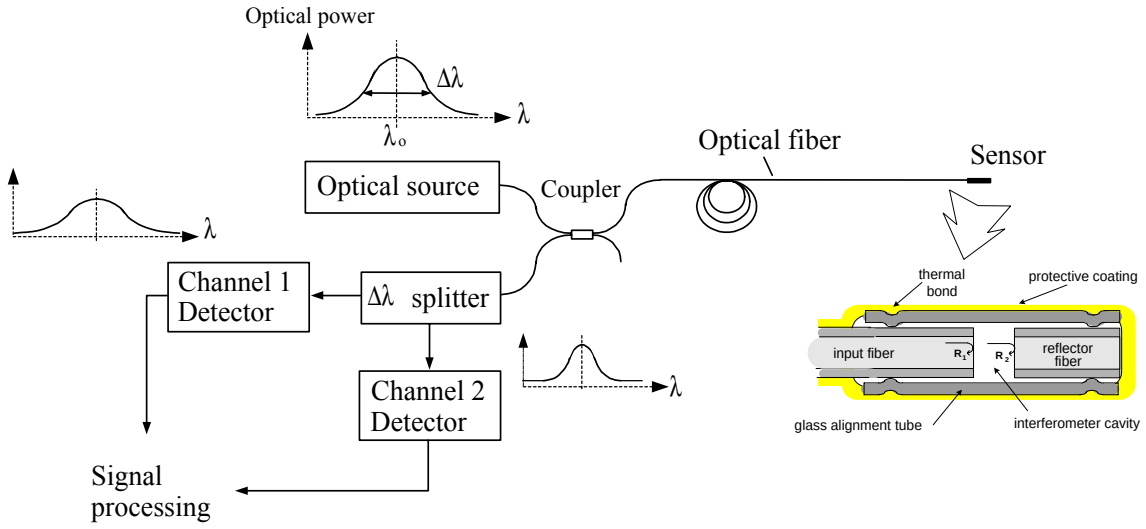

Figure 4.1. Illustration of the principle of SCIIB fiber optic sensor system.

back along the same input fiber through the same coupler to the photodetection end. The signal-processing portion of the SCIIB system extracts the information about the Fabry-Perot cavity length, which is related to various measurands governed by different physical laws.

In order to overcome problems associated with conventional fiber interferometric sensors, such as relative measurement, low frequency response, and complexity in signal demodulation, a special optoelectronic signal demodulation method is employed that allows self-calibrating absolute measurement with high frequency response. When the source coherence length is longer than the path length difference of the two legs in an interferometer, interference is observed when the two reflections are combined; when it is less than the path length difference, interference does not occur, and the combination of the two beams results in the sum of their intensities. In the SCIIB system, the coherence length of the sensor channel (Channel 2 in Figure 4.1) is engineered to exceed the path length difference in the Fabry-Perot cavity (twice the gap length), resulting in interference fringes as the gap length is changed by the measurand of interest. The coherence length of the reference channel (Channel 1 in Figure 4.1) is adjusted to be much shorter than the path length difference in the Fabry-Perot cavity. Therefore, no interference occurs and the power output of the reference channel is simply the sum of the optical power of the two reflections R1 and R2. Both channels are affected by changes in fiber loss, bending, connector loss and fluctuations in source power, while only the sensor channel exhibits changes due to the effect of the desired measurand, e.g. temperature or pressure, on the gap length.

As shown in Figure 4.2, when the cavity length changes, one photodetector exhibits an interference signal output while the other is relatively unchanged because the initial air-gap length is larger than the coherence length of the original source. The undesired fluctuations can be canceled out by taking the ratio of the two channels. To simplify the processing and interpretation of the sensor output, the sensor probe is designed so that the optical intensity of the output over the expected full range of the measurand remains within the quasi-linear

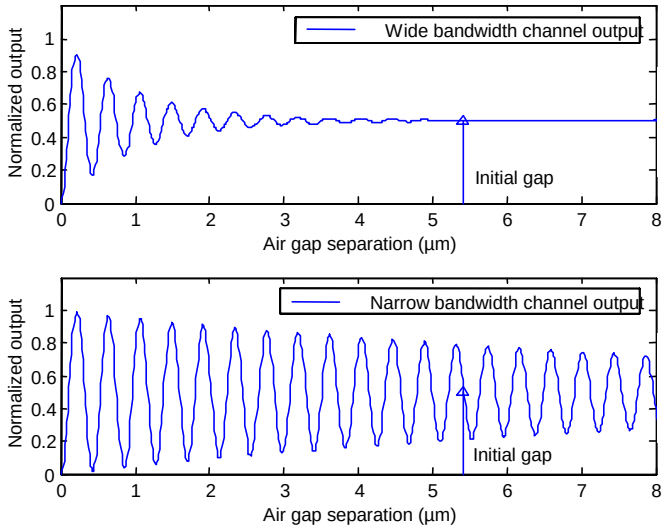

Figure 4.2. Illustration of the two channel outputs of the SCIIB sensor.

portion of the interferometric output. This is accomplished by controlling the length, diameter, wall thickness, and the modulus of elasticity of the capillary alignment tube during sensor fabrication. In this way, complicated signal processing involving fringe counting or spectral decomposition can be avoided, and a simple photodetector used.

The SCIIB fiber optic sensor system can be used to measure different physical parameters, for instance, temperature, pressure, strain and acoustic waves. The sensor head can be specially designed to be only sensitive to the parameter of interest. In general, the measurand interacts with the sensor head and causes a change of the air gap. The SCIIB sensor system relates the air gap change to the measurand according to the physical principles governing the interaction, and directly gives the measuring results.

4.1.1 Optimal Cavity Length

The coherence length of a source is inversely proportional to its spectral width. The coherence length Lc can be estimated by

$$L_c \approx \frac{\lambda_c^{\,2}}{\Delta\lambda}, \qquad \textbf{(4-1)}$$

where λ_c is the central wavelength of the source and $\Delta\lambda$ is the spectral width of the source. Assuming that the spectral characteristics of the original source spectrum and the optical bandpass filter can be approximated as Gaussian profiles with a spectral width of $\Delta\lambda_1$ and $\Delta\lambda_2$, the output spectra of the two SCIIB channels can thus be expressed by

$$I_{s1.s2}(\lambda) = \frac{2I_{10,20}}{\sqrt{\pi}\Delta\lambda_{1,2}} \exp\left(-\frac{(\lambda-\lambda_c)^2}{\Delta\lambda_{1,2}^{\,2}}\right), \qquad \textbf{(4-2)}$$

where $I_{10,20}$ are the optical powers of the two channels respectively, and λ_c is the central wavelength for both channels (here, we assume that the two channels have the same central wavelength). The interference signals resulting from the spectra of the two channels can thus be written as

$$I_{1,2} = R \cdot \int_{-\infty}^{\infty} I_{s1,s2}(\lambda)[1+\eta^2(1-R)^2 - 2\eta(1-R)\cos(\frac{4\pi}{\lambda}L)]d\lambda, \qquad \textbf{(4-3)}$$

where

$I_{s1,s2}$ are the spectral power density distribution of the two channels respectively,
R is the reflectance at the boundary of the air and the fiber endface,
L is the cavity length, and
η is the coupling coefficient of the Fabry-Perot cavity. It is a function of the cavity length L, the lateral offset, and the angular offset. Because the initial cavity length usually is chosen to be very small, the optical loss of the cavity is very small. Therefore, η can be approximated as 100%.

The reflectance *R* can be calculated by

$$R = [\frac{(n-n')}{(n+n')}]^2, \qquad \textbf{(4-4)}$$

where *n* is the refractive index of the fiber core, and *n′* is the refractive index of the medium forming the cavity between two fibers, which in our case is the air. The reflectance at the fiber endfaces is thus about 4% of the total incident optical power.

Notice that since the reflectance is relatively small, the interference signals given by Eq. 4-3 can thus be approximated by

$$I_{1,2} \approx 2R \cdot \int_0^\infty I_{s1,s2}(\lambda)[1-\cos(\frac{4\pi}{\lambda}L)]d\lambda, \qquad \textbf{(4-5)}$$

Eq. 4-5 indicates that the interference signal is the superposition of interference contribution of all the spectral components, assuming that the photodetectors have a flat response over the source emission spectrum. By taking the ratio of the two channels outputs, the SCIIB output is then given by

$$s = \frac{I_2}{I_1} \approx \frac{\int_{-\infty}^{\infty} I_{s2}(\lambda)[1-\cos(\frac{4\pi}{\lambda}L)]d\lambda}{\int_{-\infty}^{\infty} I_{s2}(\lambda)[1-\cos(\frac{4\pi}{\lambda}L)]d\lambda}. \qquad \textbf{(4-6)}$$

The output signals from the two SCIIB channels and the ratio given by Eq. 4-6 are plotted as a function of the sensor cavity length in Figure 4.3 and Figure 4.4 for the singlemode fiber sensor case, corresponding to a source spectral width of 40nm and bandpass filter spectral width of 10nm, and in Figure 4.5 and Figure 4.6 for the multimode fiber sensor system, corresponding to a source spectral width of 70nm and bandpass filter spectral width of 10nm. If the sensor probe is fabricated such that it has an initial cavity length larger than the coherence length of Channel 1 but smaller than the coherence length of Channel 2, then, as shown in Figure 4.3 and Figure 4.4, Channel 1 becomes an intensity channel with its output relatively unchanged, while Channel 2 retains its highly visible interference fringes as the cavity length changes. The output from Channel 1 (non-interference channel) and Channel 2 (interference channel) of the SCIIB sensor can then be expressed as

$$I_1 \approx 2RI_{10}, \qquad \textbf{(4-7)}$$

and

$$I_2 = 2R \cdot I_{10} \cdot \alpha \cdot [1-\gamma\cos(\frac{4\pi}{\lambda}L)], \qquad \textbf{(4-8)}$$

where, α is the power loss of the optical filter in Channel 2, given by

$$\alpha = \frac{I_{20}}{I_{10}}, \qquad \textbf{(4-9)}$$

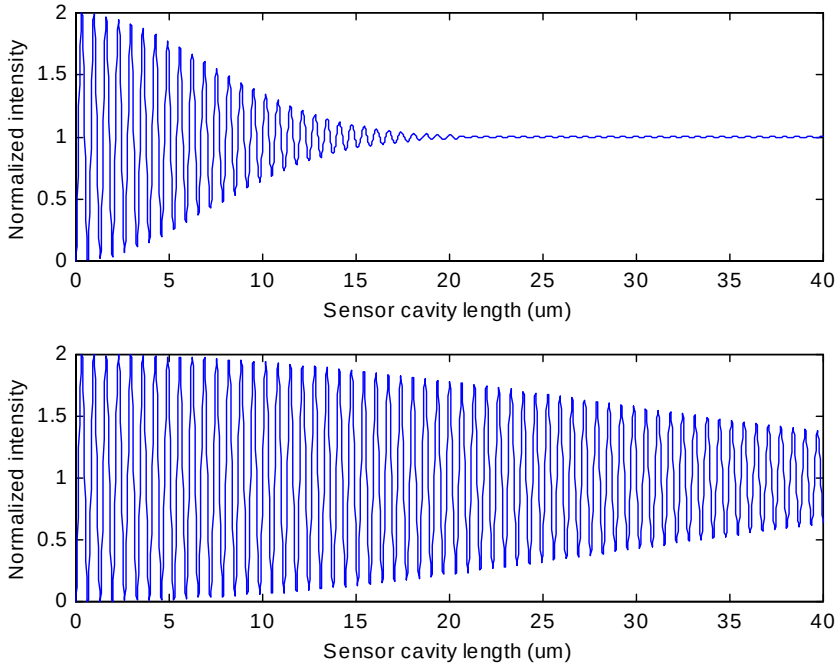

Figure 4.3. Interference fringes of the two SCIIB channels for a source spectral width of 40nm and center wavelength of 1310nm, and a bandpass filter spectral width of 10nm, corresponding to the singlemode fiber sensor system.

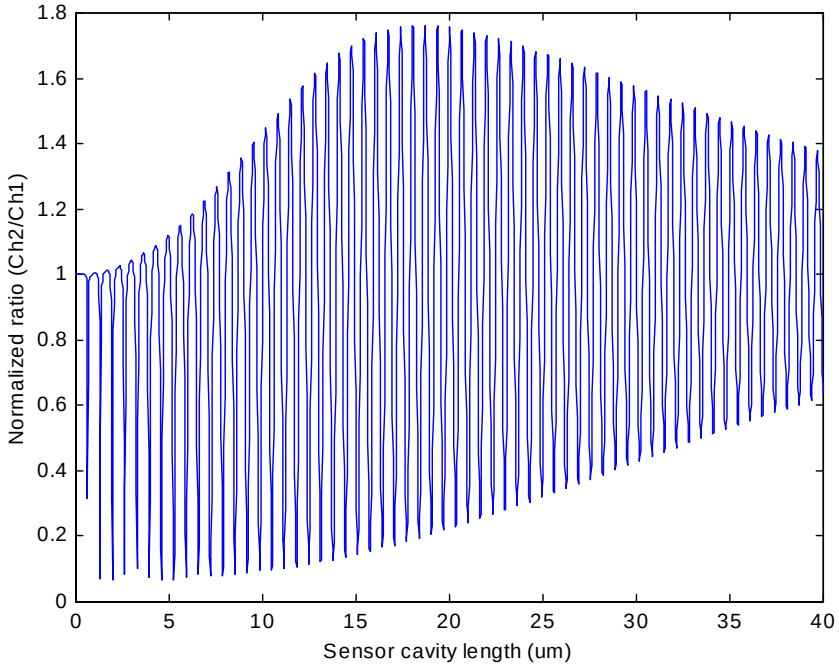

Figure 4.4. Ratio of the two channel outputs shown in Figure 4.3.

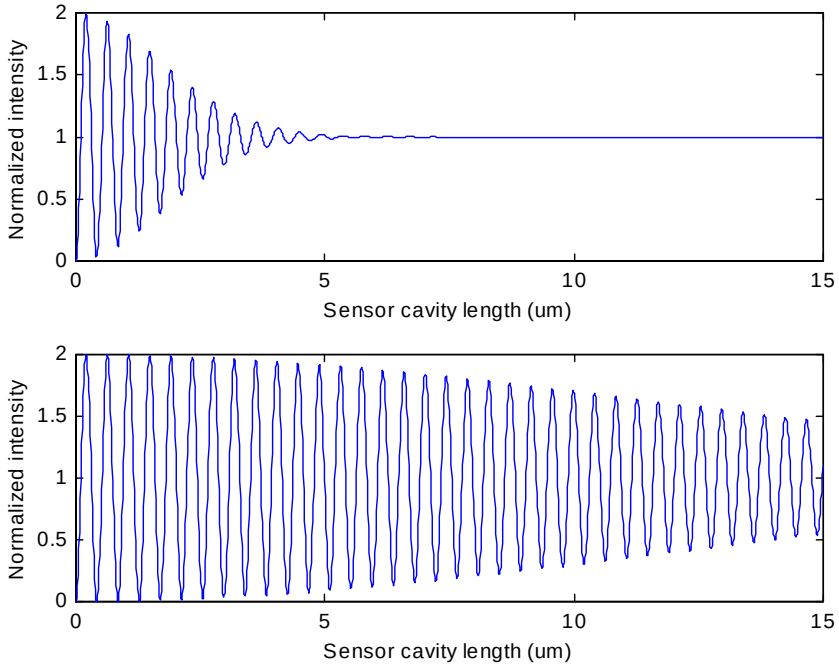

Figure 4.5. Interference fringes of the two SCIIB channels for a source spectral width of 70nm and center wavelength of 850nm, and a bandpass filter spectral width of 10nm, corresponding to the multimode fiber sensor system.

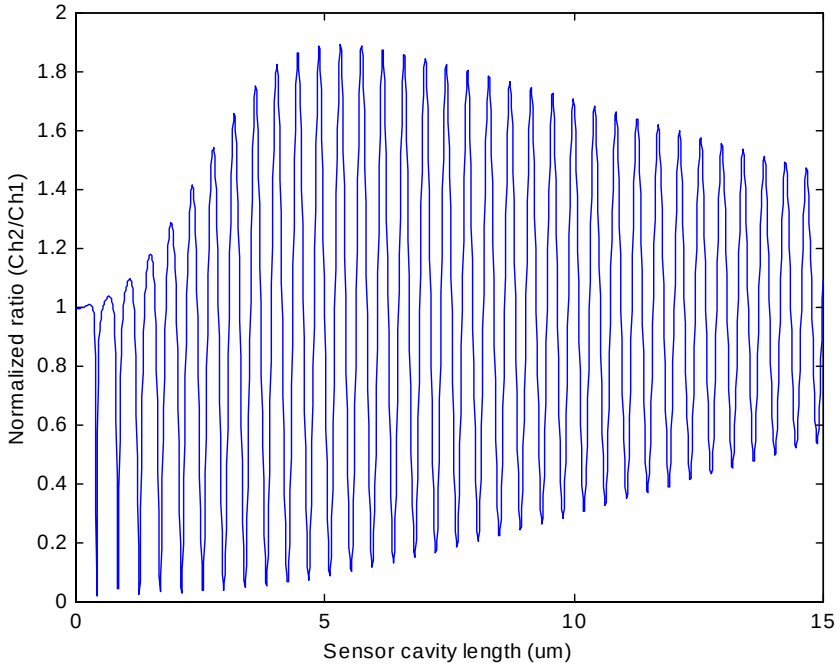

Figure 4.6. Ratio of the two channel outputs shown in Figure 4.5.

and γ is the fringe visibility of the Channel 2 signal, defined by

$$\gamma = \frac{I_{\max} - I_{\min}}{I_{\max} + I_{\min}}, \qquad \textbf{(4-10)}$$

where, I_{max} and I_{min} is the maximum and minimum intensity of the optical interference respectively. The fringe visibility in our case is a function of η, R, and $\Delta\lambda_2$.

In principle, continuously tracking the phase change of the interference fringes in Channel 2 would permit measurement of the change of the cavity length of the sensor head, and similar to the output of a regular interferometer, the measurement will have ultra-high sensitivity. One period of fringe variation corresponds to an air gap change of one-half of the optical wavelength. However, fiber loss variations and laser power drift can introduce errors in the amplitude of the interference signal and result in poor measurement accuracy. To avoid these two adverse effects, Channel 1 is used as a reference signal, and the SCIIB sensor output is evaluated as the ratio of the two signals of the two channels, given by

$$s = \frac{I_2}{I_1} \approx \frac{2RI_{10}\alpha[1-\gamma\cos(\frac{4\pi}{\lambda}L)]}{2RI_{10}} = \alpha[1-\gamma\cos(\frac{4\pi}{\lambda}L)] \qquad \textbf{(4-11)}$$

This ratio is only a function of the Fabry-Perot cavity length, eliminating these two sources of error from the final measurement result.

To assure proper self-referencing of the SCIIB sensor system, it is important to choose an optimal initial sensor cavity length that gives the signal channel maximum fringe visibility and at the same time suppresses the interference of the reference channel to minimum. The choice of the optimal initial cavity length will mainly depend on the spectral widths of the two SCIIB channels. For example, in the case shown in Figure 4.3 and Figure 4.4, the initial cavity length can be chosen between 20 and 30μm. For the case shown in Figure 4.5 and Figure 4.6, the initial cavity length can be somewhere between 7 and 12μm. Other considerations in determining an optimal initial cavity length will be discussed in greater detail in the sections below .

4.1.2 Linear Operating Range

Regular interferometric sensors suffer from the disadvantages of sensitivity reduction and fringe direction ambiguity when the sensor output reaches the peak or valley of an interference fringe. Sensitivity is reduced since at the fringe peak or valley the change in optical intensity is zero for a small change in the sensor cavity length. Fringe direction ambiguity refers to the difficulty in determining from the optical intensity whether the sensor cavity is increasing or decreasing. To avoid these two problems, the SCIIB sensor head is designed and fabricated to operate only over the semi-linear range of a half fringe, as shown in Figure 4.7, so that a one-to-one quantitative relation between output intensity and the sensor cavity length is obtained.

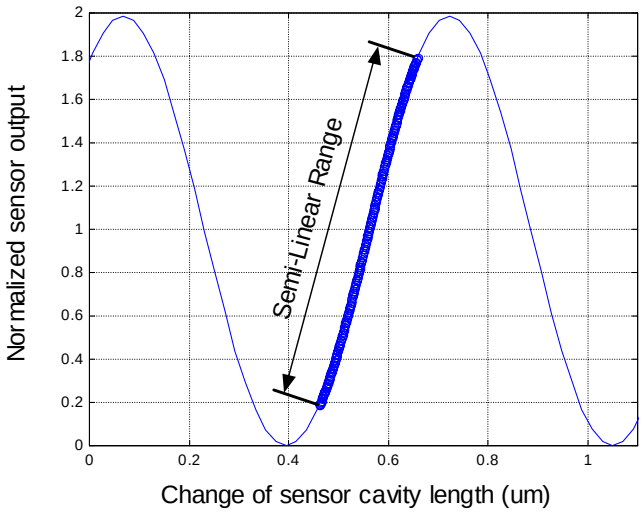

Figure 4.7. Illustration of a semi-linear fringe operating range.

The operating range of the SCIIB sensor is defined based on its sensitivity. From Eq.4-11, the sensitivity of the SCIIB sensor can be calculated as

$$Sensitivity = abs(\frac{ds}{dL}) = abs(\alpha\gamma\frac{4\pi}{\lambda}\sin(\frac{4\pi}{\lambda}L)). \qquad \textbf{(4-12)}$$

The maximum sensitivity, given by

$$Maximum \quad Sensitivity = \alpha\gamma\frac{4\pi}{\lambda}, \qquad \textbf{(4-13)}$$

is obtained at the quadrature (Q)-points of the interference fringes. Correspondingly, we define the operating range of the SCIIB sensor as the range where its sensitivity remains within 60% of the maximum sensitivity:

$$\{Operating \quad Range\} = Solution\{abs(\alpha\gamma\frac{4\pi}{\lambda}\sin(\frac{4\pi}{\lambda}L)) \le \gamma\frac{4\pi}{\lambda}\cdot 60\%\}, \qquad \textbf{(4-14)}$$

which results in the maximum change in the signal level Δs, given by

$$\Delta s_{\max} = 1.6\alpha\gamma. \qquad \textbf{(4-15)}$$

4.2 SCIIB Advantages

In addition to the generic fiber sensor advantages such as small size, lightweight, remote operation, immunity to EMI, electrically non-conducting, and chemically inert, the unique SCIIB signal processing method combines the advantages of both interferometric and intensity-based sensors providing a number of other major advantages as summarized as below.

Ultra-high sensitivity
The SCIIB fiber optic sensor can offer very high resolution since the essence of the signal processing is based on interferometry.

Absolute measurement
The operating range of the SCIIB sensor is limited to the semi-linear range of half of an interference fringe; therefore the sensor output is a unique and almost linear function of the change of the cavity length. This one-to-one relation between the sensor output and the cavity length makes it possible to measure the absolute value of the sensor cavity length after the initial cavity length is chosen and fixed. Not only is the direction ambiguity problem resolved, but the sensitivity of the sensor is also kept relatively constant over the entire operating range.

Minimized complexity in signal processing
Because the signal processing of the SCIIB sensor only involves optical power detection and a simple ratio operation of the two output signals, the complexity of the system is kept to a minimum.

Self-compensation capability
Since the original broadband source spectrum is used as a reference signal, the drift of source power and fluctuations in fiber attenuation are thus fully compensated by the SCIIB signal processing.

High frequency response
Because very simple signal processing is used, the SCIIB sensor has a very high frequency response, which may be used to detect very high-speed signals such as acoustic waves or aerodynamic forces.

Geometric flexibility
The Fabry-Perot sensor head structure offers great design flexibility to accommodate the requirements of different applications.

4.3 Multimode Fiber Sensor

Two SCIIB sensor systems were designed and fabricated; multimode fiber was used for short distance applications, and singlemode for long distance applications. Since multimode fibers have a larger core diameter than singlemode fibers, optical power can be coupled from the source into the fiber more efficiently. However, because of the relatively high loss of multimode fibers at the operating wavelength, the system is primarily designed for low cost, short distance applications, typically less than one kilometer from the actual sensing region to the signal processing unit. The multimode system was designed to operate at a center wavelength of 850 nm and uses 62.5μm/125μm standard telecommunication fibers. A schematic and photograph of the multimode SCIIB sensor system are shown in Figure 4.8. The spectrum of the LED source (Honeywell, HEF 4854-014) is shown in Figure 4.9, with its central wavelength of 850 nm, spectral width of 70 nm, and the typical output power of 120

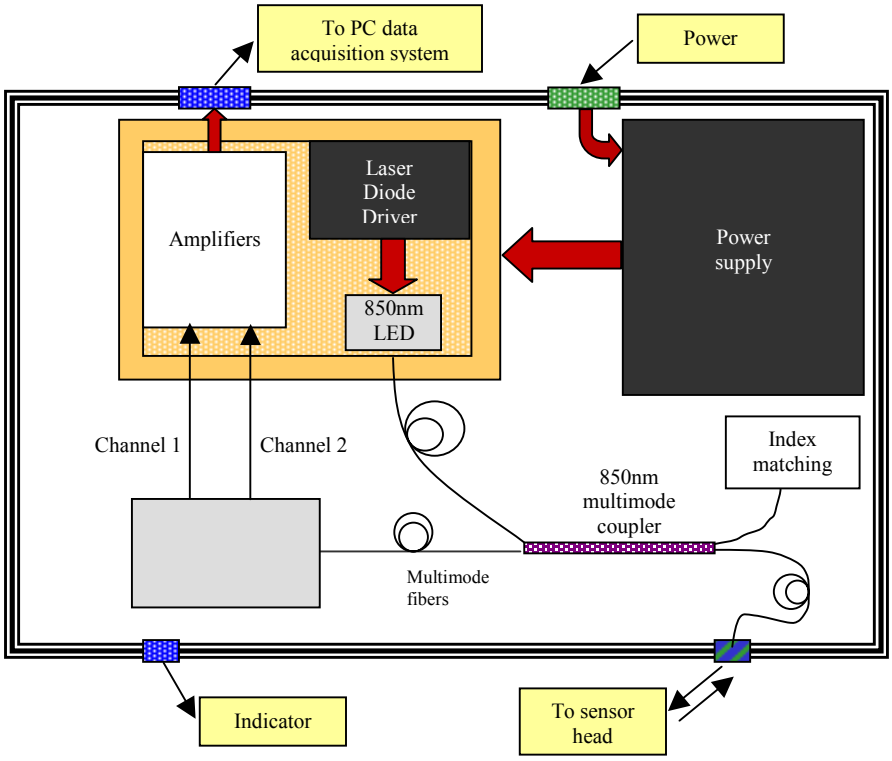

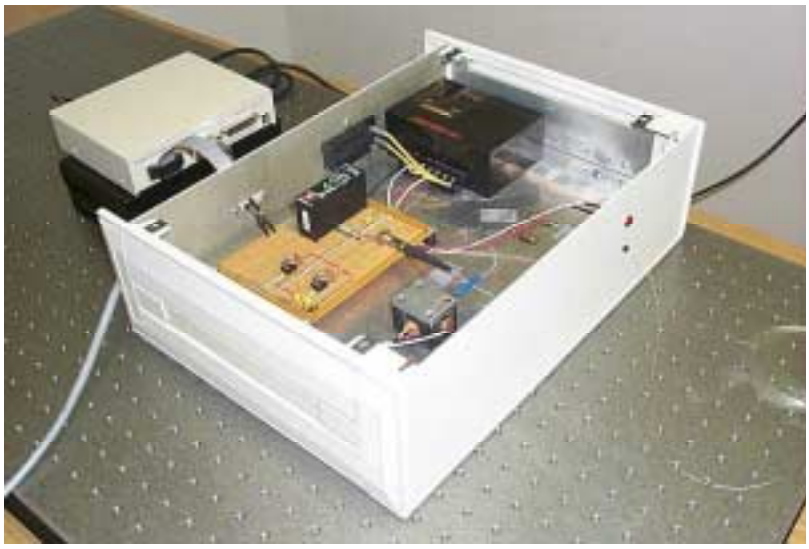

Figure 4.8. Multimode fiber SCIIB sensor system, schematic (top) and photograph (bottom).

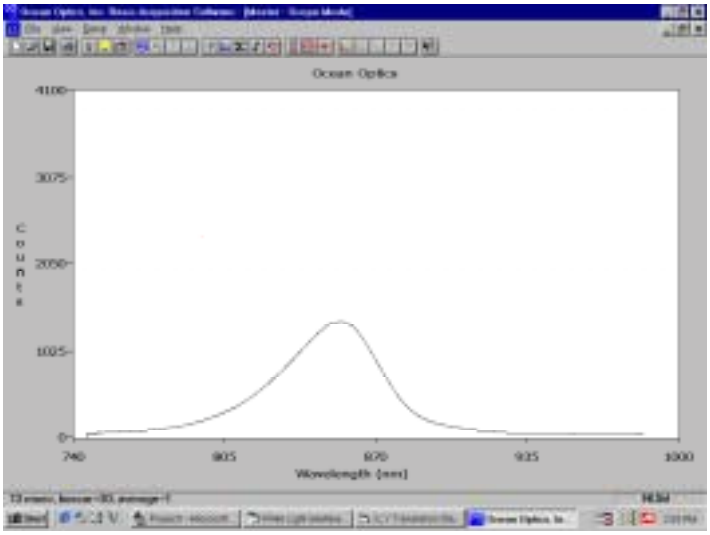

Figure 4.9. Optical spectrum of the source LED for the multimode SCIIB system (center wavelength 850 nm, spectral width 70 nm, and typical output power 120 μW).

μW. In the multimode fiber system, a polarization insensitive cubic beam splitter with a splitting ratio of 50:50 is used to split the light from the sensor head into two channels. One portion of the light from the beam splitter passes through an optical bandpass filter with a center wavelength of 850 nm and a full width at the half maximum (FWHM) of 10 nm. Two silicon detectors with large effective areas (31 mm^2) are used to receive the signals of the channels. Following the two transimpedance amplifiers, the signals from the two channels are sampled and converted to digital data by a high-precision A/D converter. The ratio of the two channel signals is then calculated by the host computer.

4.4 Singlemode Fiber Sensor

Singlemode fibers have very low optical attenuation, typically about 0.3dB/km at 1300nm and 0.2dB/km at 1550nm. Therefore, light can be transmitted for very long distances. However, due to the small core diameter of singlemode fibers, it is relatively difficult to efficiently couple light from optical sources into the fiber. Also, low-noise detection of the light at 1300nm or 1550nm requires expensive InGaAs photodetectors. Therefore, the cost of singlemode fiber-based sensor systems is much higher compared to multimode systems. The singlemode fiber-based SCIIB sensor system is primarily designed for long distance applications, typically longer than one kilometer from the actual sensing region to the signal processing unit.

The singlemode SCIIB system (Figure 4.10) is designed to operate at a center wavelength of 1310 nm using a single-mode fiber to transmit optical signals between the sensor probe and the signal processing unit. The source is a high power superluminescent light emitting diode (SLED) provided by Anritsu Corp. (AS3B281FX), with a center wavelength of 1312 nm, a spectral width of 41.5 nm, and output power of 1.21mW from a 9/125μm pigtailed single-mode fiber. Figure 4.11 shows the source spectrum measured by an Ando Optical Spectrum

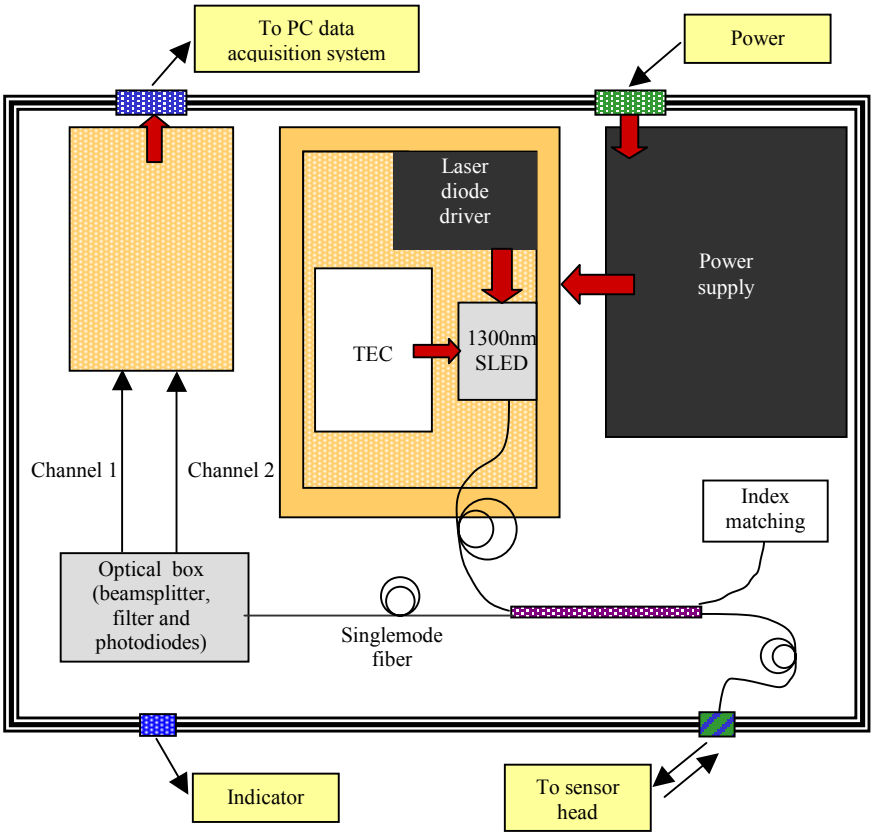

Figure 4.10. Singlemode fiber SCIIB sensor system, schematic (top) and photograph (bottom).

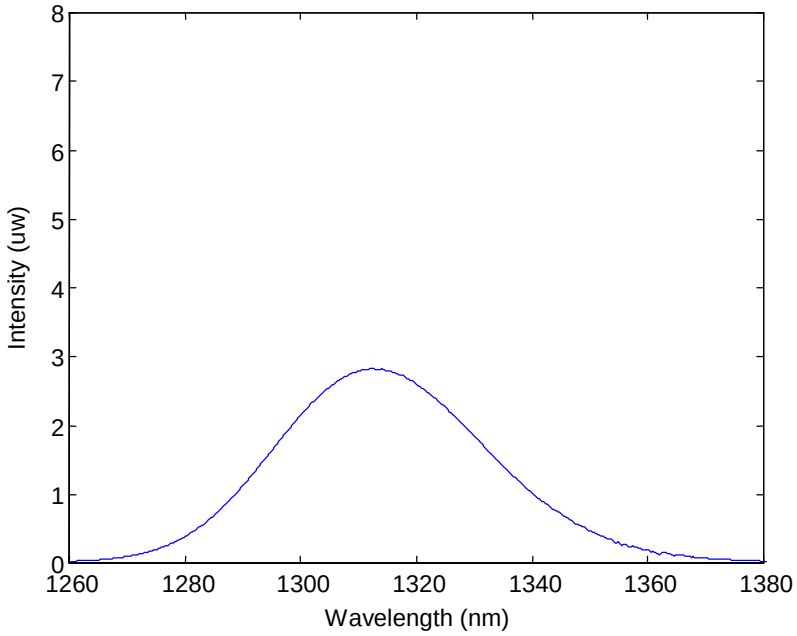

Figure 4.11. Optical spectrum of the SLED source measured by an Ando OSA (center wavelength 1312 nm, spectral width 41.5 nm, output power 1.21mW from a 9/125μm pigtailed single-mode fiber).

Analyzer (OSA). A polarization insensitive beam splitter with a splitting ratio of 50:50 at 1310nm is used to split the light signal from the sensor head into two channels. In one channel, the light passes through an optically neutral density filter in order to balance the two channels in terms of the optical power, and is detected by a large effective area InGaAs photo-detector and amplified to produce the reference signal. The light in the other channel passes through an optical bandpass filter with a center wavelength of 1310 nm and a FWHM spectral width of 10 nm. Because the spectral width of this channel is much narrower, an interferometric signal as the function of the sensor cavity length can thus be obtained after the photodetection. Similar to the multimode fiber-based system, the two channels' outputs are sampled and converted to digital signals and input to a host computer where the ratio and linearization can be performed easily.

4.5 Preliminary Sensor Testing

The self-compensating capability of the SCIIB systems were evaluated during the first two years of the program for source drift, fiber bending-induced loss, and spectral changes, which are unavoidable in actual fiber deployment.

4.5.1 Fiber loss compensation

An important advantage of the SCIIB sensor is its capability to self-compensate for fiber loss variation or source output power drift by using two channels with different coherence lengths. The self-compensation results from the fact that the optical power received at these two channels originates from the same source and experiences the same transmission path.

For instance, when fiber loss changes, it impacts both channel outputs, and by referencing one channel output to the other, we can eliminate this fluctuation.

Figure 4.12 shows experimental results from the fiber loss compensation test of the multimode fiber-based SCIIB system. The fiber used in the test was a standard telecom 62.5/125μm graded index multimode fiber, and the source was an LED with a center wavelength of 851.3 nm and a spectral width of 71.4 nm, provided by Honeywell (HEF4854-014). We introduced power loss to the system by manually bending the fiber to various diameters without changing the sensor cavity length. Two multimeters were used to record the output voltages from each channel. As expected, although the outputs of the two channels changed due to the increasing power loss, the ratio of the two channel outputs remained the same. The sensor output ratio varied less than 1% over the full testing range (up to 50% of the total power loss), which indicated that the implemented multimode fiber-based SCIIB system had an excellent self-calibration capability to compensate for variations in fiber loss.

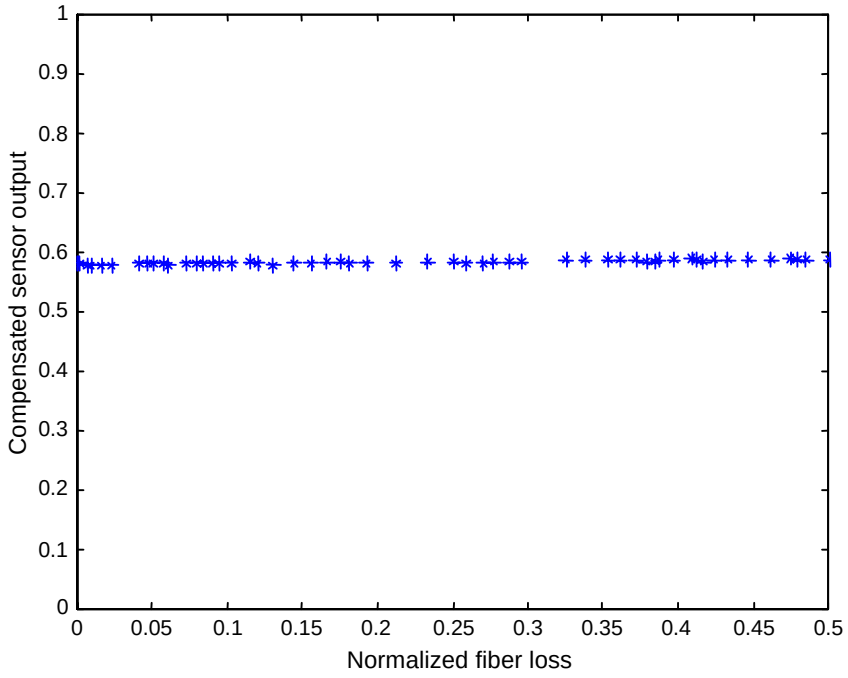

Figure 4.12. Multimode fiber SCIIB sensor output compensated for fiber bending loss.

The singlemode fiber SCIIB instrumentation was also evaluated. Without connecting to the sensor probe, the output power of the source (SLED) was varied by changing the driving current of the source chip. With the endface of the lead-out fiber well cleaved, the SCIIB instrumentation system should output a constant ratio, although each channel's output could change when the total optical power was changed. Two multimeters were used to record the two channels' output voltages and the ratio of the two channel was calculated. Figure 6-1 plots the recorded output from the two channels, as well as their ratio with respect to the driving current of the light source. Figure 4.14 magnifies the change in the SCIIB ratio as a

function of the normalized optical power of the source. The ratio of the two channels only changes by about 0.3% as the total optical power changes up to 50%.

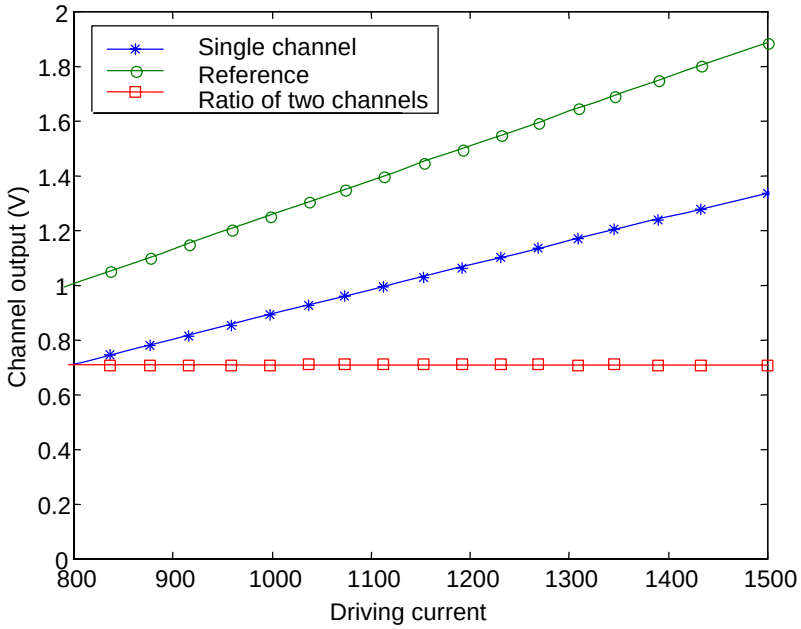

Figure 4.13. SCIIB output versus driving current of the optical source.

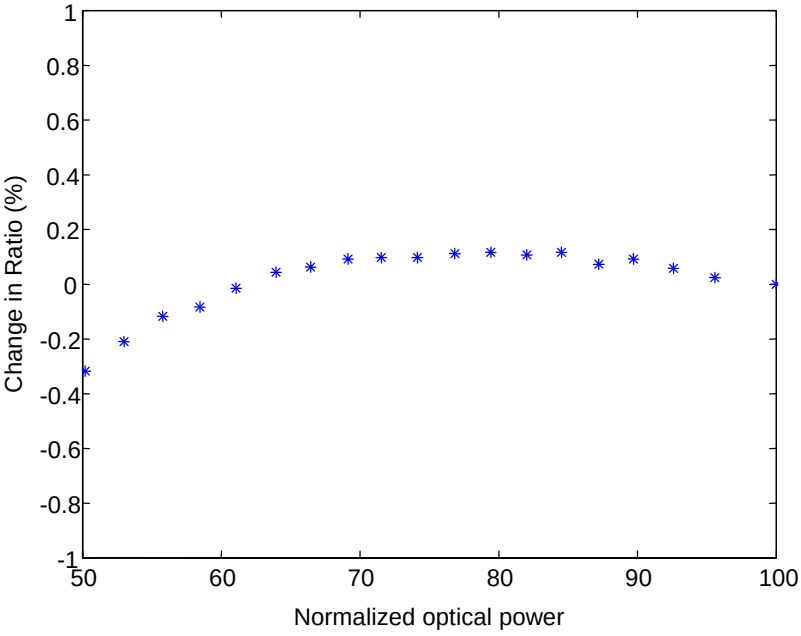

Figure 4.14. Change in SCIIB output ratio versus the normalized source power change.

Theoretically, changing the driving current of a semiconductor optical source would also change the spectrum in addition to the optical power change. The distortion of the source spectrum would also introduce error to the measurement result through the non-centered filtering effect; the measurement error is proportional to the offset between the center of the

optical bandpass filter and that of the source spectrum. Therefore, the error shown in Figure 4.14 also indicates the contribution from the source spectrum distortion. Nevertheless, the experimental results reveal that the SCIIB signal processing has a good self-compensation capability as expected.

4.5.2 Compensation for bending-induced spectral changes

In the singlemode case, changes in the optical spectrum are also induced by fiber bending. To investigate the measurement error induced by this spectral change, we conducted an experiment to study singlemode fiber bending. The schematic of the experimental setup is shown in Figure 4.15. A SLED made by Anritsu Corp. (AS3B281FX) with a center wavelength of 1310 nm, spectral width of 40 nm, and output power of 1.21mW was used as the source. The output from the source was transmitted through a section of testing fiber, and its spectrum was studied using an optical spectrum analyzer (OSA). By manually bending the fiber to certain radii, we were able to study the bending induced spectrum changes.

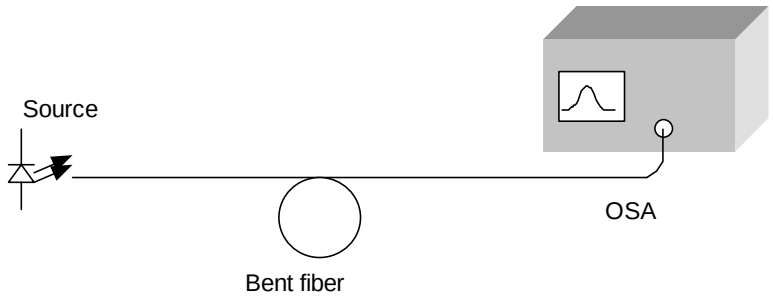

Figure 4.15. Experimental setup used to evaluate for fiber bending induced spectral changes.

In the first experiment, a section of standard telecom singlemode fiber was used. The fiber was bent to successively smaller radii of 12 mm, 5 mm, 4 mm, and 3 mm, respectively. The recorded spectra at these bending radii are plotted in Figure 4.16. The results indicate that the spectrum transmitted in standard telecom singlemode fiber can easily be distorted by bending the fiber. Within the spectral range of interest (1300 nm-1320 nm), the spectral fluctuation can reach a few dB under severe bending, which can easily introduce measurement errors to the SCIIB system.

Spectral fluctuation in telecommunications fibers is mainly due to the large mode field diameter of the waveguide. To eliminate these fluctuations, we can use bending insensitive fiber, which has a much smaller field diameter. In the second experiment, we used a section of bending insensitive single-mode fiber to repeat the above test. The fiber was purchased from Spectran Communication Fiber Technologies, Inc., and was designed for operation at the wavelength of 1300 nm. The test results are shown in Figure 4.17. Spectral fluctuations in the bending insensitive fiber are much smaller compared with that of the standard telecom fiber. Even under severe bending, the transmitted spectrum does not exhibit spectral fluctuations. Therefore, the experiment results suggest that the bending induced measurement errors can be minimized by applying bending insensitive fiber to the SCIIB system.

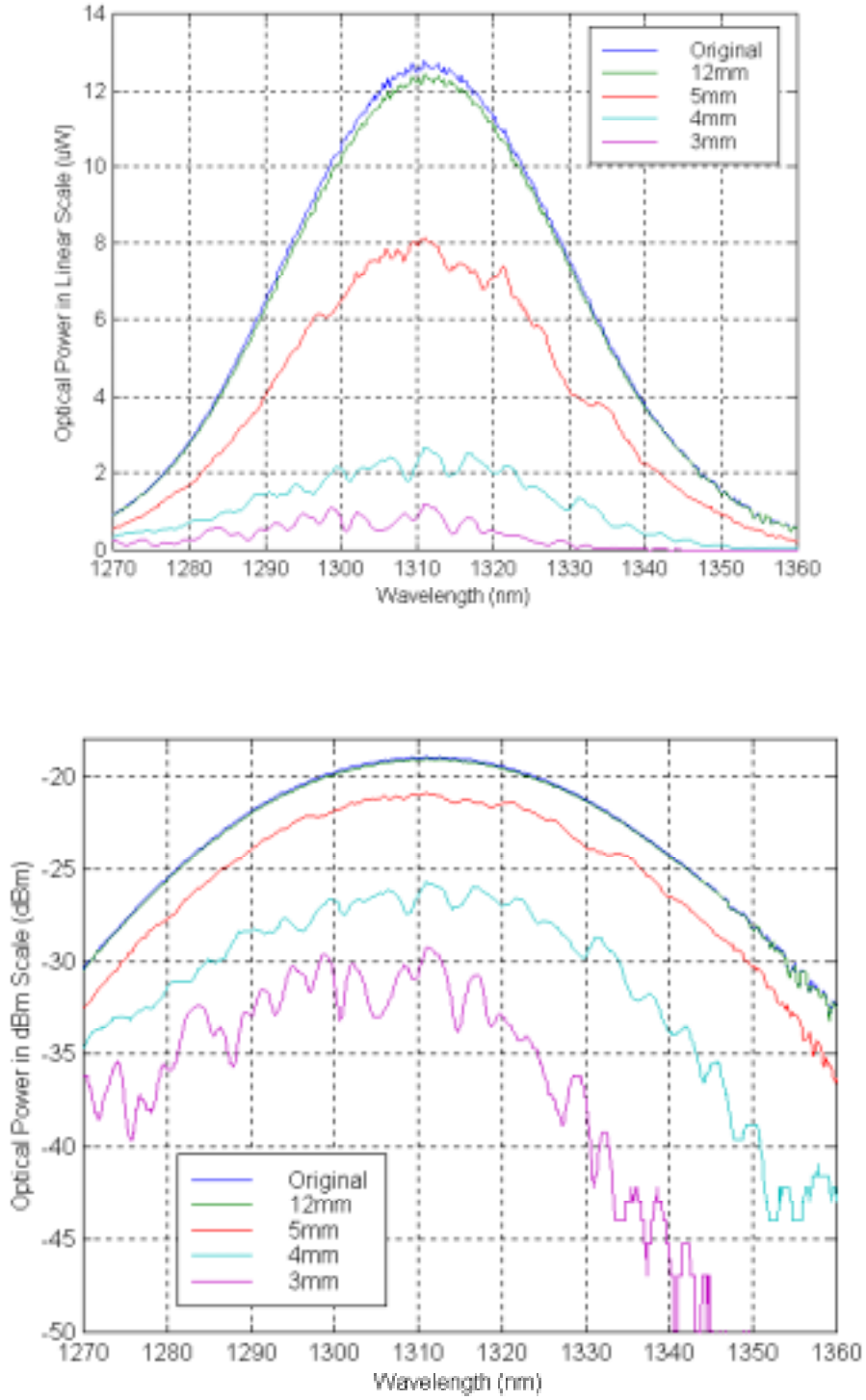

Figure 4.16. Bending induced spectral changes in standard singlemode telecommunications fiber.

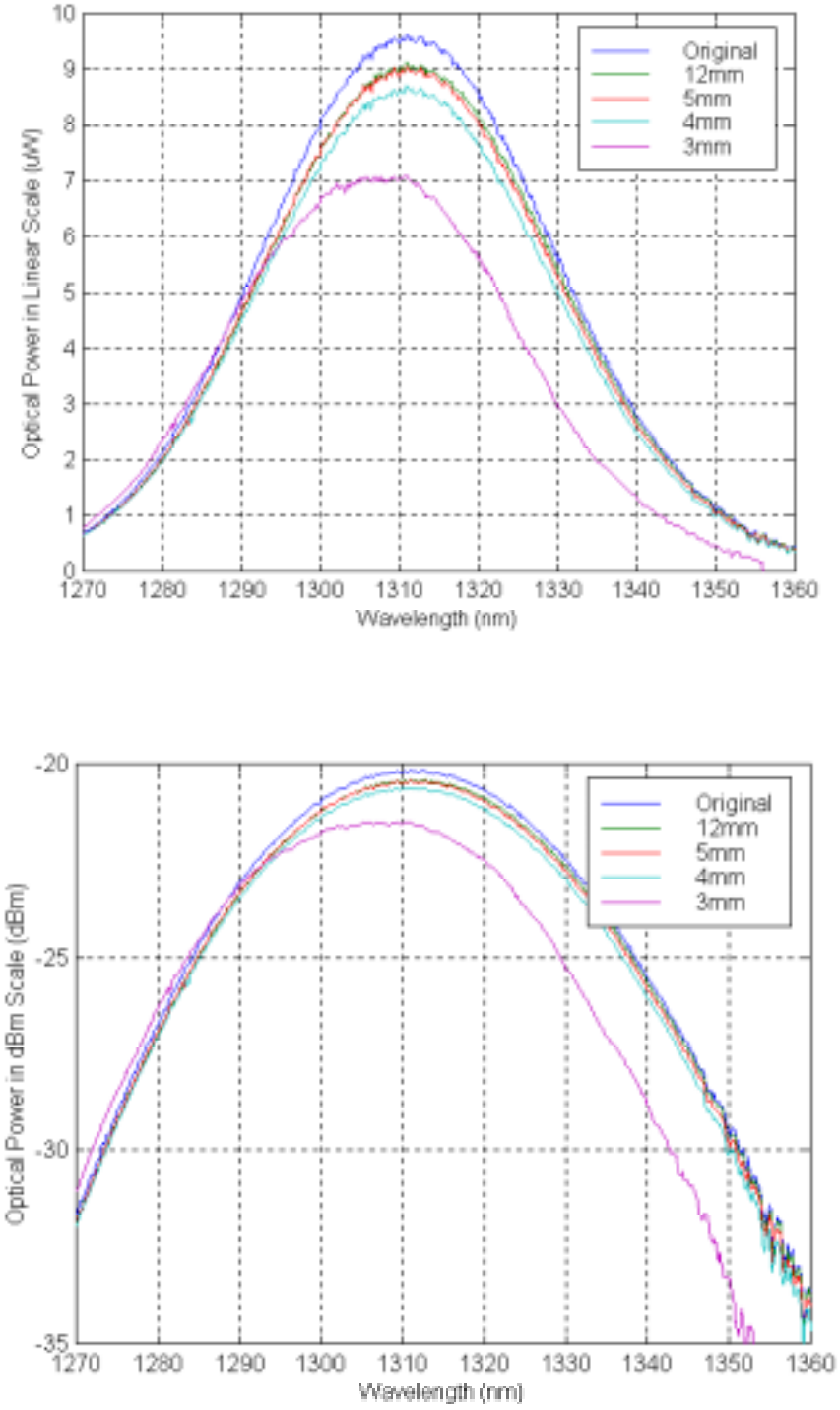

Figure 4.17. Bending induced spectral changes in bend insensitive singlemode fiber.

5.0 Instrumentation Systems

The first two years of the program were focused on the development of the SCIIB instrumentation. In the third year, a breakthrough in sensor fabrication monitoring led to the parallel development of the white light interferometer instrumentation system, which was ultimately shown to be the optimal system for high resolution, low speed applications. This chapter describes both of these efforts.

5.1 Signal Demodulation System I – SCIIB

In order to achieve high frequency response for the measurement of acoustic signals or flow, it was necessary to develop a high speed signal processing method for the SCIIB output. This section describes the design and implementation of advanced DSP-based signal processing techniques for the SCIIB sensor system.

5.1.1 Design and implementation

A schematic of the DSP-based SCIIB system, including a SCIIB sensor optical system, a DSP development platform, and an analog daughter module with A/D and D/A converters, is shown in Figure 5.1. Two important features are unique in this system. First, the output signals from the two channels of the SCIIB system are processed in the digital domain using a DSP chip. Second, in order to improve the system signal-to-noise ratio (SNR), the light source is modulated at a high frequency, and synchronously demodulated at the receiving end. These two features enable low noise detection and demodulation of the weak optical signal at a very high speed. In the multimode case, a 2 MHz sweep function generator

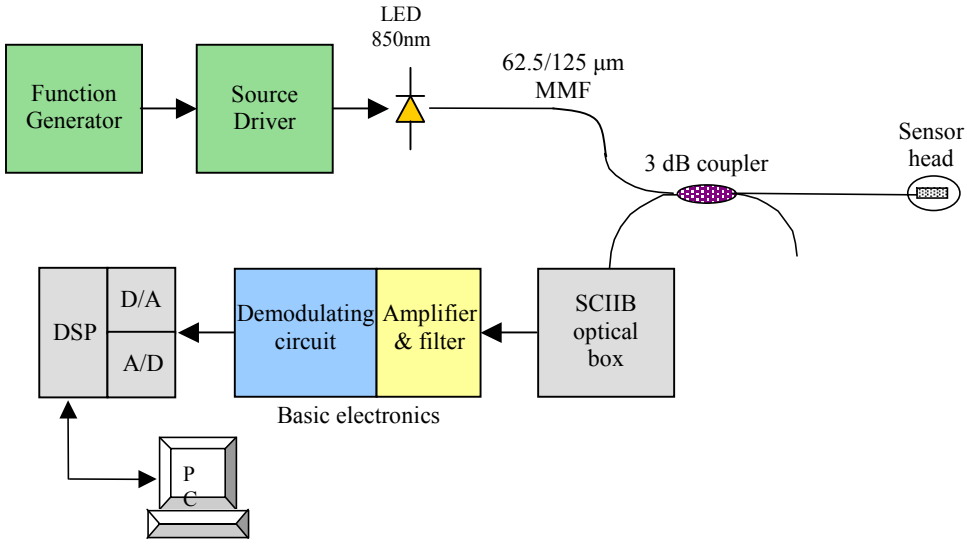

Figure 5.1. DSP based SCIIB high speed sensor system.

(TENMA, Inc.) is used to modulate an 850 nm high power fiber optic LED (HFE4854, Honeywell) through a laser diode driver (Newport Corp). As discussed above, the modulated LED light is coupled to a 62.5/125μm multimode 3-dB 2x2 fiber coupler. One output leg of the coupler is connected to a SCIIB fiber sensor head, and the other output is inserted into index matching gel to eliminate reflections from the fiber tip. The signal output from the sensor head is transmitted back to the SCIIB optical box through the same fiber coupler. The SCIIB optics box splits the input signal into a reference channel (without bandpass filter) and a signal channel (with bandpass filter). Two photodetectors are used to convert the two channel signals to electrical signals. The detected signals are amplified, filtered and demodulated by means of the basic electronics, then sampled by an A/D module (ADCA Corp.) and processed in the DSP platform.

An optimal operating modulation scheme had to be developed to support the noise-reducing amplitude modulation of the source. In order to ensure that the HFE4856 LED operated in its linear region during modulation, the current-power (I-P) curve of the LED was plotted, as shown in Figure 5.2. Based on this result, we chose an operating point of 50 mA with the modulation region from 10 mA to 90 mA. The modulating frequency was chosen to be 100 kHz.

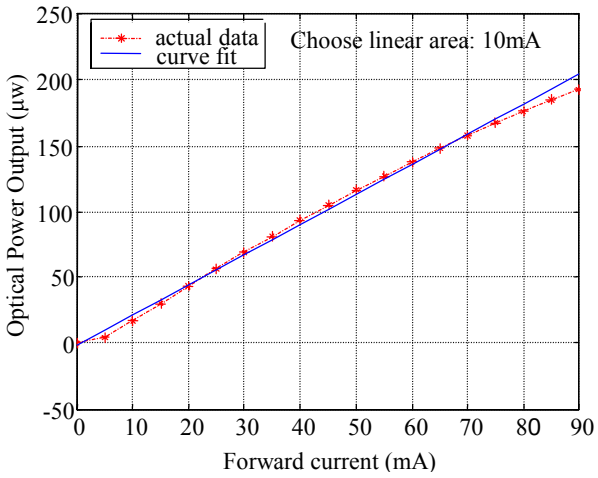

Figure 5.2. Current-power curve of the HEF4856 LED.

5.1.1.1 Basic electronics design

The basic electronics involved in the system include the high frequency preamplifier circuit, the narrow bandpass filter circuit and the amplitude demodulation circuit. The specifications of the designed basic electronics include:

Modulation frequency:	100 kHz
Signal bandwidth:	10 kHz
Current gain for reference channel:	×108 A/V
Gain for signal channel:	×109 A/V
Signal to noise ratio:	>60dB

5.1.1.2 A/D converter design

An A/D converter is necessary to convert the amplified and demodulated signal to the digital domain so that the DSP hardware can further process the signal and improve the measurement accuracy. Three factors were considered in A/D module selection: high accuracy, high throughput and ease of interface with the DSP hardware. After investigating products from a number of companies, we chose the DSP data acquisition board 5404DHR-V manufactured by ADAC, Inc. The 5404DHR-V board provides a 16-bit A/D with a maximum throughput of 100K samples/s, two 16-bit D/A voltage output channels, 8 multiplexed analog input channels and 4 C40 Comm ports to communicate with TM320C40 DSP chips.

5.1.1.3 DSP hardware design

TM320C4X series DSP chips made by Texas Instruments have successfully been used in various engineering applications. The TMS320C40 is the original member of the 'C4x family. It features a power CPU that can deliver up to 30 MIPS/60 MFLOPS, 6 built-in communication ports allowing high speed data exchange, the capability of parallel processing by group several DSP chips together, and well-developed supporting software.

We selected the SMT320 DSP system manufactured by Sundance, Inc. as the main DSP development platform for the system. The platform consists of a SMT320 PCI carrier board with 4 TIM-40 module slots and a SMT302 TIM-40 module. The advantage of this structure is ease in extension to more C40s for parallel processing. The high-speed communication between the DSP platform and the A/D module is realized by using the Comm-ports of the DSP.

5.1.1.4 Software design

The development of the supporting software for the DSP system is the most critical part of the entire system design. The software will have a significant influence on the final system performance. It is based on the mixed programming of C language and the 3L DSP function library. The main functions of the DSP supporting software include data acquisition, data transferring, digital filtering, signal demodulation, and data output.

5.1.2 SCIIB System Noise Analysis

As an optoelectronic measurement system, the performance of the SCIIB sensor is limited by the noise associated with each individual electronic and optical component and their combined effects. A detailed analysis of these noise effects on the system performance is a critical design step since it provides a guideline for achieving an optimal system performance. This section provides a detailed analysis of the noise performance of the single mode fiber (SMF) SCIIB sensor system, including both the electronic noise and the optical noise. Based on the results of the analysis, performance improvement measures are proposed.

5.1.2.1 Electronic Noise of the SMF SCIIB System

Usually, the ultimate performance limit of an optoelectronic sensor system is associated with the receiving electronics used to interrogate the sensor. This can be further decomposed into

two parts: 1) the fundamental photon noise limit (shot noise) of the photodetector, and 2) thermal noise of the electronics. In addition to the noise associated with the receiving electronics, the noise of the optical source, such as the optical power fluctuation and the source wavelength drift, can also cause measurement errors to the sensor system. Here the optical power fluctuation of the source is no longer a concern because as discussed above, the SCIIB sensor system can self-compensate for the source power fluctuation. The error caused by the optical wavelength drift of the source will be discussed in the next section as it is categorized as part of the optical noise.

Photodetector Noise:

Shot noise: Photodetector shot noise is a manifestation of the fact that the electric current consists of a stream of electrons that are generated at random times. It was first studied by Schottky in 1918 and has been thoroughly investigated since then. The photodiode current generated in response to a constant optical signal can be written as

$$\mathrm{I(t)} = I_p + i_s(t)\,, \qquad \textbf{(5-1)}$$

where $I_p=RP_{in}$ is the average current and $i_s(t)$ is a current fluctuation related to shot noise. P_{in} is the input optical power to the photodetector and R is the responsivity of the photodetector.

Mathematically, $i_s(t)$ is a stationary random process with Poisson statistics which in practice can be approximated by the Gaussian statistics. The autocorrelation function of $i_s(t)$ is related to the spectral density $S_s(f)$ by the Wiener-Khinchin theorem

$$\langle i_s(t) i_s(t+\tau)\rangle = \int_{-\infty}^{\infty} S_s(f)\exp(2\pi i f\tau)df\,. \qquad \textbf{(5-2)}$$

The spectral density of shot noise is constant and is given by $S_s(f)=qI_p$ (shot noise is called white for this reason). q is the charge on an electron (1.6×10^{-19} C). Note that $S_s(f)$ is a two-sided spectral density, as negative frequencies are also included in (5-2). If only positive frequencies are considered by changing the lower limit of integration to zero, the one-sided spectral density becomes $2qI_p$. The noise variance is obtained by setting τ=0 in (5-2) and is given by

$$\sigma_s^{\,2} = \langle i_s^{\,2}(t)\rangle = 2qI_p\Delta f\,, \qquad \textbf{(5-3)}$$

where Δf is the effective noise bandwidth of the receiver. The actual value of Δf depends on where the noise is measured and it is usually corresponds to the bandwidth of the amplifying circuits.

Dark current: All photodetectors generate some current noise even in the absence of an optical signal because of stray light or thermal generation of electron-hole pairs. This residual current is referred to as the dark current. Since the dark current I_d also generates shot noise, its contribution is included in the following equation

$$\sigma_s^{\,2} = 2q(I_p + I_d)\Delta f\,. \qquad \textbf{(5-4)}$$

Thermal noise: At a finite temperature, electrons in any conductor move randomly. Random thermal motion of electrons in a resistor manifests as a fluctuating current even in the absence of an applied voltage. The load resistor in the front end of an optical receiver adds such fluctuations to the current generated by the photodiode. This additional noise component is referred to as thermal noise. It is also called Johnson noise or Nyquist noise after the two scientists who first studied it experimentally and theoretically. Thermal noise can be defined as the current fluctuation $i_T(t)$. Mathematically, $i_T(t)$ is modeled as a stationary Gaussian random process with a spectral density that is frequency independent up to 1Thz (nearly white noise) and is given by [3]

$$S_T(f) = \frac{2k_B T}{R_L}, \qquad \textbf{(5-5)}$$

where k_B is the Boltzmann constant (1.38×10^{-23}J/°K), T is the absolute temperature, and R_L is the load resistor. As mentioned before, $S_T(f)$ is also the two-sided spectral density. The autocorrelation function of $i_T(t)$ is given by

$$\langle i_T(t) i_T(t+\tau)\rangle = \int_{-\infty}^{\infty} S_T(f)\exp(2\pi i f\tau)df \ . \qquad \textbf{(5-6)}$$

Therefore, the noise variance is obtained by setting $\tau=0$ and becomes

$$\sigma_s^{\ 2} = \langle i_s^{\ 2}(t)\rangle = \int_{-\infty}^{\infty} S_T(f)df = \frac{4k_B T}{R_L}\Delta f \ , \qquad \textbf{(5-7)}$$

where Δf is the effective noise bandwidth which is defined the same as for the shot noise case.

Noise assumption at the transimpedance amplifier:

The developed SCIIB system uses two transimpedance amplifiers to convert the optical current signals to the voltage outputs of the two channels. It is thus worthwhile to describe the noise performance of the transimpedance amplifier as it converges the shot noise and the thermal noise, and also introduce other noises to the final sensor output.

The noise equivalent circuit of the transimpedance amplifier is given in Figure 5.3. The bandwidth of the transimpedance amplifier is RC limit and given by

$$\Delta f = \frac{1}{2\pi R_f C_f}, \qquad \textbf{(5-8)}$$

where R_f is the feedback resistance, and C_f is the feedback capacitance. The output voltage (e_o) from the transimpedance amplifier can be calculated by

$$e_o = e_s + e_{no} = I_p R_f + e_{no}, \qquad \textbf{(5-9)}$$

where e_s is the signal voltage of the amplifier, I_p is the signal generated photocurrent from the photodetector, and e_{no} is the voltage noise of the amplifier which includes the shot noise of the detector generated a noise voltage, the thermal noise of the feedback resistor (e_{noR}), the amplifier's input current noise (e_{noi}), and the amplifier's input voltage noise (e_{noe}).

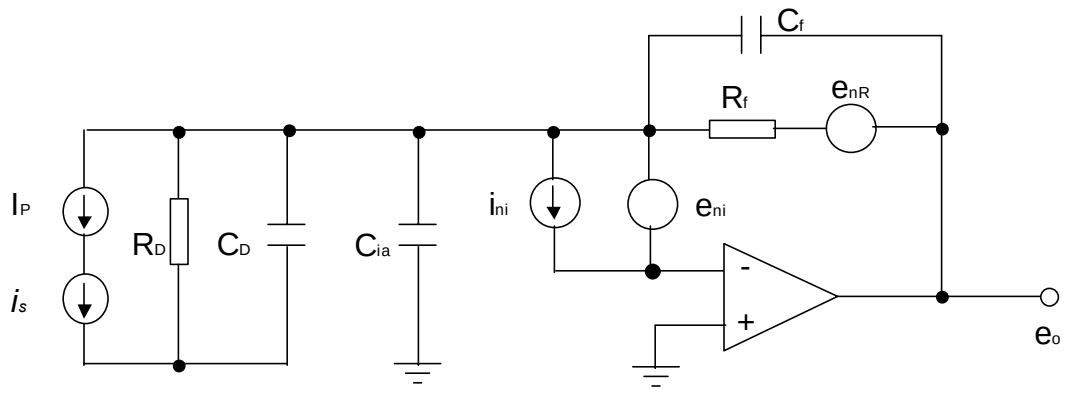

Figure 5.3. Noise equivalent circuit of the transimpedance amplifier.

PD shot noise: The shot noise generated at the photodetector (i_s) will be amplified by the feedback resistor and gives the corresponding voltage noise (e_{nos}) given by

$$e_{nos} = i_s R_f = \sqrt{2q(I_p + I_d)\Delta f}\, R_f \,. \qquad \textbf{(5-10)}$$

Thermal noise: The thermal noise of the feedback resistor generates a voltage noise e_{noR} that can be expressed by

$$\mathrm{e}_{\mathrm{noR}} = \sqrt{4k_B T R_f \Delta f} \,. \qquad \textbf{(5-11)}$$

Amplifier input current noise: e_{noi} is the output noise components produced by the amplifier's input current noise ($i_{ni} = \sqrt{2qI_{B-}\Delta f}$) which is a shot noise produced by the input bias current I_{B-}. This noise current flows directly through the feedback resistor, producing a noise voltage of

$$\mathrm{e}_{\mathrm{noi}} = R_f \sqrt{2qI_{B-}\Delta f} \,. \qquad \textbf{(5-12)}$$

Choosing a FET-input operational amplifier with an I_{B-} in the picoampere range generally makes this noise component negligible for practical levels of feedback resistance. For the AD795 operational amplifier, the input current noise is $I_{B-} = 13fA$.

Amplifier input voltage noise: e_{noe} represents output noise components produced by the amplifier's input voltage noise e_{ni}. Within the response boundary of the op amp, this noise can be calculated by

$$e_{noe} = \frac{1 + R_f C_i s}{1 + R_f C_f s} e_{ni} \,. \qquad \textbf{(5-13)}$$

This will be a high frequency noise when the capacitors dominate the noise gain. For the AD795 amplifier, $e_{ni}=3\mu V$ below 10Hz.

Total voltage noise: The total voltage noise (e_{no}) can be obtained by adding the contributions of all the above noises. Since these noises are independent random processes which can be approximately modeled by Gaussian statistics, the total variance of voltage fluctuation at the output of the transimpedance amplifier can be obtained by adding individual variances. Therefore, the combined output voltage noise of all components is given by

$$e_{no} = \sqrt{e^2_{nos} + e^2_{noR} + e^2_{noi} + e^2_{noe}} \quad . \qquad \textbf{(5-14)}$$

In consideration of the power budget of the developed SCIIB system: Assume that the maximum output power from the SLED source is 1.6 mW. The coupler introduces a loss of 6dB (75%) because of the double passes. The Fresnel reflection of the fiber endface is 4%. If counting for the two reflections at the sensor head, the total average reflected power will be 8% of the incident power. There are other losses associated with the SCIIB system. For example, the coupling loss of the fiber to the GRIN lens is about 0.2dB (4.5%). The beamsplitter splits the light into the two channels with a ratio of 50:50, which introduces another 50% power loss to each channel. The power seen by the narrow band channel will only be 25% of the original power of the full spectrum because the bandpass filter only slices a portion (10nm spectral width) of the original source bandwidth (40nm). The bandpass filter used in the system also introduces an optical loss of 60%. The maximum operating distance for the single mode fiber sensor is 10km, which will introduce a fiber loss of 2×0.3dB/km×10km=6dB (74.88%) because of the double pass of the light, where 0.3dB/km is the assumed loss at λ=1310nm of the singlemode fiber used in connecting the sensor to the signal processing unit. Finally, it is wise to allow a loss margin of 10dB (90%) power loss for the fiber deployment. The loss items with their estimated values are listed in Table 5.1.

Table 5.1. Optical loss mechanisms in singlemode fiber SCIIB system.

Optical loss mechanisms	Value
Coupler loss (L_C):	75%
Average Fresnel reflection of the fiber ends (r_f):	8%
GRIN lens pigtail loss (L_{GRIN}):	0.2dB (or 4.5%)
Beamsplitter loss (L_{BS}):	50%
Filtering loss (L_{ft}):	75%
Bandpass filter loss (η_{BP}):	60%
Fiber attenuation loss (L_f):	10km × 0.3dB/km × 2 = 6dB (or 74.88%)
Loss margin for fiber deployment (L_{Mrg}):	10dB (90%)

Therefore the optical power seen by the photodetector at the signal channel can be estimated to be

$$\begin{aligned} P_{in} &= P_s \times (1-L_c) \times r_f \times (1-L_{GRIN}) \times (1-L_{BS}) \times (1-L_{ft}) \times \eta_{BP} \times (1-L_f) \times (1-L_{Mrg}) \\ &= 57.6nW \end{aligned} \quad \textbf{(5-15)}$$

Signal-to-noise ratio estimation of SCIIB electronics:

Based on the above analysis and the estimated optical power seen by the photodetectors of the SCIIB signal channel, we can calculate the estimated signal-to-noise ratio (SNR) of the developed SCIIB system, where is SNR is defined as

$$SNR = 10\log(\frac{\text{average signal power}}{\text{noise power}}) = 20\log(\frac{\text{average signal voltage}}{\text{noise voltage}}) = 20\log(\frac{e_s}{e_{no}}) = 20\log(\frac{I_p R_f}{\sqrt{e^2_{nos} + e^2_{noR} + e^2_{noi} + e^2_{noe}}}) \quad \textbf{(5-16)}$$

where we used the fact that electrical power varies as square of the voltage.

Therefore, the signal-to-noise ratio (SNR) of the electronics of the singlemode fiber SCIIB sensor system can be calculated as shown in Table 5.2, where the noise terms are listed separately. From the table, we can see that the theoretical signal-to-noise ratio of the receiving electronics of the singlemode fiber SCIIB system is about 98.8dB (equivalent to a normalized noise level of 1.148×10^{-5}). This is, however, by no means the actual SNR of the entire system. As we will see in the analyses of next section, the optical noise will dominate the performance characteristics of the system.

Table 5.2. SNR calculation of the singlemode fiber SCIIB electronics

	Value
Shot noise generated voltage noise (e_{nos}):	5.28 (μV)
Thermal noise of the feedback resistor (e_{noR}):	1.62 (μV)
Amplifier's input current noise (e_{noi}):	2.57 (nV)
Amplifier's input voltage noise (e_{noe}):	3 (μV)
Total noise voltage (e_{no}):	6.28 (μV)
Average signal current (I_p):	57.6nW × 0.95A/W = 54.7 (nA)
Dark current of the photodetector (I_D):	15 (pA)
Average signal voltage (e_s):	547 nA × $10^7\Omega$ = 0.547 (V)
Signal-to-noise ratio (*SNR*):	98.8 (dB)
Equivalent normalized noise level:	1.148×10^{-5}

5.1.2.2 Optical Noise of the SMF SCIIB System

As discussed previously, the basic optical components in the SMF SCIIB sensor system include the optical source (SLED), fiber coupler, optical fibers, GRIN lens, beamsplitter, and optical bandpass filter. In order to achieve the desired sensor system performance, it is necessary for those optical components to perform their functions accurately. Unfortunately, environmental perturbations, such as temperature changes and mechanical vibrations, can easily introduce noises to the system through the interaction between the optical components

and the outside medium. These noises may deviate the optical components from their desired functions and result in measurement errors. Therefore, it is the purpose of this section to examine the noise performance of the optical system to ensure a reliable optical design.

The interaction between the optical components and the environment disturbance could affect the optical performance of the component in four different aspects: intensity, phase, wavelength, and state of polarization (SOP). The resultant noise from these four aspects is system and component dependent. The SCIIB system is immune to the intensity noise since it has the full capability of self-compensation for the intensity fluctuation by taking the ratio of the two channels' outputs. The phase fluctuation of the optical components will not affect the system performance because the phase of the interference signal from the Fabry-Perot cavity purely depends on the sensor probe itself. The phase shift of the optical components only adds the same amount of phase change to both of the interference components. This common phase shift will be eliminated from the final interference signal of interest. The analysis can thus be narrowed down to the effects of wavelength drifts and changes of the state of polarization.

Wavelength Drift Induced Noise:

The SCIIB system measures the pressure signal by monitoring the sensor cavity length change resulting from the applied pressure. Although the sensor cavity length change is read directly from the intensity change, the generation of the signal is based on the basic principle of optical interference. The interference of two optical waves is a sinusoidal function of the phase difference between these two waves, which is inversely proportional to the optical wavelength of the source. It can be imagined that wavelength drifts will introduce a change to the interference signal and result in measurement errors. Usually, the wavelength drift induced error can be analyzed directly from the interference equation. However, the case for the SCIIB system is somewhat different because it is the spectral characteristic of the optical filter that determines the interference signal. Therefore, a detailed investigation of the wavelength drift induced error needs more careful consideration.

Considering the spectral change of the optical bandpass filter: Without any doubt, a spectral change after the optical bandpass filter will directly shift the interference signal. A careful examination of the system reveals that the wavelength drift before the optical bandpass filter can also cause an error through the non-centered filtering and the residual interference fringe in the reference channels.

The optical bandpass filter used in the SCIIB signal channel is a Fabry-Perot type multilayer thin film filter. The spectrum characteristics of the filter are dependent on the thickness and the refractive index of the multilayer thin film, which will change with the ambient temperature because of the thermal expansion effect and the temperature dependence of the refractive index. Assuming that the center wavelength of the filter has a temperature sensitivity of 0.001nm/°C, a temperature change of 70°C (from -15°C to 55°C) will cause a maximum change of 0.07nm in the center wavelength.

Taking the derivative of both sides of Eq. (4-1) with respect to λ, we have

$$\frac{ds}{d\lambda} = -\gamma \frac{4\pi L}{\lambda^2} \sin(\frac{4\pi}{\lambda} L) . \qquad \textbf{(5-17)}$$

The wavelength drift induced error can thus be calculated by

$$\delta s = abs\left\{ \gamma \frac{4\pi L}{\lambda^2} \sin(\frac{4\pi}{\lambda} L)\delta\lambda \right\}, \qquad \textbf{(5-18)}$$

which reaches a maximum at the quadrature points where the sinusoidal function gives its maximum values of ±1, whereas,

$$\delta s_{\max} = \gamma \frac{4\pi L}{\lambda^2} \delta\lambda , \qquad \textbf{(5-19)}$$

We have defined the operating range of the SCIIB system in Eq. (4-14). Therefore, the normalized error can be calculated by

$$\frac{\delta s_{\max}}{\Delta s_{\max}} = \frac{\gamma \frac{4\pi L}{\lambda^2} \delta\lambda}{1.6\gamma} = \frac{4\pi L}{1.6\lambda^2} \delta\lambda . \qquad \textbf{(5-20)}$$

The normalized error resulting from the wavelength drift of the optical filter is plotted in Figure 5.4 as a function of the initial cavity length of the sensor probe, where the wavelength drift of the filter is assumed to be 0.07nm for the operating temperature range from -15°C to 55°C. As indicated in the figure, the error is proportional to the initial cavity length. For an initial cavity length of 25μm, the normalized error is about 0.8% of the full scale of measurement.

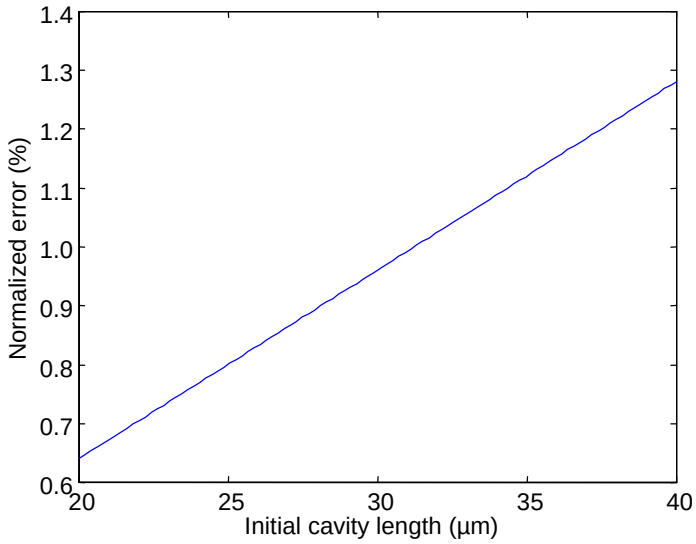

Figure 5.4. Normalized error induced by the wavelength drift of the filter.

In order to reduce the error induced by the wavelength drift of the optical filter, and also to ensure good fringe visibility of the signal channel, the initial sensor cavity length needs to be as small as possible. On the other hand, reducing the initial cavity length would generate an

optical interference in the reference channel. This residual interference in the reference channel can cause an error in the measurement results as demonstrated by the following discussion.

Assuming that the residual interference in the reference channel has a fringe visibility of γ_r, the output from the reference channel can be written as

$$I_1' = 2RI_0[1 - \gamma_r \cos(\frac{4\pi}{\lambda} L)]. \qquad \textbf{(5-21)}$$

The output of the SCIIB system is then

$$s' = \frac{I_2}{I_1'} = \alpha \cdot \frac{1 - \gamma_s \cos(\frac{4\pi}{\lambda} L)}{1 - \gamma_r \cos(\frac{4\pi}{\lambda} L)}, \qquad \textbf{(5-22)}$$

$$\approx s[1 + \frac{\gamma_r}{2} \cos(\frac{4\pi}{\lambda} L)]$$

where s is the original SCIIB output as given by Eq. (4-11).

Both the SLED source and the optical bandpass filter used in the SCIIB system have a center wavelength of 1310nm. However, the actual center wavelength of the source is 3.1nm off from its nominal center wavelength. As schematically shown in Figure 5.5, this will have two effects on the output of the SCIIB system: 1) the center wavelength used to calculate the output of the reference channel in Eq. (5-21) is no longer the same as the signal channel, and 2) the intensity of the signal channel will deviate from the original level of αI.

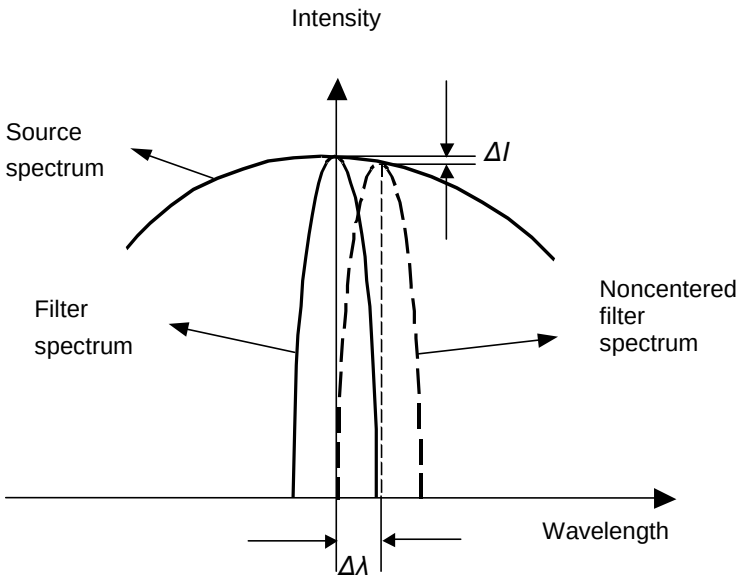

Figure 5.5. Schematic illustration of non-centered filtering.

Therefore, Eq. (5-22) can be modified to give the new output of the SCIIB system, given by

$$s' \approx s(1-\frac{\Delta I}{I_0})[1+\frac{\gamma_r}{2}\cos(\frac{4\pi}{\lambda-\Delta\lambda}L)], \qquad \textbf{(5-23)}$$

where ΔI is the intensity change, and $\Delta\lambda$ is the center wavelength offset. Both the residual interference in the reference channel and the non-centered filtering themselves will not cause measurement errors directly because once the system is calibrated these deviations are fixed. However, if the wavelength of the light drifts from the original spectrum, for example, because of the temperature induced drift of the source wavelength and the fiber bending induced spectral distortion, there will be errors resulting from these changes.

From Eq. (5-23), the normalized measurement error resulting from the wavelength drift $\delta\lambda$ can thus be calculated by

$$\left.\frac{\delta s}{s}\right|_{\max} \approx \left\{ abs(\frac{1}{I_0}\frac{dI}{d\lambda}) + \frac{\gamma_r}{2}\cdot\frac{4\pi L}{\lambda^2} \right\}\Bigg|_{\lambda-\Delta\lambda} \cdot \delta\lambda, \qquad \textbf{(5-24)}$$

where I is the normalized spectrum of the optical source, which can be modeled by the following Gaussian function

$$I(\lambda) = \frac{2I_0}{\sqrt{\pi}\Delta\lambda_0}\exp\left(-\frac{(\lambda-\lambda_c)^2}{{\Delta\lambda_0}^2}\right), \qquad \textbf{(5-25)}$$

where I_0 is the total optical power, $\Delta\lambda_0$ is the e^{-1} half spectral width, and λ_0 is the central wavelength. Therefore, we have

$$\frac{1}{I_0}\frac{dI(\lambda)}{d\lambda} = -\frac{2(\lambda-\lambda_c)}{\sqrt{\pi}{\Delta\lambda_0}^3}\exp\left(-\frac{(\lambda-\lambda_c)^2}{{\Delta\lambda_0}^2}\right), \qquad \textbf{(5-26)}$$

Figure 5.6 shows the calculated results of the normalized measurement error as a function of the wavelength drift given by Eq. (5-24).

The spectrum of a semiconductor optical source is temperature dependent. A change in temperature will cause changes to both the index of refraction of the active medium and the dimensions of the resonant cavity, and hence change the spectrum of the emitting light. To reduce the spectral fluctuation of the source, a thermo-resistor and a thermal electrical controller (TEC) are usually installed very close to the source chip. These two together with the external controlling circuits form a feedback loop that helps to keep the chip temperature unchanged. With the help of the automatic thermal electrical cooling mechanism, the wavelength drift of the optical source can thus be minimized to the level of about 0.2nm.

The spectrum of the light waves transmitted in a fiber will change when the fiber is bent. The fiber bending induced spectrum change (or the fiber bending loss spectrum) is a very complicated phenomenon. Although theoretical modeling of this process is possible, it will be easier and more direct to investigate this phenomenon experimentally. The experimental setup was the same as that described in Section 4.5 and shown in Figure 4.15. As discussed

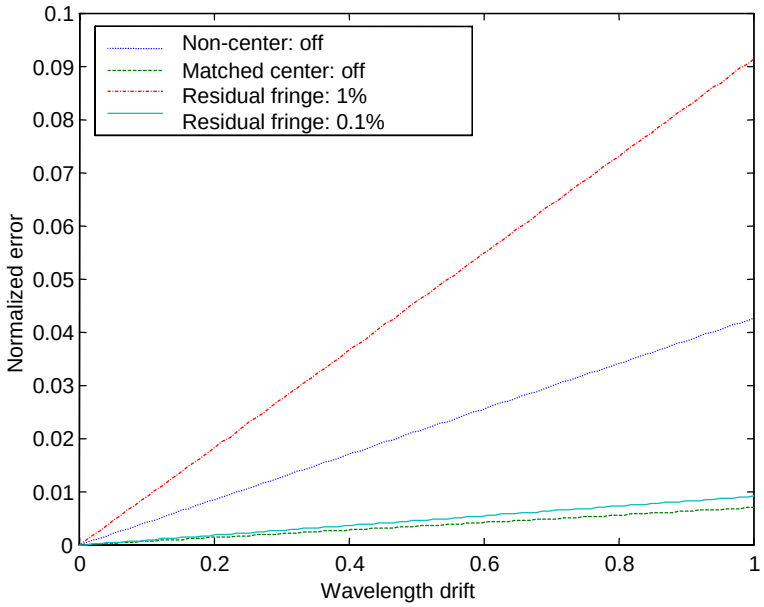

Figure 5.6. Normalized measurement error resulting from the residual interference in the reference channel and the noncentered filtering, where the initial sensor cavity length is set to be L_0=25μm.

above, two types of singlemode fibers were evaluated. In the first experiment, a section of standard telecom singlemode fiber (SMF28^{TM} fiber made by Corning Inc.) was used to run the test. The fiber was bent to a series of radii from 12mm to 3mm. The smallest bend that might be encountered when the sensor is deployed in an oil well is about 12mm. The typical spectra of light transmitted in the original and the bent fiber are repeated in Figure 5.7 for convenience. Similar tests were also conducted using a section of bending insensitive singlemode fiber at 1300nm (purchased from Spectran Communication Fiber Technologies, Inc.), with the recorded spectra repeated in Figure 5.8. For the purpose of evaluating the spectral distortion induced phase shift to the interference signal, the change of the effective central wavelength can be calculated from the recorded spectrum data. The calculated typical effective center wavelength change for regular singlemode fiber is about 0.3nm, and that of the bending insensitive fiber is about 0.2nm.

From fiber optic theory, the mode field radius $w(\lambda)$ of a step-index singlemode fiber can be approximated by [3]

$$w(\lambda) = a\left(0.65 + \frac{1.619}{V^{3/2}} + \frac{2.879}{V^{6}}\right), \qquad \textbf{(5-27)}$$

where the electric field of the guided mode is assumed to have a Gaussian distribution in shape, and V is the normalized frequency of the fiber, defined as

$$V = \frac{2\pi}{\lambda} a\sqrt{n_1^{\,2} - n_2^{\,2}}\,. \qquad \textbf{(5-28)}$$

Here, a is the core radius, n_1 and n_2 are the refractive indices of the core and cladding respectively.

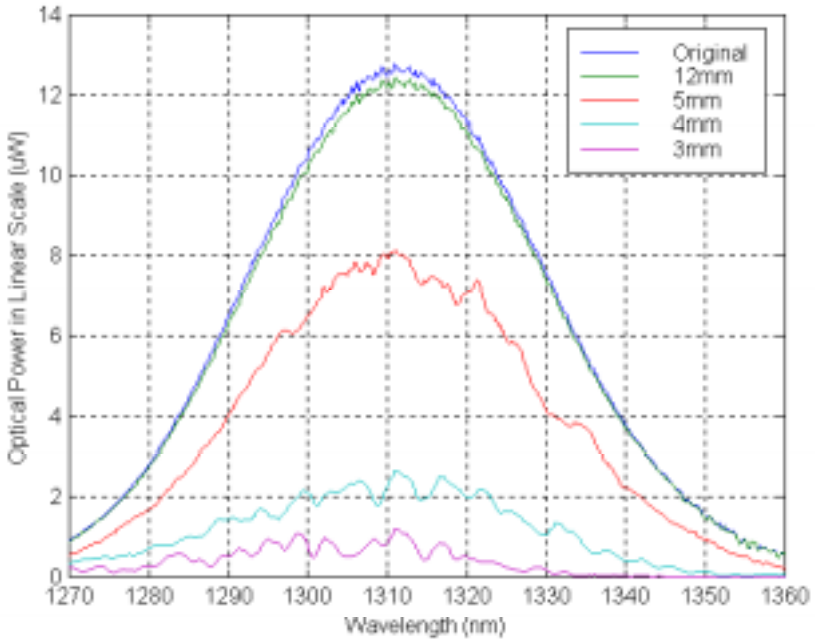

Figure 5.7. Bending induced spectral changes in standard telecommunications singlemode fiber.

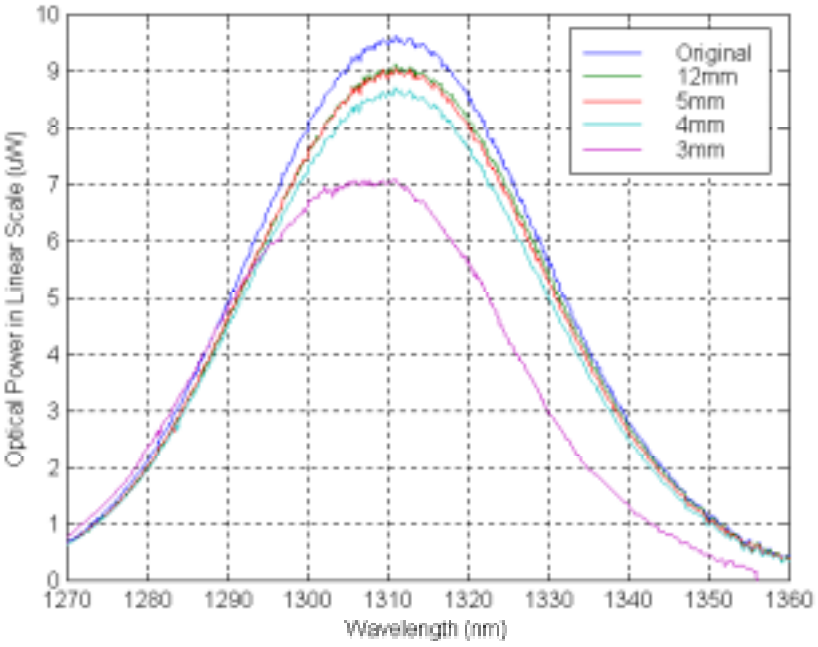

Figure 5.8. Bending induced spectral changes in bending insensitive singlemode fiber.

Examining Eq. (5-27) and (5-28) reveals that the mode field diameter of a step-index singlemode fiber is proportional to the wavelength of the light. Longer wavelength light will have a larger mode field diameter when it is transmitted in the fiber. Intuitively, the larger the mode field diameter, the higher the loss when the fiber is bent because the optical energy is less confined inside the waveguide. This explains qualitatively why the long wavelength end of the spectra suffers larger loss compared to the short wavelength end. Because the mode field diameter of the regular telecommunication fiber is larger than that of the bending insensitive fiber, the loss of the regular fiber is higher than that of the bending insensitive fiber.

Bending a singlemode fiber can also cause the coupling between the guided mode and the cladding modes. The coupling between modes results in the transfer of energy between these modes, which is both wavelength and bending radius dependent. Within the spectral range of the source, the coupling can be more favorable to some wavelengths than to others depending on the status of bending. This explains the ripples exhibited in the transmitted spectrum when the fiber was bent.

In general, comparing the experimental results shown in Figure 5.7 and Figure 5.8, the distortions of the spectrum in the bending insensitive fiber are smaller than that of the regular telecom fiber with the same bending radius. Even under severe bending, the transmitted spectrum of the bending insensitive fiber still does not exhibit spectral ripples. The larger distortion of the spectrum in regular telecom fibers is mainly due to the large mode field diameter of the waveguide. However, the difference is small for a relatively large bending radius (>12mm).

SOP Induced Noise

The SLED used in the SCIIB system outputs almost linearly polarized light. As the light propagates inside the SMF, the state of polarization will be changed due to both intrinsic and extrinsic birefringence. Although the fiber Fabry-Perot sensor probe is polarization insensitive, the receiving optics of the SCIIB system are polarization dependent. This is largely due to the residual polarization dependence of the optical beamsplitter.

Residual polarization sensitivity of the beamsplitter: The SCIIB receiving optics use a low polarizing cubic beamsplitter (made by OptoSigma Inc.) with a central operating wavelength of 1310nm to separate the signal and reference channels. As shown in Figure 5.9, the beamsplitter has a residual polarization dependence of about 10% in the wavelength range 1250nm-1350nm. This will result in a nonconstant splitting ratio that is dependent on the state of polarization of the input light.

Assuming that the splitting ratio of the beamsplitter as a function of the input SOP is given by

$$r(SOP) = \frac{I_1(SOP)}{I_2(SOP)} \neq 1:1, \qquad \textbf{(5-29)}$$

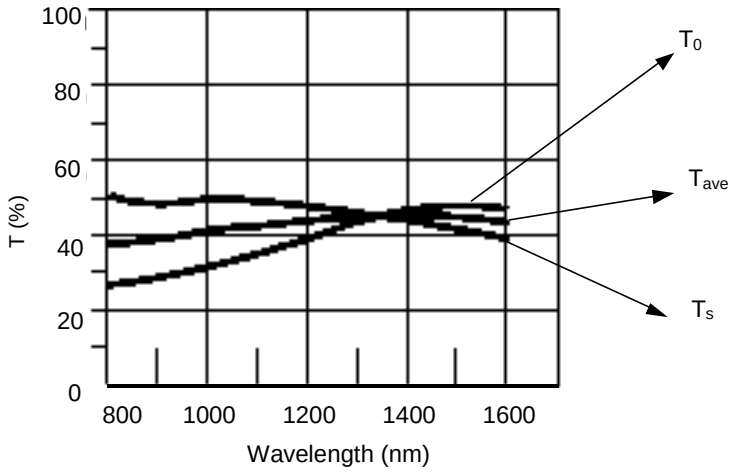

Figure 5.9. Beam splitter transmission characteristics.

the SCIIB output thus becomes

$$\begin{aligned} s' &= r(SOP)s \\ &= r(SOP)\alpha[1-\gamma\cos(\frac{4\pi}{\lambda}L)] \end{aligned}. \qquad \textbf{(5-30)}$$

As indicated in Eq. (5-30), the change in SOP will directly cause a normalized measurement error which can be calculated as

$$\frac{\Delta s}{s} = r(SOP) - 1. \qquad \textbf{(5-31)}$$

From Figure 5.9, the maximum deviation of *r(SOP)* from its desired value (1:1) can reach 10% if the SOP of the light input to the beamsplitter changes from one polarization (*p*) to another (*s*). Therefore, the change of SOP can potentially introduce a normalized measurement error as large as 10%.

Polarization of single-mode fibers: If the fiber is perfectly circular with a circularly symmetric refractive index distribution, the two LP_{01} (or HE_{11}) modes will perfectly degenerate, *i.e.* both x-polarized (*Ey=0*) and y-polarized (*Ex=0*) LP_{01} modes will have the same propagation constant. However, actual fibers generally exhibit some ellipticity of the core and/or some anisotropy in the refractive index distribution due to anisotropic stresses. This results in two different propagation constants for the x-polarized (β_x) and y-polarized (β_y) LP_{01} modes, leading to perturbations of the state of polarization of the light transmitted by the fiber. The birefringence of the fiber ($\Delta\beta$) is usually defined as

$$\Delta\beta = \beta_y - \beta_x. \qquad \textbf{(5-32)}$$

Singlemode fiber in a bent configuration can be viewed as a wave plate with its phase delay unknown due to the random number of bends and the random value of bending radius when the fiber is deployed into an oil well. For a linearly polarized input light, the SOP of the output light can thus be arbitrary (linearly polarized in any possible direction, circularly

polarized, or elliptically polarized). To be conservative, the maximum estimated error of 10% as given by Eq. (5-31) is valid for the entire case.

5.1.2.3 Noise Summary

In the two previous sections, the electronic and the optical noise sources of the SCIIB sensor system were studied in detail. Typical values for the induced error are summarized in Table 5.3 for comparison. The electronic noise is very small compared to the optical noise. Therefore, the emphasis of system optimization was placed on improvement of the optical system. Among the 4 categories of optical noise, change in SOP has the most significant effect on the system performance. Noise resulting from residual interference in the reference channel and noncentered filtering can also be reduced by the proper system design. However, temperature dependence of the optical bandpass filter is an almost fixed error for which little can be done due to the limited commercial availability of the components.

Table 5.3. Typical electronic and optical noise for the SCIIB sensor system.

Noise sources	Typical Values
Electronic noise	0.00115%
Optical noise	
1. Spectral drift of the optical bandpass filter	0.8% (from -15°C to 55°C @ L_0 = 25μm)
2. Residual interference in the reference channel	0.0458% (0.5nm wavelength drift @ L_0 = 25μm)
3. Noncentered filtering	0.0213% (0.5nm wavelength drift)
4. Change of SOP	10%

5.1.2.4 Optical System Optimization

Residual interference in the reference channel

As indicated in Eq. (5-22), the measurement error resulting from the residual interference in the reference channel is proportional to the fringe visibility of the residual interference (γ_r), which is inversely proportional to the initial sensor cavity length. Therefore, increasing the initial sensor cavity length will help to reduce the residual fringe visibility in the reference channel and hence reduce the corresponding measurement error.

On the other hand, Eq. (5-22) reveals that the measurement error is also proportional to the initial cavity length (L_0). The longer the initial sensor cavity, the larger the measurement error. Therefore, the smallest measurement error will result from the balance between these two effects. In order to find an optimal initial sensor cavity length, several sensors with different cavity lengths were made. The experimental results and the theoretical simulation as shown in Figure 4.3 through Figure 4.7 indicate that the visibility of the residual interference in the reference channel decreases very quickly as the cavity length increases before it reaches 20μm. However, after 25μm, the visibility decreases very slowly as the sensor cavity length increases. Therefore, a sensor cavity length of 25μm was selected.

Reduction of the non-centered filtering induced error

As shown in Figure 5.6, the measurement error is proportional to the offset between the center of the optical bandpass filter and that of the source spectrum. A closer match of the two center wavelengths will reduce the measurement error. The optical bandpass filter was rotated by an angle of about 10° from the normal incidence in which it was installed in order to reduce the mismatch between the two center wavelengths to within 0.5nm. The corresponding measurement error was estimated to be reduced from 0.0213% to 0.0035%.

Reduction of the change of SOP induced error

A change in SOP can cause a large measurement error mainly through the residual polarization sensitivity of the beamsplitter used in the SCIIB system. Due to the limitation of the technology used in making the beamsplitter, it is difficult to find a beamsplitter with a splitting ratio purely independent of the state of polarization of the input light. However, if the input light is totally unpolarized natural light, even using a polarization-sensitive beamsplitter, the splitting ratio can be maintained constant and the polarization issue will not be a concern at all. This led us to use a depolarizer to minimize the SOP induced error.

By definition, a depolarizer is an optical device that transforms polarized (or partially polarized) light into naturally unpolarized or depolarized light. The Loyt depolarizer is made of two optical crystals (L_1 and L_2) cut from the same material. The neutral lines of crystal L_2 are aligned perfectly with the bisectors of the neutral lines of L_1. These two optical crystals can be characterized by the optical phase delays δ_1 and δ_2. If the optical conditions of the two crystals satisfy 1) the phase lag of the first crystal is larger than the coherence length L_c of the light, and 2) the second crystal (L_2) is more than twice as thick as the first one (L_1). If these two conditions are satisfied, the light emerging from the Loyt depolarizer will be effectively unpolarized when it is seen by a wide-spectrum detector.

All the above discussions suggest that if a Loyt depolarizer can be installed immediately preceding the beamsplitter, so that the beamsplitter and the photodetectors behind effectively see unpolarized light emerging from the depolarizer no matter how the state of polarization changes in front of the depolarizer. Thereafter the splitting ratio of the beamsplitter becomes insensitive to the polarization disturbance associated with the fiber bending or other causes. In our system, an optical fiber-based Loyt depolarizer, which has two polarization maintaining fibers replacing the two optical crystals described above, was used. The optical fiber Loyt depolarizer, made by the Noah Industries, Inc., has an extinction ratio of 20dB (100:1). The change of SOP induced measurement error was estimated to be reduced from 10% to 0.1% by.

To evaluate the effectiveness of the depolarizer, the SCIIB instrumentation was first tested without the depolarizer. Again, the system was tested without the sensor probe and the signal was directly from the reflection of the fiber endface. To change the SOP, we bent the fiber into a circle of different radii and flipped the fiber circle to different orientations. The two SCIIB channel outputs were recorded using an oscilloscope as shown in Figure 5.10. The ratio of these two outputs are plotted in Figure 5.11. It was evident that the two channel outputs were sensitive to the change of SOP, and moreover, they did not follow each other

due to the polarization effect. The peak-to-peak variation in this case was about 5% of the average ratio.

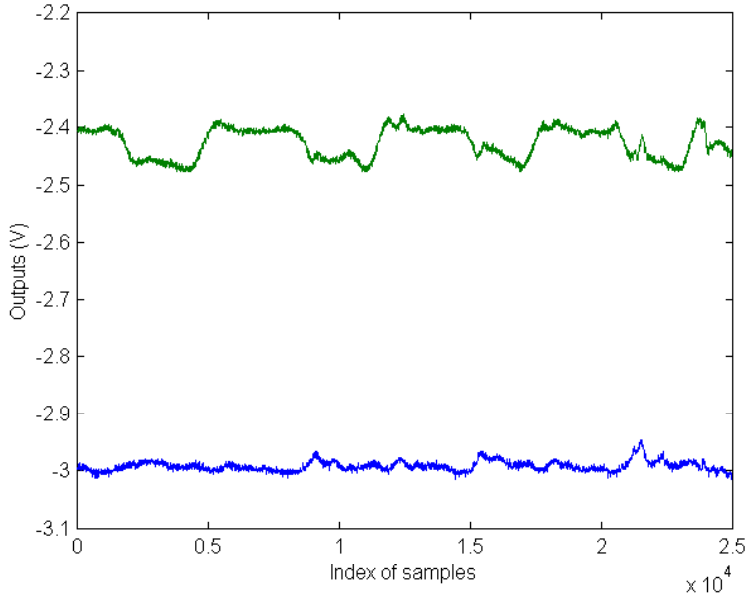

Figure 5.10. Both SCIIB channel outputs as SOP of the fiber changes (without the depolarizer).

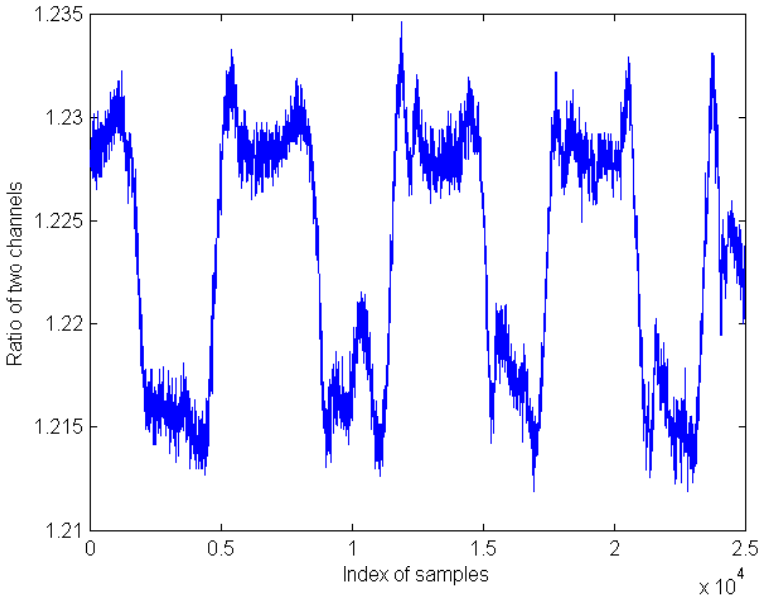

Figure 5.11. Ratio of the two SCIIB channel outputs as SOP of the fiber changes (without the depolarizer).

The experiment was repeated with the depolarizer connected to the system. Both channel outputs are shown in Figure 5.12, and their ratio in Figure 5.13. With the fiber optic depolarizer, the two outputs followed each other very closely. The maximum variation of the ratio was reduced to about 0.5%, showing an improvement of one order of magnitude. However, the experiment also indicated that the dependence of the SCIIB ratio was still large compared to the analytical prediction. The fiber optic Lyot depolarizer purchased from Noah

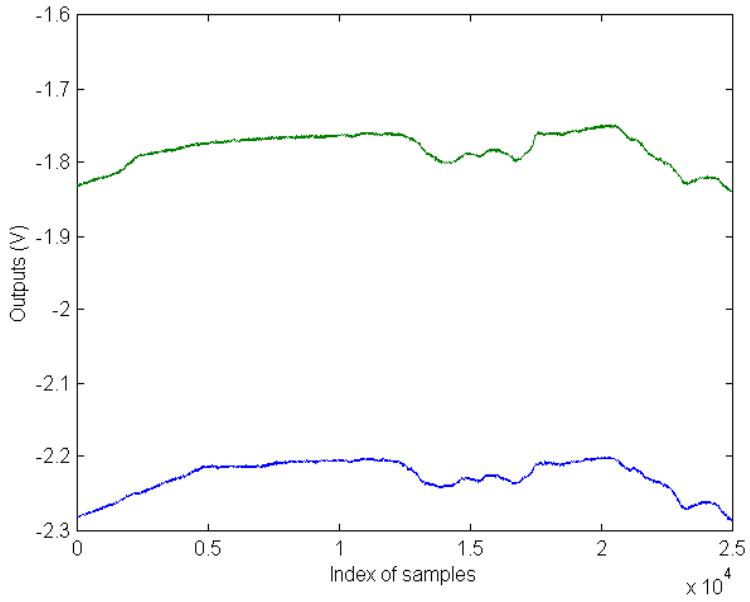

Figure 5.12. SCIIB channel outputs as SOP of the fiber changes (with the depolarizer).

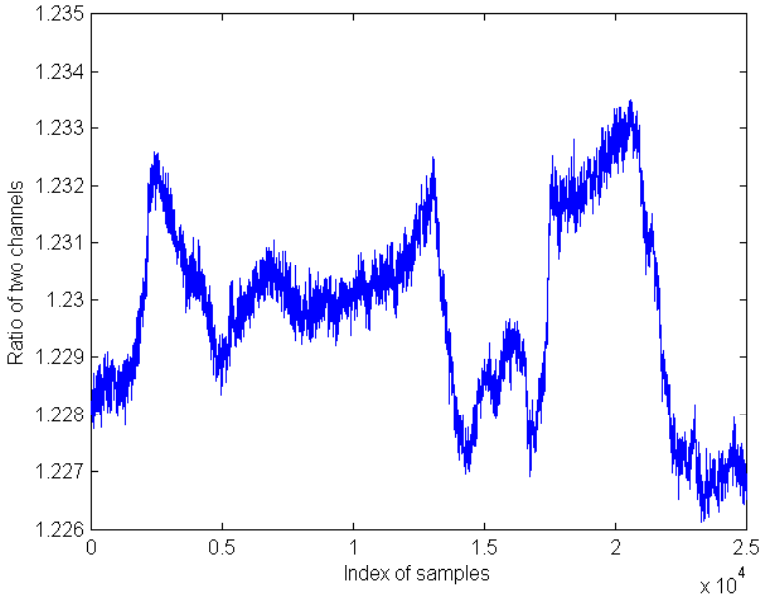

Figure 5.13. Ratio of the two SCIIB channel outputs as SOP of the fiber changes (with the depolarizer).

Industries, Inc. was then tested using a wide-spectrum light source. The optical bandpass filter used in the system had a spectral width of 10nm, which was narrower than the spectral width of the light source that had been used to test the depolarizer. The specified 20dB extinction ratio of polarization suppression might not be true for the signal channel. Therefore, we would expect to have larger polarization dependence of the SCIIB output ratio than the analytical prediction.

5.1.2.5 Other System Optimization Measures

In addition to the electronic and optical noise sources discussed in Sections 5.1.2.1 and 5.1.2.2, other sources of errors could potentially affect the system performance. These include the dark current induced bias and the nonlinearity caused by the unmatched electronic amplifiers. Methods to minimize the errors resultant from these two are presented in this section.

Correction for the dark current induced bias

The dark current of the photodetector will add a constant bias to the photocurrent of interest. Although the dark current of the InGaAs detector used in the SCIIB system is very small (on the order of 15 pA), the resultant bias can affect the measurement result to some extent due to the relatively low optical power reflected from the sensor probe. To investigate the dark current induced error, let's assume that the signal currents of the two channels are I_{p1} and I_{p2} with the corresponding the dark currents of I_{d1} and I_{d2} respectively. The SCIIB ratio can thus be written as

$$s' = \frac{I_{p1} + I_{d1}}{I_{p2} + I_{d1}} = \frac{I_{p1}}{I_{p2}} + \frac{I_{d1}}{I_{p2}} + O^2, \qquad \textbf{(5-33)}$$

where O^2 is the second or higher order terms of I_{d1} and I_{d2}, which will be neglected from the analysis. The corresponding deviation from the ideal output ratio is

$$\Delta s = s' - s \approx \frac{I_{d1}}{I_{p2}}. \qquad \textbf{(5-34)}$$

Therefore, the normalized error resulting from the dark current bias within the linear range of operation becomes

$$\frac{\Delta s}{s} = \frac{I_{d1} \big/ I_{p2}}{I_{p1} \big/ I_{p2}} = \frac{I_{d1}}{I_{p1}}, \qquad \textbf{(5-35)}$$

where, I_{p1} should be confined in the linear operating range of the system.

The normalized error is plotted as a function of the normalized signal level in Figure 5.14, where the average signal current is assumed to be 54.7nA and the dark current is 15pA. As shown in the figure, the measurement error resulting from the dark current bias can reach 0.07% when the signal level is low (close to the valley of the interference fringe).

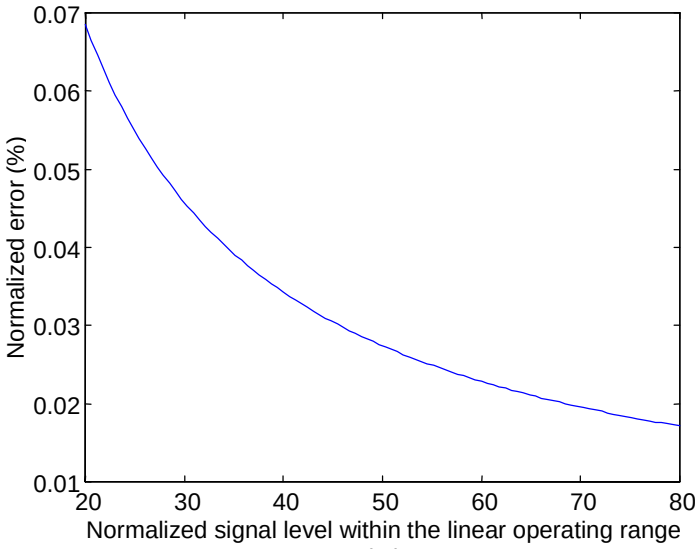

Figure 5.14. Normalized measurement error resulting from the dark current bias.

Because the final ratio function is performed digitally by the host computer, the correction of the dark current bias becomes relatively easy. We can record in advance the output voltage of the two SCIIB channels when the optical source is turned off. The dark current is almost a constant when the photodetector is chosen. Therefore, the dark current bias can be eliminated from the final ratio using

$$s = \frac{V_1 - V_{d1}}{V_2 - V_{d2}}, \qquad \textbf{(5-36)}$$

where V_1 and V_2 are the output signal voltages, and V_{d1} and V_{d2} are the recorded dark-current voltages of the two channels respectively.

Balancing the optical power of the two channels

Because of the very large amplification factors of the transimpedance amplifiers used in the SCIIB system, the nonlinearity of the amplifiers could be a concern. However, the nonlinearity of the amplifiers can be compensated if the two amplifiers are exactly the same. Another reason to match these two amplifiers is the temperature dependence consideration. The resistance of the feedback resistors used in the transimpedance amplifiers will change as the environmental temperature fluctuates. If they change in the same direction and in the same amount, by taking the ratio of the two outputs, the temperature fluctuation will have very little effects on the system output.

To be able to match the two transimpedance amplifiers, we need to balance the optical power input to the two photodetectors. Because an optical bandpass filter is used in the signal channel to increase the coherence length, the signal channel will see less optical power than the reference channel. In order to balance the two channels in terms of the optical power, an optical neutral density filter can be inserted into the reference channel with a flat spectral response within the spectral range of interest, which introduces additional attenuation to the optical intensity of the reference channel.

5.1.2.6 Thermal dependence of the SCIIB instrumentation

The most important environmental disturbance to the measurement system is the temperature fluctuation. Changes in the environmental temperature could have multiple effects on the SCIIB instrumentation system. The spectrum of the light source, the spectral characteristics of the optical bandpass filter, the beamsplitter, the amplifiers and the photodetectors are all temperature dependent. However, if the thermal characteristics of the entire system are repeatable, they can be compensated for by using a temperature sensor. In this section, both a theoretical analysis and experiment results for the SCIIB system thermal characteristics are presented.

The experimental setup is shown in Figure 5.15 was used in the temperature experiments. The entire SCIIB system, except the FABRY-PEROT sensor head and connecting fiber, was placed inside a resistance heated electrical furnace (Blue M inc. Type 60406). In this way, the temperature dependence of FABRY-PEROT sensor head and the temperature dependence of the SCIIB system could be studied separately. Although the electrical furnace itself has a temperature output, to realize a high-resolution measurement, a thermocouple was put inside the electrical box of the SCIIB system. The outputs from the thermocouple and the SCIIB system were sampled by a 22 1/2 bit A/D converter. A notebook computer was used to store and analyze the experimental results. The optical spectrum reflected from the endface of a bare fiber is far different from that reflected from a Fabry-Perot sensor. In the case of a bare fiber, the reflected spectrum will be same as that of the light source, which approximates a Gaussian profile. When connected with a Fabry-Perot sensor, a reflected interference spectrum is expected. To obtain more useful information, the temperature experiments were conducted under two different conditions: 1)only a bare fiber was connected with the SCIIB system, and the end-face of the fiber was cut by a cleaver to obtain a 4% reflection; 2) a Fabry-Perot sensor was connected to the SCIIB system.

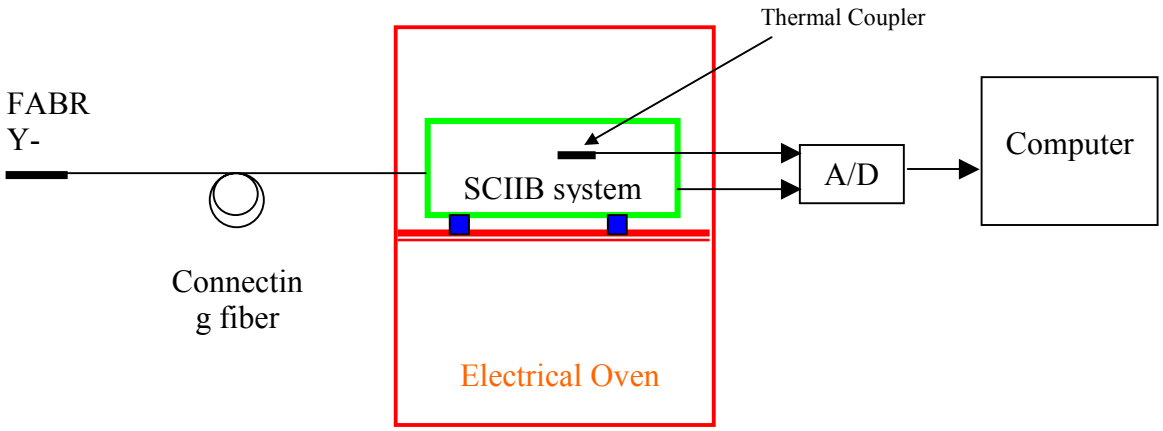

Figure 5.15. Experimental setup for SCIIB thermal testing.

Condition one: (no sensor connected)

The temperature of a recirculating drying oven (with the SCIIB system inside) was increased to about 40˚C. To ensure that a uniform temperature distribution inside the whole system was achieved, the oven was maintained at 40˚C for about one hour. Then the power was shut off to the oven, and the SCIIB system was allowed to cool down very slowly. Both the output from the SCIIB system and that from the thermocouple were sampled during this period. The signal transmitting path is shown in Figure 5.16 to assist in the analysis of the temperature characteristics of reference channel

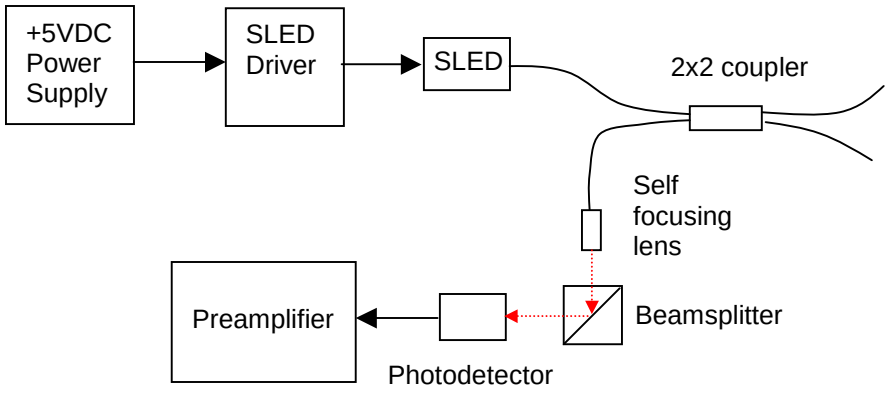

Figure 5.16. Reference channel signal transmitting path.

The temperature dependence of each component is described as follows.

a. Power supply: A +5V regulated power source (AAK Corporation) was used in the SCIIB system as the power supply for both the amplifier and the SLED driver. The temperature coefficient of this product is about 0.015% per ˚C. Because both the SLED driver and amplifier have a large compliance voltage range, the temperature dependence of the power supply can be neglected.

b. SLED driver: A PLD-200 laser diode driver (Wavelength Electronics Inc.) was used to supply a very stable current for the light source. The temperature coefficient of the driver is about 0.01% per ˚C. The drift of the output power of light source can be eliminated when the ratio of two channels is calculated.

c. Light source: The light source used in the singlemode fiber-based SCIIB system is a high power superluminescent light emitting diode (SLED) provided by Anritsu Corp. (AS3B281FX), with a center wavelength of 1312 nm, a spectral width of 41.5 nm, and a maximum output power of 1.21mW from a 9/125μm pigtailed singlemode fiber. Figure 5.17 shows the source spectrum measured by an Ando Optical Spectrum Analyzer (OSA). The center wavelength shifts with temperature changes. In general, the temperature-induced drift

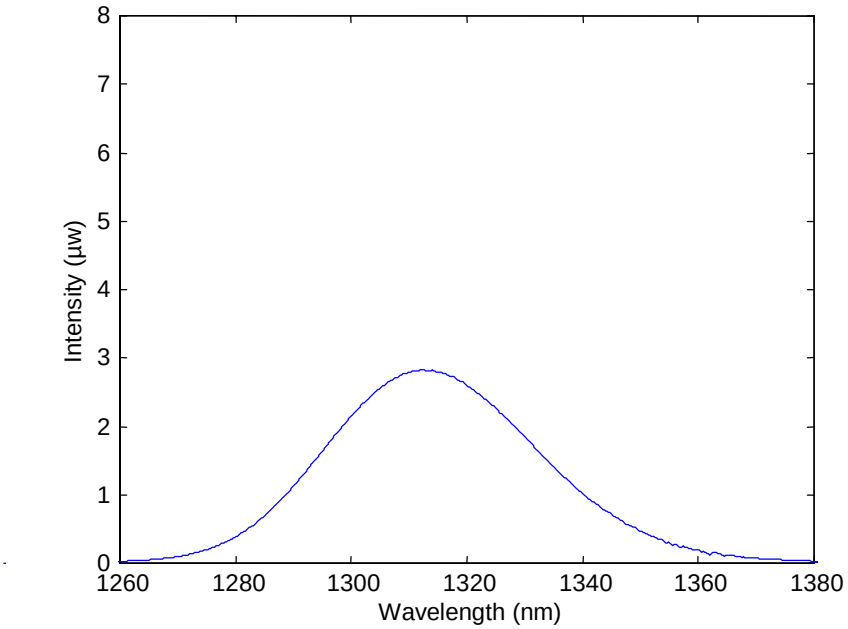

Figure 5.17. Output spectrum of the SLED (Ando OSA).

is about 0.2-0.3nm per ˚C. This will obviously induce errors in the interferometric-based measurement system. To increase the stability of the whole system, a TEC was used to control the temperature of the SLED.

d. Optical alignment: The received light signal will be collimated by a self-focusing lens, pass through a beam splitter and then be coupled into a TO-packaged large area photodetector. All optical components are installed inside a small aluminum box. The total length from the self-focusing lens to the active area of the photodetector is about 20mm. When the temperature changes, the status of alignment will change slightly, which will induce errors in the measurement results. However, it is difficult to predict how the status of the alignment changes with temperature, or if the self-calibration can work or not. All these had to be resolved based on the experimental results.

e. Photodetector: The singlemode SCIIB system works at 1300nm. A large effective area InGaAs photo-detector was used to provide a high response in this spectral range. Again, both the dark current and the responsivity of the InGaAs detector are functions of temperature. The compensating technique works only when two channels have exactly the same temperature dependence, which is almost impossible in reality.

f. Preamplifier: The electronics for the preamplifier are very simple: a transimpedance amplifier was employed to convert the photocurrent from the photo detector to a voltage output. The schematic of the circuit is shown in Figure 5.18. The stability of this amplifier is mainly decided by the feedback resistor R1 and the operational amplifier AD795. The feedback resistor is type MK lead precision power resistor (CADDOCK). Its temperature coefficient is about 0.008% /˚C. The AD795 is a low noise, precision, FET input operational amplifier. It offers both the low voltage noise and low offset drift of a bipolar input op amp

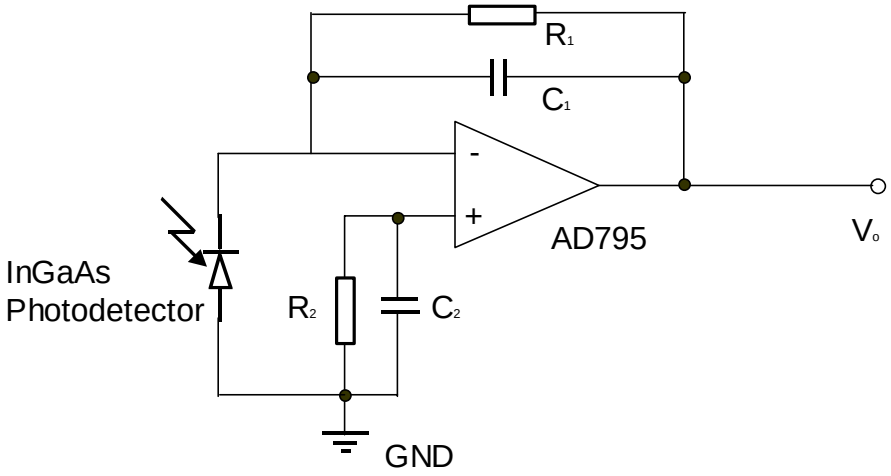

Figure 5.18. Schematic of the preamplifier.

and the very low bias current of a FET-input device. The 1014Ω common-mode impedance insures that the input bias current is essentially independent of common-mode voltage and supply voltage variations.

The experimental temperature dependence of the broadband channel, the narrow band channel and the ratio R are shown in Figure 5.19-Figure 5.21. Both the reference channel and the signal channel have large temperature dependence (in the temperature range of 26-30 ˚C, the drift is about 0.5%/˚C), which can't be explained by the temperature characteristics of the separate components (most are on the order of 0.01%/˚C). This maybe induced by the change in optical alignment. The curves in Figure 5.19 and Figure 5.20 are similar, which means part of the temperature dependence can be eliminated by calculating the ratio of the two channels. Figure 5.21 shows a monotonic decreasing relationship between the ratio R and temperature. The temperature dependence of the ratio R is due to the asymmetry between the two channels. The most important difference between the signal channel and the reference channel is the narrowband optical filter used in the signal channel. Other differences include: a different photodetector, different amplifier, and different optical path. The error induced by the optical filter is dependent on the spectrum of the receiving light signal, while the errors induced by other factors are insensitive to the spectrum. According to the experimental results described later, the temperature dependence of the SCIIB system is primarily due to the optical filter.

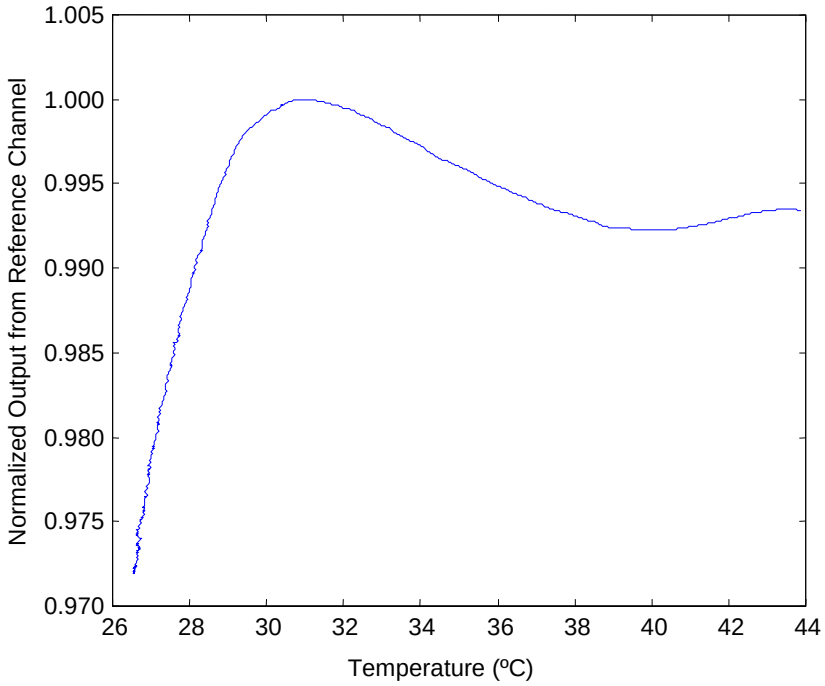

Figure 5.19. Temperature dependence of the reference channel.

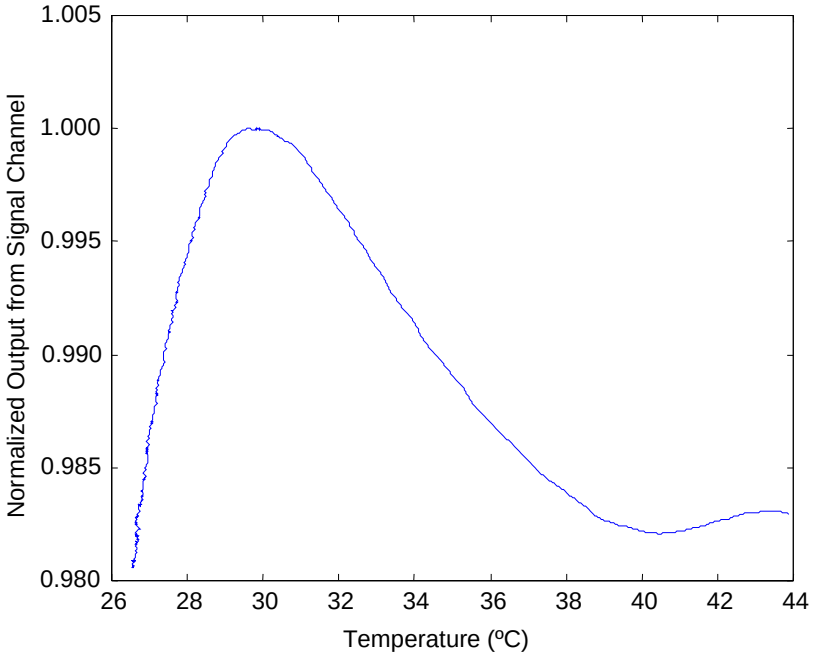

Figure 5.20. Temperature dependence of the signal channel.

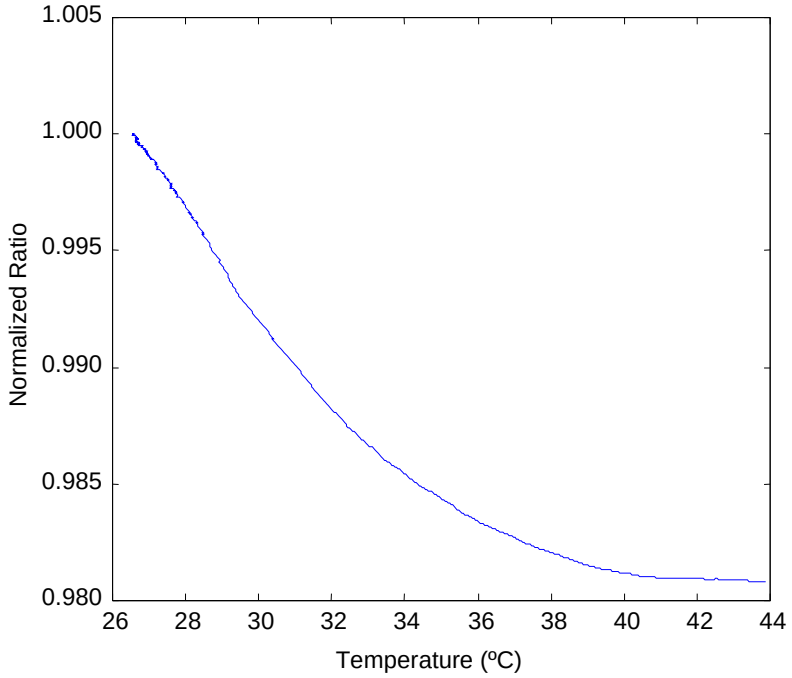

Figure 5.21. Temperature dependence of the SCIIB ratio (signal channel / reference channel).

As discussed above, the temperature dependence of the SCIIB system includes two parts: the first part is spectrum dependent; the second part is insensitive to the spectrum. The second part can be eliminated easily by using an optical switch in the system. Figure 5.22 shows the experimental setup of optical switch. A 1x2 optical switch (Lightech fiber optics Inc.) was used in this experiment to eliminate errors induced by the asymmetry between Channel 1 and Channel 2. For spectrum-insensitive components like the photodetector (the bandwidth of the light source is only 60nm; in this range, the response of the detector can be treated as a constant.), amplifier, etc., this method works well. However, for spectrum sensitive components, like the optical narrowband filter, this method is of almost no use.

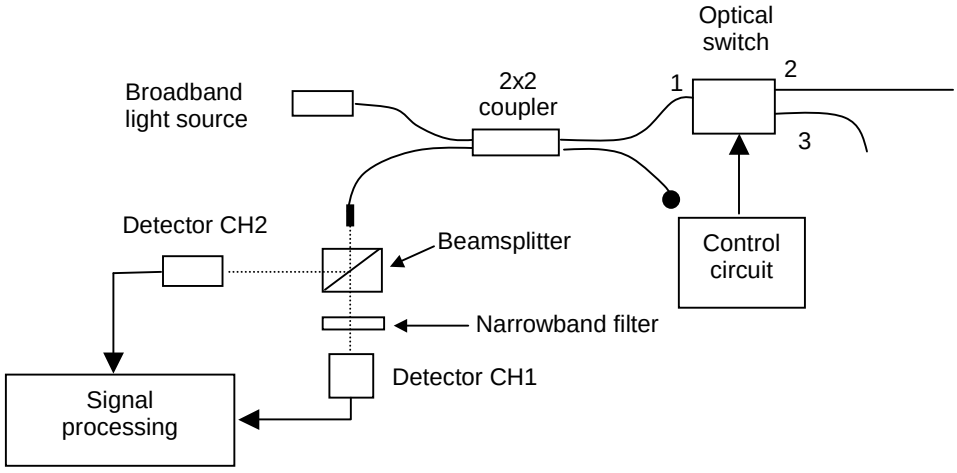

Figure 5.22. Experimental setup to investigate the use of an optical switch to reduce the spectrum independent temperature dependence of the SCIIB system.

In the first experiment, no FABRY-PEROT sensor head was connected in the system. Both Port 2 and Port 3 of the optical switch are connected to a standard 4% reflector (a polished fiber endface). Because the spectra of the reflected light from these two fiber endfaces are identical (same as the spectrum of the light source), all the errors induced by the asymmetry can be viewed as light spectrum insensitive. Under PC control, the optical switch is alternated between two status: 1↔2 or 1↔3. The process can be described as follows.

The optical switch was first set at position one, S_{12}; the received Channel 1 signal is

$$I_{s1} = K_1 L_1 I_{01}, \qquad \textbf{(5-37)}$$

where I_{01} is the output power from the light source at the time when the data is sampled; L_1 includes the effect of the reflector and the fiber loss; K_1 includes the effect of the optical alignment loss, the photodetector and the amplifier in Channel 1.

Similarly, the received signal in Channel 2 can be described as

$$I_{s2} = K_2 L_1 I_{01}. \qquad \textbf{(5-38)}$$

Therefore, in this situation, the ratio R_1 is

$$R_1 = \frac{I_{s1}}{I_{s2}} = \frac{K_1}{K_2}. \qquad \textbf{(5-39)}$$

If the two channels in the SCIIB system are matched perfectly, then $K_1=K_2$, $R_1=1$, meaning the ratio will not change with temperature. Yet, based on the experimental results described above, this requirement cannot be satisfied.

The optical switch was then set at position two, S_{13}, the two received signals and their ratio can be expressed as

$$I_{R1} = K_1 L_2 I_{02}. \qquad \textbf{(5-40)}$$

$$I_{R2} = K_2 L_2 I_{02}. \qquad \textbf{(5-41)}$$

$$R_2 = \frac{I_{R1}}{I_{R2}} = \frac{K_1}{K_2}. \qquad \textbf{(5-42)}$$

To eliminate the error induced by the asymmetry between K_1 and K_2, the ratio of R_1 and R_2 must be calculated: $R=R_1/R_2$. The optical switch experiment results are shown in Figure 5.23. The R_1 and R_2 curves match each other almost perfectly, and the final ratio R shows almost no change, and therefore, is insensitive to temperature. Therefore by introducing an optical switch into the SCIIB system, a portion of the temperature dependence can be eliminated.

Condition two: (with sensor connected)

The optical switch works well when no sensors are connected with the system; however, when the SCIIB system is connected to a Fabry-Perot sensor head, the situation is much different. The critical component is the narrowband optical filter. Because the light spectrum reflected from a Fabry-Perot sensor is much different from that reflected from a reflector, the

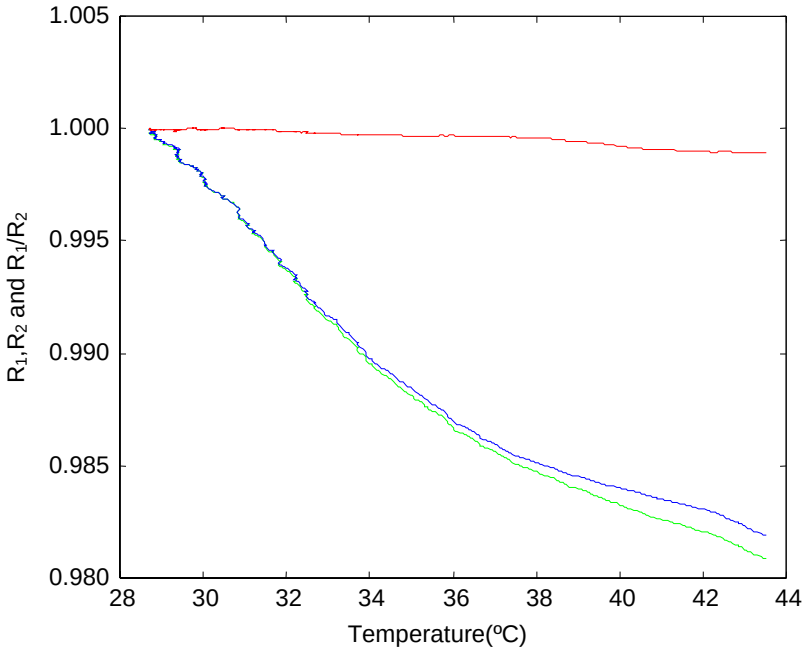

Figure 5.23. Optical switch experimental results (Green line—R_1; Blue line—R_2; Red line—R).

errors induced by the optical filter are different in these two conditions. It's difficult to use the signal from the fiber endface to compensate the signal from a sensor head.

Figure 5.24 shows the normalized spectrum from a Fabry-Perot sensor and from a polished fiber endface. The dashed black line indicates the operating point of the SCIIB system (the ideal center wavelength of the optical filter). When temperature increases, the center wavelength of the optical filter will move to longer wavelengths due to the thermal expansion. These two curves describe how the output of the SCIIB system changes when the center wavelength of the optical filter drifts. Because the slopes of the two curves are very different near the operating point, the induced output errors are also different. In fact, if the center wavelengths of the optical filter and the light source are matched perfectly, the slope of the Gaussian function near the operating point is almost zero, which means only slight errors are produced when a fiber endface is used as the reflector. On the other hand, when a Fabry-Perot sensor is connected in the system, the slope of the received spectrum near the operating point is very large, and the slope will change with the air-gap (or the physical parameter to be measured). The maximum error induced by the optical filter wavelength drift can be described as:

$$\frac{\delta s_{\max}}{\Delta s_{\max}} = \frac{\gamma \frac{4\pi L}{\lambda^2}\delta\lambda}{1.6\gamma} = \frac{4\pi L}{1.6\lambda^2}\delta\lambda \,. \qquad \textbf{(5-43)}$$

In general, the air gap L is about 10000nm, the wavelength is about 1300nm, the temperature dependence of the optical filter is about 0.02nm/°C. So, the error induced by the drift of the optical filter is about 0.1%/°C.

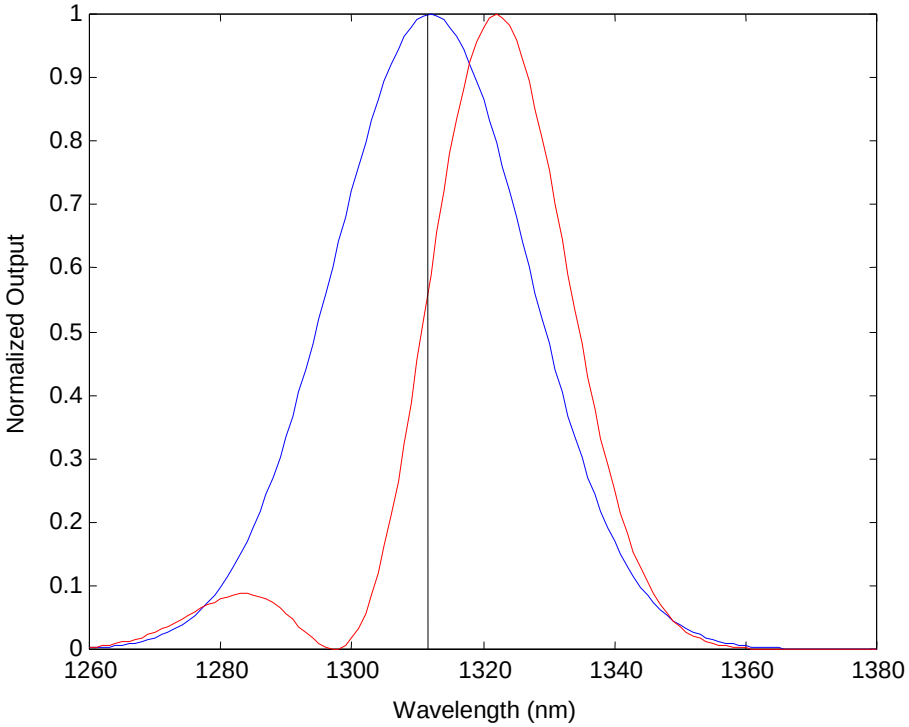

Figure 5.24. Light spectrum reflected from a Fabry-Perot sensor (Red line, the initial air gap of the sensor head is 12000nm); blue line, that from a polished fiber endface).

Figure 5.25 shows the experimental results when a Fabry-Perot sensor head was connected in the system. In this case, the temperature characteristics of the sensor path (optical switch was in position one, the SCIIB system was connected with a Fabry-Perot sensor) is different from that of the reference path (optical switch was in position two, the SCIIB system was connected with a polished fiber end-face.) The use of an optical switch makes the temperature dependence even worse. To decrease the temperature dependence of the SCIIB system, another approach is to use a standard temperature sensor to measure the temperature inside the SCIIB system (especially the temperature of the optical filter). Without losing universality, the output of SCIIB system can be simplified as

$$R = \tfrac{1}{2}(1+\cos(\frac{4\pi L(P)}{\lambda(T)})). \qquad \textbf{(5-44)}$$

Here a Fabry-Perot pressure sensor head was used *(L(P))*, and the center wavelength of the optical filter $\lambda(T)$ is a function of temperature. Differentiating the above equation; the change on R can be expressed as

$$\begin{aligned}\Delta R &= -\frac{4\pi}{\lambda}\sin\frac{4\pi L}{\lambda}\Delta L(P)+\frac{4\pi L}{\lambda^2}\sin\frac{4\pi L}{\lambda}\Delta\lambda(T) \\ &= K_1(P)\Delta L(P)+K_2(P)\Delta\lambda(T)\end{aligned}, \qquad \textbf{(5-45)}$$

where

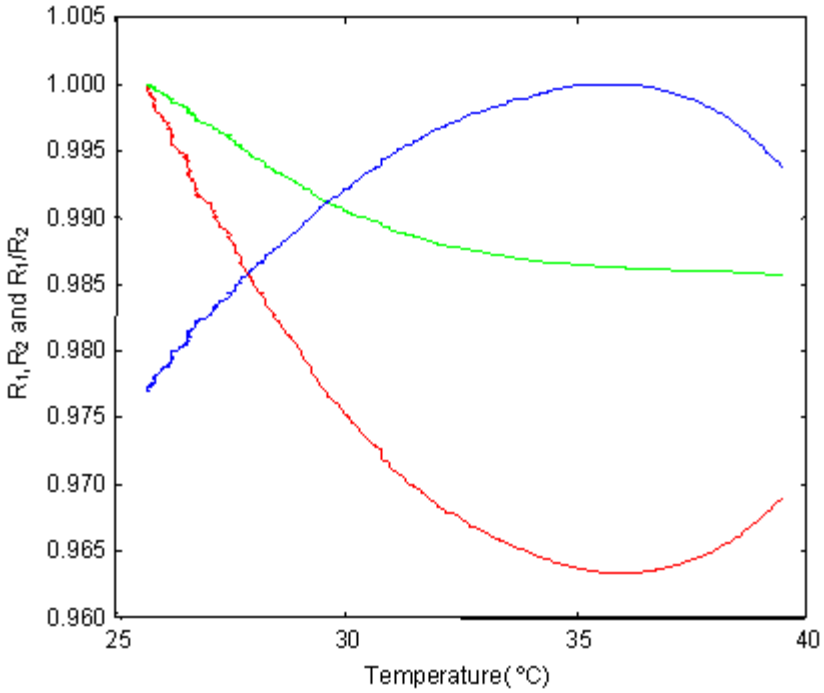

Figure 5.25. Experimental results from the FABRY-PEROT sensor (Green line—Sensor Path R_1; Blue line—Reference Path R_2; Red line—$R=R_1/R_2$).

$$K_1(P) = -\frac{4\pi}{\lambda}\sin\frac{4\pi L}{\lambda}$$
$$K_2(P) = \frac{4\pi L}{\lambda^2}\sin\frac{4\pi L}{\lambda}$$

The first item on the right side provides the pressure sensitivity of the SCIIB system; the second item shows how the system output drifts with the temperature. Compared with the center wavelength itself, the wavelength drift of the optical filter is very small, so λ can be treated as a constant. Both K_1 and K_2 are functions of the air gap L (the pressure to be measured), which means when the pressure changes, the relationship between R and T also changes. This makes compensation of the ratio R complicated. The form of the equation can be changed to

$$\Delta R = K_1(\Delta L - \frac{L}{\lambda}\Delta\lambda)$$
$$\Delta P <=> \Delta L <=> \frac{\Delta R}{K_1} <=> -\frac{L}{\lambda}\Delta\lambda \quad \textit{(5-46)}$$

Compared with L (10000nm), the change ΔL (about 200nm) is pretty small; L/λ can be considered as a constant, so ΔL (or ΔP) is linearly dependent on $\Delta\lambda$ (ΔT). Instead of compensating R with T, we can compensate pressure P with T directly.

A thermal resistor was placed inside the SCIIB system just beside the optical filter, and the whole system was put inside the electrical oven. A Fabry-Perot sensor outside the oven was connected to the system through 1km of singlemode fiber. The temperature of the oven first was increased to about 40°C, and then decreased to room temperature (about 25°C). Figure 5.26 shows the output of the SCIIB system and the thermal resistor during this period. The relationship of the ratio R and temperature T (here, we use the voltage output of thermal resistor directly) can be determined, as shown in Figure 5.27. To set up the relation between ΔP and ΔT (ΔV), the calibration curve of the sensor head must be acquired first, as shown in Figure 5.28. The temperature coefficient of the SCIIB system is then be expressed as

$$\frac{\Delta P}{\Delta V} = \frac{\Delta P}{\Delta R}\frac{\Delta R}{\Delta V}. \qquad \textbf{(5-47)}$$

Based on the method discussed above, several sensors were tested. Yet, the residual errors were still greater than the requirements. The one-day stability level achieved was only about 0.1%. The residual errors come from several sources: the characteristics of some components will drift with time (aging process); the spectrum and the status of polarization changes induced by fiber bending, etc.

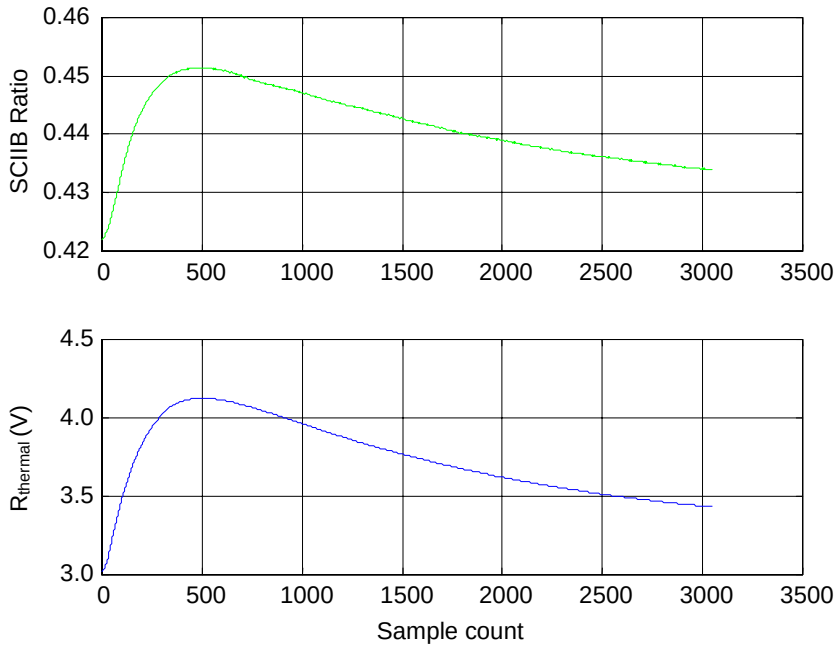

Figure 5.26. SCIIB system temperature experiment (The X axis is time; The unit of the output from thermal resistor is volts).

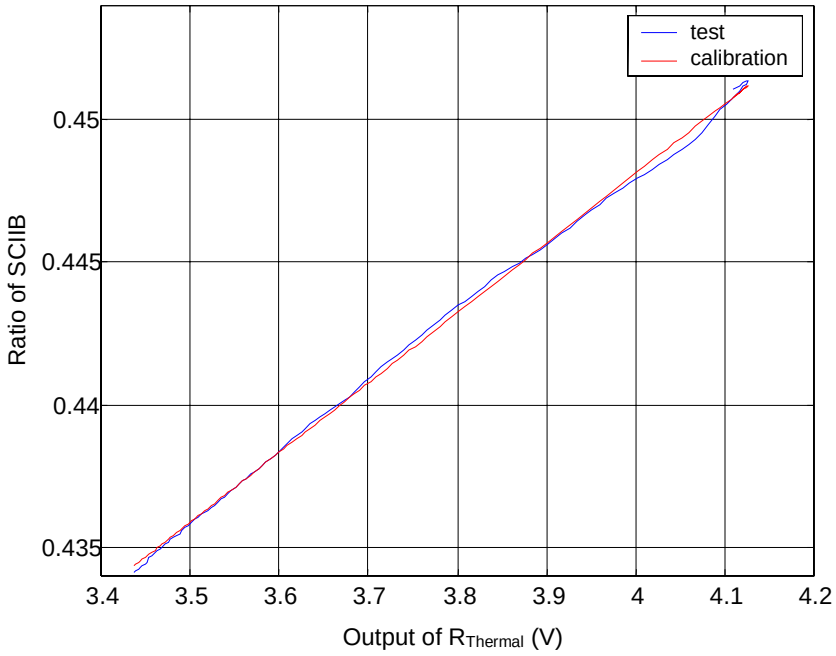

Figure 5.27. Temperature dependence of the ratio R.

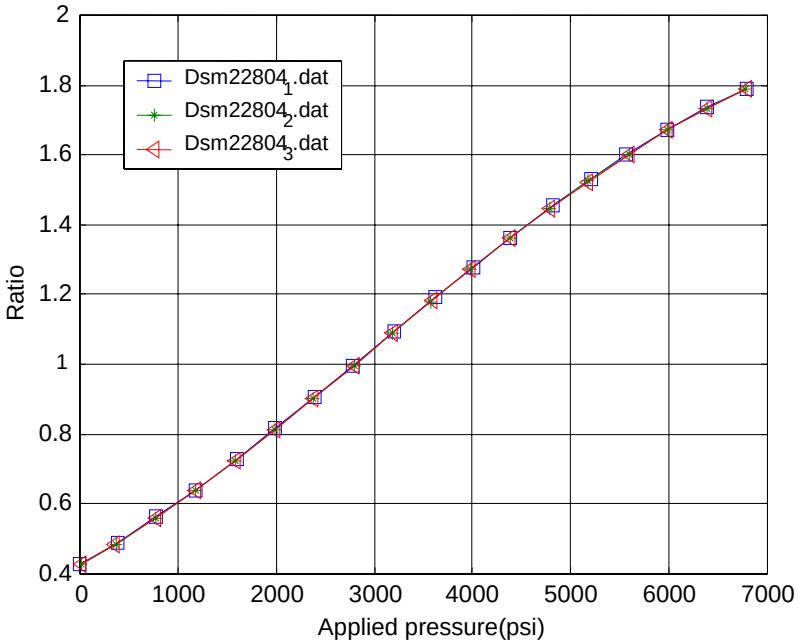

Figure 5.28. Calibration curve of the sensor head.

5.1.3 Other Proposed Signal Demodulating Structures

In parallel with the optimization of the SCIIB system, other signal demodulating structures were also considered, including the white light interferometer discussed in Section 5.2 and the dual-sensor structure described here. One of the major problems of the SCIIB system is the limited dynamic range, which is only about 200-300nm. If the required accuracy is 0.01%, then the accuracy of the air gap measurement needs to be 0.01nm, which is about one tenth of the size of an atom. A second problem is associated with the optical component performance. Most are sensitive to the spectrum or the state of polarization; the spectrum or polarization change induced by a long singlemode fiber is difficult to control. One possible solution for these problems is the dual sensor configuration shown in Figure 5.29.

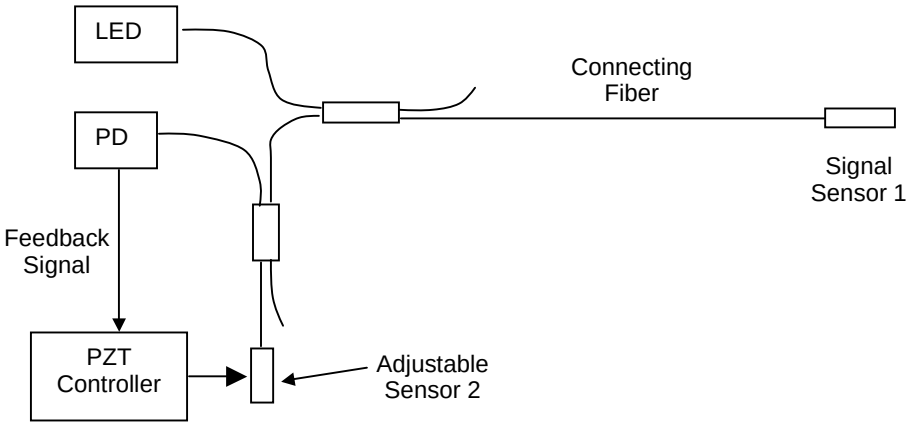

Figure 5.29. Proposed dual-sensor structure design.

Two FABRY-PEROT sensors were used in this system; the signal sensor is a normal FABRY-PEROT sensor, which is used to measure the pressure (or temperature) in the oil site. Another sensor, which is located in the electrical box, is used to trace the air gap of the signal sensor. The air gap of the inside sensor is controlled and measured by a commercialized PZT control system. The photodiode is used to measure the interference between Sensor 1 and Sensor 2. To obtain the maximum output from the PD, the two air gaps must be equal. When the air gap of the signal sensor changes, the output of the PD will decrease. Using the feedback signal from the PD, the PZT controller will adjust the air gap of Sensor 2 until it matches Sensor 1. The PZT controller measures Sensor 2's air gap at the balance point. In this system, the dynamic range of the air gap is determined by the PZT system. When the two air gaps are matched to each other, the signal received by the PD is always a global maximum. A commercialized PZT system can reach 1nm repeatability with tens of microns of dynamic range, so the potential accuracy of this system is better than 0.01%. Additional advantages of this structure include insensitivity to changes in polarization and light spectrum and ease of multiplexing. Positive preliminary results were obtained with this structure. However, due the enormous success achieved with the white light system, attention was focused on that area for the remainder of the program.

5.2 Signal Demodulation System II – White Light Interferometer

In parallel with the SCIIB system development, another interferometric-based fiber optic sensor system, the white light interferometer, was developed at CPT. The initial intent was to monitor the air gap of the FABRY-PEROT sensor during sensor fabrication. (The operating point of the SCIIB system is determined by the initial air gap of the FABRY-PEROT sensor head. To achieve the maximum dynamic range and sensitivity, the deviation of the air gap from the optimum point should be less than 10nm). During this process, several important breakthroughs were achieved by thoroughly studying the white light system. By combining elaborate hardware design with novel data processing methods, the system reaches sub-nanometer resolution with a 10 μm dynamic range. The white light system was proven to be the best choice for high-resolution, low speed applications. In this section, the development of the white light interferometer system is detailed.

5.2.1 Principle of operation

White light or low coherence interferometry is a technique that dates back to 1913 and was reapplied to optical fiber sensing in 1983. In most conventional interferometric systems, high coherence light sources such as single line lasers are used to obtain a large coherence length. For such narrowband light sources, spectral measurements are impossible; only power measurements can be realized. For this kind of system, a tradeoff is required between absolute measurement and a large dynamic range. To achieve absolute measurement, the change in optical length must be limited to half the wavelength, just like in the SCIIB system. By using an fringe counting method, the potential dynamic range can be as large as the coherence length of the light source, but only the relative change of the optical path can be measured. When a long length of optical fiber is involved, the instability induced by the propagation of highly coherent light in the optical fiber also becomes an issue. To realize both absolute measurement and high resolution, the white light interferometer was developed. Instead of a highly coherent laser, a broadband light source, such as an LED, is used in this system. (That's where the terminology "white light" comes from, and in this sense, the SCIIB system also belongs to the white light system family.) Although power detection can still be used, to fully exploit the advantages of the white light source, spectrometer-based detection systems are more popular.

The white light interferometric fiber optic sensor system inherits most of the advantages from conventional interferometer, such as immunity to light source drift and change in transmission loss, high resolution, large dynamic range, etc. On another hand, the use of a long life, low price broadband light source (such as LED) improves the stability of the whole system dramatically. The basic structure of spectrometer-based white light system is shown in Figure 5.30. Similar to the SCIIB system, a Fabry-Perot sensor head is used to measure pressure or temperature. The broadband light source is an 850nm LED with a 60nm bandwidth. This kind of light source encompasses many virtues, such as high stability, long life, high efficiency, small size, low price, etc. A compact spectrometer fabricated by Ocean Optics Inc is used to measure the interference spectrum. The whole system is very compact and robust.

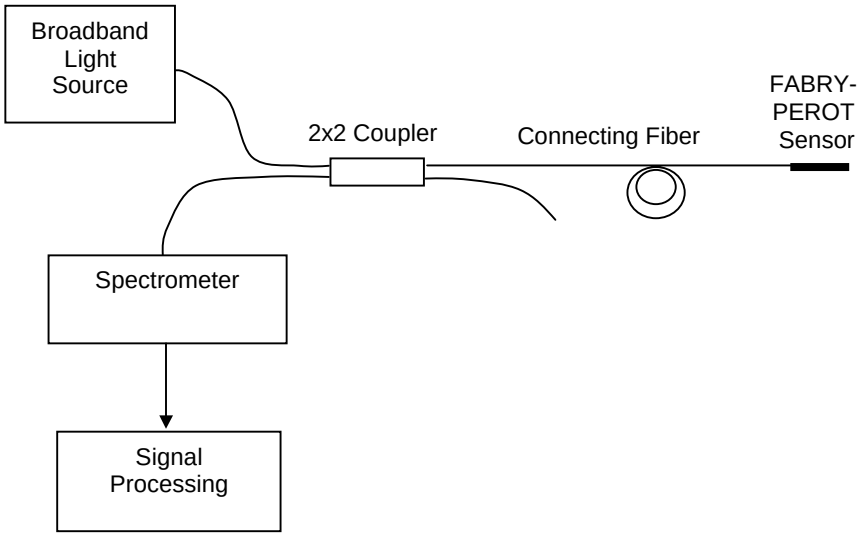

Figure 5.30. Basic structure of interferometer-based white light system.

The optical power output from the light source is launched into the connecting fiber through a 2x2 fiber coupler and propagates to the FABRY-PEROT sensor head. The light signal reflected from the sensor head travels back along the same fiber and is launched out to the one dimension CCD based interferometer from the other port of the 2x2 coupler. Then, the measured spectrum is transferred to PC for data processing. To obtain an interference spectrum with high visibility, the air gap cannot be greater than the coherence length of the system. In this system, the coherence length is primarily dependent on the spectral resolution of the spectrometer, the numerical aperture (NA) of the optical fiber and the quality of the FABRY-PEROT sensor head. In general, the coherence length in the white light system is larger than that of the SCIIB system.

The interference spectrum measured by the spectrometer is given by:

$$I(\lambda) = 2I_s(\lambda) \bullet (1 + \gamma \cos(\frac{4\pi G}{\lambda} + \varphi_0)) . \qquad \textbf{(5-48)}$$

where $I_s(\lambda)$ is the spectral power distribution of light source, γ is the visibility of the interference spectrum, φ_0 is the arbitrary initial phase difference, G is the air gap, which is determined by the physical parameter (such as pressure or temperature) to be measured. By normalizing Eq. (5-48) with respect to the Gaussian spectrum of the light source, the normalized interference output can be expressed as

$$I_n(\lambda) = 2(1 + \gamma \cos(\frac{4\pi G}{\lambda} + \varphi_0)) . \qquad \textbf{(5-49)}$$

The value of the air gap G can be calculated from Eq. (5-49) and then used to demodulate the physical parameter.

5.2.2 Novel data processing method

Various methods had been developed to demodulate the air gap G from the normalized spectrum using Eq. (5-49). Most of these can be grouped into two classes. The first class can achieve high resolution (which primarily depends on the resolution of spectrometer), but the dynamic range of the air gap must be limited in the half wavelength range; the second class can achieve a large dynamic range, yet only a low resolution achieved. The basis of these methods is discussed below.

5.2.2.1 Class One

The first type of demodulation is based on locating a specific point in the interference spectrum (such as peak point or valley point). The value of air-gap can be demodulated from the wavelength of this point. The wavelength λ_m of a peak point in interference spectrum satisfies the equation

$$\frac{4\pi G}{\lambda_m} + \varphi_0 = m2\pi , \qquad \textbf{(5-50)}$$

where the spectral order m is a non-negative integer.

Eq. (5-49) can be transformed into:

$$\begin{aligned} G &= \frac{(m2\pi - \varphi_0)\lambda_m}{4\pi} = \frac{K_m}{2}\lambda_m \\ K_m &= \frac{(2m\pi - \varphi_0)}{4\pi} = m - \frac{\varphi_0}{2\pi} \end{aligned} . \qquad \textbf{(5-51)}$$

To demodulate the air-gap G from the wavelength λ_m, K_m must be acquired first. The identification of the interference order m is so difficult that the unambiguous operating range of the air gap is limited to only half of the wavelength. The resolution of measurement result is primarily dependent on the resolution of spectrometer. From Eq. (5-51), the relative error of this system can be described as

$$\left|\frac{\Delta G}{G}\right| \cong \left|\frac{\Delta \lambda}{\lambda}\right| . \qquad \textbf{(5-52)}$$

5.2.2.2 Class Two

To realize absolute measurement, at least two special points in the interference spectrum must be used. In fact, there are 2048 pixels in the CCD detector of spectrometer, of which 1000 are located in the spectral range of the light source. The more information that is used, the higher the resolution that can be achieved. Suppose λ_1 and λ_2 ($\lambda_1 > \lambda_2$) are the wavelengths of two adjacent peak points in the interference spectrum. Their interference orders are m and $m+1$. From Eq. (5-50):

$$\frac{4\pi G}{\lambda_1} + \varphi_0 = m2\pi . \qquad \textbf{(5-53)}$$

$$\frac{4\pi G}{\lambda_2} + \varphi_0 = (m+1)2\pi \,. \qquad \textbf{(5-54)}$$

The air gap G can be demodulated from

$$G = \frac{\lambda_1 \cdot \lambda_2}{2(\lambda_2 - \lambda_1)} \,. \qquad \textbf{(5-55)}$$

Here, the dynamic range is only limited by the coherence of the white light system. In this case, the relative error induced by the spectrometer is

$$\left|\frac{\Delta G}{G}\right| \cong \sqrt{2}\left|\frac{\lambda_2}{\lambda_2 - \lambda_1}\right| \bullet \left|\frac{\Delta\lambda_1}{\lambda_1}\right| \,. \qquad \textbf{(5-56)}$$

Compared to Class 1 (Eq. (5-52)), in Class 2 demodulation the relative error induced by the spectrometer will be enlarged by a factor of $\sqrt{2}\left|\frac{\lambda_2}{\lambda_2 - \lambda_1}\right|$. The center wavelength of the light source (LED) is 850nm. In the normal operating range (air-gap 5-15 μm), this factor $\sqrt{2}\left|\frac{\lambda_2}{\lambda_2 - \lambda_1}\right|$ is about 15—50. So, this method has a large dynamic range but lower resolution.

5.2.2.3 New Algorithm

To combine the advantages of these two types of methods, a novel data processing method, which can realize both the high resolution and a large dynamic range, was developed at CPT. The basic idea is to use two peak points in the interference spectrum to obtain coarse air gap (large dynamic range is achieved); this coarse air gap is then used to determine the order number m and a rough K_m of a special peak point. Then, an accurate K_m will be recovered from the rough K_m. From Eq. (5-51), the accurate air gap can be calculated from the accurate K_m and the peak wavelength (high resolution is achieved).

If the coarse K_m is used directly, high resolution cannot be achieved. The technique used to recover the fine K_m is discussed here. In the equation $G=K_m\lambda/2$, although K_m is not an integer, for a given peak, it is a constant. And for adjacent peaks, the difference in K_m is 1. For example, if the K_m of one peak is 12.34, then, for other peaks, the K_m will be 13.34, 14.34, 15.34…and 11.34, 10.34, 9.34…

By calibration, the K_m value for a special peak (K_m^0) can be acquired and stored in computer. When the coarse K_m value for any peak has been acquired, the fine K_m is then calculated from K_m^0 by adding the integer part in the difference between the coarse K_m and K_m^0. The entire process of demodulating air gap G from the interference spectrum can be separated into two steps: the calibration process and the measurement process.

The calibration process is described as follows. With the white light interferometer system in a stable condition, set the air gap G to a known value G_0 (or put the FABRY-PEROT sensor head in a given pressure environment). The K_m^0 of a peak in the interference spectrum can be calculated from G_0 and the wavelength λ_0 of this peak. As long as the K_m^0 is acquired, the measuriement process can be carried out as follows.

1. Use two peak points in the interference spectrum to acquire a rough value of air gap G'.
2. Select a peak point near the center of interference spectrum and use the wavelength of this peak and the rough G' from the last step to calculate a rough K_m'.
3. The accurate K_m can be calculated from K_m' and the stored K_m^0 from

$$K_m = K_m^0 + \text{int}(K_m^{'} - K_m^0 + 0.5)\,. \qquad \textbf{(5-57)}$$

   where function *int(...)* indicates the integral portion.
4. The accurate air gap G can be calculated from the accurate K_m and the wavelength of this peak by Eq.(5-51).

If the white system operates in a harsh environment, occasionally, an outside disturbance can introduce a large "jump" in the measuring result. The magnitude of these "jumps" are equal to half of the wavelength exactly. These “jumps” in the measured output are due to the inability of the spectral analyzer to resolve adjacent K_m values. As described in the discussion above, the low resolution G' value is used to determine the low resolution K_m' value. An error can occur in the determination of the low resolution K_m' value due to inaccuracies in the G' value. If this error is large enough this will result in shifting the K_m value by an integer number. This shifting of the K_m value by an integer number results in a calculated change in the air gap of an integer multiple of one half of the wavelength of the light source. When monitoring a physical parameter such as pressure, the observed result is that the pressure detected from the sensor appears to “jump” to a higher or lower value when indeed the real pressure has not changed. This “jump” can occur at any time during the operation of the system and appears in a more or less random fashion. In order to overcome this problem, another data processing method was used to monitor the value of the air gap calculated from the previous time interval. The new air gap value G_n calculated during the present time interval is compared to the air gap value G_0 from the previous time interval:

$$\Delta G = \left| G_n - G_o \right|. \qquad \textbf{(5-58)}$$

If the ΔG value is larger than one half of the wavelength of the light source used, then the air gap will be modified according to:

$$\begin{aligned} G &= G_n - \frac{\lambda}{2} \quad \text{when } G_n > G_0 \\ G &= G_n + \frac{\lambda}{2} \quad \text{when } G_n < G_0 \end{aligned} \,. \qquad \textbf{(5-59)}$$

Therefore, when the condition is detected that G_n differs from G_0 by more than one half of the wavelength, a new air gap G is calculated based on the formulas above. This new air gap G is then used to demodulate the physical parameter to be measured. The system checks for this condition during every measurement. In this manner, the jump problem has been completely eliminated.

This novel data processing method was realized in Visual Basic, and applied in the oil field. Its performance was confirmed by the experimental results.

5.2.3 Design and implementation

Both singlemode and multimode white light systems were set up at CPT. A VB program, integrated functions of system control and date processing, were also developed. Details on the system setup and program development are presented in this section.

5.2.3.1 Hardware design and system fabrication

The most critical part of white light system is the spectrometer. The performance of the entire system, such as resolution and stability, are highly dependent on the performance of spectrometer. In a traditional spectrometer-based system where a cumbersome and expensive spectrometer is used, strict requirements on the environmental conditions exclude the use of this kind of instrument in the field. Here, a compact fiber optic spectrometer (USB2000 manufactured by Ocean Optics, Inc.) was used in the white light system. The input fiber is connected to the USB2000 directly through a SMA connector. Inside the spectrometer, a 1200 line holographic grating is used to diffract the input light on a 2048-pixel CCD array. The electrical signal output from each pixel can be read out serially. After conversion to digital format by a built-in A/D card, the measured spectrum can be transferred into a PC. The interface between the computer and the spectrometer is very flexible; Ocean Optics supports most of the common ports, including USB, ISA, etc. The key features of the USB2000 are listed in Table 5.4 below.

Both singlemode and multimode white light systems were built based on the USB2000 spectrometer. In the multimode system, the light source is an 850nm LED (Honeywell HEF 4857-014). In the singlemode system, a super-luminescent diode (SLED from EG&G Inc.) was used. To satisfy the requirements of different applications, a two-channel multimode system was also developed. Figure 3.2a and b shows the structure of single channel multimode white light system. The two channel multimode white light system is shown in Figure 3.3. The dual channel and single channel multimode systems are shown in Figure 5.32 and Figure 5.31, respectively.

5.2.4 Software design and program development

Advanced computer software was developed to demodulate the air gap from the interference spectral signal. This program is based on the novel data processing method discussed in the previous section. The program is implemented in a combination of Visual Basic and C languages so that both graphic interfaces and high computational speed are achieved and optimized. A block diagram of the program is shown in Figure 5.33, and the program details are described in the remainder of this section.

5.2.4.1 Initialization

Hardware initialization includes initialization of the spectrometer, temperature measurement system (for compensation), etc. Then most of the important parameters, which are stored on the hard disc, will be restored to memory, including the parameters for setting up spectrometer, the K_0 value, the reference spectrum of the light source, the dark current of the spectrometer, and the calibration curve of the FABRY-PEROT sensor head.

Table 5.4. Key features of the Ocean Optics USB2000 fiber spectrometer.

Computer interface:	Universal Serial Bus (RS-232 available on side connector)
Spectrometer channels:	One or two
Integration time:	3 milliseconds-65 seconds
Data transfer rate:	Full scans (2048 wavelengths) into memory every 13 ms OOIBase32 time acquisition approximately every 25 ms
Dimensions:	3.5" x 2.5"x 1.31" LWH 89 mm x 64 mm x 34 mm LWH
Weight:	0.45 lb. (200g) without cable 0.60 lb. with cable
Detector:	2048-element linear silicon CCD array
Effective range:	200-1100 nm
Dynamic range:	2×10^8
Sensitivity (estimate):	86 photons/count
Signal-to-noise:	250:1 (at full signal)
Dark noise:	2.5-4.0 (RMS)
Gratings:	Multiple grating choices, optimized for UV, VIS or NIR
Slits:	Optical fiber is entrance aperture
Focal length:	42 mm (input); 68 mm (output)
Resolution:	~ 0.3 nm-10.0 nm FWHM
Stray light:	< 0.05% at 600 nm; < 0.10% at 435 nm; <0.10% at 250 nm
Fiber optic connector:	SMA 905 to single-strand optical fiber (0.22 NA)

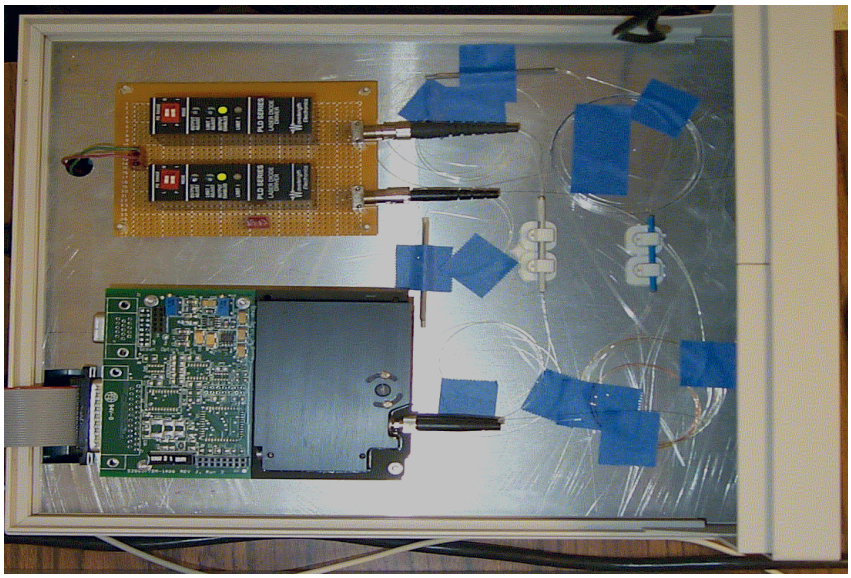

Figure 5.31. Two channel multimode white light system.

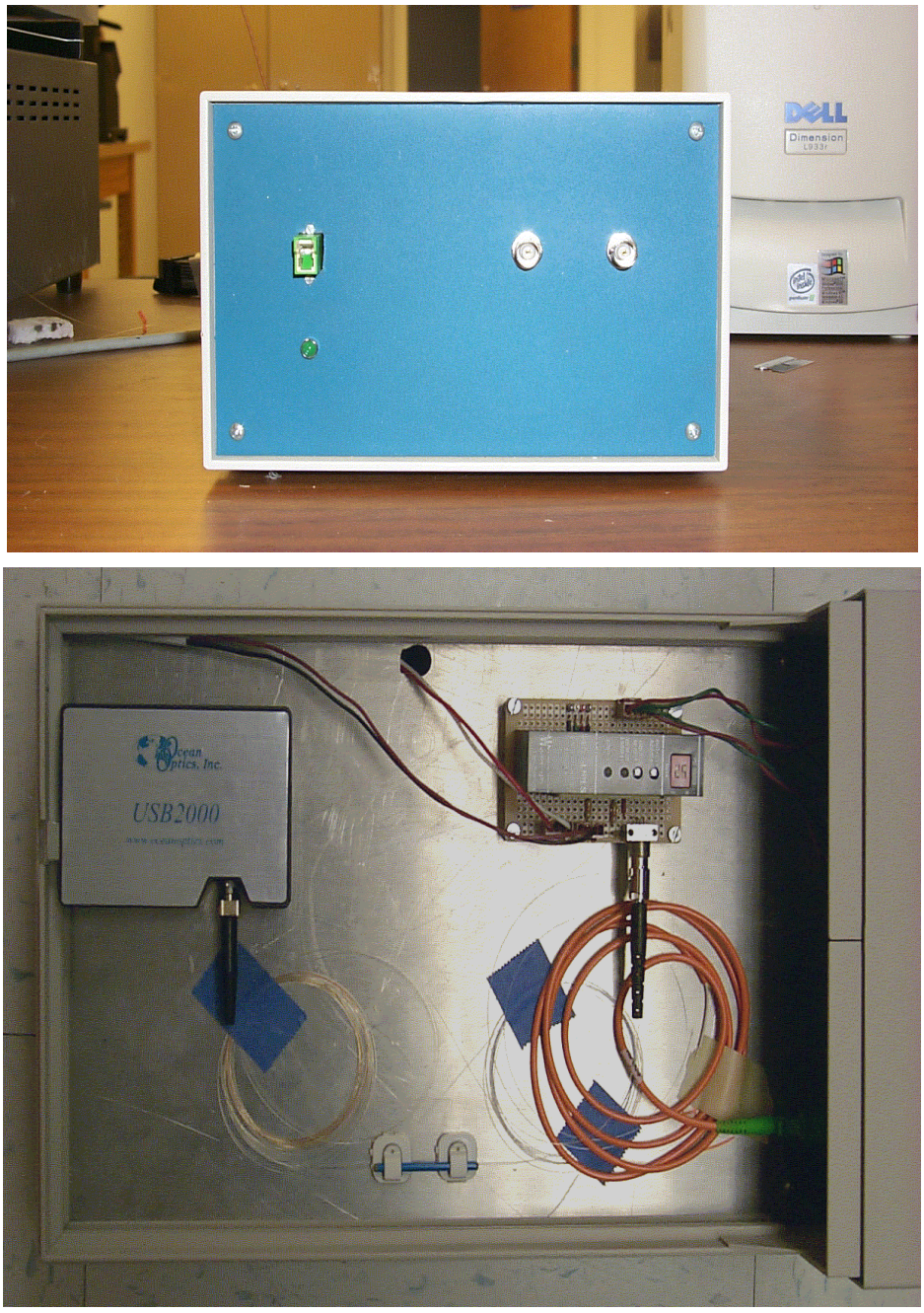

Figure 5.32. Single channel multimode white light system.

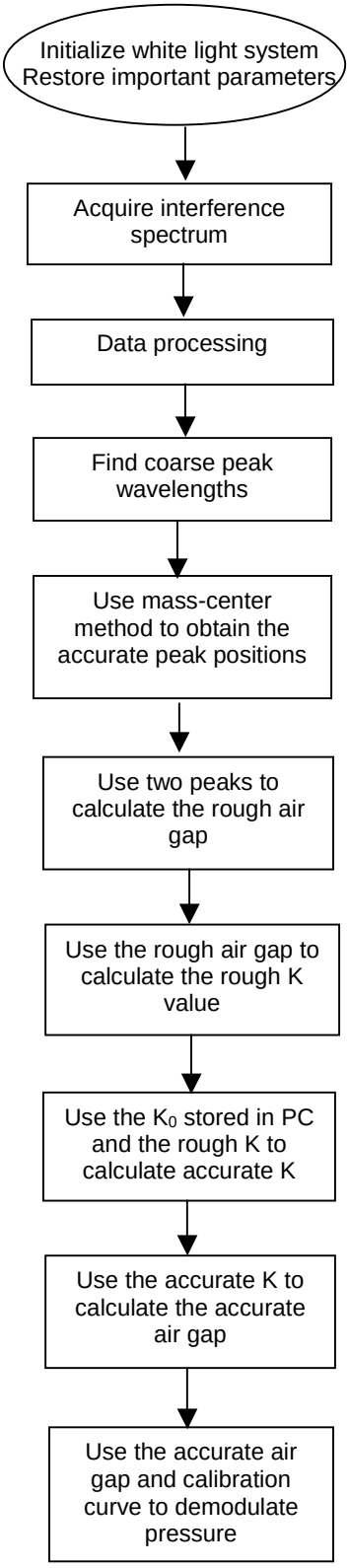

Figure 5.33. Block diagram of demodulation program.

5.2.4.2 Spectrum measurement

The interference spectrum from the FABRY-PEROT sensor head will be sampled according to the given time interval. Once the received light signal emerges from the optical fiber, it is coupled into the spectrometer through a SMA connector. Once in the spectrometer, the divergent light is collimated by a spherical mirror. Then, a plane grating is employed to diffract the collimated light. A second spherical mirror focuses the resulting diffracted light and an image of the spectrum is projected onto a one-dimensional 2048-pixel linear CCD array. These reverse-biased photodiodes discharge a capacitor at a rate proportional to the photon flux. When the integration period of the detector is complete, a series of switches close and transfer the charge of each pixel to a shift register. After the transfer to the shift register is complete, the switches open, the capacitors attached to the photodiodes are recharged and a new integration period begins. At the same time as the light energy is being integrated, the spectrum data is read out of the shift register by a built-in A/D card. Finally, the spectral data is sent to the PC through an USB port.

5.2.4.3 Data processing

To demodulate the pressure (or temperature) signal from the interference spectrum accurately, an advanced data processing algorithm was developed and realized in Visual Basic. This part is the core of the whole program, and will be discussed in several sub-steps:

Pre-processing

The original spectral data from the spectrometer is a 1x2048 array, which is composed of the received light signals of the 2048 pixels of CCD detector. To recover the interference spectrum, the calibration curve of the CCD is used to calculate the real wavelength from the serial number of array. To remove the dark current noise of the CCD detector and other background noise, a dark spectrum stored in the PC is deducted from the measured spectrum. The dark spectrum was acquired when the light source was powered off. Figure 5.34 shows the spectrum after this step.

Smoothing and Normalization

In Figure 5.34 noise is apparent in the received spectrum. To improve the signal-to-noise ratio (SNR), a boxcar algorithm was developed to filter and smooth the raw data. The spectrum after smoothing is shown in Figure 5.35, where the spectrum is automatically truncated according to its signal level. This ensures that only the high SNR region of the spectrum is included in the calculations. Then the measured spectrum will be normalized by the Gaussian profile reference spectrum of the light source (Figure 5.36).

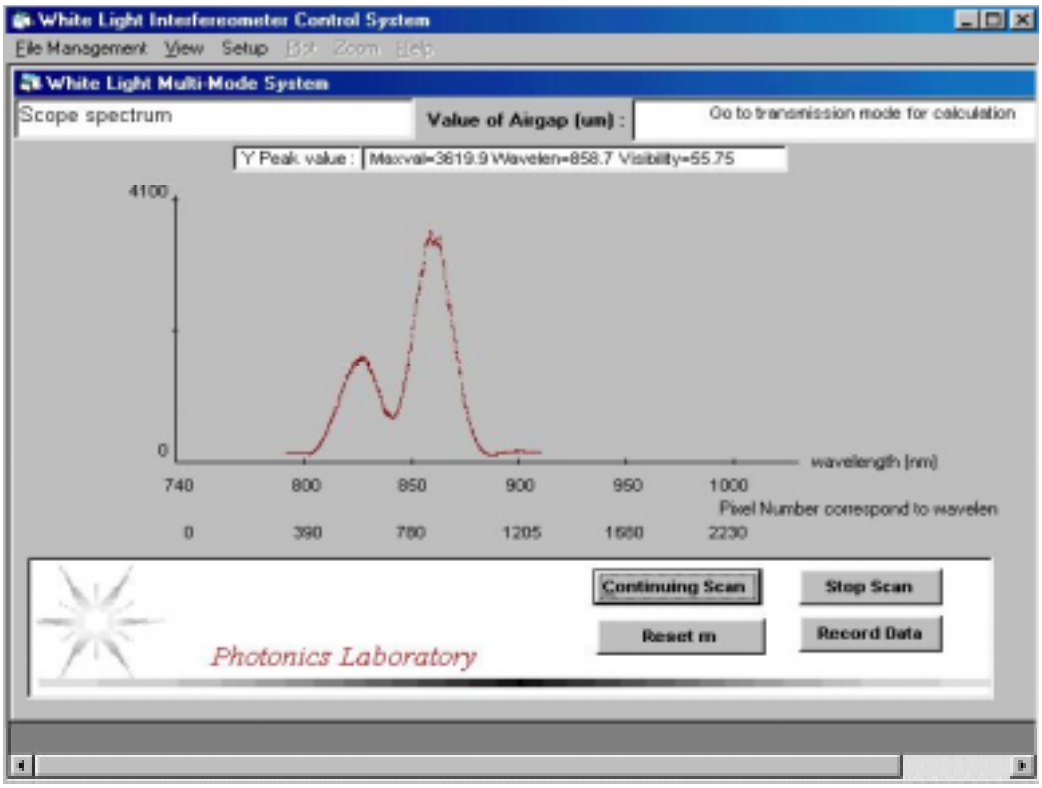

Figure 5.34. The interference spectrum after pre-processing.

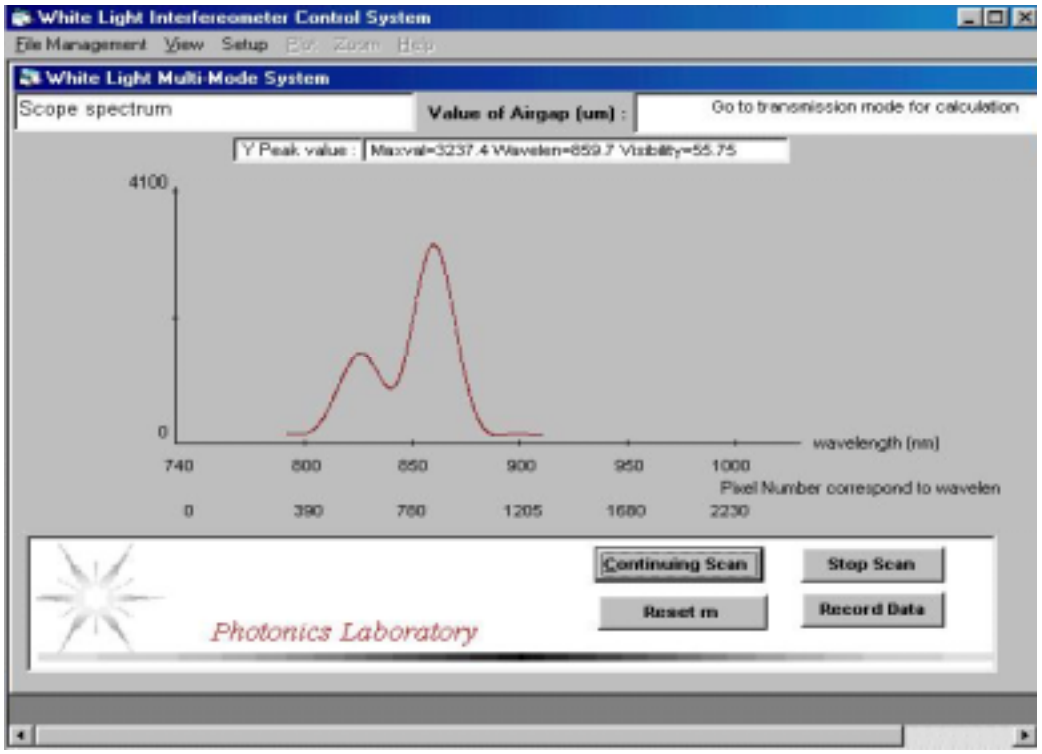

Figure 5.35. The interference spectrum after smoothing.

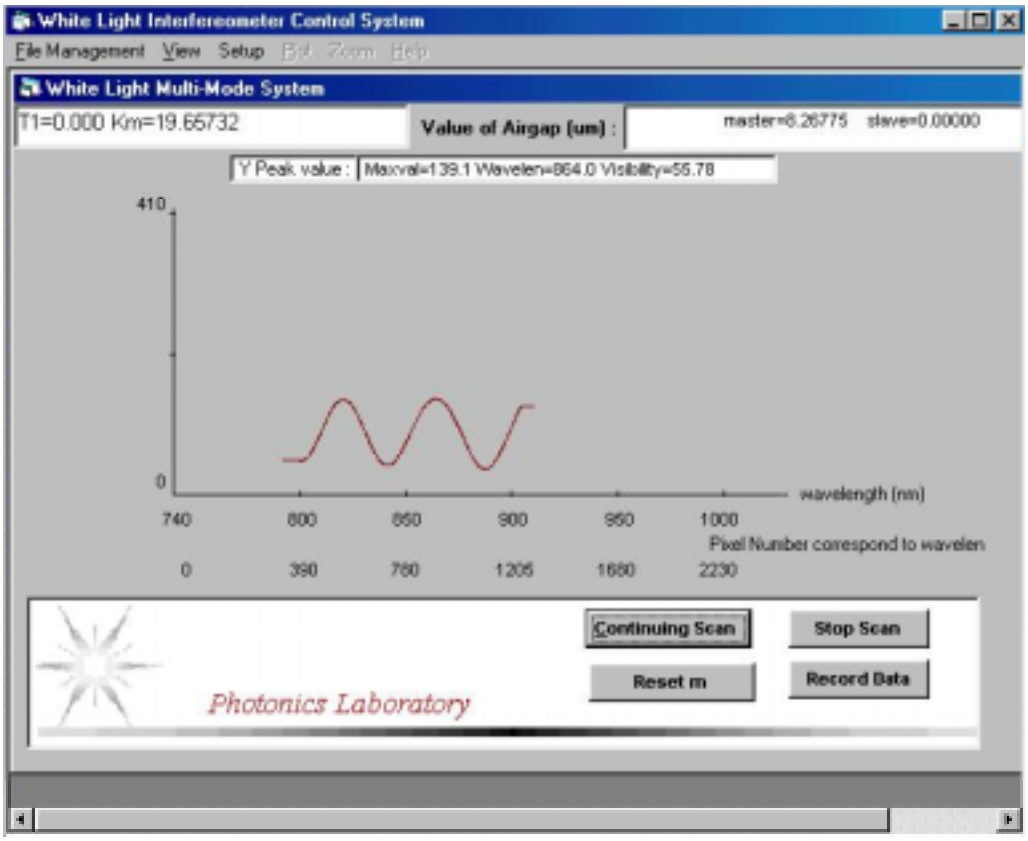

Figure 5.36. Normalized interference spectrum.

An important parameter of the boxcar smoother is the window width, which must be selected very carefully. An unsuitable window width may induce deformation of the interference spectrum. Suppose the measured spectrum is $\{f(i),\ i=1,2..,\ 2048\}$, then the boxcar smoothing process can be described as:

$$f_s(i) = \frac{1}{2w+1} \sum_{j=-w}^{j=w} f(i+j). \qquad \textbf{(5-60)}$$

where w is the window width. Obviously, the larger the window width of the filter is, the better the performance that can be achieved. On the other hand, a large window width will cause two problems. First, the visibility of the spectrum will decrease when the window width is increased due to the averaging arithmetic. Second, because the interference spectrum is not a symmetric function of wavelength, the average process will induce the deformation of interference spectrum and shift of peak positions. Figure 5.37 shows the simulated results for a small window width ($w=5$; air gap $G=11\mu m$). In this case, no obvious deformation is observed, and a high visibility was achieved.

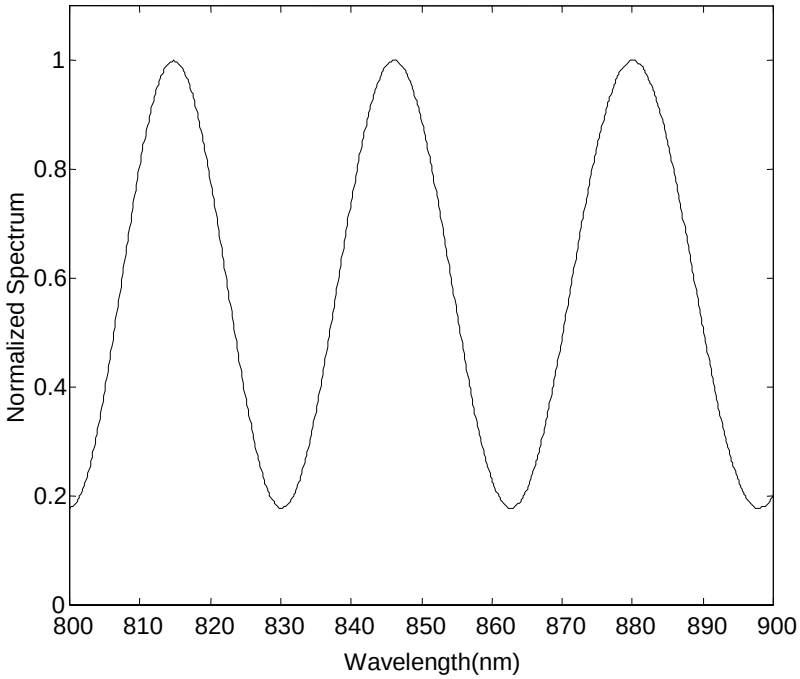

Figure 5.37. Simulated result for small window width (*w=5*).

In comparison, Figure 5.38 shows the simulated result for a large window width (*w=80; G=11*). The visibility of interference spectrum decreases substantially and obvious deformation can be observed. Figure 5.39 shows the measured results when a large window width was used (*w=61*), the result is very similar to the simulated results shown in Figure 5.38. To get the best performance and prevent the deformation of the interference spectrum, the window width needs to be optimized for each different CCD detector, light source and air gap of the FABRY-PEROT sensor. The basic principles are: 1) the more CCD pixels per unit wavelength space, the larger the window width that can be used; 2) the smaller the FABRY-PEROT sensor air gap (which means the space between adjacent peaks is large), the larger the window width can be.

Peak location

Demodulation of the air gap is based on the peak positions in the interference spectrum. The technique for peak location is described here.

The first step is to find the coarse locations of the peaks and valleys by a smart comparison algorithm. The basic idea is to find all the local maximum points within a specific range in the interference spectrum. The size of the searching range, which is defined as the window size of peak searching, must be large enough to eliminate the influence of noise. On the other hand, to avoid missing some peaks, the window size must be smaller than the space between adjacent peaks. An FFT algorithm is used to automatically estimate the optimum window size for peak searching. After the coarse position of the peaks has been found, a mass-centroid algorithm is applied to find the accurate peak positions. The basic theory of the

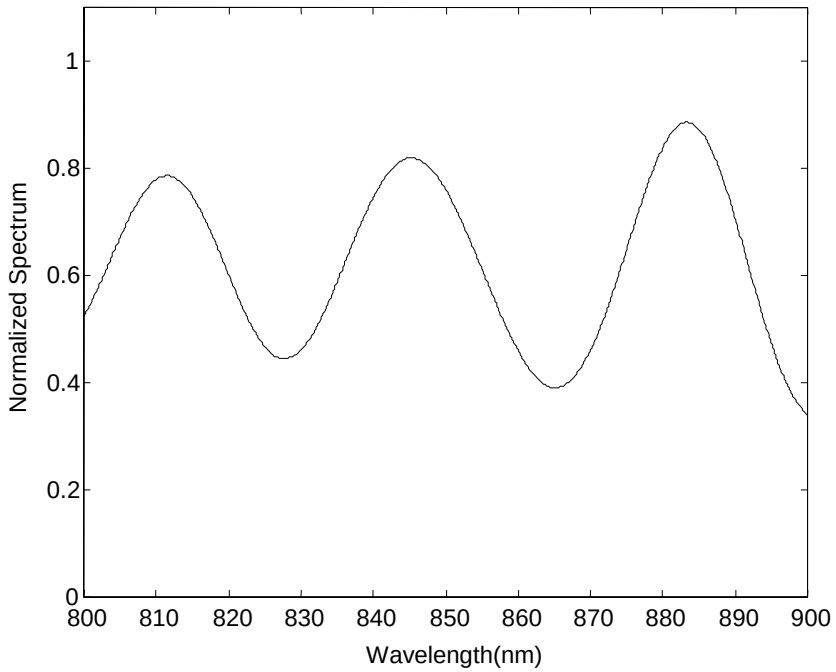

Figure 5.38. Simulated result for large window width (*w=80*).

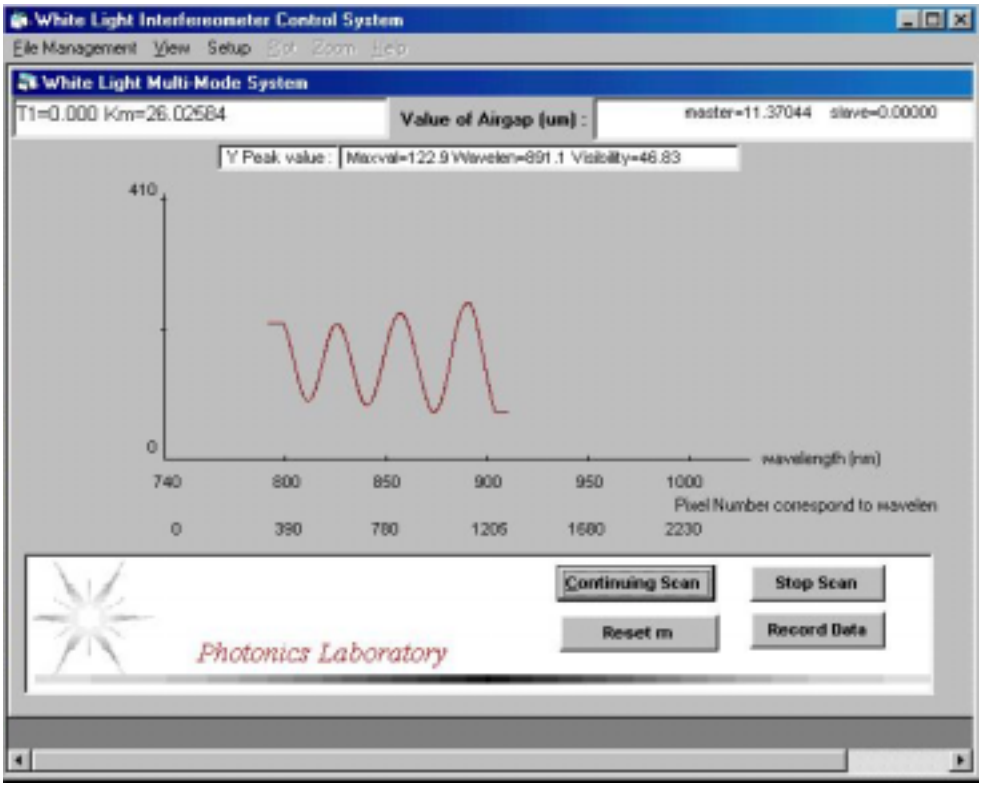

Figure 5.39. Measured result when a large window width was used.

mass-centroid algorithm is shown in Figure 3.11. If the function Y (x) is symmetry around its peak position, then the peak position coincides with the x coordinate of the centriod of Y (x).

As shown in Figure 5.40, the peak position X_0 can be calculated from

$$X_0 = \frac{\int xf(x)dx}{\int f(x)dx}. \qquad \textbf{(5-61)}$$

From the equation $I_n(\lambda) = 2(1+\cos(\frac{4\pi G}{\lambda} + \varphi_0))$, around the peak point, the spectrum is a symmetrical function of $k=1/\lambda$. Therefore, the spectrum $y(\lambda)$ must be changed into k-space first (from $\{y_i, \lambda_i\}$ to $\{y_i, k_i\}$).

Starting from the normalized spectrum $\{y_i, k_i\}$, the accurate peak positions can be calculated from the coarse peak positions:

$$\begin{aligned} k_i &= \frac{1}{\lambda_i} \\ k_m^p &= \frac{\sum y_i k_i (k_i - k_{i-1})}{\sum y_i (k_i - k_{i-1})} \\ \lambda_m^p &= \frac{1}{k_m^p} \end{aligned} \qquad \textbf{(5-62)}$$

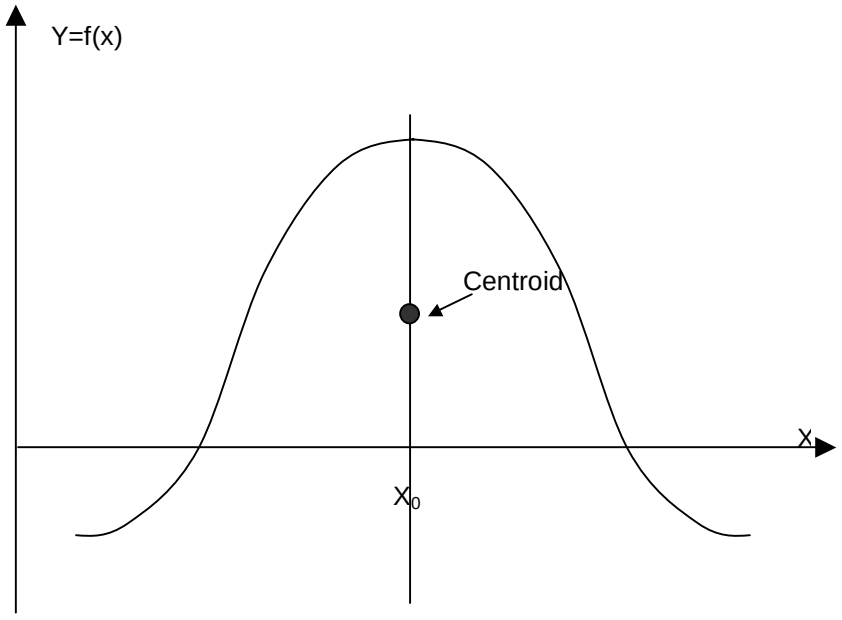

Figure 5.40. The mass-centroid method.

Demodulation of the measured physical parameter

Once the peak positions were determined, the physical parameter to be measured can be demodulated. A coarse air gap will be calculated using two peak positions, and then the coarse *k* value for a specific peak will be determined. From the K_0 value stored in the PC, the accurate *k* value will be determined, which in turn is used to calculate the accurate air gap. The current air gap will be compared with the previous air gap measurement value to judge if a "jump" happened during this process. If it does happen, the measurement results will be modified by a suitable value. Finally, using the calibration curve, the pressure (or temperature) will be demodulated from the accurate air gap.

5.2.5 White light system performance

The multimode white light system has been used as the signal demodulation system for pressure, temperature and flow sensors. Here, some common results are discussed. Other characteristics of the white light system, such as repeatability, long-term stability, etc, will be discussed with a specific sensor in the following chapters.

5.2.5.1 Large dynamic range and linearity

The major advantage of the white light system is the large dynamic range. Figure 5.41 shows the testing results from a Fabry-Perot temperature sensor. During this experiment, the signal demodulating system was kept in a stable environment; the FABRY-PEROT sensor head was put into an electrical oven. While the temperature of electrical oven increased from room

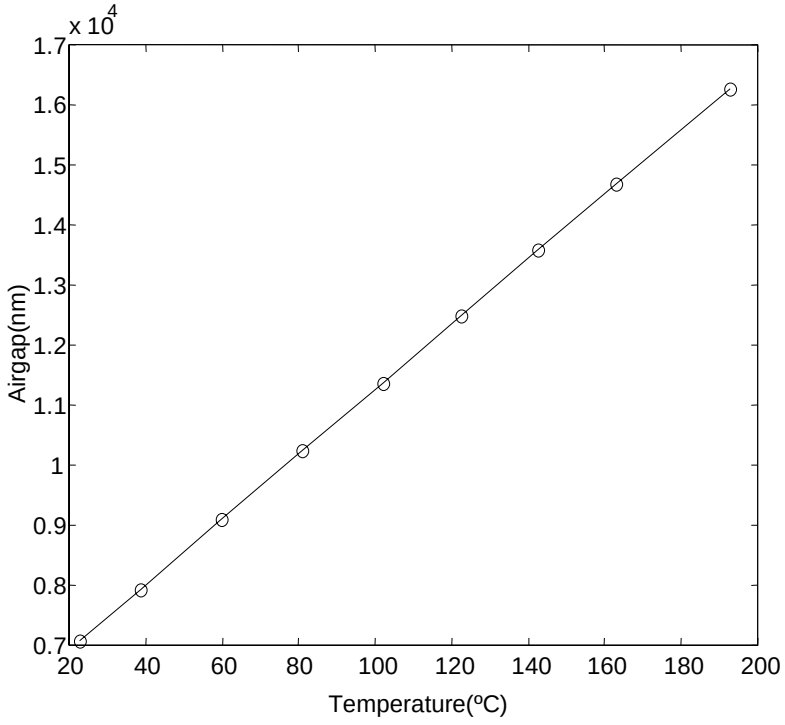

Figure 5.41. Testing results from the FABRY-PEROT temperature sensor.

temperature to about 200°C, the air gap of the FABRY-PEROT sensor head increased from 7μm to about 16μm, giving a dynamic range of about 9μm. Compared with the 200nm dynamic range of SCIIB sensors, the dynamic range was increased about 45 times. Figure 5.41 also shows very good linearity. In fact, as long as the coefficient of thermal expansion (CTE) of the material is a constant, the measuement results will have a linear relationship with the temperature.

5.2.5.2 High resolution

One characteristic of the interferometric-based sensor is the high resolution. Figure 5.42 shows the testing results for a pressure sensor over 30 seconds. The sample rate is about 5 Hz. During this experiment, the whole system (white light and FABRY-PEROT sensor) was kept in a stable environment (both temperature and pressure). The resolution of the sensor system is usually interpreted by the standard deviation of a series of air gap measurements. It is common to use twice the standard deviation as the direct measure of resolution. In Figure 5.42, the standard deviation is about 0.015nm, which gives a resolution of about 0.03nm. This is the resolution limit of the white light system. In field application, due to various noise sources (such as temperature fluctuation, mechanical vibration, etc), it's very difficult to reach this limit.

5.2.5.3 Temperature characteristics

The temperature dependence of the white light system comes from two sources: the LED and the spectrometer. Their contributions will be discussed separately as follows.

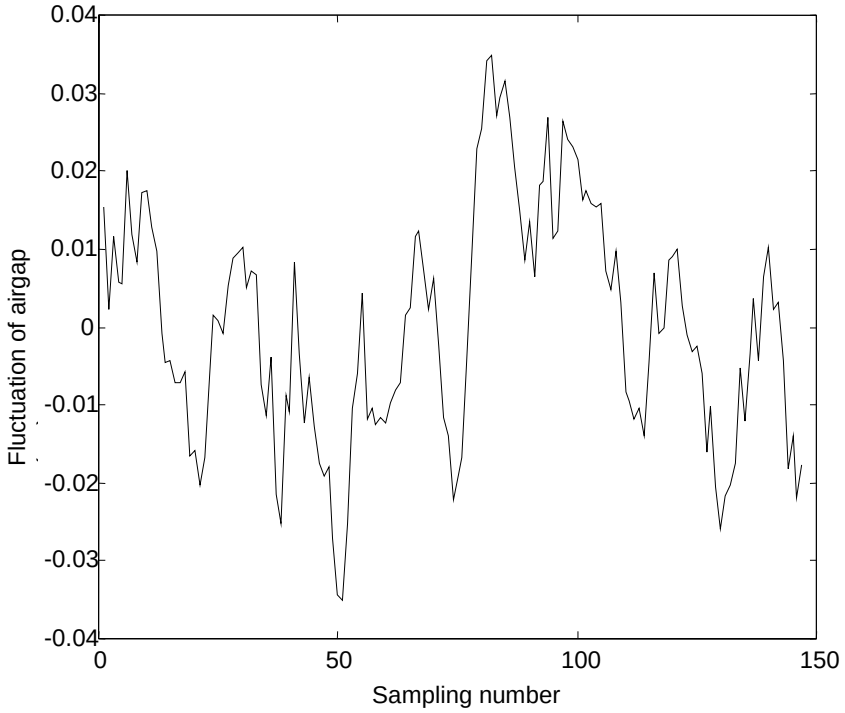

Figure 5.42. Short term fluctuation of the white light system.

LED

Although the spectrum of the LED had been measured and stored in the PC as the reference spectrum, when the ambient conditions change, the spectrum of LED may drift. The center wavelength of the LED will shift to a longer wavelength determined by the material characteristics as the temperature increases. Suppose the reference spectrum was acquired at temperature T_0, and the central wavelength at that temperature is λ_0 then, the reference spectrum can be described as

$$R(\lambda) = I_0 \exp(-\frac{(\lambda - \lambda_0)^2}{w^2}), \qquad \textbf{(5-63)}$$

where w is the spectral width of the light source. When the temperature increases to T, the center wavelength of the LED will shift to λ_T. Since no method can be used to acquire the spectrum of LED in real time, the reference spectrum acquired at temperature T_0 will be used to normalize the interference spectrum acquired at temperature T. The normalized spectrum $N(\lambda)$ calculated in this way can be expressed as

$$N(\lambda) = \frac{\exp(-\frac{(\lambda - \lambda_T)^2}{w^2})}{\exp(-\frac{(\lambda - \lambda_0)^2}{w^2})}(1 + \gamma\cos(\frac{4\pi G}{\lambda})). \qquad \textbf{(5-64)}$$

The simulated curve N(λ) is shown in Figure 5.43. Here the air gap G is supposed to be 9.2μm, the spectral width w is 27nm, the visibility of the interference spectrum γ is 0.5, and the shift of central wavelength is 5nm. Figure 5.44 shows the measured result of a Fabry-Perot sensor when the temperature was increased to about 45°C (the reference spectrum was acquired at 25°C). The theoretical analysis and the experimental result match very well. Obviously, since the reference spectrum acquired at a different temperature, the peak positions in interference spectrum shifted.

Suppose the LED center wavelength shift is

$$\delta = \lambda_T - \lambda_0 = a\Delta T << \lambda_0. \qquad \textbf{(5-65)}$$

Then

$$\frac{\exp(-\frac{(\lambda - \lambda_T)^2}{w^2})}{\exp(-\frac{(\lambda - \lambda_0)^2}{w^2})} \approx (1 + \frac{2(\lambda - \lambda_0)}{w^2}\delta). \qquad \textbf{(5-66)}$$

So Eq. (5-64) becomes

$$N(\lambda) = (1 + \frac{2(\lambda - \lambda_0)}{w^2}\delta) \bullet (1 + \gamma\cos(\frac{4\pi G}{\lambda})). \qquad \textbf{(5-67)}$$

The peak position shift Δλ can be acquired by differentiating the last equation.

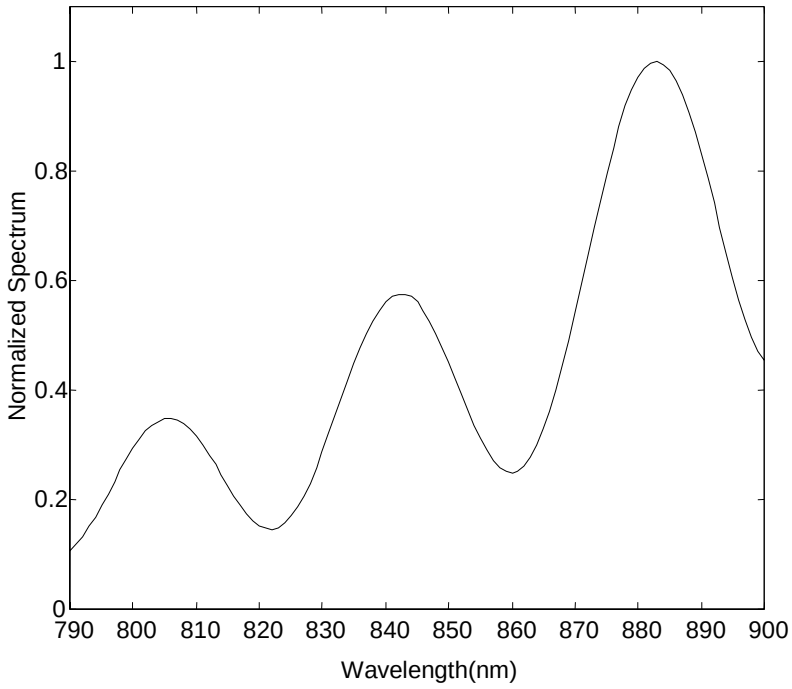

Figure 5.43 Simulated normalized spectrum.

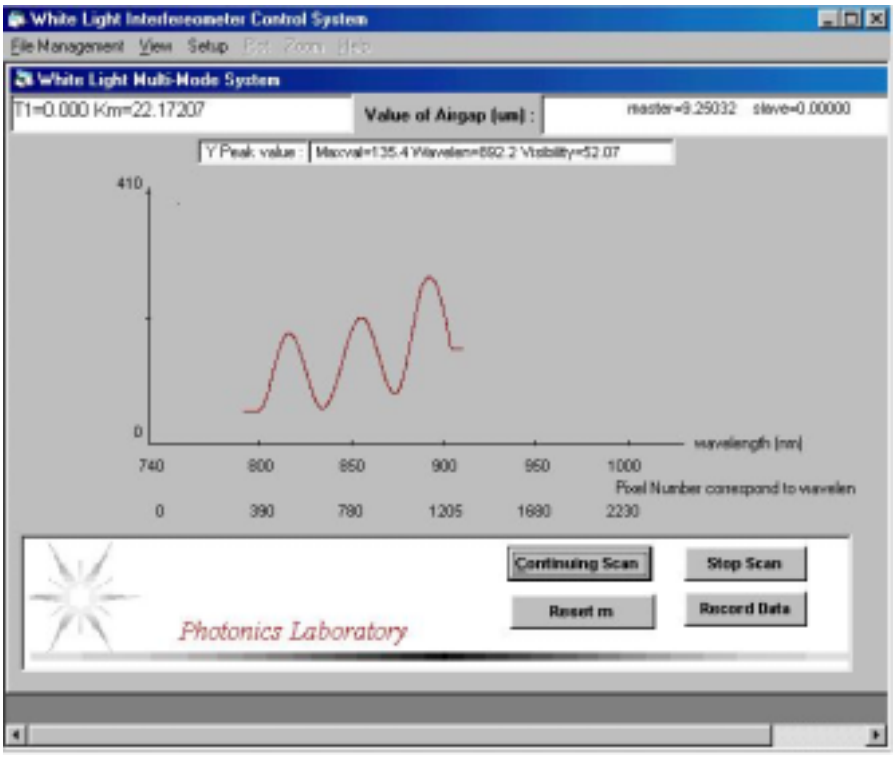

Figure 5.44. Measurement results of the normalized spectrum at 45°C.

)

$$\frac{\partial N}{\partial \lambda} = \frac{2\delta}{w^2} + \frac{4\pi G\gamma}{\lambda^2}\sin\frac{4\pi G}{\lambda} + \frac{2\delta}{w^2}\gamma\cos\frac{4\pi G}{\lambda} + \frac{2(\lambda-\lambda_0)\delta\gamma}{w^2}\cdot\frac{4\pi G}{\lambda^2}\cdot\sin\frac{4\pi G}{\lambda} = 0$$
$$\Delta\lambda = \frac{(1+\gamma)\lambda^4}{8\pi^2\gamma G^2 w^2}\cdot\delta \qquad \textbf{(5-68}$$

Using $G=m\lambda/2$, the error in air gap ΔG induced by peak position shift $\Delta\lambda$ is

$$\Delta G_L = \frac{(1+\gamma)\lambda^3}{8\pi^2\gamma G w^2}\cdot\delta_L = \frac{(1+\gamma)a\lambda^3}{8\pi^2\gamma G w^2}\cdot\Delta T\,. \qquad \textbf{(5-69)}$$

In general, the temperature coefficient of an LED (a in Eq. (5-69)) can be treated as a constant; when the air gap G is a fixed number, the air gap error induced by the light source temperature change is linearly dependent on the temperature change.

The temperature dependence of the light source was measured experimentally. During this experiment, the light source was kept in an electric oven; the spectrometer and other parts were kept in the room environment. The temperature of the oven was increased to about 50°C, and kept at that temperature for about 2 hours. Then the temperature was decreased to room temperature slowly (in about 3 hours). During the temperature decreasing process, a thermocouple was used to sample the temperature in the oven, and the spectrum of the LED was sampled by the Ocean Optics card. Figure 5.45 shows the test results. The temperature coefficient of the LED is about 0.27nm/°C. For a regular FABRY-PEROT sensor ($G=10000nm,\ \gamma=0.6$) the temperature characteristics induced by the shift of LED central wavelength is about 0.77nm//°C.

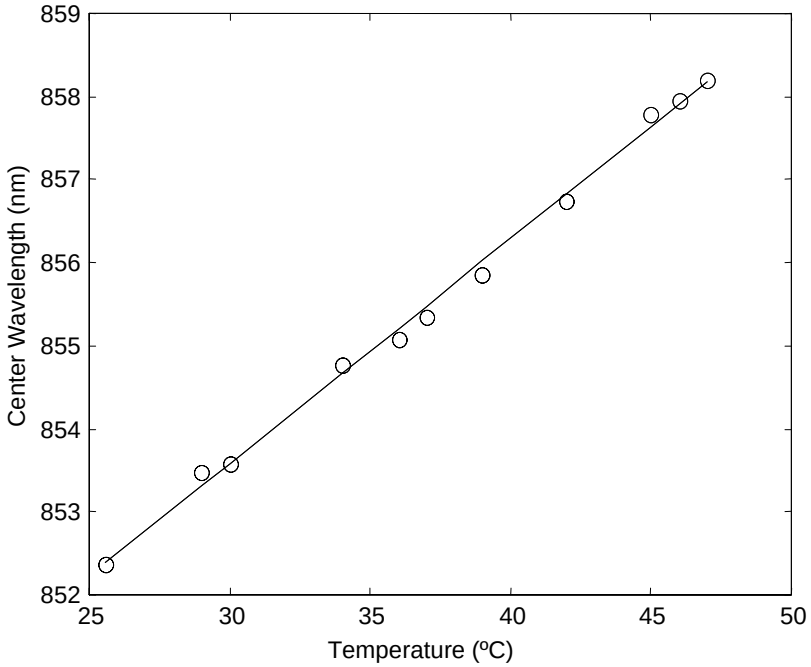

Figure 5.45. Relationship between center wavelength of the LED and temperature.

Spectrometer

Although the spectrometer was set up on a temperature-regulated bench, the residual temperature dependence is still critical for high-resolution measurement. Suppose the wavelength drift of spectrometer is δ_s. Obviously, the peak positions in the interference spectrum will also shift this amount. On the other hand, similar to the LED, the wavelength shift will induce the deformation of normalized spectrum. So the total air gap error induced by the spectrometer is

$$\Delta G_s = (\frac{G}{\lambda} + \frac{(1+\gamma)\lambda^3}{8\pi^2 \gamma G w^2}) \cdot \delta_s = b \cdot (\frac{G}{\lambda} + \frac{(1+\gamma)\lambda^3}{8\pi^2 \gamma G w^2}) \cdot \Delta T \ . \qquad \textbf{(5-70)}$$

The gross temperature dependence of the white light system can be expressed as

$$\begin{aligned} \Delta G &= \Delta G_L + \Delta G_s \\ &= \frac{(1+\gamma)\lambda^3}{8\pi^2 \gamma G w^2} \delta_L + (\frac{G}{\lambda} + \frac{(1+\gamma)\lambda^3}{8\pi^2 \gamma G w^2}) \cdot \delta_s \qquad . \qquad \textbf{(5-71)} \\ &= [a \cdot \frac{(1+\gamma)\lambda^3}{8\pi^2 \gamma G w^2} + b \cdot (\frac{G}{\lambda} + \frac{(1+\gamma)\lambda^3}{8\pi^2 \gamma G w^2})] \cdot \Delta T \end{aligned}$$

From the last equation, the temperature coefficient of the white light system is a function of the air gap G. That means for FABRY-PEROT sensors with a different air gap, or for the same sensor under different pressure (or temperature), the temperature coefficient of the white light system will be different. To realize temperature compensation, the air gap dependent temperature coefficient $K(G)$ must be determined experimentally. As long as $K(G)$ is determined, the compensation steps are as follows.

1. The rough air gap G' (without temperature compensation) is acquired.
2. Use G' to determine $K(G)$: $K(G) \approx K(G')$.
3. Use $K(G)$ and the temperature acquired by a thermocouple to calculate the accurate air gap G: $G = G' + K(G')\,\Delta T$

5.3 Comparison Between the SCIIB System and the White Light System

Both the SCIIB system and the white light system have their advantages and disadvantages. Compared to the white light system, the major advantage of the SCIIB system is the high speed. In the case where very high frequency response is not an important issue, such as pressure, temperature and flow measurement, the white light system has superiority over the SCIIB system. The main advantages of the white light system over the SCIIB system are discussed in this section.

5.3.1 Dynamic range

The most important advantage of the white light system is the large dynamic range. Different from the SCIIB system, the operating range of the white light system is not limited to a half wavelength. In fact, the dynamic range of the white light system is only limited by the

coherence length and the structure of the sensor head. By choosing a large gauge length or suitable material, the sensitivity of the sensor head can be increased dramatically.

In the multimode white light system, the lower limit of the air gap is decided by the spectral width of the light source. From the data processing method discussed above, at least two peak points are needed to demodulate the air gap from the interference spectrum. For the 850nm LED used in the multimode white light system, the effective spectral range (the range in which a high signal noise ration can be realized) is about 80nm, so the minimum air gap of the FABRY-PEROT sensor is about

$$G_{\min} = \frac{\lambda_1 \lambda_2}{2\Delta\lambda} \approx 4.5\mu m . \qquad \textbf{(5-72)}$$

In actual application, the lower limit of the air gap was set to 5μm.

The upper limit of the air gap is decided by the coherence length of the white light system. To achieve high-resolution measurement, high visibility of the interference spectrum is needed. Because the spectrometer has a high wavelength resolution (<1nm), the coherence length determined by this factor is pretty large:

$$L_c \approx \frac{\lambda^2}{\Delta\lambda} \approx 700\mu m . \qquad \textbf{(5-73)}$$

So, in the working range (usually smaller than 20μm), this factor can be neglected. A more important factor is the large numerical aperture (NA) of the multimode fiber. There are numerous modes propagating in a multimode fiber, and different fiber modes take different light paths. Obviously, the shortest path in a Fabry-Perot sensor is $P_{min}=2G$ and the longest one is about $P_{max}=2G/\cos\theta$ ($\theta=\sin^{-1}(NA)$). Roughly, when the path difference is larger than λ/2, the visibility was considered as too low to achieve high-resolution measurement. The NA of multimode fiber used in this system is about 0.15, so the upper limit of the air gap is

$$\begin{aligned} \frac{2G_{\max}}{\cos\theta} - 2G_{\max} &= \frac{\lambda}{2} \\ G_{\max} &= \frac{\lambda}{4}\frac{\cos\theta}{1-\cos\theta} \approx 19.2\mu m \end{aligned} . \qquad \textbf{(5-74)}$$

By choosing a suitable initial air gap and suitable materials for the sensor head, the dynamic range of the FABRY-PEROT sensor can be limited to 5—18 μm. Comparing with the 200nm dynamic range of the SCIIB system, it has increased more than 50 times. That's the main advantage of the white light system over the SCIIB system.

5.3.2 Insensitivity to the change of the polarization status

As discussed in Section 5.1, some optical components in the SCIIB system are polarization dependent. Even though a fiber optic depolarizer is connected in this system, the error induced by the change of the polarization status is still as high as 0.5% when the fiber is bent and flipped. In the white light system, the grating of the spectrometer is also a strong polarizer; it polarizes light along the vertical axis of the spectrometer. Yet, all the CCD pixels

receive the diffractive light from the same grating, so the polarization dependence of all pixels will be same. When the polarization status changes, the outputs from 2048 pixels will change by the same scale, so the shape of the interference spectrum will not change. The white light system is therefore insensitive to the change of polarization status.

5.3.3 Demands on the Geometrical Parameters of the FABRY-PEROT Sensor

The white light system demodulates the air gap from the interference spectrum directly. Many physical parameters, such as pressure, temperature, etc, have a linear relationship with the air gap change, which means the white system will have a linear output in the whole dynamic range. The sensitivity is decided by the materials for the sensor head and the gauge length of the FABRY-PEROT sensor. It's not necessary to set the initial gap at a very accurate value. Yet, in the SCIIB system, to fully use the limited linear range, the initial air-gap must be set at an accurate value. This makes the sensor fabrication for the SCIIB system much more difficult than that for the white light system.

Both the SCIIB system and the white light system have their special advantages. In general, for high-resolution applications, the white light system is the best candidate; when the measurement speed becomes an important issue, the SCIIB system is a good choice. In this project, for pressure, temperature and flow measurement, the white light system was employed.

6.0 Automated Sensor Fabrication System

Prior to this program, the method used in fabricating extrinsic Fabry-Perot interferometer (FABRY-PEROT) sensors was limited to epoxy bonding of two fibers (with their endfaces cleaved) inserted into a capillary tube with the proper inner diameter. Although extensive research has been conducted to find high performance epoxies to fabricate FABRY-PEROT sensor probes, the fabricated sensors generally failed to provide satisfactory performance in terms of mechanical strength and thermal stability due to the viscoelastic nature of all epoxies and due to the low decomposition temperatures. Another constraint of the epoxy-based sensors is that the maximum operating temperature is limited to temperature below about 300°C due to decomposition and for for sensors which undergo a mechanical load, even room temperature is to high to avoid the viscoelastic creep . Because epoxies have a relatively high coefficient of thermal expansion (CTE) which is significantly different from that of the fibers and the tube, epoxy bonded sensors are usually very sensitive to temperature changes, which makes it difficult to use those sensors to measure parameters other than temperature. Upon heating, large thermal stresses are generated in the bonding region due to the CTE mismatch. Control of the sensor initial cavity length (a critical factor in the sensor manufacturing) and the bonding area are very difficult with epoxy bonding because the relatively long curing time of the epoxy. Furthermore, due to the viscoelastic nature of the polymer, epoxy bonding will also degrade the frequency response of the FABRY-PEROT sensor in case of high frequency signals need to be measured.

Telecommunication optical fibers are usually made by doping very small amounts of germania into pure silica glass. Fused silica capillary tubes of various sizes are commercially available. In contrast to the well-defined melting points of crystalline materials, silica glass is an amorphous material. As the fused silica glass is heated, the viscosity continuously drops to the point at which the article is no longer able to support it's own weight. For the fused silica capillary tubes used in sensor fabrication, at a temperature of about 1500°C, it becomes soft enough that it begins to deform around the optical fiber when heated rapidly with a CO_2 laser. This softening of the fused silica capillary tube allows the use of thermal fusion techniques to bond the fiber and the capillary tube together. By locally heating the fiber and tube assembly to a temperature above which the glass is softened sufficiently, the tube and the fiber can flow into each other and locally join to form a solid bond.

A major research task of the program was to develop an automated sensor fabrication system. The sensor fabrication system uses a high-energy carbon dioxide (CO_2) laser to provide the heating power and a white light spectrum interferometer measurement system to monitor the cavity length of the sensor in real-time during fabrication. This system allows the automatic fabrication of a large quantity of high performance sensors at a low cost.

6.1 System Configuration

As shown in Figure 6.1, the automated SCIIB sensor fabrication system includes three sub-systems: the carbon dioxide (CO_2) laser heating sub-system, the white light fiber optic interferometric air gap monitoring sub-system, and the micropositioning sub-system. A high-energy CO_2 laser is used as the heating source. It generates high-energy optical pulses at a wavelength of 10.6μm. When the silica glass material is exposed to the CO_2 laser output, it absorbs the optical energy and converts it to thermal energy, which allows the silica glass materials to be heated locally up to very high temperatures. The white light fiber optic interferometric system is used to allow accurate on-line monitoring of the SCIIB sensor air gap. Several ultra-precise micropositioning stages are also used in the system to allow precise movement of the two fibers in three dimensions. A computer is used to control and coordinate these three sub-systems so that the CO_2 laser output power, the motion of the stages and the sensor air gaps can be automatically and precisely controlled during the sensor fabrication process. Figure 6.2 shows the picture of the automated SCIIB sensor fabrication system.

6.2 CO_2 Laser Sub-System

The CO_2 laser used in the system is a SYNRAD, Inc Model 48-2. The wavelength emitted by the laser is 10.6 μm, and the maximum output optical power under continuous mode operation is 25 W. The original beam diameter of the laser output is 3.5 mm. After using a germanium lens with a focal length of 2.5 inches, a spot size of about 100 μm in diameter can

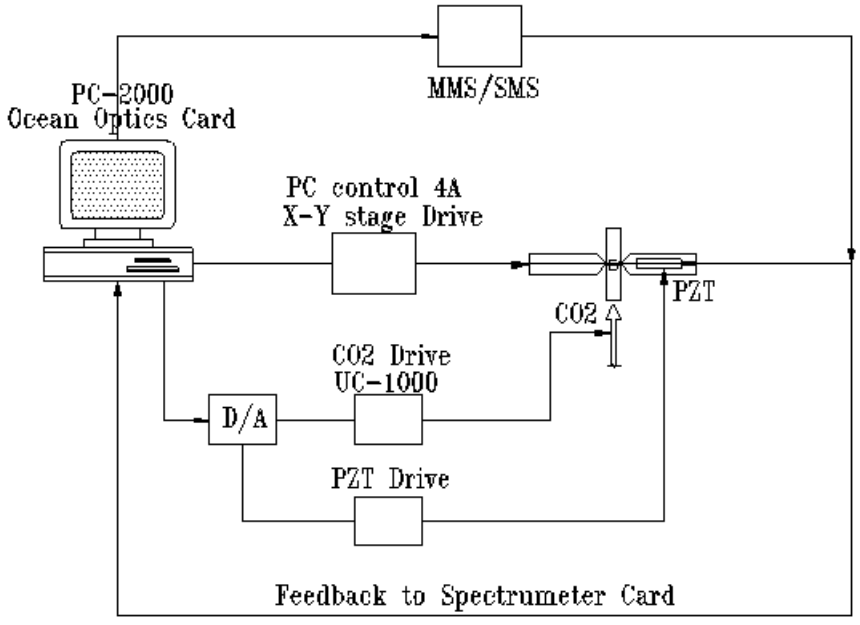

Figure 6.1. Schematic of the automated sensor fabrication system.

Figure 6.2. Automated SCIIB sensor fabrication system.

be achieved at the focal point, which results in a divergence angle of about 4 milliradians. The laser can also be used to generate short optical pulses that are externally modulated through a controller, producing a minimum pulse duration of about 200 μs.

6.3 CO_2 Laser Sub-System

The CO_2 laser used in the system is a SYNRAD, Inc Model 48-2. The wavelength emitted by the laser is 10.6 μm, and the maximum output optical power under continuous mode operation is 25 W. The original beam diameter of the laser output is 3.5 mm. After using a germanium lens with a focal length of 2.5 inches, a spot size of about 100 μm in diameter can be achieved at the focal point, which results in a divergence angle of about 4 milliradians. The laser can also be used to generate short optical pulses that are externally modulated through a controller, producing a minimum pulse duration of about 200 μs.

The control of the CO_2 laser output involves two parts: the power level control and the lasing duration control. The power level control can be accessed by externally applying a 0-10 V voltage signal (corresponding to 0-25 W output power) and the pulse duration can be controlled by inputting a standard TTL gating signal to enable or disable the laser output. Because it is necessary to precisely control the heating time and the temperature during the sensor fabrication, we designed and implemented a special circuit to allow computer programmable control of the CO_2 laser. The block diagram of the CO_2 laser control subsystem is given in Figure 6.3. By properly programming the DIO-24 interface card (National Instruments), the power control signal is sent out to the D/A circuit, which converts the digital signal to an analog output from 0 to 10 volts at a resolution of 16 bits. The laser enabling or disabling signal is also converted to a TTL gating signal through the same circuit.

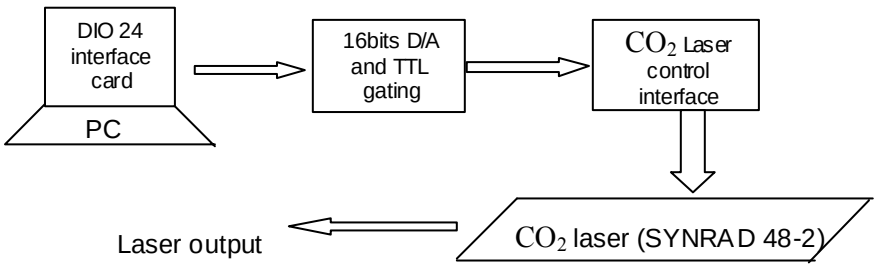

Figure 6.3. Block diagram of the CO_2 laser control subsystem.

6.3.1 Mechanical strength improvements

To improve the mechanical strength of the sensor probe, a mirror subassembly was designed and incorporated into the system. In the initial design, the output beam from the CO_2 laser heated the capillary tube and fiber assembly from one direction, which resulted in nonuniform temperature increases in the fused silica capillary tube. Many sensors fabricated were found either not completely sealed or with too many residual stresses after fabrication. Improvement in the mechanical strength of the sensor probe was achieved by adding a set of copper mirrors to the fabrication stage, as shown schematically in Figure 6.4. Two mirrors (made by polishing precisely fabricated copper plates) were placed underneath the sensor assembly. The angle between the two copper mirrors was set to be 120°. The CO_2 laser beam was also aligned to input to the assembly at an angle of 60°. Therefore, the input beam and the two reflected beams from the mirrors heat the sensor assembly at the three evenly distributed directions. Experiments were also conducted to find the optimal CO_2 laser power and the duration. With the mirror set described above, the sensor assembly can be bonded uniformly to minimize the residual stresses.

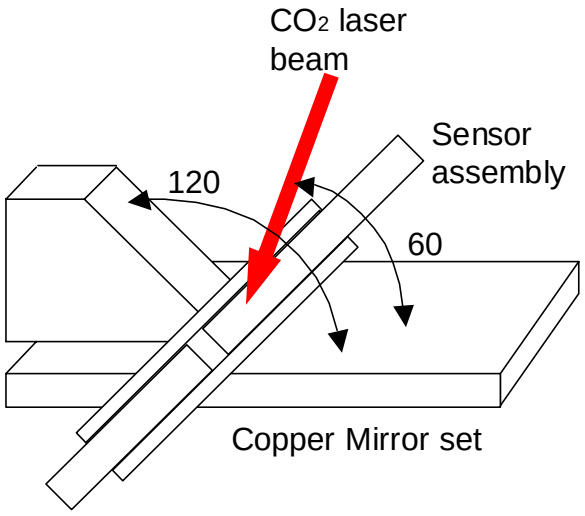

Figure 6.4. Schematic of the copper mirror set in sensor fabrication system.

6.4 White Light Fiber Optic Interferometer Sub-System

This sub-system is the main part of the automatic sensor fabrication system. It allows on-line monitoring of the length of the SCIIB sensor air gap with a very high accuracy. The measurement of air gap length is achieved by demodulating the interference spectrum of the sensor output as described in the section below. The spectrum is obtained through a computer-interfaced spectrometer. In order to retain the design flexibility to be able to fabricate both multimode and singlemode SCIIB sensors, two white light interferometric air gap monitoring systems were constructed. The two systems share the same spectrometer but use different sources and fibers.

6.4.1 Principle of white light interferometric air gap monitoring

The basic principle of the white light interferometric air gap monitoring can be illustrated using Figure 6.5. When the sensor is fabricated, two fibers with cleaved endfaces are inserted into a capillary tube. The partially reflected optical waves at these two endfaces will generate an interference signal that is transmitted back to the spectrometer through a 2x2 fiber coupler.

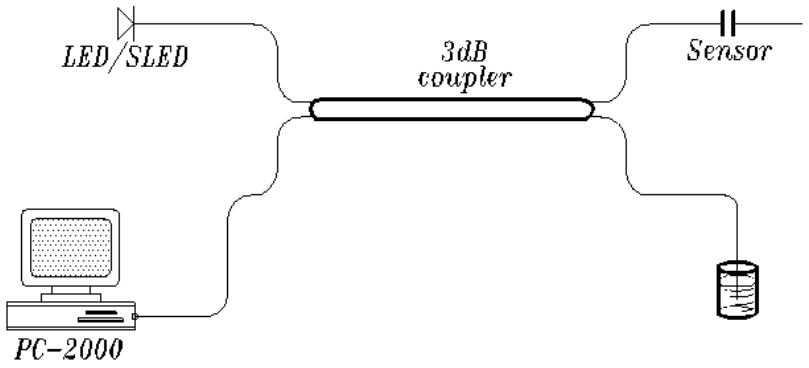

Figure 6.5. Basic principle of the white light interferometric air gap monitoring system.

If we assume that the white light source (LED or SLED) has a Gaussian spectral power distribution given by

$$I_s(\lambda) = I_0 \exp\left[\frac{-(\lambda-\lambda_0)^2}{(\Delta\lambda)^2}\right], \qquad \textbf{(6-1)}$$

where λ_0 is the central wavelength, I_0 is the peak value, and $\Delta\lambda$ is the source spectral width. The output interference signal is then given by

$$I_s(\lambda) = I_0 \exp\left[\frac{-(\lambda-\lambda_0)^2}{(\Delta\lambda)^2}\right], \qquad \textbf{(6-2)}$$

where the factor γ takes into account the decreased visibility due to the numerical aperture of the fiber as well as other attenuating effects, and where φ_0 is the arbitrary initial phase difference between the two interference signals. If we normalize the interference spectrum given by Eq. (6-2) with respect to the source spectrum, we have the normalized interference output expressed as

$$I_n = 2\left[1+\gamma(L)\cos\left(\frac{4\pi L}{\lambda}+\varphi_0\right)\right], \qquad \textbf{(6-3)}$$

It is shown in Eq. (6-3) that the spectrum output by the sensor is modulated by a sinusoidal function due to the interference. Because the interference spectrum is a function of the sensor air gap length L, the successful demodulation of this spectral signal can render an accurate and absolute measurement of the sensor air gap length.

A simple case can be considered in which two different spectral components of the source (λ_1 and λ_2) are utilized. These two wavelength components arrive at the spectrometer with different phases, which can be expressed as

$$\varphi_{1,2} = \frac{4\pi L}{\lambda_{1,2}} + \varphi_0 . \qquad \textbf{(6-4)}$$

Thus the phase difference between these two spectral components is given by

$$\Delta\varphi = \varphi_1 - \varphi_2 = \frac{4\pi L(\lambda_2 - \lambda_1)}{\lambda_1 \cdot \lambda_2} . \qquad \textbf{(6-5)}$$

Rewriting Eq. (6-5), we have

$$L = \frac{\Delta\varphi \cdot \lambda_1 \cdot \lambda_2}{4\pi(\lambda_2 - \lambda_1)} . \qquad \textbf{(6-6)}$$

If the phase difference of these two spectral components are known, the absolute value of the sensor air gap length L can be calculated by Eq. (6-6). Although it is not easy to measure the phase difference of two spectral components, there exist a few special points with a fixed phase relationship. For example, the phase difference between two adjacent peaks (or valleys) is 2π. Therefore, by detecting the spectral locations of the peaks or valleys in the interference spectrum, we can obtain the cavity length L by applying Eq. (6-6).

6.4.2 Implementation of multimode and singlemode white light subsystems

The spectrometer used in the white light subsystem is a fiber optic PC plug-in spectrometer (PC2000 manufactured by Ocean Optics, Inc.). The PC-2000 spectrometer card uses a 600-line holographic grating to diffract the input light to a CCD array, and interfaces with the computer using a 12 bit A/D through the ISA bus. The blaze wavelength is 850 nm, and the best efficiency is from 750 nm to 950 nm, which covers the whole light source spectrum of interest. The resolution of this spectrometer is approximately 0.3 nm, and the highest data acquisition speed is 1000 kHz.

6.4.2.1 Multimode white light air gap monitoring system

The configuration of the multimode white light air gap monitoring system is shown in Figure 6.6. It uses an LED with center wavelength of 850 nm and spectral width of 74 nm as the source. The fiber used is a standard multimode graded index 62.5/125μm telecom fiber. A picture of the system is shown in Figure 6.7.

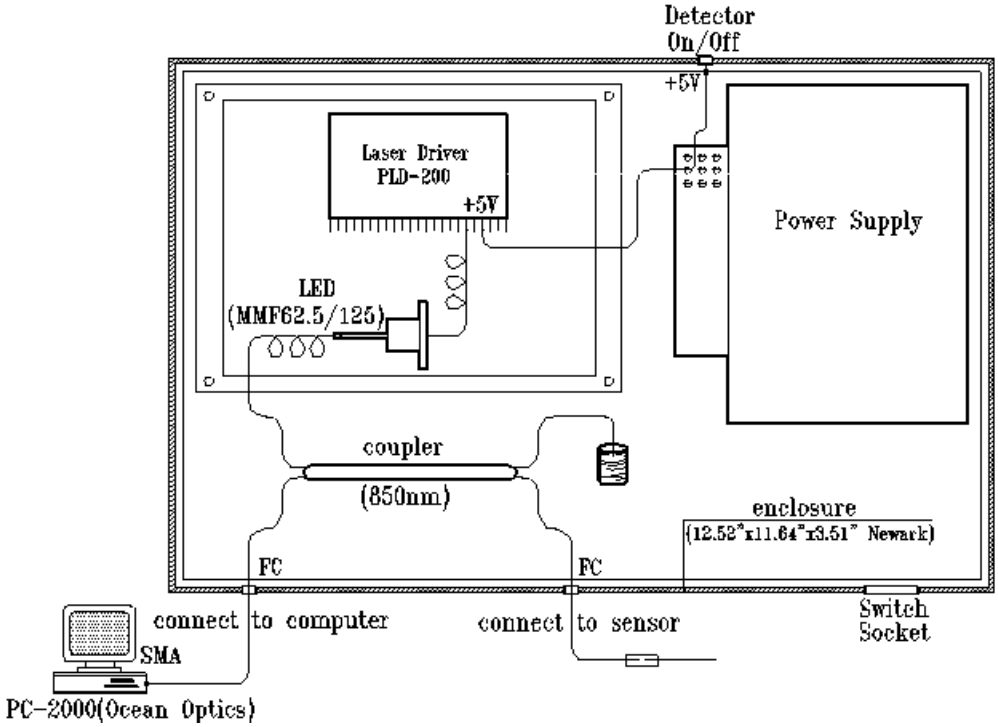

Figure 6.6. Configuration of the multimode white light air gap monitoring system.

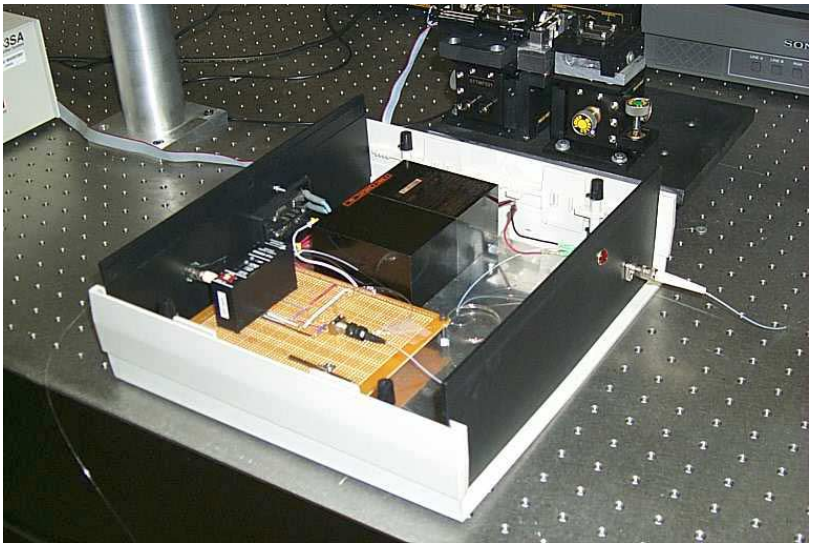

Figure 6.7. Picture of the multimode white light air gap monitoring system.

6.4.2.2 Singlemode white light air gap monitoring system

The configuration of the singlemode white light air gap monitoring system is shown in Figure 6.8. It uses a SLED with center wavelength of 1310 nm and a spectral width of 40 nm as the source. The fiber used inside the system is a standard 9/125 μm singlemode telecom fiber. A picture of the system is shown in Figure 6.9.

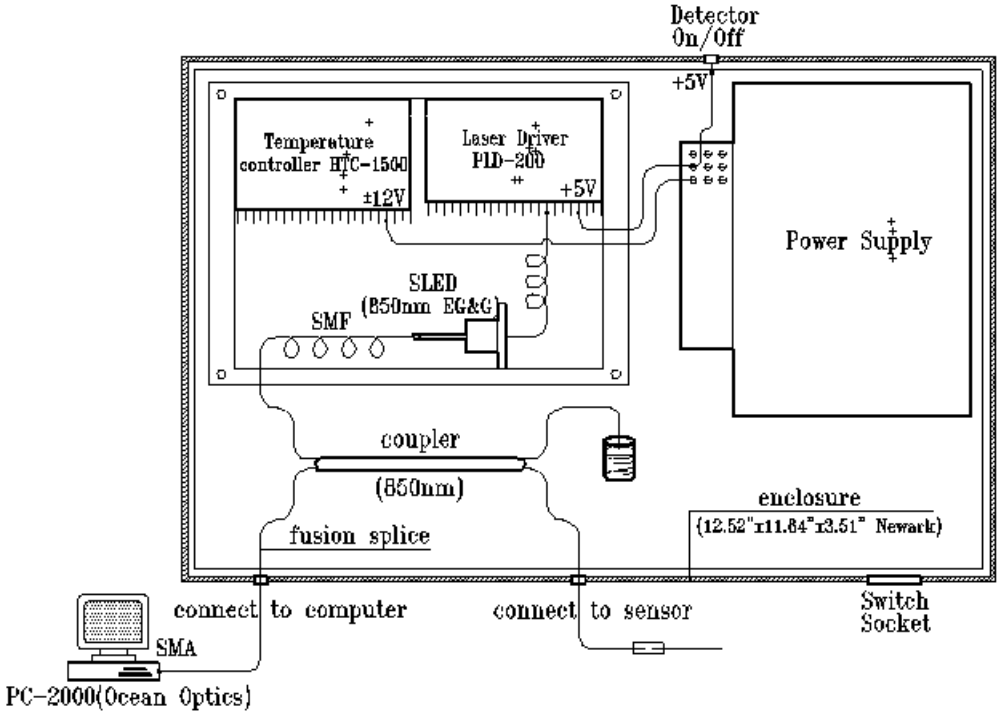

Figure 6.8. Configuration of the singlemode white light air gap monitoring system.

Figure 6.9. Picture of the singlemode white light air gap monitoring system.

6.4.3 Software design of white light sub-system

The software discussed in Section 5.2 was initially developed to monitor the air gap length during sensor fabrication. A block diagram of the monitoring software is shown in Figure 6.10. The graphical interfaces of the designed software are shown in Figure 6.11. The major functions of this software are described in this section.

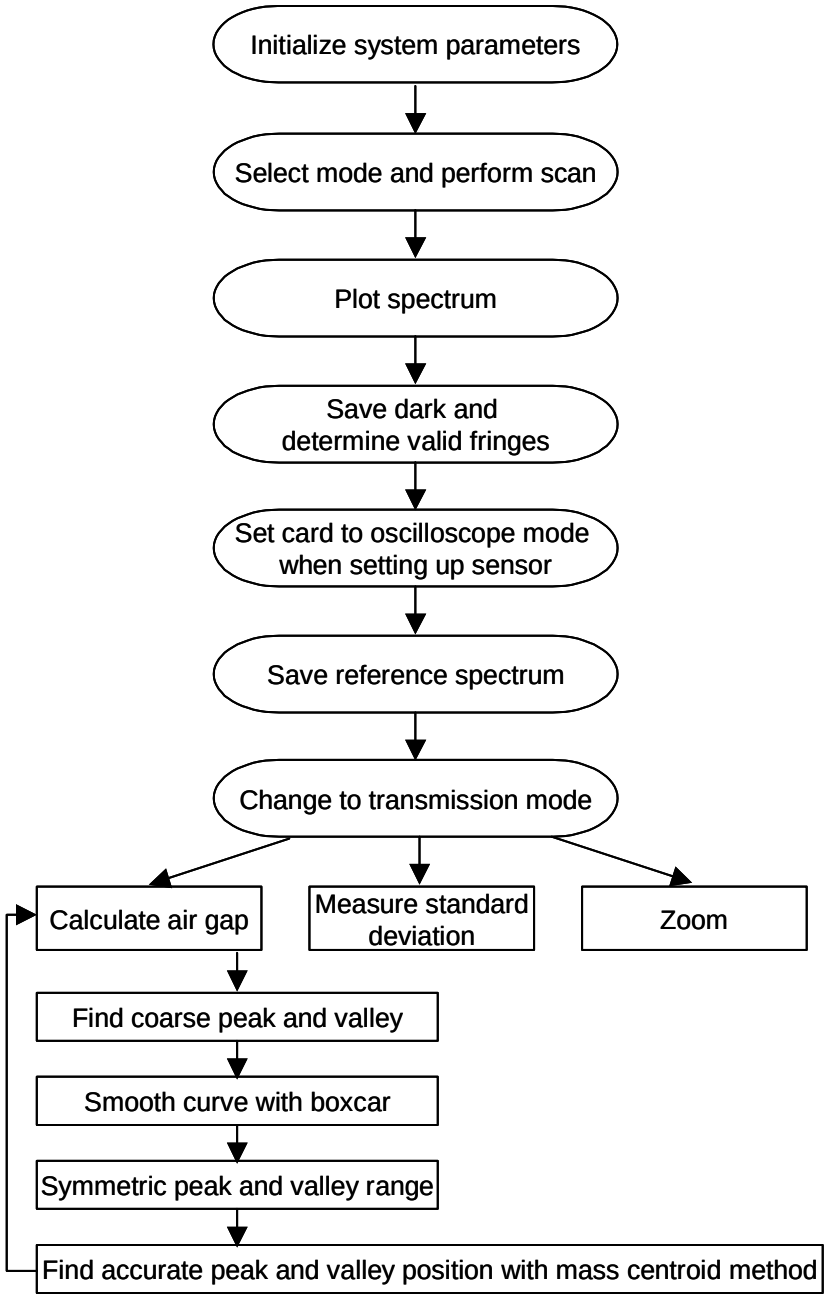

Figure 6.10. Block diagram of air gap monitoring software.

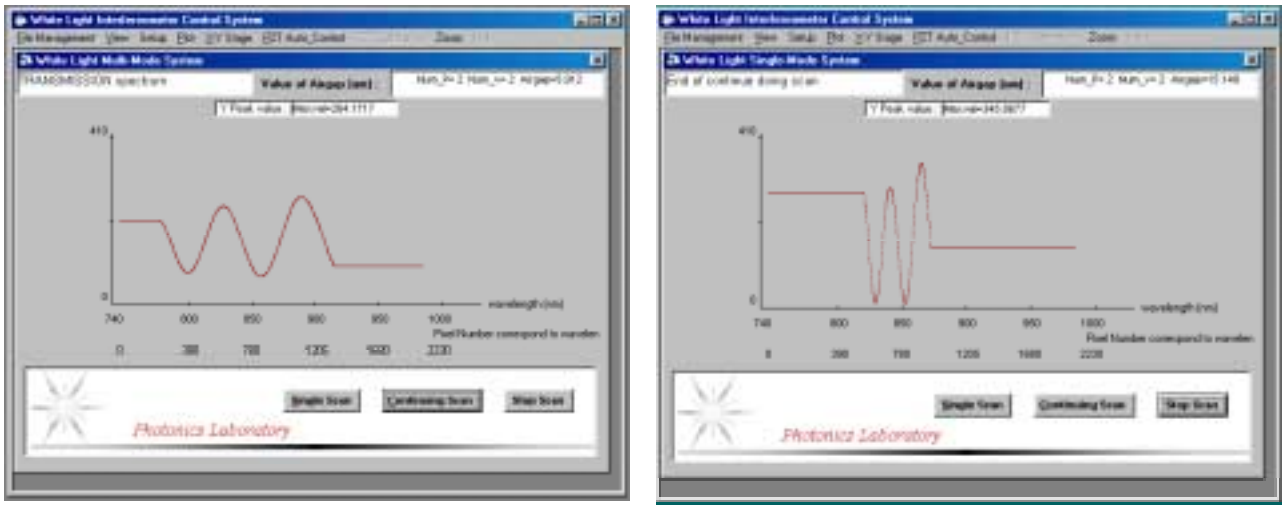

(a) Multimode **(b) Singlemode**

Figure 6.11. White light air gap monitoring software under operation.

6.4.3.1 Initialization

The program begins with the system parameter initialization, including initialization of the spectrometer, initialization of the system configuration, and initialization of the system constants necessary for the air gap calculation. The program automatically saves all the parameters of the last experiment. However, each individual parameter can also be changed manually during the operation.

6.4.3.2 Pre-processing

The main purpose of this part is to improve the signal-to-noise ratio (SNR) of the system and improve the air gap length measuring accuracy.

1) The dark spectrum is saved to allow only pure spectral data to be processed after the subtraction algorithm.
2) The original spectrum of the light source is saved as the reference so that the interference spectrum can be normalized to eliminate the distortions induced by the source spectrum.
3) A boxcar algorithm is developed to filter and smooth the raw data so that the noise of the spectrometer is minimized.
4) The interference spectrum is automatically truncated according to its signal level. This ensures that only the high SNR region of the spectrum is included in calculations of the air gap length.

6.4.3.3 Demodulation

This part includes the most important functions of the software.

1) The saved dark spectrum is subtracted from the input spectrum, and the saved reference spectrum is used to normalize the interference spectrum so that the source spectrum effects are eliminated.

2) Coarse locations of the peaks and valleys are found by a smart comparison algorithm. These coarse locations are used as reference marks in the demodulation.
3) An FFT algorithm is used to automatically estimate the window size of the interference spectrum. This allows an optimal number of data points to be used in the signal demodulation.
4) A mass-centroid algorithm is applied to find the interference peaks (or valleys) and the corresponding wavelengths.
5) The final air gap length is calculated according to Eq. (6-6).

6.5 Micropositioning Subsystem

During the sensor fabrication, the fibers and capillary tube must be kept precisely aligned, the sensor air gap must be accurately adjusted to the preset value, and the bonding distance, which determines the sensor effective gauge length, also needs to be precisely controlled. Therefore it was necessary to design a fiber positioning system for the sensor fabrication to accurately position the fibers and tubes. The computer controlled micromotion fiber and tube positioning system is illustrated in Figure 6.12. The two fibers are positioned on two V-grooves using magnets, and the V-grooves are fixed to a 3-dimentional translation stage, respectively. Between the two translation stages, a supporting block with another V-groove on top is used to position the capillary tube. All the V-grooves are specially designed and manufactured to hold the fibers or the capillary tube tightly. After installation, the three V-grooves are precisely aligned to fall in a straight line so that there is no offset angle during

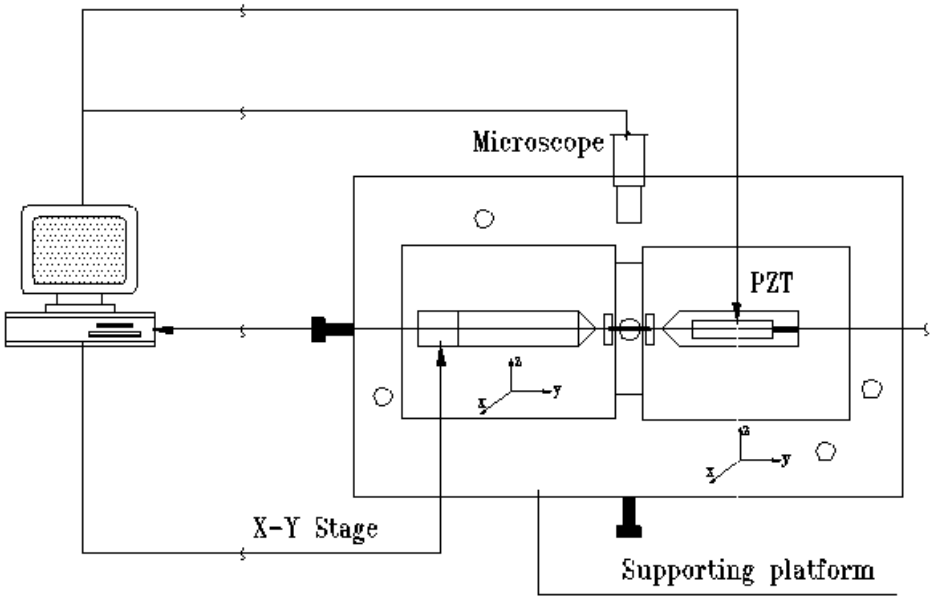

Figure 6.12. Computer controlled micro-motion fiber and tube positioning system.

sensor fabrication. Fibers can be inserted into the central capillary tube by moving the two translation stages in three dimensions. To allow precise adjustment of the sensor air gap length, another small PZT-actuated stage is used to move the target fiber with ultra-high resolution along z-direction. The movement of the stage is controlled by the central computer through a PZT driver and a 16 bit D/A circuit. In order to control the sensor gauge length, a big translation stage is used to move the whole setup in two directions with respect to the CO_2 laser beam. After the tube is bonded to the lead-in fiber, this stage can precisely position the second bonding point with respect to the CO_2 laser beam. A video microscope system is used to help the aligning procedure and to monitor the whole sensor fabrication process. A picture of the sensor fabrication stage system is shown in Figure 6.13.

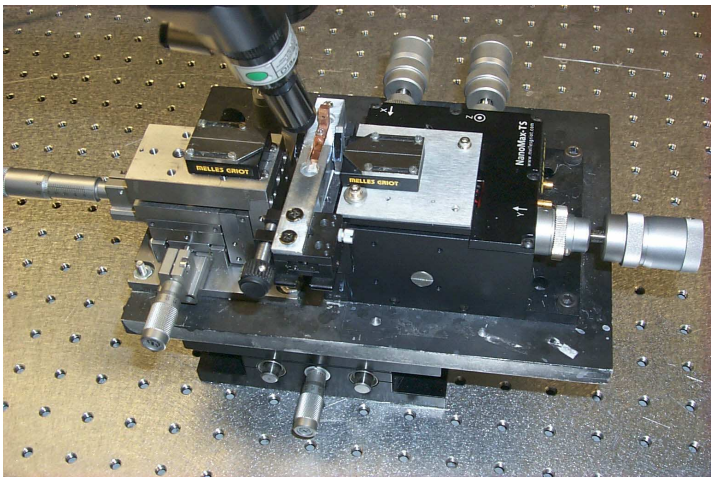

Figure 6.13. Micropositioning stage system.

6.6 System Testing Results

A number of tests and experiments were conducted using the implemented automatic sensor fabrication system. The main purpose of these tests is two-fold: 1) to verify the design and to check out the functions of each subsystem, 2) to fabricate SCIIB sensors for further evaluation.

6.6.1 White light subsystem performance test and results

The purpose of designing the white light subsystem is to realize on-line monitoring of the sensor air gap length during sensor fabrication. There are a few key performance characteristics that required testing before it could be used. These include the accuracy, dynamic range, and frequency response of the air gap measurement.

6.6.1.1 Standard deviation

The standard deviation of the white light subsystem air gap measurement was determined by using a fiber optic extrinsic Fabry-Perot interferometric (FABRY-PEROT) sensor with a fixed air gap. Using the white light system, we measured the FABRY-PEROT sensor air gap 100 times. Based on the measurement results, we can calculate the standard deviation of the white light system. Actually, this function is built in the software so that we can perform the

standard deviation measurement at anytime. The standard deviation of the multimode system was calculated to be σ=0.003μm. The standard deviation for the singlemode system was found to be σ=0.02μm.

6.6.1.2 Frequency response

Using the software, the sensor air gap length can be calculated in less than 0.1 second. The corresponding frequency response of the system is higher than 10 Hz. The average fabrication time of the SCIIB sensor is about 20 seconds, therefore the frequency response of the white light system is high enough for our applications.

6.6.1.3 Dynamic range

The multimode system can measure sensor air gap lengths from 4 μm to 20 μm, and the singlemode system can measure from 8 μm to 70 μm. The standard deviation of the sensor air gap measurement is constant over the whole dynamic range. The typical initial air gap is about 6 μm for multimode and 15 μm for singlemode; therefore, the dynamic ranges of the white light system for both systems are large enough.

6.6.2 CO_2 laser power calibration

The CO_2 laser is used as the heating source during the sensor fabrication. It is important to control the laser output power and exposure duration to ensure solid bonding between fibers and tube. Laser power that is too large and exposure time that is too long can result in degradation of the optical properties of the optical fiber and the too much built-in stress at the bonding region. On the other hand, laser power that is too weak or exposure time that is too short can result in incomplete bonding.

The CO_2 laser output is quite nonlinear when it is controlled through the external analog port. To achieve precise control of the output power, we conducted a calibration experiment for the CO_2 laser. The laser output power was measured using a power meter. The results are plotted in Figure 6.14. Based on the calibration data, the CO_2 laser power can be accurately mapped to the external control voltages. Thereafter, precise control of the laser output power can be realized through curve-fitting method.

6.6.3 PZT Stage calibration

The final fine adjustment of the sensor air gap is achieved by moving the PZT stage. The movement of the PZT stage is controlled by the computer programs through a 16 bit D/A circuit and a PZT driver. However, the relationship between the PZT displacement and the external control voltage is not linear. In order to adjust the air gap to a preset value at a ultra-high accuracy, the PZT stage movement was calibrated with respect to the input control voltages. The calibration was conducted by using the white light interferometer and an extrinsic Fabry-Perot interferometric (FABRY-PEROT) sensor. First we implemented a Fabry-Perot micro-displacement sensor with one fiber sealed to the tube, and the other fiber fixed to the PZT stage. When the PZT stage moves, it generates an interferometric displacement signal through the FABRY-PEROT sensor. At the same time, this interferometric signal was measured by the white light interferometric air gap monitoring system. Relating the PZT control voltage to the white light interferometer output, the PZT stage can be precisely calibrated. Figure 6.15 shows the PZT calibration results. By using curve-fitting method, we can control the PZT stage movement with a very high accuracy by referring to the stored calibration data.

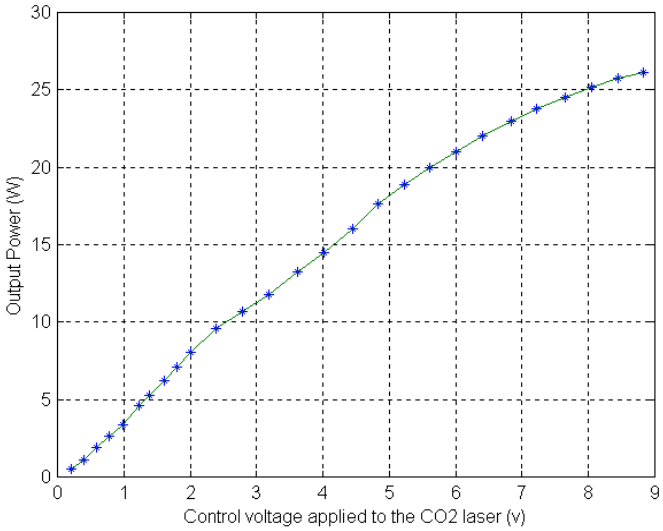

Figure 6.14. CO_2 laser output power calibration results.

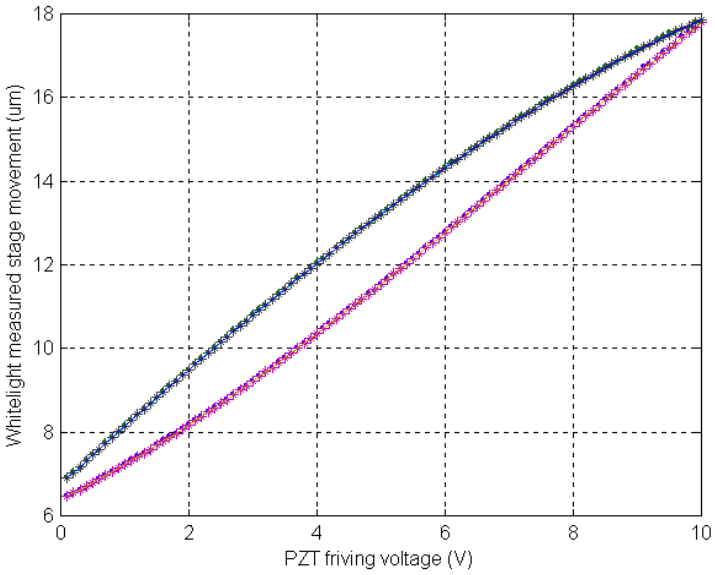

Figure 6.15. PZT stage movement calibration results.

6.7 Fabrication Procedure Optimization

6.7.1 CO_2 laser power and exposure time optimization

Thermal bonding is the most important step in SCIIB sensor fabrication. When the tube and fiber assembly are exposed to CO_2 laser light, the optical energy is converted to thermal energy which results in an increase in temperature at the exposure area. If the temperature reaches the softening point of the glass material (about 1500°C), the tube and the fiber start to flow and join together. After the cooling, a solid bond is formed at the CO_2 laser exposure area. In order to achieve the best optical and mechanical performance of the fabricated sensor, the CO_2 laser exposure time and the power level must be set to their optimal values. There are a few points that must be considered in choosing the exposure time and the power level. First, to avoid excess residual stress from building in the bonding area, the increase and the decrease of the temperature should not be too fast. This results in an optimal design of the temperature increasing and the decreasing slope. Second, the glass materials should not be overheated; otherwise the gravity will bend the fiber, which results in a large optical power loss at the bonding region. Therefore, the laser power needs to be set to an optimal level. Third, there is an optimal time duration in which the glass materials are soft and fluid. A review of fiber optic fusion splicer design reported in the technical literature suggests that the duration at which the glass is softened should be limited to a few seconds. Based these considerations, we designed our CO_2 laser power and exposure time curve as shown in Figure 6.16. This design allows 2 seconds of preheating time, 3 seconds of heating time and 10 seconds of annealing time. The total fabrication time is about 15 seconds.

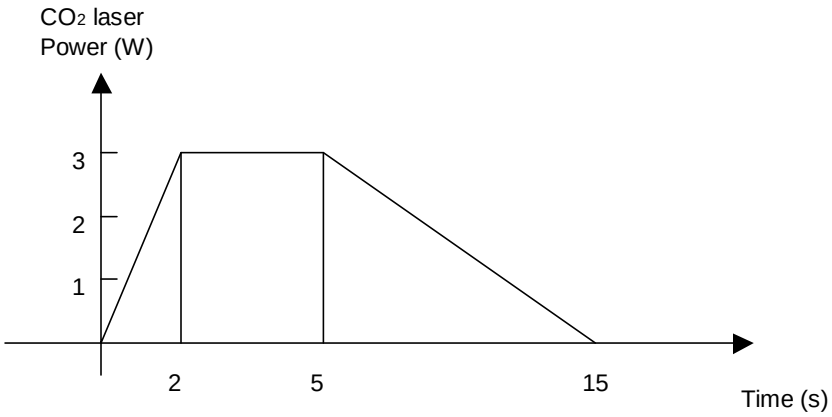

Figure 6.16. CO_2 laser power level and exposure time.

6.7.2 SCIIB sensor fabrication and results

After numerous experiments, we finalized all the parameters involved in SCIIB sensor fabrication. The final setup allows the tube and fiber assembly to be positioned 7.5 cm away from the CO_2 laser focal point. For multimode SCIIB sensors, the full laser power is 2.9 W, and for singlemode sensors the full laser power is 3.1 W. The sensor bonding region has a

typical size of 300 μm. The sensor gauge length can be chosen from 0.8 mm to 5 mm. The initial gap can be adjusted to any value with an accuracy of 0.02 μm. The bonding points have been tested to show good strength, and the sensor fabrication has a very good repeatability.

6.7.3 Repeatability improvements

To improve the repeatability of sensor fabrication, several measures were taken, including improvement of the measurement accuracy of the whitelight interferometric cavity length monitoring system, addition of a PZT stage system to tune the initial cavity length precisely, and a computer program to control the adjustment of the initial cavity length after sensor is bonded.

Initial tests demonstrated an accuracy of 0.02μm for singlemode whitelight system and 0.002 μm for the multimode whitelight system. This is however not high enough to meet the sensor fabrication requirements. The mass centroid algorithm described in Section 5.2 was implemented to realize a large improvement in peak locating. Also, the peak or valley tracking algorithms were added to the system which dramatically improved the wavelength resolution of the system. The current accuracy of the whitelight system has been tested to be 0.001μm for singlemode fiber sensors and 0.0005 μm for multimode fiber sensors. This is more than one order of magnitude improvement.

In addition to the improvement of the accuracy of the whitelight system, a high resolution PZT stage was also incorporated to the sensor fabrication system. With the completion of the driving circuits, and the computer control algorithms, the PZT stage allowed us to tune the sensor cavity length after the capillary tube and fiber was bonded together. By reheating the assembly with 80% of the CO_2 laser power required for bonding, and by controlling the PZT stage to pull the fiber with a resolution of 2nm, SCIIB sensors can now be fabricated repeatedly with the initial cavity lengths adjusted exactly to the starting point of the linear region.

6.8 Performance of Fabricated Sensors

Hundreds of SCIIB sensor probes have been made using the developed fabrication system. Fibers used to fabricate the sensor probe are carefully cleaned and cleaved using a York fiber cleaver. The capillary tube is also cleaned and cleaved to the desired length. With the help of the microscope, two fiber ends prepared by the cleaver are then inserted into the capillary tube and held on the positioning stages. By adjusting the micropositioning stage system, the two fibers are moved to the preset positions where the desired initial sensor cavity length is obtained. By moving the two-dimensional translation stage underneath the micropositioning stage system, the fiber and capillary tube assembly is brought to the center of the laser spot. The CO_2 laser emits light to heat the assembly with its power level and duration controlled by the computer program. After one side of the sensor is fused, the fiber and capillary assembly is then move to the other side to perform the same fusion process.

Figure 6.17 shows a photograph of a typical sensor probe imaged by the microscope. In the picture, we can clearly see the sensor cavity formed by the fiber endfaces and the two fusion points. So far, the shortest sensor gauge length that can be fabricated with the system is 0.5mm for the single-mode fiber-based sensor and 0.7mm for the multimode fiber-based sensor, respectively. It is very difficult to further reduce the sensor gauge length because the fiber endfaces can be damaged resulting from the too close fusion point.

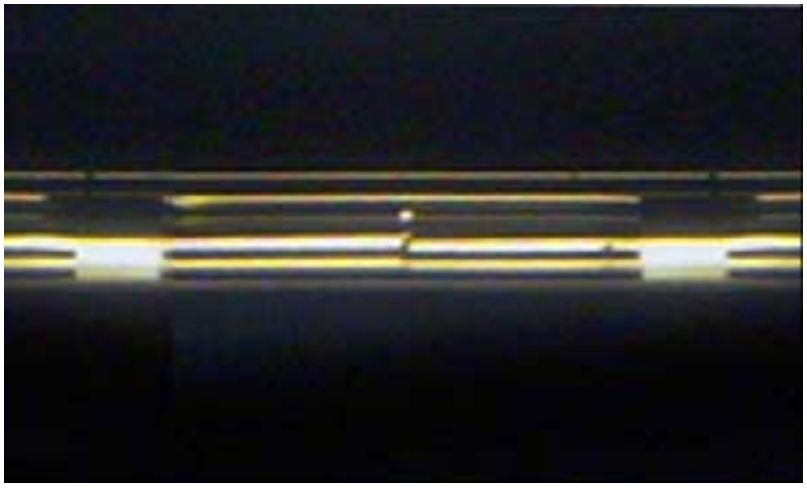

Figure 6.17. Micrograph of the SCIIB sensor probe (Gauge length: 1.5mm, initial cavity length: 25.74μm).

The sensor probes were expected to have high mechanical strength and sustain high pressures. This section describes experiments conducted to evaluate the sensor's survivability and temperature dependence.

6.8.1 Survivability of the sensor probe

Before the sensors can be used in harsh environments, they must be tested to ensure a complete sealing at the two fusion points because an imperfect sealing would result in the intrusion of the outside medium and degradation of the sensor performance. More than one hundred sensors were first tested in a high pressure (>3000 psi) and high temperature (>200°C) water environment. Only two sensors were found to leak water into the cavities during the test. The majority of the sensors successfully survived the test. This made us believe that the controlled thermal bonding method could provide sensor probes strong enough to survive in harsh environments.

6.8.2 SCIIB sensor annealing

The capillary tube and glass fibers are fused together in a very short time period during the sensor fabrication process. It is a reasonable concern that residual stresses might build up in the bonding regions due to the very large temperature difference. These residual stresses, when released slowly, will cause a sensor to drift from its original calibrated operating point. Therefore, the sensor must be properly annealed to release the built-in stresses prior to sensor calibration.

Sensor annealing was performed using an electrical furnace at a temperature of 600°C for 24 hours. During the annealing process, the temperature was increased and decreased slowly to avoid further stress build up. In order to see how the annealing affects the sensor performance, five sensors were annealed twice under the same experimental conditions, and the cavity lengths of the five sensors were monitored using the whitelight interferometer during the entire annealing process. The recorded changes in cavity length are listed in Table 6.1.

Table 6.1. Sensor cavity length change before and after annealing.

Sensor index	Gauge Length (mm)	Cavity length before annealing (μm)	Cavity change first annealing (nm)	Cavity change second annealing (nm)
1	0.7	20.0872	-37.2	2.7
2	1.0	39.6614	-15.8	3.3
3	1.0	29.1794	-68.4	*
4	1.0	20.4749	-32.2	1.9
5	0.7	21.3901	-13.1	3.4

***The sensor was broken after the first annealing because of mishandling.**

As shown in the table, the changes in sensor cavity lengths after the second annealing became very small compared to the first one, which indicate that the annealing process did improve the stability of the sensor. Although the sensors used in the experiment were chosen with different parameters (gauge lengths and initial cavity lengths) in hope to demonstrate the regularity of the annealing effect on the sensors, the results shown in Table 6.1 did not indicate an obvious relationship between the sensor parameters and changes in cavity lengths except that all the sensors showed a decrease in their cavity lengths after the annealing process. Nevertheless, the experiment indicated that the annealing process did cause a large change in sensor cavity length with respect to the linear range of operation (about 200nm). Therefore, the sensor annealing was proven to be necessary to assure the performance of the sensor.

6.8.3 Temperature dependence of the SCIIB sensor probe

The theoretical analysis discussed above showed that the temperature sensitivity depends on the sensor gauge length, the initial cavity length, and the CTEs of the fiber and the capillary tube. It is possible to design the sensor according to the temperature model to have very small or even zero temperature sensitivity. The actual CTEs of the fiber and the tube can deviate from the nominal values due to the small difference in the chemical composition among the materials used by different manufacturers. It is very difficult to determine the actual temperature dependence of the sensor probe just by referencing the nominal CTEs due to the extremely high accuracy required. The actual temperature dependence of the sensor probe therefore has to be measured experimentally.

6.8.3.1 Multimode SCIIB sensor probe

The experimental set-up included an electric furnace with a maximum temperature of 1100°C and an Omega CN76000 thermometer to read the temperature with an accuracy of 0.1°C. The multimode sensor probe and the thermocouple were put side by side in the furnace, and the temperature was increased from room temperature (30°C) to 810°C in steps of 10°C. Both the SCIIB sensor output and the thermometer output were recorded for comparison. The capillary tube used to fabricate the multimode sensor was made of fused silica purchased from Polymicro Technologies, Inc. The inner diameter of the tube is 130 μm, and the outer diameter is 365 μm. The sensor had an effective gauge length of 0.7 mm, and the initial cavity length of 5.160 μm. The sensor output versus the increase of the temperature is plotted in Figure 6.18.

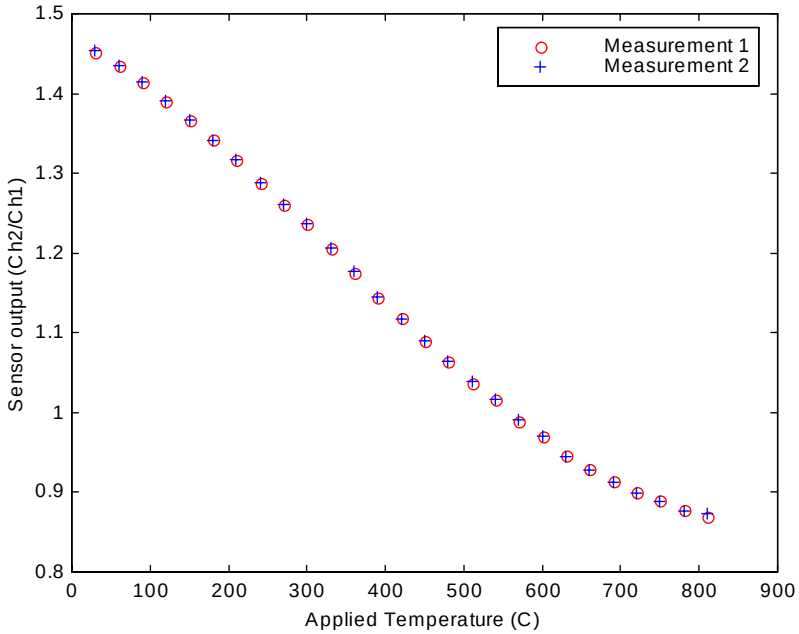

Figure 6.18. Multimode SCIIB sensor temperature sensitivity test result

As shown in Figure 6.18, the SCIIB system output was estimated to cover about 70% of the change from the peak to the valley of an interference fringe when the temperature changed from 30°C to 810°C. It was known that half of the interference fringe corresponded to a sensor cavity length change of a quarter of the central wavelength. Therefore, with the source central wavelength of 850 nm, the temperature sensitivity of the multimode sensor could be estimated by the following equation.

$$s_{t,m} = \frac{70\% \times \frac{1}{4} \times 850[nm]}{(810-30)[^{\circ}C] \times 0.7[mm]} = 2.7 \times 10^{-7}[\frac{1}{^{\circ}C}] \qquad \textbf{(6-7)}$$

Although the temperature sensitivity given in Eq. (6-7)) is only an estimation, the result agrees with what the temperature model predicts. The experimental results indicate that the

multimode fiber-based sensor probe has a large temperature dependence compared to its linear operating range. This is mainly due to the large CTE of the fiber which results from the large quantity of dopants used to increase the core refractive index and fill the relatively large core. The large difference between the CTE of the fiber and that of the fused silica tube makes the multimode fiber-based sensor probe have a large temperature dependence. When the multimode fiber-based sensor is used for pressure measurement in harsh environments where the temperature variation could be large, the large temperature dependence can introduce an unacceptable error to the final result.

6.8.3.2 Singlemode fiber SCIIB sensor probe

Singlemode fibers have a smaller core diameter and refractive index difference compared to multimode fibers. The smaller amount of dopants in single-mode fibers makes the singlemode fiber have a CTE very close to that of fused silica, and hence less temperature dependence compared to the multimode fiber sensor. To determine the actual temperature sensitivity of the singlemode fiber-based sensor probe and also in hopes of finding an optimal design of the sensor probe to achieve zero temperature dependence, we fabricated five singlemode fiber sensors and measured their temperature sensitivity experimentally. The experiments were conducted using the same electrical furnace for the sensor annealing. Because the temperature sensitivity of the single-mode sensor is very low, it is almost impossible to increase the temperature high enough to cover one-half interference fringe as we did for the multimode fiber sensor. Whitelight interferometry was thus used to measure the sensor cavity length. Figure 6.19 shows the recorded sensor cavity lengths measured as

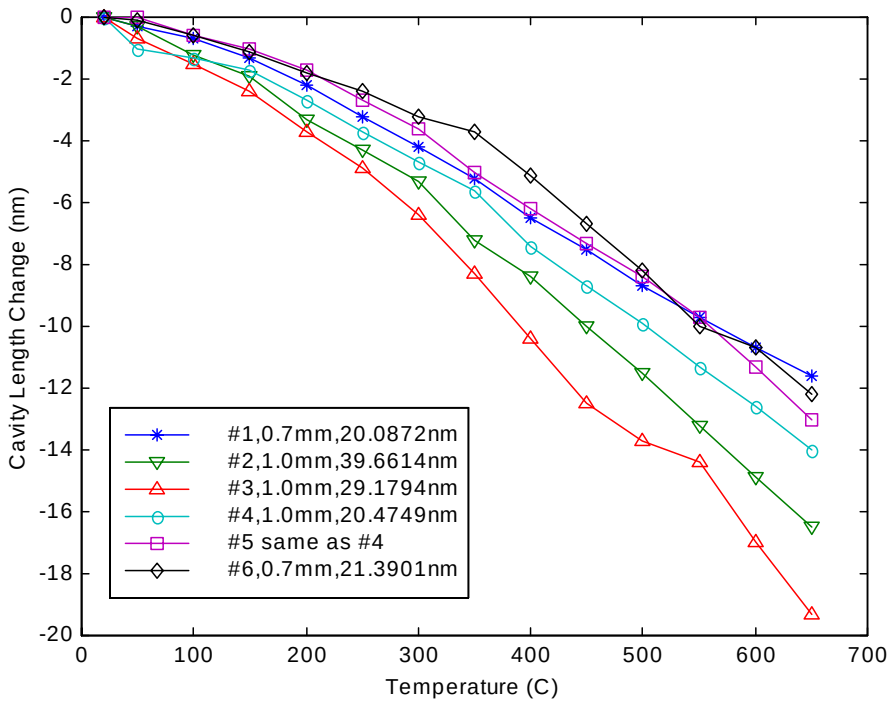

Figure 6.19 Temperature sensitivity test results of singlemode sensor probes.

the temperature inside the furnace increased from room temperature up to 650°C in steps of 50°C. All the sensors showed a decrease in the cavity length as the temperature increased. Also, it was found that a shorter gauge length resulted in smaller temperature sensitivity.

Although efforts were made to find the exact CTEs of the fiber and the capillary tube by solving the linear equations formed by the experimental data, the results conflicted with each other. The reason was believed to be that the accuracy of the whitelight interferometry was not high enough compared to the required resolution. In order to provide meaningful data for the equation solving to find the actual CTEs, a more accurate method for displacement measurement must be used. Nevertheless, the experimental data did provide some information on the temperature dependence of the sensor. For example, a sensor with a gauge length of 0.7mm (corresponding to 4000psi pressure measurement range), and an initial cavity length from 20 μm to 30 μm will have a temperature sensitivity of 0.02nm/°C (or 2.86×10^{-8}/°C), which is an order of magnitude lower compared to that of the multimode fiber sensors.

7.0 Pressure Sensors

Monitoring of high pressures with high accuracy in oil reservoirs is vitally important for downhole oil exploration and oil recovery applications. In this chapter, we present the details of the pressure sensor system design, sensor fabrication methods and test results.

7.1 Pressure Sensor Design

The primary design issues of FABRY-PEROT pressure sensor include the sensor head geometry, material, sensor sensitivity, and sensor dynamic range. The geometry of a pressure sensor is shown in Figure 7.1. The sensor head is made by inserting two fibers into a fused silica capillary tube and thermally sealing them together so that an air gap is formed between the two cleaved fiber endfaces. When a hydrostatic pressure is applied, the capillary tube will deform, and as a consequence the cavity length will change. Effects in both the longitudinal and the transverse directions should be considered.

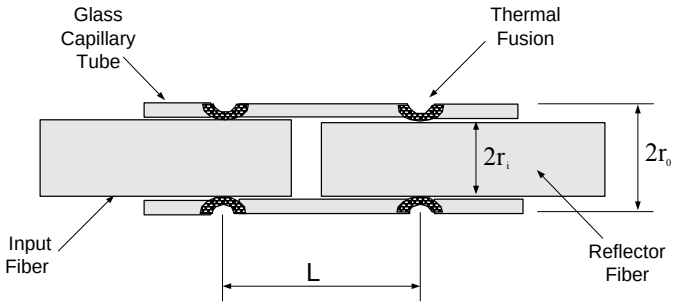

Figure 7.1. Geometry of SCIIB pressure sensor head.

Assume that the capillary tube has an outer radius of r_o and an inner radius of r_i. When the applied pressure changes from p_1 to p_2 the sensor air gap change (ΔL) can be expressed as

$$\Delta L = \frac{L}{E}[\sigma_z - \mu(\sigma_r - \sigma_t)], \qquad \textbf{(7-1)}$$

where L is the effective sensor gauge length defined as the distance between the two thermal bonding points; E is the Young's Modulus and μ is the Poisson's ratio of the capillary tube. For the fused silica materials used, $E=74$ *GPa,* and $\mu=0.17$. Three strains are concerned in the analysis: σ_r is the radial strain, σ_t is the lateral strain, and σ_z is the longitudinal strain generated by the applied pressure. Those three strains can be calculated by the following equations.

$$\sigma_r = \frac{(p_2 - p_1) r_o^{\,2}}{r_o^{\,2} - r_i^{\,2}} \left(1 - \frac{r_i^{\,2}}{r_0^{\,2}}\right) \qquad \textbf{(7-2)}$$

$$\sigma_t = \frac{(p_2 - p_1) r_o^{\,2}}{r_o^{\,2} - r_i^{\,2}} \left(1 + \frac{r_i^{\,2}}{r_0^{\,2}}\right) \qquad \textbf{(7-3)}$$

$$\sigma_z = \frac{(p_2 - p_1) r_o^{\,2}}{r_o^{\,2} - r_i^{\,2}} \qquad \textbf{(7-4)}$$

After combining Eq. (7-2) through (7-4), the sensor cavity length change caused by the applied pressure can be expressed as

$$\Delta L = \frac{L(p_2 - p_1) r_o^{\,2}}{E(r_o^{\,2} - r_i^{\,2})} (1 - 2\mu). \qquad \textbf{(7-5)}$$

Eq. (7-5) clearly shows that the change in applied pressure can be measured by the change in the air gap length of the sensor. If we calibrate the sensor cavity length at known pressure, we can measure the absolute applied pressure by measuring the change of the sensor cavity length. For SCIIB sensors, to avoid the phase ambiguity problem, the sensor must operate over the linear range of a half interference fringe, which is approximately a quarter of a fringe. It is very important to design the sensor head so that the sensor operation is constrained to this linear range. The geometrical parameters can be selected limit the measuring pressure to the linear portion of the interference fringe.

The maximum pressure measurement range is plotted versus the sensor effective gauge length and the outer diameter of the capillary tube in Figure 7.2. Here we assume that the

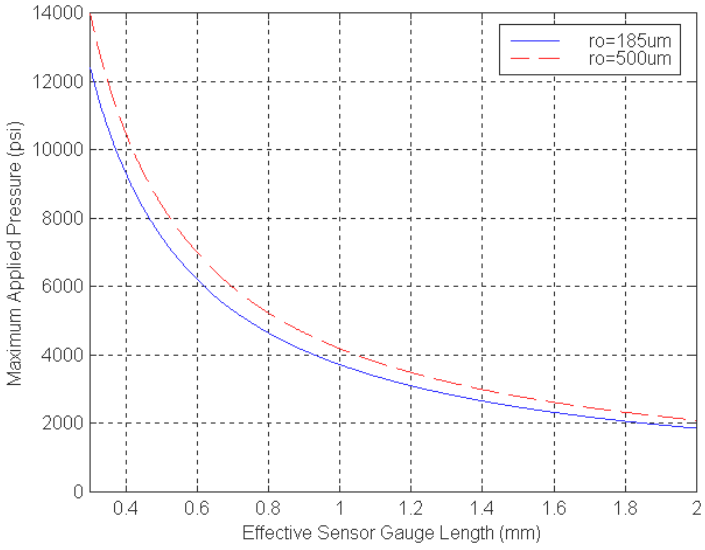

Figure 7.2. Relationship between the sensor geometric parameters and the maximum pressure.

inner diameter of the tube is 130 μm and the wavelength of the source is 1300 nm. The maximum applied pressure is set to cover only the linear portion of the interference fringe, which is a quarter of the source wavelength. As indicated in the plot, the change in outer diameter of the tube doesn't affect the sensor performance significantly. On the other hand, the choice of the effective gauge length can allow us to effectively design the sensor for different dynamic ranges.

7.2 Pressure Sensor Fabrication

The sensor head is fabricated by inserting two fibers into a silica glass capillary tube. The tube has an inner diameter of 130 μm, which is slightly larger than the fiber-cladding diameter of 125 μm. The outer diameter of the glass tube can be varied as required to achieve different dynamic ranges and resolutions according to Equation (7-5). In order to obtain good interference signals, the two fibers inside the capillary tube must be maintained in good alignment. Thereafter, the geometric parameters that can be used to modify the sensor performances are the effective sensor gauge L and the outer diameter of the capillary tube.

With the automated sensor fabrication system discussed in Chapter 6, we can fabricate high-performance sensor heads. First, fiber with the buffer removed are carefully cleaned using alcohol and well cleaved using a fiber cleaver. The capillary tube, also with the buffer removed, is also cleaned and well cleaved to the desired length. Second, with the help of the microscope, the two pieces of fiber are inserted into the capillary tube and clamped on the positioning stages by magnetic holders. By adjusting the micropositioning stage system, the two pieces of fiber are moved to the preset positions where the desired initial sensor F-P cavity length is obtained. By moving the two-dimensional translation stage underneath the micromotion stage system, the fiber and capillary tube assembly is brought to the center of the laser spot. The CO_2 laser emits light to heat the assembly with certain power level and duration controlled by the computer. For good quality, hermetically sealed sensor heads, the proper power level and duration of CO_2 laser exposure must be selected. After one side of the sensor head is bonded, the fiber and capillary assembly is then moved to the other side to perform an identical bonding process for the second bonding point. After completion of the second bonding process, a sensor head is produced.

7.2.1 Singlemode fiber sensor

The geometry of sensor head is the same as that shown in Figure 7.1. Both the input fiber and reflector fiber are 9/125μm standard singlemode fiber. The fiber and the tubing are coposed of the same material. The singlemode white light system is used to monitor the air gap. The measurement range is 15~50μm, and the accuracy is 10nm. Figure 7.3 shows the singlemode white light monitoring window.

7.2.2 Multimode fiber sensor

The geometry of sensor head is the same as that shown in Figure 7.1. Both the input fiber and reflector fiber are 62.5/125μm (or in some cases 50/125μm) regular multimode fiber. The fiber has a slightly larger CTE (coefficient of thermal expansion) than the tubing. When fabricating the sensor head, we use the multimode white light system to monitor the air gap.

The measurement range is 4.5~20 μm, and the accuracy is 1nm. Figure 7.4 shows the multimode white light monitoring window.

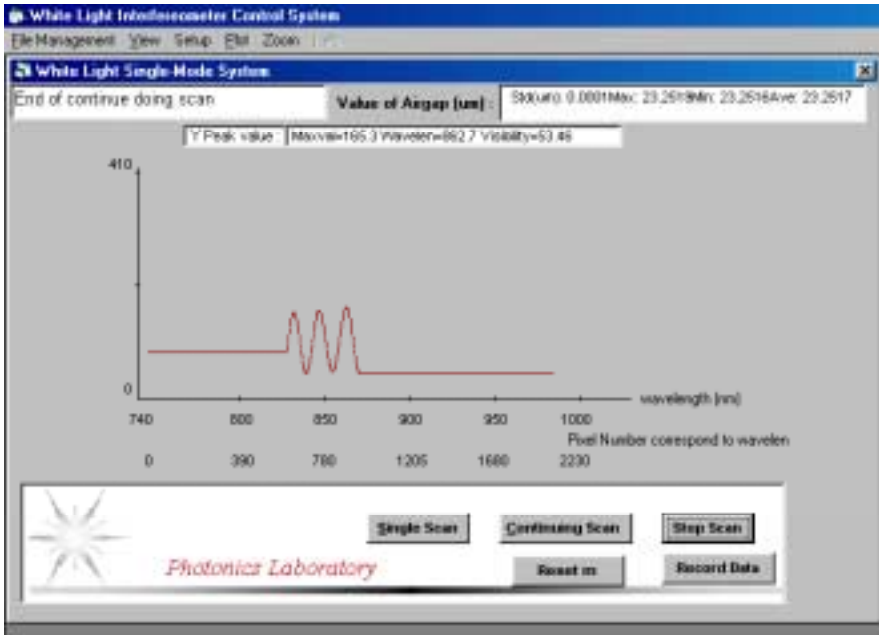

Figure 7.3. Singlemode white light monitoring window.

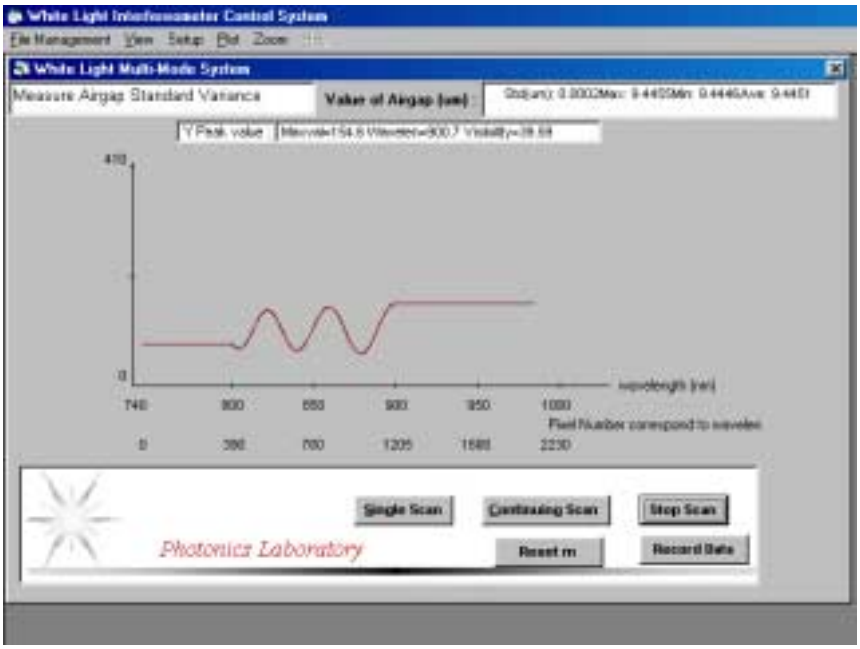

Figure 7.4. Multimode white light monitoring window.

7.3 Carbon Coated Multimode-Singlemode Combo Fiber Sensor

In order to protect the sensor head from water penetration, we choose a carbon coated multimode fiber for sensor head fabrication instead of regular fiber. The geometry of the carbon coated multimode fiber is shown in Figure 7.5.

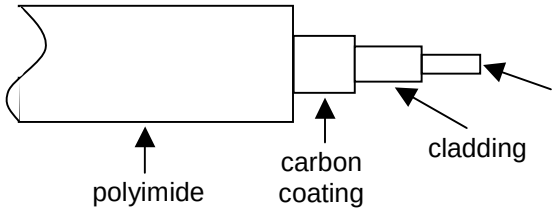

Figure 7.5. Schematic of carbon-coated fiber.

Before sensor fabrication, the polyimide must be removed so that the fiber can be put into the tubing. It was not easy to remove the polyamide from the glass fiber Two methods were developed for this polyimide removal process:

(1) Sulfuric acid: Heat sulfuric acid to 130°C in a test tube. Immerse fiber in the tube until the fiber color changes from brown to silvery. Then rinse the fiber with deionized water. This method is not difficult but time consuming and somewhat dangerous. Polyimide removal requires one hour and before sensor fabrication, the carbon coated fiber must be spliced with the output fiber of the white-light system.

(2) Blade: After much practice and experiment, we developed a technique to remove the polyimide from the carbon coating using a sharp blade to remove the polyimide. It is simple, but difficult because the carbon coatied fiber was very brittle. The angle and the force of the blade must be controlled very carefully in order to avoid fracturing the fiber. When the technique was mastered it only took several minutes to remove the polyimide and the fiber was not as brittle as the one handled by the first method. Figure 7.6 illustrates the process.

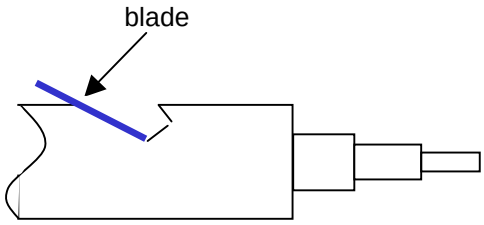

Figure 7.6. Polyimide removal from carbon-coated fiber using a blade.

7.3.1 Leakage prevention

In the downhole application, the optical fiber sensor must endure over 10000 psi pressure, and the bonding of the sensor must be strong enough to prevent leaking. After numerous

experiments, a three-point bonding method was developed. The sensors have three bonding points on both sides of the air gap as shown in Figure 7.7. In fact, the three points are continuous along the fiber and tubing, so the splice length is longer than it is for single point bonding.

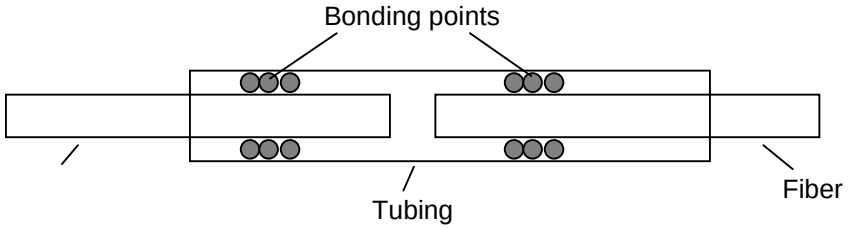

Figure 7.7. Schematic of three-point bonding.

7.3.2 Temperature sensitivity reduction

Since the carbon coated multimode fiber has a slightly larger CTE than the tubing, temperature changes will cause a change in air gap (Fabry-Perot cavity), causing a large error in the pressure measurement when the environmental temperature is not stable. After many trials, we designed a combination structure sensor head, shown in Figure 7.8. Between the two bonding points, the length of singlemode fiber used in the sensor fabrication is much longer than the carbon coated multimode fiber. Because the CTE of the singlemode fiber more closely matches the CTE of the tubing, the sensor head thermal dependence was greatly reduced.

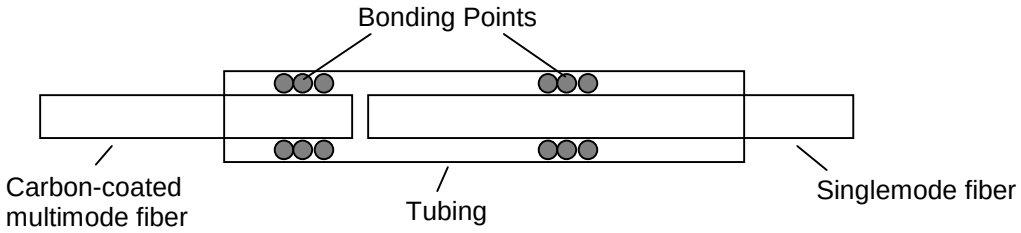

Figure 7.8. Combo structure sensor head to reduce temperature sensitivity.

7.3.3 Precise air gap control

The air gap of the fiber sensor must be controlled for two reasons.

(1) The visibility will be related to the air gap.
(2) Air gap measurement by the white-light system has a minimum and maximum limit.

We found that the air gap can be controlled during the CO_2 laser bonding process by bonding the reflector fiber side about 10 times. For the first 5 times, the laser power is adjusted through the series, 1.8w→ 2.0w→ 2.2→ 2.3w→ 2.33w. Then a power between 1.9~2.2w is used for the final five bonding repetitions. If the samepower is used for each repitition of the laser pulse, the air gap value will change linearly with the bonding times. Figure 7.9 shows the air gap adjustment process. After the first five bonding repetitions, the air gap changed from 21.6680 to 23.0665μm. Selecting the laser power between 2.0~2.2w, the air gap changes linearly during the last five times bonding. Therefore, by using the last five bondings to adjust the air gap to the desired value, a very close tolerance can be maintained on the initial air gap after fabrication. Finally, the air gap that was obtained in this way was very close to the desired value of 23.1945 μm.

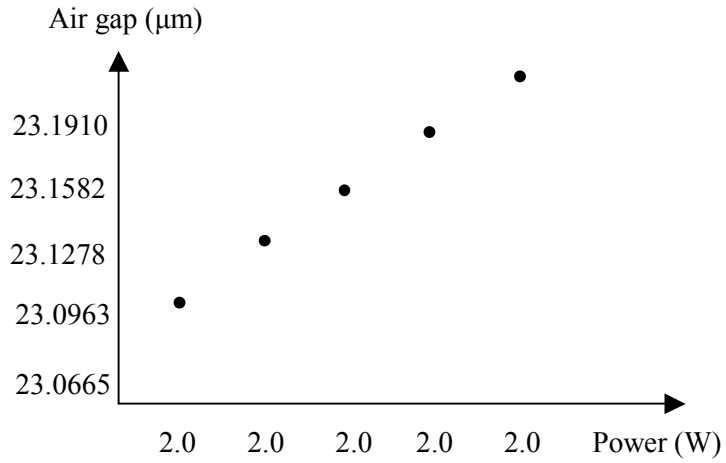

Figure 7.9. Air gap control by laser bonding power.

In Figure 7.9, bonding with a laser power of approximately 2.0W changes the air gap about 30nm for each laser pulse. The number of additional laser pulses required depends upon how close the air gap is to the desired value. If the airgap after the first five pulses of the laser is far from the desired value, more than 5 laser pulse may be required to bring the air gap to the desired value. Conversely, if the air gap after the first five laser pulses is very close to the desired value, fewer additional laser pulses will be required. The first five laser pulses can be thought of as the coarse adjustment and successive laser pulses as the fine adjustment. For even finer resolution air gap setting, the laser power of the last pulses can be changed as well. We can use a lower power to change the air gap more precisely and in practice, the highest precision that has been achieved is about 3nm.

7.3.4 Gauge length

The sensitivity of the pressure sensor is directly determined by the gauge length of the FABRY-PEROT sensor head. On another hand, to make the sensor head deployable, the sensor size should be small enough. After many experiment and tests, a 10mm gauge length was chosen. When pressure increases from 0~5000psi, the air-gap will decrease about 5μm.

7.3.5 Elimination of nonlinearity

The air gap will be decreased as the pressure applied on the sensor increases, *i.e.*, the Fabry-Perot cavity will become smaller. The change in air gap should be linear with the change in pressure because the Young's modulus of the tubing is a constant. But some sensors exhibit nonlinearity when the pressure is relative low. After many tests, we determined that the reason is the frictional force between the fiber and tubing in the region between the bonding points (which will be referred to as the gauge region), which may be caused by some dust or electrostatic charge. Although the shorter the multimode fiber, the smaller the thermal dependence, there is a tradeoff between thermal stability and nonlinearity. By numerous experiments, the optimum structure was found to consist of a 3mm carbon coating multimode fiber plus a 7mm singlemode fiber.

4.3.Pressure Sensor Testing System

Before the pressure sensor probe could be used for actual pressure measurement, it had to be calibrated to relate the output ratio to the applied pressure. Sensor calibration is usually conducted by applying known pressures within its operating range. The one-to-one relation between the sensor original output and the applied pressure forms the calibration curve which can be stored in the host computer and later used to convert the sensor output to the pressure reading.

7.3.6 System construction

The sensor calibration system was constructed based on a computer-controlled high-performance pressure generator/controller manufactured by *Advanced Pressure Products, Inc*. The system configuration is shown in Figure 7.10. The pressure controller/generator can supply a hydrostatic pressure up to 20,000 psi, and the accuracy of the pressure output is 0.1% of the full scale. The construction of this system allowed us to precisely and automatically calibrate the fiber optic pressure sensor over the entire operating range. The system also allowed us to test many performance characteristics of the pressure sensors such as the linearity, hysteresis, repeatability, and dynamic range.

Multiple pressure channels were fabricated on the APP pressure system, which could be controlled separately through several valves installed in the system piping. With this configuration, three pressure sensors could be tested at the same time. The sensors could also be tested under high pressures at elevated temperatures by heating one of the pressure test chambers using a flexible electric heating tape, which could achieve a temperature up to 700°C. This test was very important to evaluate the temperature dependence of the pressure sensor. The temperature sensitivity testing results were useful feedback to the sensor fabrication improvement.

A second pressure testing system was designed for testing the pressure sensors based on the Model 9035 pressure calibrator purchased from *Pressure Systems, Inc*. (*PSI*). This system has a relatively small pressure range but very high accuracy. The system configuration is shown in Figure 7.11. The calibration pressure range is from 0 to 250 psia, and the long-term accuracy is ±0.02% of the full range. This system allowed us to test the resolution and accuracy of the pressure sensor with a very high accuracy.

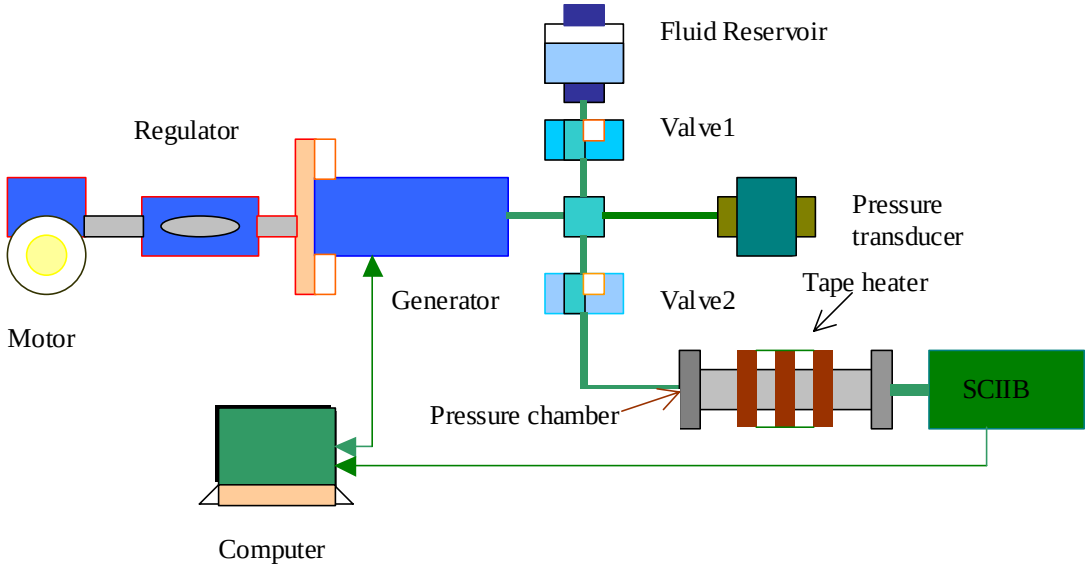

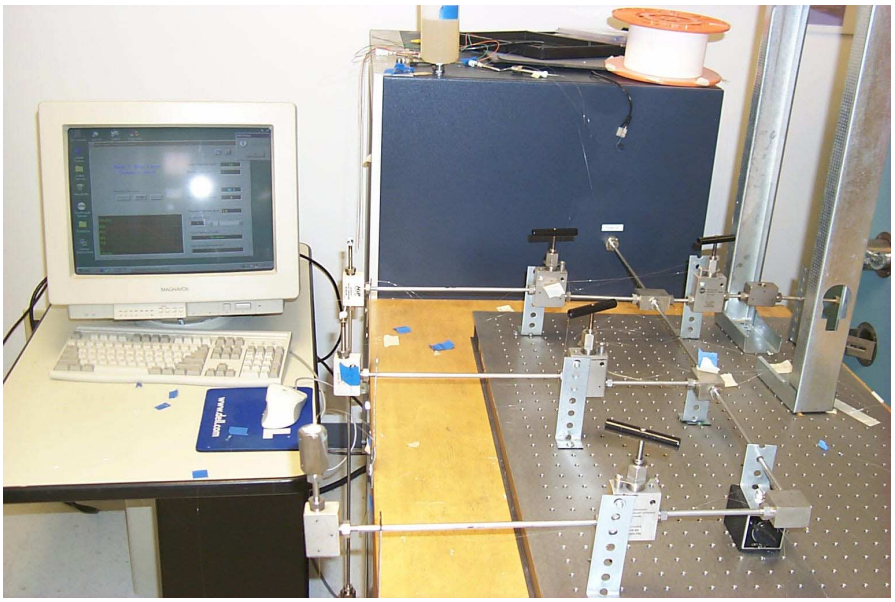

Figure 7.10. APP pressure sensor test system.

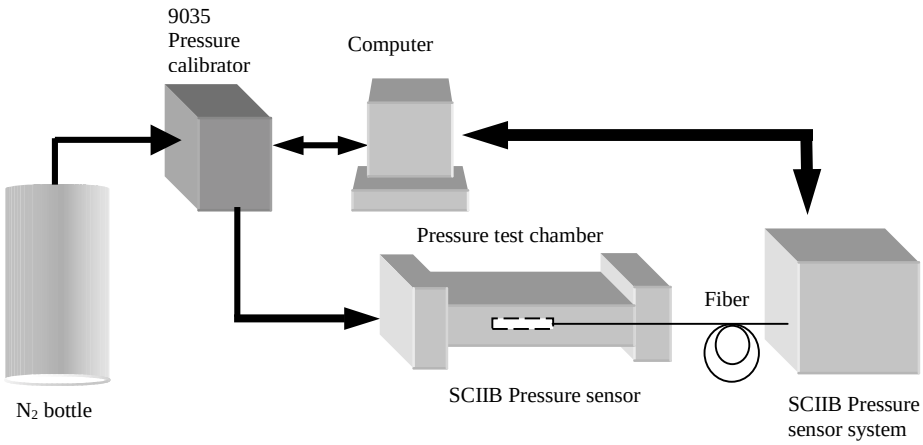

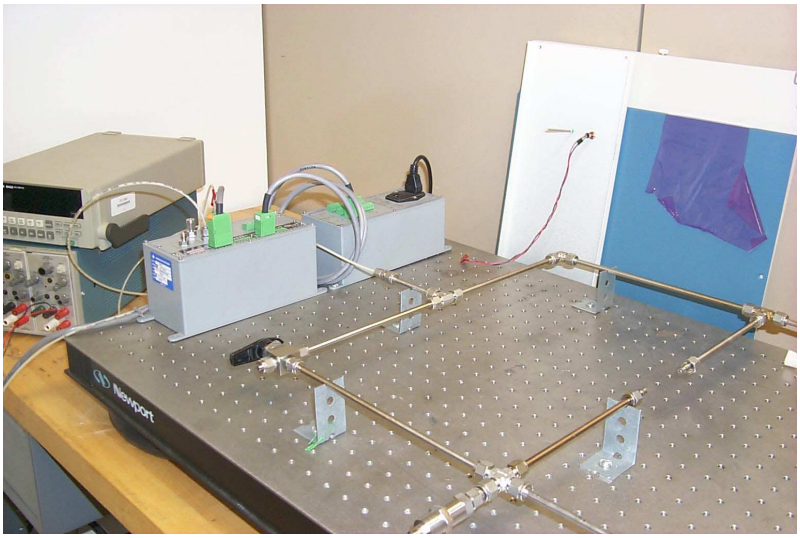

Figure 7.11. PSI 9035 based high accuracy pressure testing system configuration.

7.3.7 Calibration procedures

During the calibration process, the pressure sensor was installed inside the pressure calibration chamber. Through the computer programs, the hydrostatic pressure was applied to the sensor at increments of 1/40 of the estimated linear range of the pressure sensor. The pressure gauge inside the APP system measured the hydrostatic pressure inside the chamber and the system saved the data as applied pressure. At the same time, the output of the sensor system was sampled through the A/D converter and stored in another data file. To ensure the accuracy of the calibration, the system held the pressure at each step for about 50 seconds before moving to the next step. By taking the average within the pressure holding period, the error was minimized.

Figure 7.12 shows typical applied pressure data, and Figure 7.13 is the SCIIB output data recorded during the sensor calibration. The sensor used in the test was a singlemode fiber sensor with the gauge length of 0.5mm, initial cavity length of 25.46μm, and interference fringe visibility of 70%. Figure 7.14 plots the SCIIB output versus the applied pressure after averaging. A one-to-one relation of the applied pressure and the SCIIB output was then used to find the calibration equation through polynomial fitting. Experimental results revealed that the optimal order of the polynomial fitting was 10. Usually, the calibration curve was obtained by taking the average of several consecutive calibration data to further ensure the accuracy of calibration.

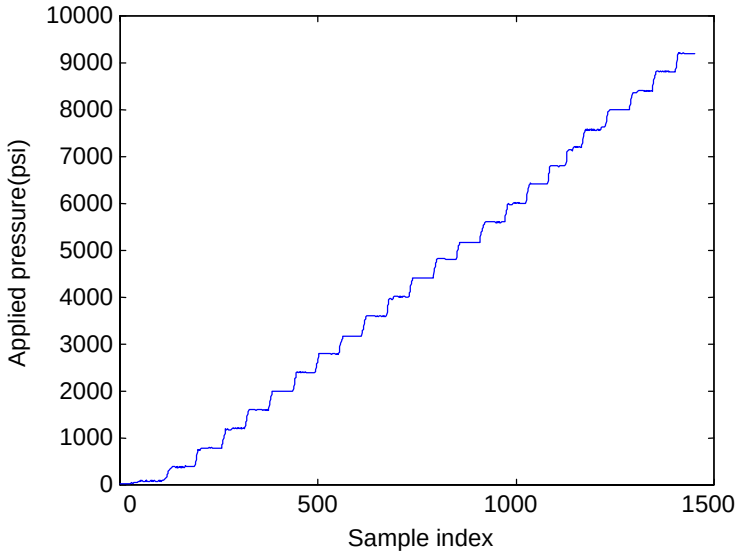

Figure 7.12. Applied pressure recorded during sensor calibration.

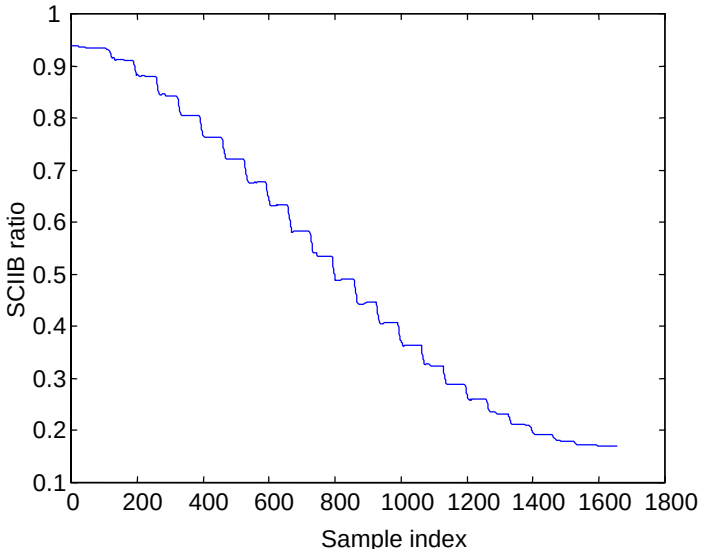

Figure 7.13. SCIIB output ratio recorded during sensor calibration.

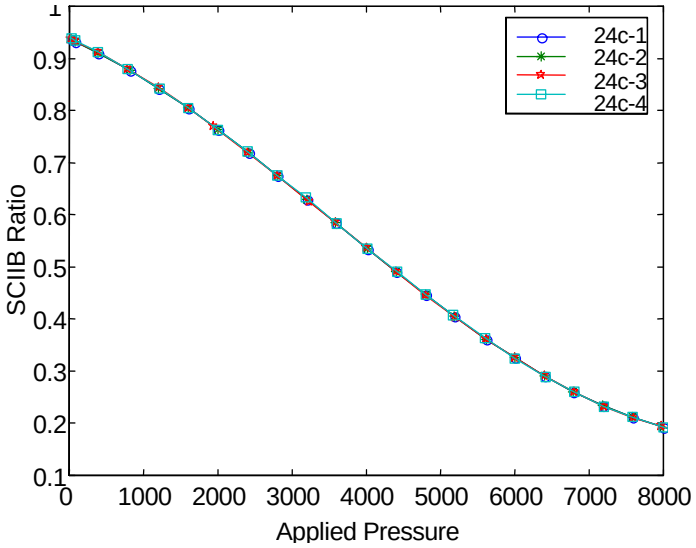

Figure 7.14. SCIIB pressure sensor calibration curve.

7.4 Experimental Results1

7.4.1SCIIB pressure sensors

After calibration of the sensors, the performance characteristics of the developed SCIIB pressure sensor system were evaluated, including linearity, hysteresis, resolution, repeatability, system stability, temperature cross sensitivity, and over pressure capability. These are each discussed in detail below.

7.4.1.1 Linearity

Due to the sinusoidal nature of the interference signal, the direct output from the SCIIB pressure sensor is a nonlinear function of the applied pressure. However, the calibration process can linearize the SCIIB output data by polynomial curve fitting. To assess the residual nonlinearity of the sensor system, we examined the measurement results after calibration, as shown in Figure 7.15, with respect to the applied pressure given by the *APP* system. The sensor used in the test was a singlemode fiber sensor with a gauge length of 0.5mm, initial cavity length of 25.46μm, and interference fringe visibility of 70%. The magnified deviation between the calibration line and the straight line is plotted in Figure 7.16. The maximum deviation is about 9psi. If we normalized the nonlinearity with respect the its full dynamic range of 8500psi, the normalized nonlinearity error is less than 0.1% of the full scale of pressure measurements, which is the best accuracy offered by the pressure calibration system.

7.4.1.2 Hysteresis

Hysteresis of the pressure sensor can be measured by cycling the applied pressure between the minimum and the maximum of the operating range in both increasing and decreasing directions. The hysteresis can be calculated as the largest difference between the output readings of the pressure cycles. The SCIIB pressure sensor probe is made of silica glass

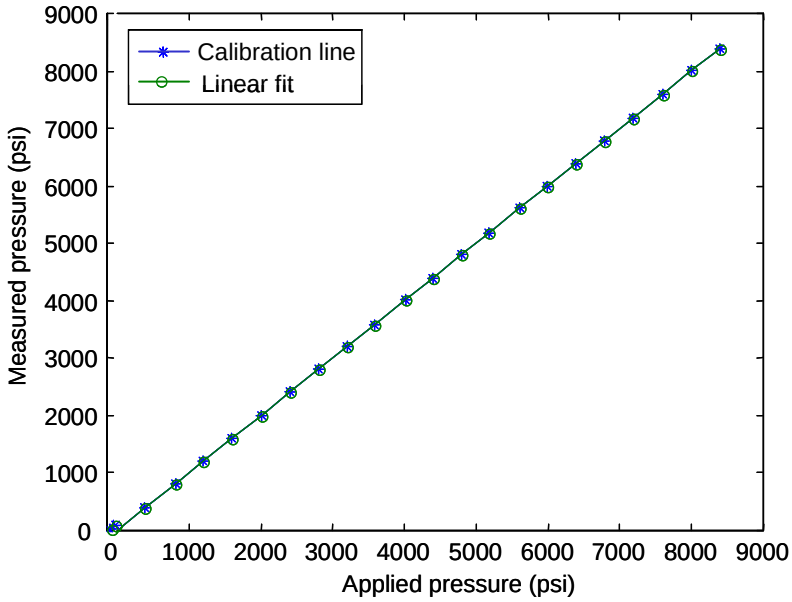

Figure 7.15. SCIIB pressure sensor system calibration lines.

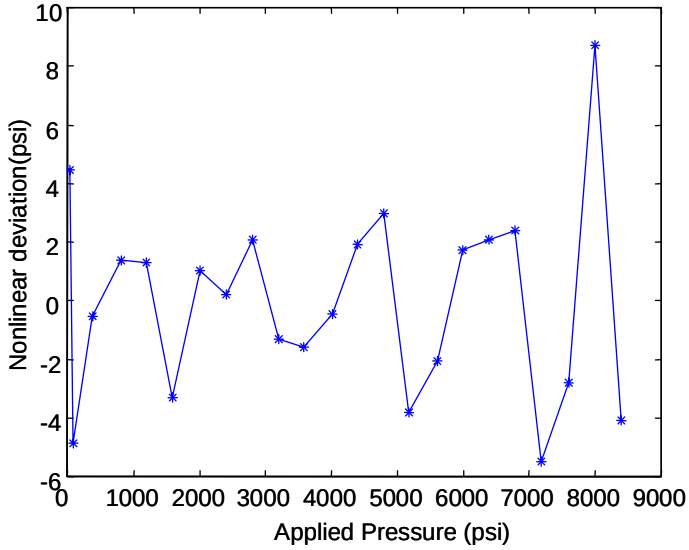

Figure 7.16. Nonlinearity of the SCIIB pressure sensor system

material and the operating range of the sensor in terms of pressure-induced strain is very small. Therefore, the hysteresis of the sensor probe is expected to be very small. Nevertheless, experiments were conducted to evaluate the actual hysteresis of the SCIIB sensor probe. The evaluation was conducted using the *APP* pressure system after the sensor system was calibrated. The applied pressure was first increased to the maximum operating range of 8500psi at the step of 400psi. The pressure was then decreased to atmospheric pressure after it was maintained at 8500psi for several minutes. The measurement results are

shown in Figure 7.17. The experimental results confirm our expectation. There was no noticeable hysteresis found within the entire operating range.

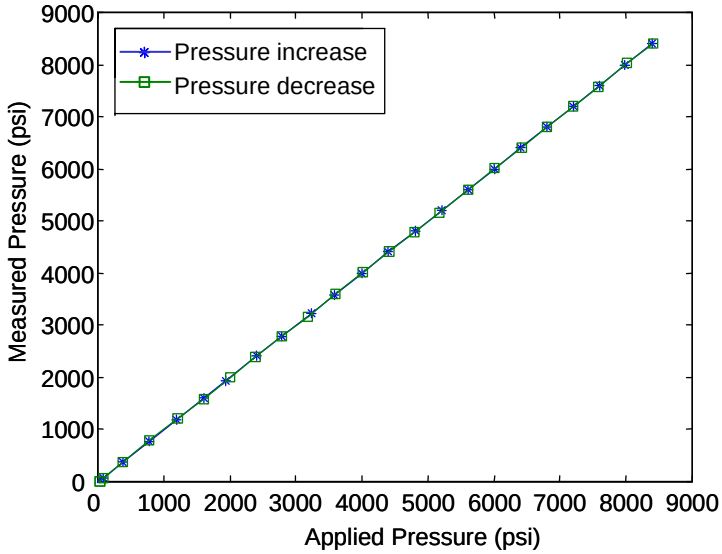

Figure 7.17. Hysteresis of the SCIIB pressure sensor.

7.4.1.3 Resolution

The resolution of the sensor system is usually interpreted as the standard deviation of a series of pressure measurements. It is common to use twice the standard deviation as the direct measure of resolution. The evaluation of the sensor resolution was performed using a calibrated sensor with the linear range of 8500psi. The sensor was exposed to the atmosphere where the pressure reading from the sensor should be around 15 psi. The data from the SCIIB system was sampled at a rate of 50 samples per second for one minute, which should be high enough compared to the system's frequency response of 15Hz. The pressure measurement outputs within the one-minute sampling period are plotted in Figure 7.18. The standard deviation of the pressure data within this time period was calculated to be σ=0.121psi. Therefore the resolution of the sensor system was estimated to be $2\ \sigma$ =0.242psi. The normalized resolution with respect to the dynamic range of the system was 0.003% of the full scale.

It must be pointed out that the resolution of the sensor is not constant within the entire operating range due to the non-linear nature of the interference signal. However, by confining the operating range of the SCIIB sensor within its semi-linear range, the resolution of the system should be retained within 60% of the maximum resolution as defined by Eq. (4-14).

7.4.1.4 Repeatability

Repeatability of the sensor can be measured by applying pressure to a certain preset point repeatedly from only one direction (increasing or decreasing). The largest difference of the sensor output readings can be used to specify the repeatability of the sensor. The same calibrated singlemode sensor was used to evaluate the repeatability of the system. Using the

APP system, two consecutive measurements up to the full operating range of the sensor were performed with the results shown in Figure 7.19. For comparison purposes, the original calibration data is also shown. The deviation of the two measurement results with respect to the calibration data are plotted in Figure 7.20. The maximum deviation between the measured pressure and the calibrated pressure was within ±13psi. The normalized repeatability of the sensor system with respect to its dynamic range was therefore ±0.15% of the full scale.

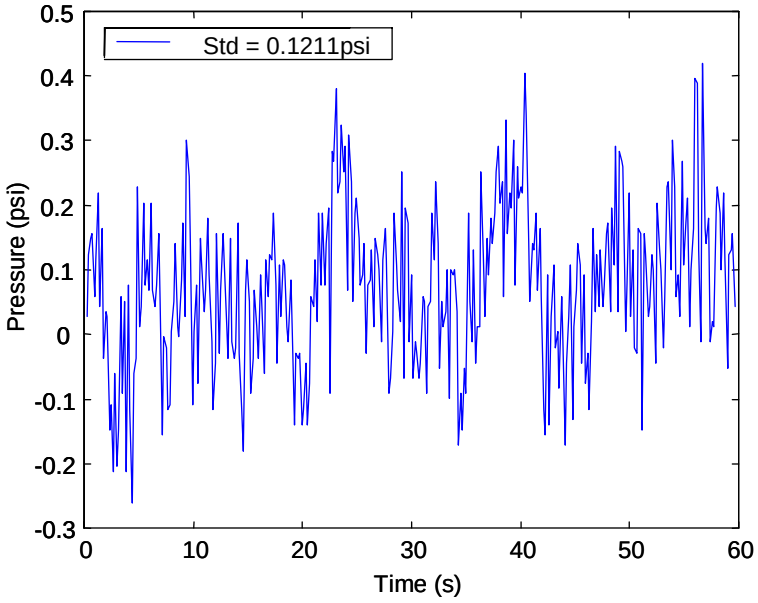

Figure 7.18. Standard deviation measurement of the SCIIB pressure sensor.

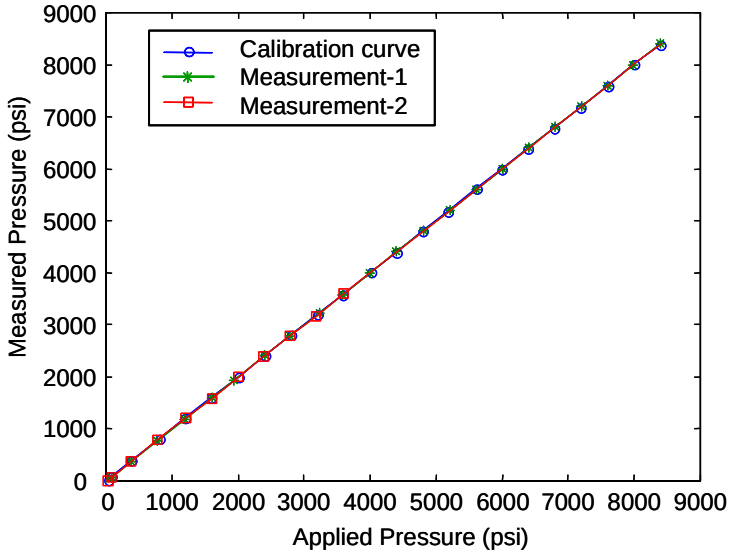

Figure 7.19. Repeatability of the pressure measurement.

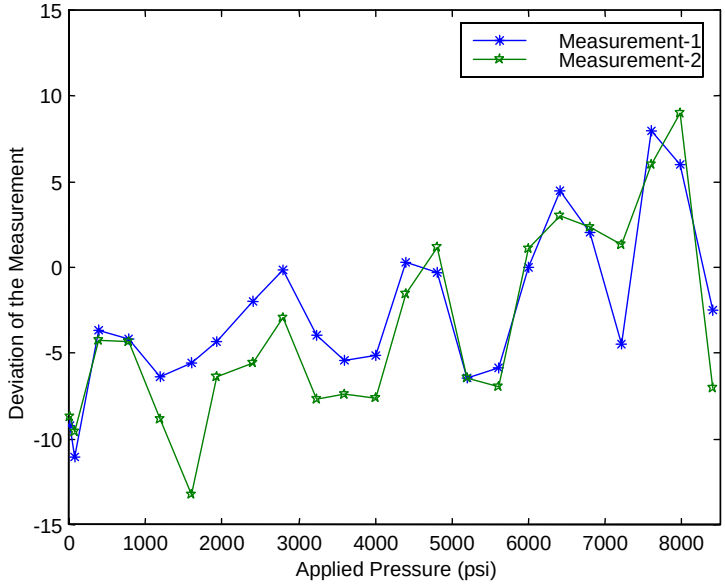

Figure 7.20. Deviation of the measured pressure with respect to the calibration data

7.4.1.5 System stability test

The same singlemode sensor with an operating range of 8500psi was also used to test the system stability. The sensor was kept in the pressure test chamber of the *APP* system for 24 hours starting from 4:00pm in the afternoon. The pressure of the chamber was maintained to the atmosphere pressure. The data acquisition system was programmed to sample the sensor's output every 20 seconds. The test result is shown in Figure 7.21. By processing the

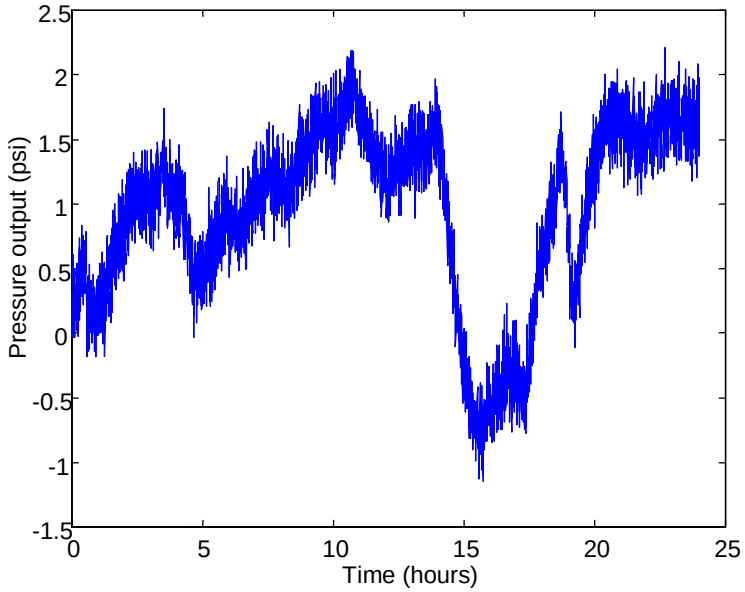

Figure 7.21. System stability over 24 hours.

data, the maximum peak-to-peak pressure variation within the 24-hour time period was 3.3 psi. The normalized maximum variation was thus 0.04% of the full dynamic range. The test results also showed that the variation of the data was not one-directional.

It must be said that the complete evaluation of the system stability needs much longer test period (for example, one year). Therefore, the stability test result of 24-hour period was hence not quite conclusive.

7.4.1.6 Temperature cross-sensitivity

The cross sensitivity to temperature could result in errors of the pressure measurement when the environmental temperature changes. The construction of the APP pressure calibration system allowed us to characterize the temperature cross sensitivity of the SCIIB pressure sensor by measuring pressures at different elevated temperatures. As shown in Figure 7.22, the same singlemode fiber sensor with a dynamic range of 8500psi was tested at temperatures of 24°C, 88°C, and 206°C respectively. Figure 7.23 shows clearly the measurement errors at the two elevated temperatures. The maximum deviation was 215psi at 88°C and 307psi at 206°C respectively. The maximum temperature cross sensitivity was thus calculated to be 0.04% per degree Celsius. It was also noticed that the large errors were found at the low and high pressure range where the nonlinear effects became the largest. The temperature cross sensitivity could thus be reduced by sacrificing the dynamic range of the sensor.

7.4.1.7 Overpressure capability test

In real downhole applications, pressures higher than the nominal values might be encountered due to the use of steam flood to pump the oil to the surface. It is therefore very important for the sensor to be able to sustain burst pressures higher than its dynamic range. The overpressure capability of the SCIIB pressure sensors was thus tested. The sensor used in the overpressure tests was a multimode fiber-based sensor with a gauge length of 1.0mm,

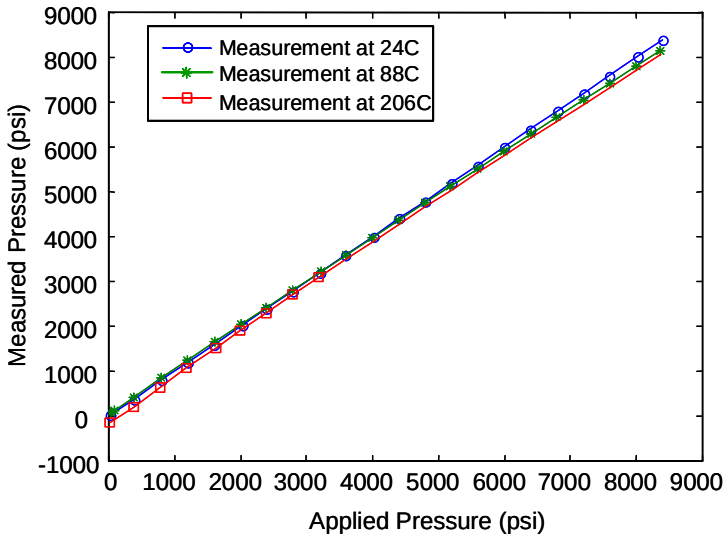

Figure 7.22. Temperature cross sensitivity of the SCIIB pressure sensor.

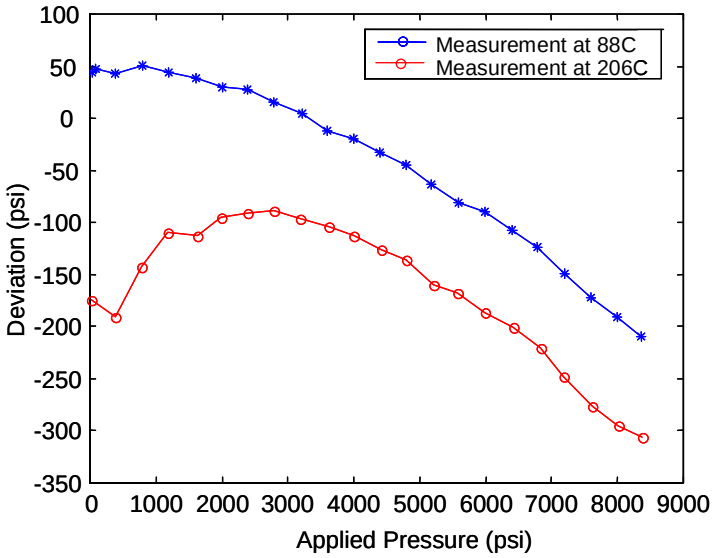

Figure 7.23. Pressure measurement errors resulting from the temperature dependence.

an initial cavity length of 5.67μm, and a fringe visibility of 49%. The sensor was calibrated to have a dynamic range of 1800psi.

The overpressure tests were conducted at room temperature. The sensor was first overpressured to 4000psi and kept in the pressurized chamber for one hour. After the pressure was released, the sensor was evaluated for the measurement of pressures within its dynamic range. The same experiment was also conducted at an overpressure of 6000psi for one hour. The experimental results are shown in Figure 7.24. The deviations from the original calibration line after the overpressures are shown in Figure 7.25. The overpressures do not show any observable effect on the sensor performance. The deviations shown in Figure 7.25 are within the range governed by the repeatability of the sensor.

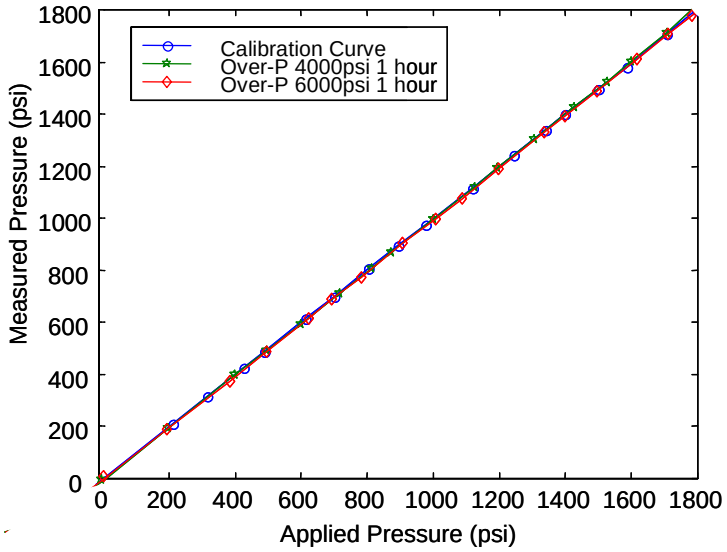

Figure 7.24. Overpressure test results of the multimode SCIIB sensor.

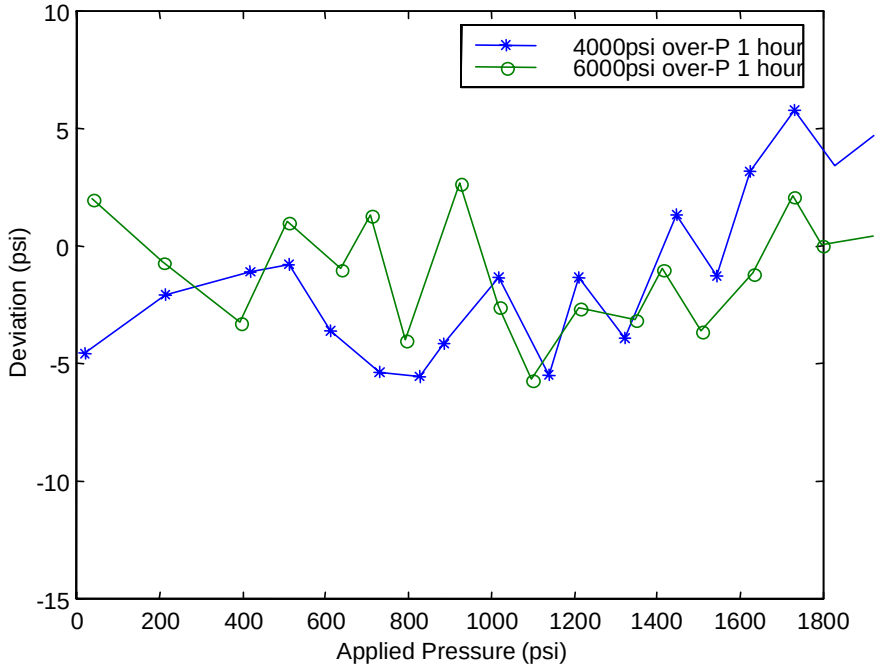

Figure 7.25. Sensor deviation of the overpressure tests.

7.4.1.8 Dynamic pressure measurement

To demonstrate the sensor's dynamic response, the calibrated SCIIB pressure sensors were applied for dynamic pressure measurements. The pressure signal was provided by the *APP* system after it was programmed to pressurize the chamber from atmospheric pressure to the preset pressure in even steps. Both a multimode sensor with an operating range of 1800psi and a singlemode sensor with an operating range of 8500psi were tested. The testing range for the multimode sensor was 900psi and that for single-mode sensor was 8500psi.

The pressure increases measured by the SCIIB pressure sensors are shown in Figure 7.26 and Figure 7.27 for the multimode and singlemode fiber sensors, respectively. The sampling rates of both the SCIIB sensor systems and the pressure gauge were set to one sample per second. The output of the built-in pressure gauge of the APP system is also plotted for comparison purposes. As shown in the two figures, the measurement results of both the multimode and single-mode fiber SCIIB sensors agreed very well with that of the built-in pressure gauge.

7.4.2 Multimode white light pressure sensors

Typical test results for the white light pressure sensor are shown in Figure 7.28. The pressure sensor was tested up to 6000psi five separate times. Two of them were performed at about 176 °C; others were performed at room temperature. The temperature dependence of the pressure sensor shown in Figure 7.28 is about 0.2psi/°C.

The results of the resolution testing of the pressure system are shown in Figure 7.29. In general, two times the standard deviation was taken as a measure of the resolution. The whole system was run continuously for 30 seconds. The sampling rate is about 5

points/second. The standard deviation calculated from the testing results is about 0.015nm, so the resolution of this system is about 0.03nm, which corresponds to 0.03psi.

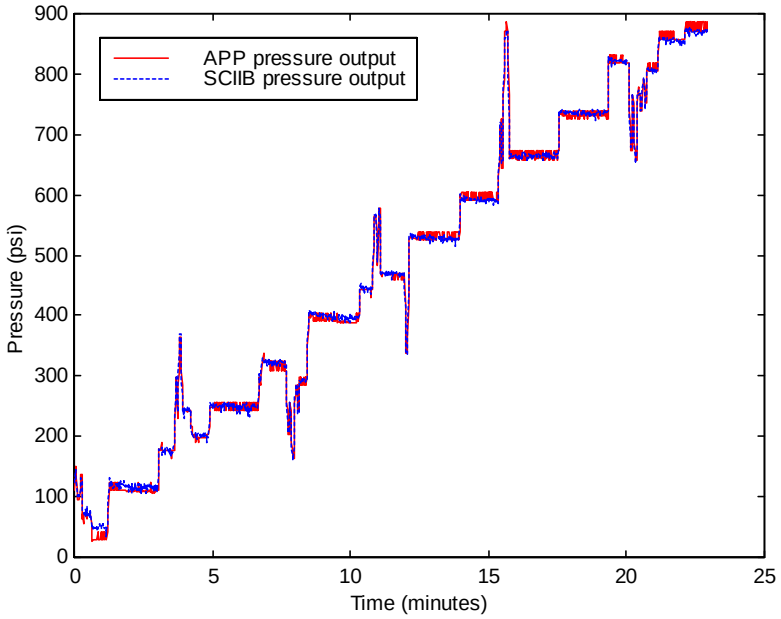

Figure 7.26. Dynamic pressure measurement results for the multimode sensor.

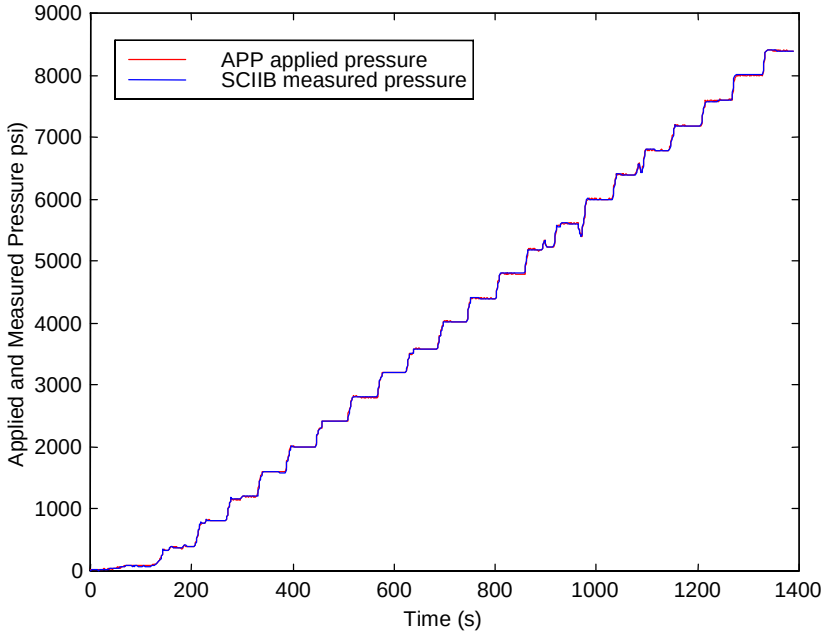

Figure 7.27. Dynamic pressure measurement results for the singlemode sensor.

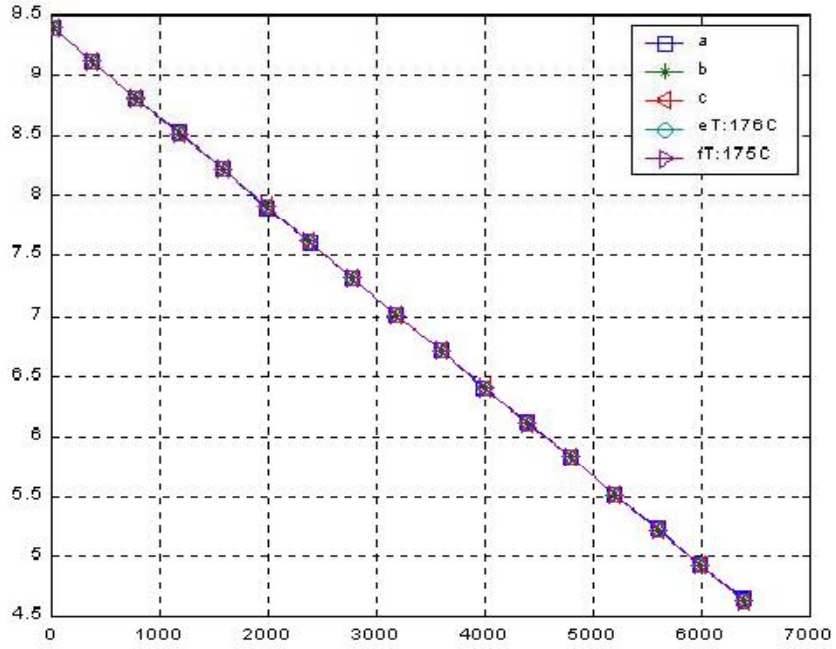

Figure 7.28. Testing results of a pressure sensor under different temperatures.

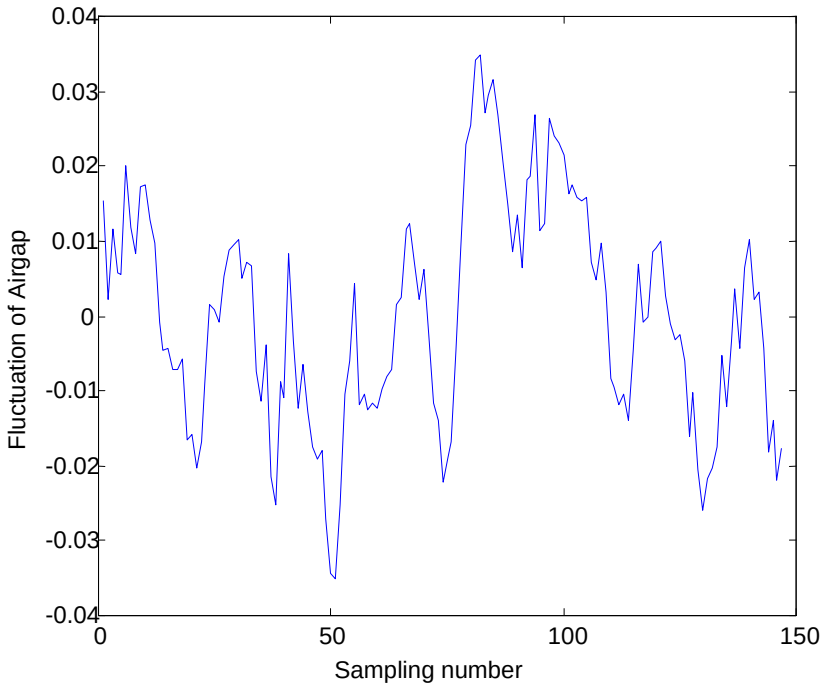

Figure 7.29. Resolution of pressure system.

The stability of the pressure system over 48 hours is shown in Figure 7.30. The maximum air gap error is less than ±0.5 nm, which corresponds to about ±0.5psi. Compared with the dynamic range of 6000psi, the stability is better than 0.01%.

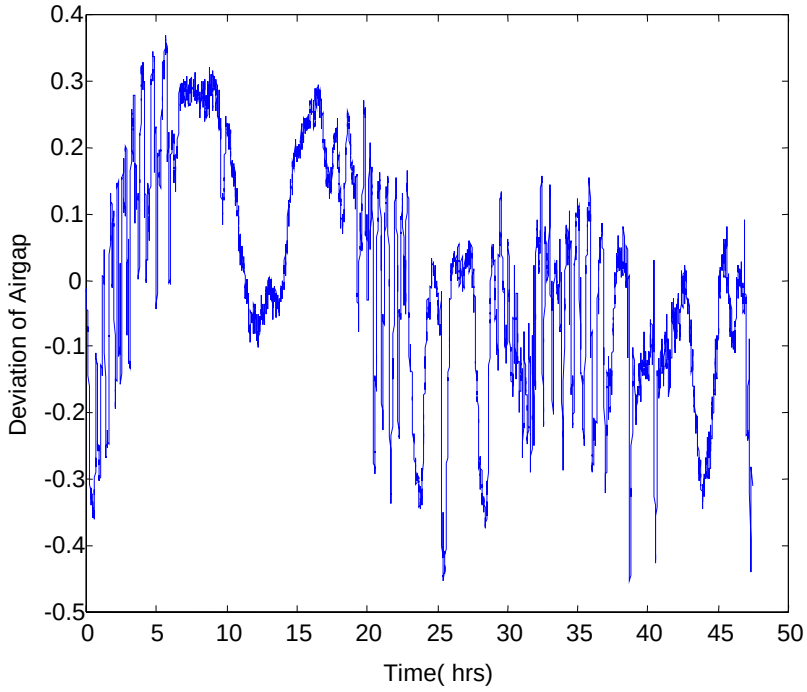

Figure 7.30. 48-hour stability testing of the pressure sensor.

8.0 Temperature Sensors

Temperature measurement and monitoring for downhole oil recovery was an important objective in this research project. The goal was to precisely measure the temperature between –40ºC and +200ºC with an accuracy of ±1.0ºC and resolution of a 0.01ºC under pressure up to 20,000 psia. In this chapter, we present the detailed design of the temperature sensor system, including the sensor geometric design, sensor fabrication, sensor testing, calibration and characterization.

8.1 Temperature Sensor Design

The geometry of the SCIIB fiber optic temperature sensor is illustrated in Figure 8.1. The structure of the temperature sensor resembles that of the pressure sensor except for differences in the geometric parameters and the material used for the alignment tube. When the ambient temperature changes, the physical length of the capillary tube and the fibers will change, which results in a change in the air gap between the two fiber endfaces. Using the white light system, this air gap change can be demodulated from the interference spectrum and thus enable precise measurement of the temperature. Since the same structure was used for both pressure and temperature sensor, the fabrication processes are similar.

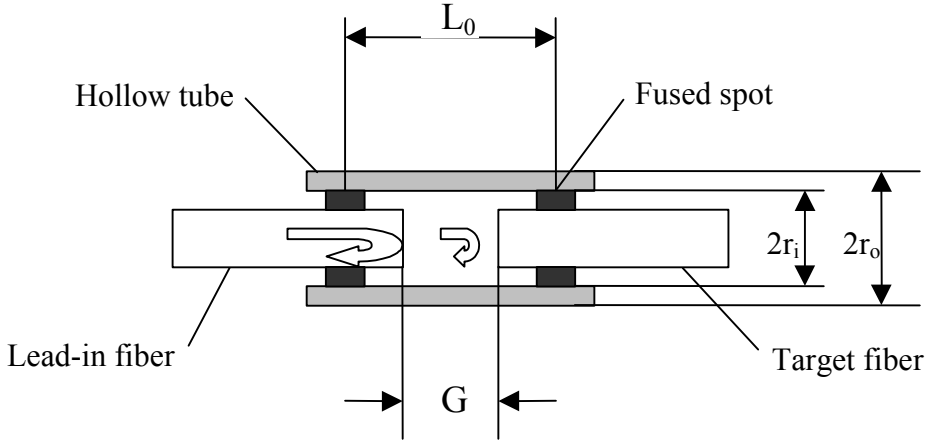

Figure 8.1. Geometry of FABRY-PEROT temperature sensor.

To increase the temperature sensitivity, the geometric parameters and the material used for the alignment tube are different from that for the pressure sensor. The operating principle of FABRY-PEROT temperature sensor can be described by

$$\Delta G = (\alpha_0 L_0 - \alpha_1 L_1 - \alpha_2 L_2)\Delta T\,, \qquad \textbf{(8-1)}$$

where ΔG is the air-gap change induced by the temperature change ΔT, L_0 is the gauge length of sensor head; L_1 is the length of input fiber defined from the input bonding point to the end-face of input fiber; L_2 is the length of reflecting fiber defined from the other bonding point to the end-face of reflecting fiber; α_0, α_1, α_2 are thermal expansion coefficients (CTE) of glass tube, input fiber and reflecting fiber, respectively.

Design of the temperature sensor was focused on selecting suitable materials for the glass tube and the reflecting fiber to increase the temperature sensitivity. Borosilicate glass was selected for the capillary tube, with a CTE of $\alpha_0=3.2*10\text{-}6/℃$. In general, the optical fiber is made by doping small amount of germanium into pure silica material. Typical optical fibers have a CTE of about $7.5*10^{-7}$/°C, which is very close to that of pure silica.

The maximum temperature measurement range is plotted versus the sensor effective gauge length in Figure 8.2. Here, we assume that the source wavelength is 1300 nm, the fiber is singlemode, and the maximum temperature change generates a gap change corresponding to 1/8 of the source wavelength, which covers the whole linear range of the interference fringe. The maximum measurement temperature decreases with increasing effective gauge length. The sensor can be designed to have a maximum temperature measuring range from 100°C to 800°C when it is fabricated to have a gauge length between 1 and 8 mm.

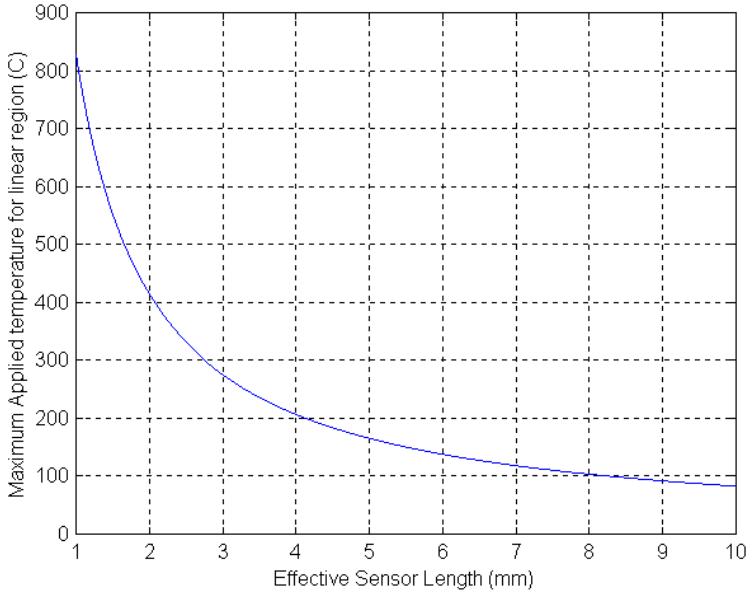

Figure 8.2. Relationship between sensor gauge length and temperature measurement range.

8.2 Temperature Sensor Fabrication

FABRY-PEROT temperature sensors can be fabricated on the automated sensor fabrication station described in Chapter 6. The fabrication process involves inserting two cleaved fibers inside a capillary tube and using the CO_2 laser to thermally fuse the fibers and the tube together. In our experiments, we used the fused borosilicate tube available from Vitrocom,

Inc. The inner diameter of the tube is 150 μm, and the outer diameter is 250 μm. The sensor effective gauge length can be controlled during the fabrication by using a translation stage to move the bonding point with respect to the CO_2 laser beam. After the sensor is fabricated, another CO_2 laser exposure is applied to provide proper annealing of the bonding region to remove residual stresses.

8.3 Pressure Cross-Sensitivity

In the downhole environment, both high pressure and high temperature exist. To eliminate the pressure dependence of the temperature sensor, a special tube was used to isolate pressure from the temperature sensor. The pressure isolator structure is shown in Figure 8.3. Isolation is achieved by bonding borosilicate glass tubing outside the temperature sensor. The borosilicate tubing is sealed at one end, and is bonded to the borosilicate alignment tubing of the FABRY-PEROT sensor on the other end, separating the outside pressure from the temperature sensor head. The borosilicate glass tubing can also provide mechanical protection for the lead-in fiber / sensor tubing joint.

There are three reasons to choose borosilicate as the material for both inner and outer tube: First, borosilicate has much larger CTE compared to fused silicate. From Eq.8-1, a large CTE difference between the tube and optical fiber will increase the sensitivity, resolution and dynamic range of temperature sensor dramatically. Second, bonding between identical materials is much stronger than that between different materials. Third, the laser power required for bonding the borosilicate tubing is much lower than the power required for bonding the fused silicate tubing. Thus the isolating tube bonding process will be harmless to the fiber.

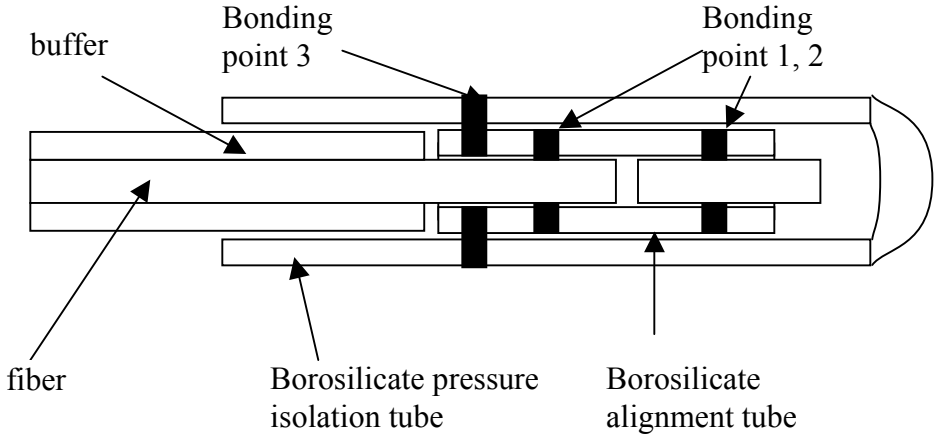

Figure 8.3. Pressure isolating tube of the temperature sensor.

8.4 Temperature Sensor Testing Results

8.4.1 SCIIB thermal stability

The robustness and stability of SCIIB temperature sensors were evaluated under conditions representative of the downhole environment. The experimental setup includes an electrical furnace with a maximum temperature of 1100°C and an Omega CN76000 thermometer to read the temperature at an accuracy of 0.1°C. The SCIIB fiber optic sensor and the thermometer were put side by side in the oven, and the temperature was increased from room temperature to 900°C in steps of 10°C. Both the SCIIB sensor output and the thermometer output were recorded for comparison. The temperature sensor under test had an effective gauge length of 1 mm, and the initial air gap of 5.93 μm. The temperature sensor was tested in the furnace several times. The test results are plotted in Figure 8.4. The sensor successfully survived the test and the output was quite repeatable. The testing results also indicate that the sensor has a very good thermal stability.

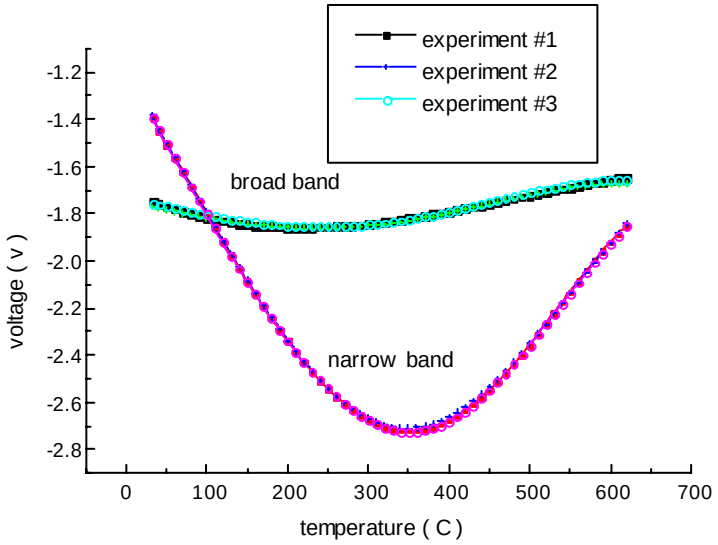

Figure 8.4. SCIIB temperature sensor survivability and stability test results.

8.4.2 SCIIB differential coefficient of thermal expansion (ΔCTE)

The ΔCTE is an important parameter in designing the dynamic range of the SCIIB temperature sensors. Theoretically, the ΔCTE of the sensor can be calculated by referring to the nominal CTEs of the tube material and that of the fibers. However, the actual CTEs of the fiber and the tube can deviate from their theoretical values due to the small chemical or physical differences among the materials used by different manufacturers. Therefore, the precise value of the ΔCTE can only be determined experimentally.

In order to measure the ΔCTE of the SCIIB sensor assembly, we fabricated another sensor with an effective gauge length of 2.5 mm, and an initial air gap length of 5.75 μm. The sensor was tested using the same experimental setup as described in the survivability test. The

sensor output versus the increase of the temperature is plotted in Figure 8.5. Because the sensor had a gauge length longer than the first sensor, when temperature increased, the air gap change covered more than half of an interference fringe. We know that the change from the peak to the valley of an interference fringe corresponds to an air gap change of a quarter wavelength; therefore, the ΔCTE can be calculated by determining the corresponding increase of the temperature between these two points. We used the multimode SCIIB system during the experiments, which has a source central wavelength of 850 nm. The temperature increase from the peak point to the valley point was ΔT=420°C. Therefore, according to Eq. 8-1, the ΔCTE of the sensor is 2.0238×10^{-7}/°C.

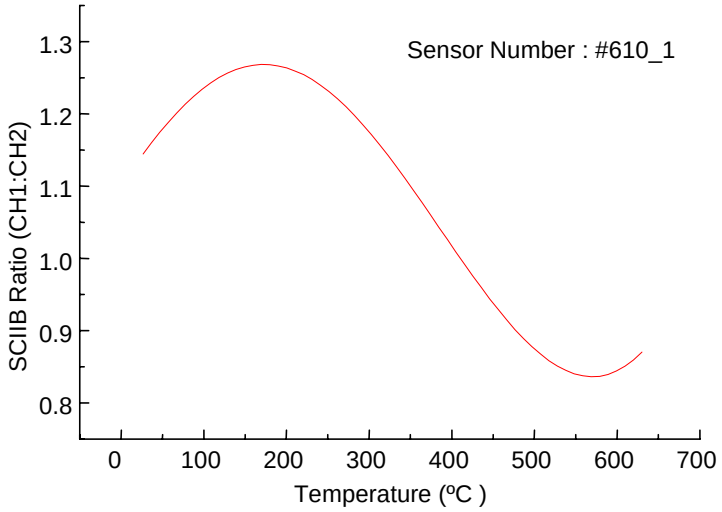

Figure 8.5. Test result used to calculate the ΔCTE of the SCIIB sensor.

8.4.3 SCIIB standard deviation

The standard deviation of the temperature measurement was tested by placing the SCIIB temperature sensor in a controlled environment with a constant temperature. After the temperature of the environment was stabilized, we continuously measured the ambient temperature 100 times. The sensor used in this experiment was a multimode sensor with an effective gauge length of 2 mm and an initial air gap of 5.6 μm. The deviation of the measured data is plotted in Figure 8.6. Based on this data, we conclude that the standard deviation of temperature measurement is σ = 0.0044°C.

8.4.4 White light interferometer temperature sensor

To evaluate the performance of the white light temperature sensor, a type-48000 furnace (Thermolyne Corporation) was used for the temperature test. The temperature range of this furnace is from room temperature to 1200 °C. To increase the resolution of the temperature test, a thermocouple placed beside the FABRY-PEROT temperature sensor was used as the temperature standard. Signals from the thermocouple and the FABRY-PEROT sensor were sampled into the PC synchronously, and a self-developed program was used to evaluate the performance of the temperature sensor.

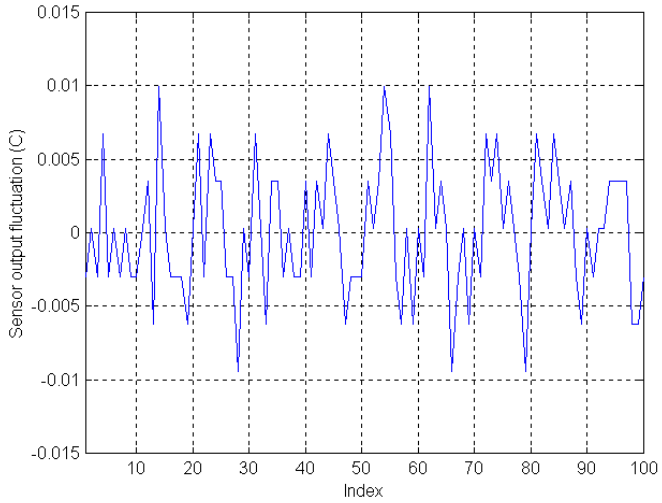

Figure 8.6. SCIIB temperature sensor standard deviation test results.

Figure 8.7 shows a typical testing result of the temperature sensor. While the temperature of the oven increased from room temperature to about 190 °C, the air gap of the sensor head increased from 7 μm to about 16 μm. One difficulty encountered in the temperature testing was the hysteresis effect. In general, a relatively long time period is necessary for the oven to reach a stable temperature. While the heating element is heating, the temperature distribution inside the oven may be large. This induces a hysteresis effect of about 1.5°C between the output of thermocouple and the FABRY-PEROT temperature sensor (Figure 8.8).

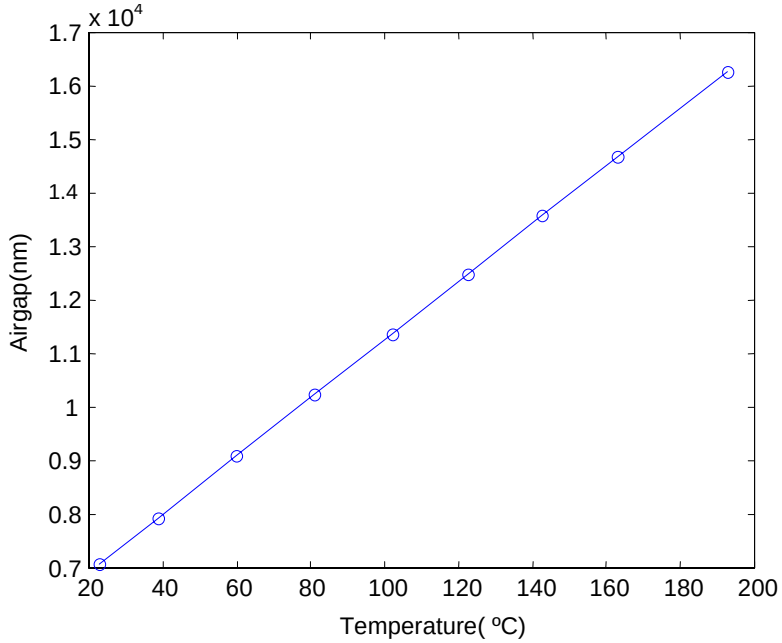

Figure 8.7. Calibration curve of white light temperature sensor.

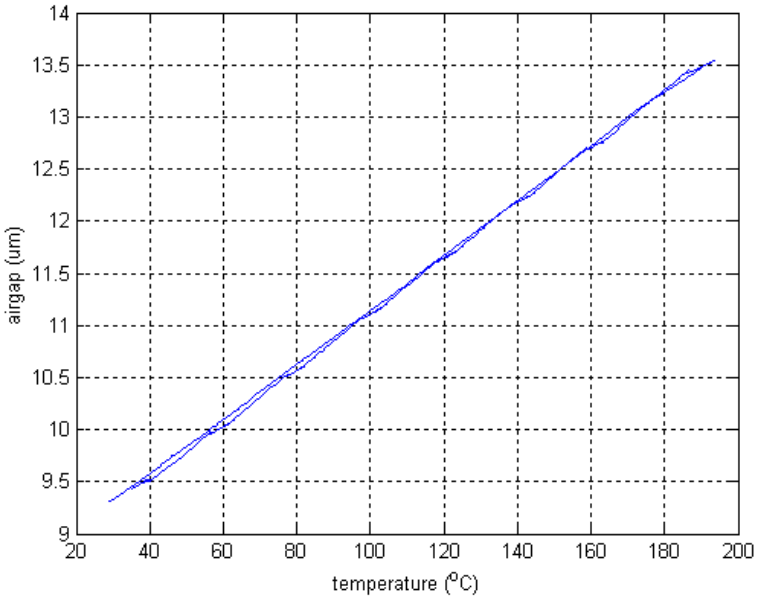

Figure 8.8. Hysteresis effect in temperature measurement.

9.0 Flow Sensors

Monitoring of oil flow velocity in the oil reservoirs with a high accuracy is vitally important for downhole oil exploration and oil recovery applications. Since the FABRY-PEROT sensor scheme has been proven to be effective for highly sensitive and accurate measurement of pressure and temperature, it is thus possible to design flow meters based on the combination of the FABRY-PEROT sensor technology with various mechanical configurations, such as pitot tubes, orifices, thermal dispersion, acoustic dispersion and vortex shedding-induced vibration schemes.

After investigating various flow meter configurations and possible combinations with FABRY-PEROT sensors, the strain-based FABRY-PEROT sensor was chosen for design, fabrication, experimental testing and evaluation to meet the requirements for oil field instrumentation. In this chapter, we report the details of the fiber optic flow sensor system design, fabrication method and test results.

9.1 Flow Sensor Design

Flow rate measurement was achieved by using a Fabry-Perot fiber optic sensor head with the multimode white light demodulating system. Special consideration was given to the requirements for the downhole applications, including temperature stability, high-pressure isolation, high sensitivity, large dynamic range, etc. The basic principle of the self-compensating fiber optic flow sensor is illustrated in Figure 9.1. The system is composed of a sensor probe, optical spectrum analyzer (OSA) for optoelectronic signal processing and a dual core multimode fiber cable linking the sensor probe and the signal-processing unit. The broadband light from two light-emitting diodes (LEDs) is launched into two 3dB 2x2 multimode fiber couplers, which splits each beam into two equal signals. One beam propagates along the lead-in fiber to the sensor head, while the other is terminated at the end-face of one of the coupler's output fibers. The reflected signal from the sensor head also propagates along the same fiber to the same coupler, and then both of the light beams are detected by the fiber optic spectrometer. A multimode white light interferometric spectrum analyzer is used to obtain the flow rate by demodulating the light signal fringes from the detected spectrums.

The configuration of the fiber optic flow sensor head shown in Figure 9.1 is a combination of the broadband white light interferometer and cantilever beam designs. Based on the strain principle of cantilever beams [4], the flow rate can be determined by detecting the air-gap changes from two fiber sensors caused by the bending of the cantilever beam. The sensor head is fabricated by bonding two identical fiber optic tube-based sensors on a cantilever-beam. Each sensor is fabricated by inserting two fibers into a fused silica hollow glass tube. The process is somewhat different from normal tube-based fiber optic sensor fabrication [5],

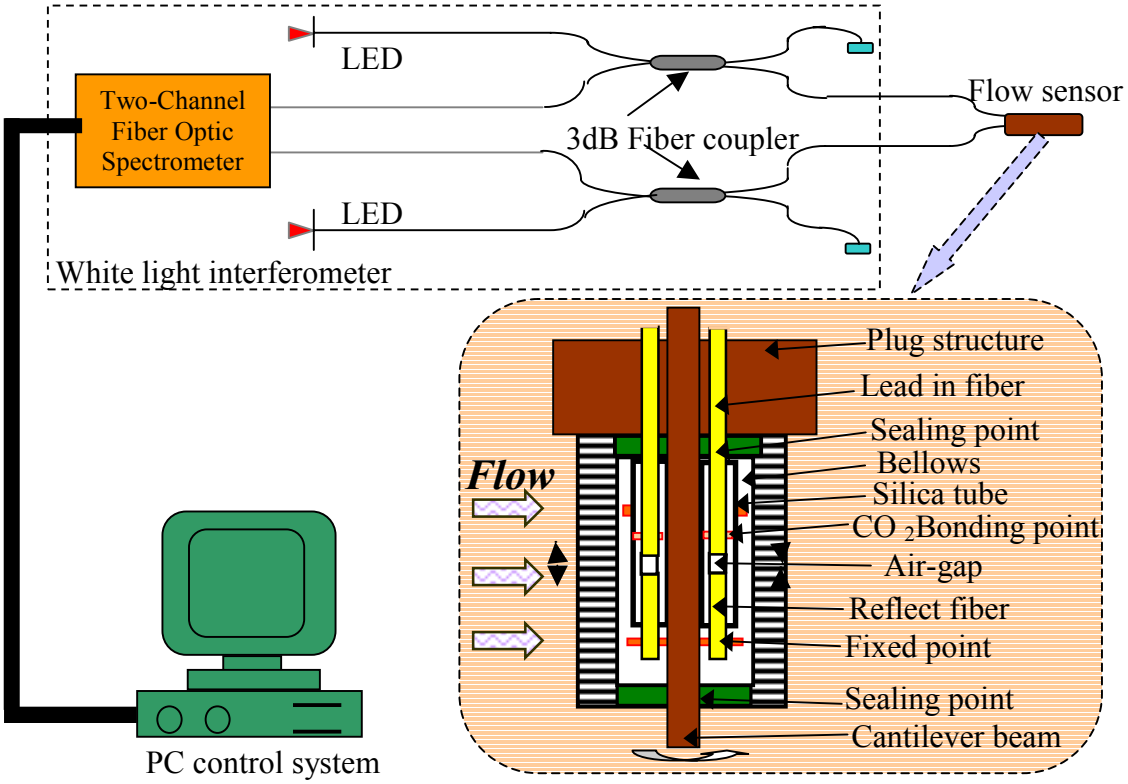

Figure 9.1. Fiber optic flow sensor system.

because while one end of the capillary tube is thermally bonded to the lead-in fiber, the reflecting fiber is left free to move in the other end of tube. Therefore, an air gap is formed between the two cleaved fiber end faces. The sensor fabrication process is then repeated for the other side of the beam. Both ends of the tube and both reflecting fibers are firmly bonded to the metal cantilever beam at a predetermined gauge length. This allows the air gap to change freely without restriction by the capillary tube and only related with the changes in bending of the cantilever beam caused by the flow rate of the fluid. This dual sensor combination is then inserted into the central hole of a metal tube or plug, which allows easy installation of the sensor plug into the flow pipes for measurement. Finally a small metal bellows is used to cover the beam and sensors. This bellows allows the flow to bend the cantilever beam located inside without allowing the fluid to contact the cantilever beam or sensors. In this manner, the sensor can be isolated from the fluids (which may be corrosive) in the outside environment. When the fluid flows past the sensor, the cantilever beam will be bent by the force caused by the momentum of the fluid passing the beam.

When a fluid impinges on the beam, all its momentum can be considered converted into force, which can be expressed as

$$F \times t = m \times v \qquad (9\text{-}1)$$

where F is the force on the cantilever, t is the unit of time, v is the velocity of the fluid, and m is the quantity of the passing fluid within the unit time. These quantities are related as follows.

$$\begin{cases} m = \rho \times V \\ V = S \times v \times t \\ S = c \times L \end{cases} \quad \textbf{(9-2)}$$

where ρ is the density of the fluid, V is the volume of flow in unit time; S is the area of the cantilever beam, c is width of cantilever, d is thickness of cantilever, L_b is the length of the cantilever beam. From Eq. (9-1) and (9-2) the applied force per unit time t is:

$$F = \rho \times c \times L_b \times v^2 \quad \textbf{(9-3)}$$

Suppose F is a uniform force, the maximum strain ε will be at the fixed end of the cantilever

$$\varepsilon = \frac{6FL_b}{Ecd^2} \quad \textbf{(9-4)}$$

where E is theYoung's modulus. When the flow passes by, because each of the sensor's free fibers are bonded to cantilever, bending of the beam will be manifested as an air gap change. The air gap variation caused by the gauge length change ΔL between the two bonding points can be represented as

$$\Delta L = \varepsilon \times L \quad \textbf{(9-5)}$$

where L is the gauge length between two bonding points. Then from Eq. (9-2) to (9-5), we obtain

$$\Delta L = \frac{6\rho v^2 L_b{}^2 L}{Ed^2} = \beta(v) \quad \textbf{(9-6)}$$

where β denotes the relationship between the air-gap change ΔL and the velocity of the flow v.

When the cantilever-beam bends due to the flow of the fluid, the air-gap of the sensor on the side facing the fluid flow will increase, while the air-gap of the sensor located on the opposite side of the cantilever beam will decrease. For a given material, the volume compressibility and thermal expansion should be approximately linear for small pressure and temperature changes. Therefore, when fluid passes by the sensor, the air gap of both sensors will change but in opposite directions. However, both sensors will have the same magnitude and direction of air gap change due to the temperature and pressure changes:

$$\begin{cases} \Delta L_1 = a_1 \Delta T + K a_1 \Delta P + \beta_1(v) \\ \Delta L_2 = a_2 \Delta T + K a_2 \Delta P + \beta_2(v) \end{cases} \quad \textbf{(9-7)}$$

where ΔL_1, ΔL_2 represent the gauge length changes of the two sensors, α_1, α_2 are the temperature effects of the two sensors, K is the relationship between the effects of thermal extension and pressure extension, and β_1, β_2 refer to the flow coefficients of the two sensors as shown in Eq.(9-6). We can cancel the effects from temperature and pressure based on the

above equations to obtain the relationship F between the flow rate and system output based on the two air-gap changes.

$$F(v) = a_2 \Delta L_1 - a_1 \Delta L_2 = a_2 \beta_1(v) - a_1 \beta_2(v) \qquad \textbf{(9-8)}$$

From Eq. (9-8), we can see that by analyzing the outputs of the two sensors, this sensor system can detect the applied flow velocity while being insensitive to pressure and temperature changes by automatically compensating for temperature and pressure effects. If we select the cantilever-beam to be brass with $E = 4.2 \times 10^{10}$ kg/m^2, $L_b = 25mm$, $c=5mm$, $d=0.5mm$, and the two fiber sensors with gage length of $L=20mm$, original air gap of a= $12.00mm$, then the relationship between the air gap changes and the applied flow velocity can be calculated as shown in Figure 9.2. According to this simulation, we can see that when the cantilever beam temperature is changed, both the front and back sensor air gaps are affected, causing the relationship between sensor output and the applied flow rate very repeatable, which illustrates that the sensor can compensate for temperature automatically.

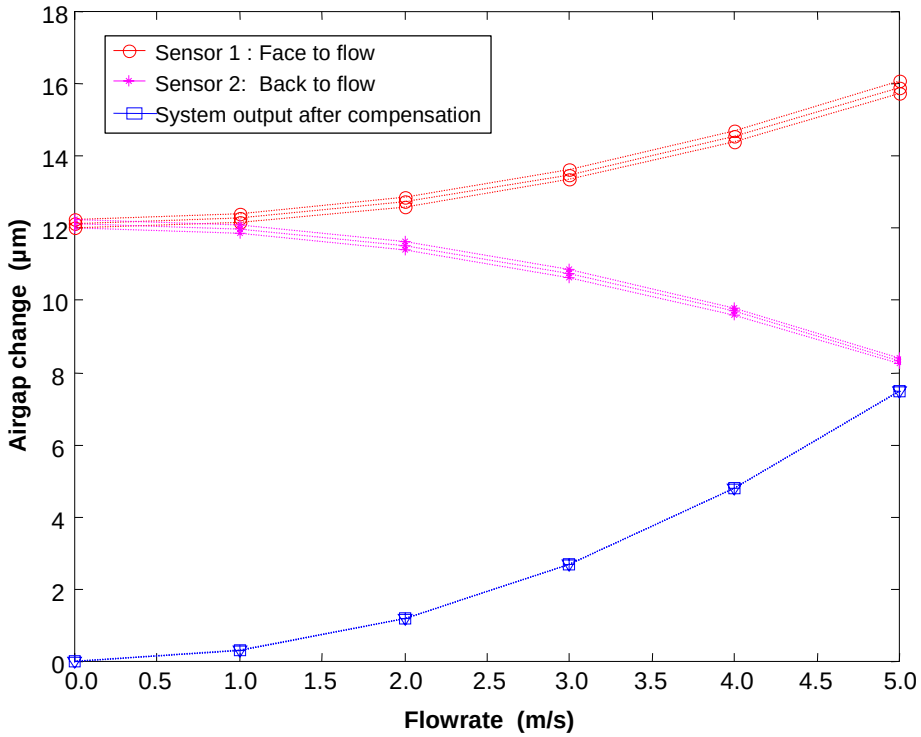

Figure 9.2. Simulation of flow sensor self-compensation.

In industrial practice, flow measurements are usually used to obtain the flow rate rather than the flow velocity, so the related cross sectional area of the flow pipes must be added to Eq. (9-8) to obtain the relationship between the air gap changes and flow rate. It is also possible that the relationship between air gap changes and flow velocity will differ from the theoretical value due to materials processing and fabrication techniques, but these factors can all be combined within Eq. (9-8) and will be adjusted for during system calibration.

9.2 Flow Sensor Construction

The prototype flow sensor system was constructed as shown in Figure 9.1. A dual channel white light interferometer system was used for optoelectronic signal processing. Two Honeywell 4854 LEDs with center wavelengths around 850nm pigtailed with standard 50/125 multimode fibers were used as broadband light sources. A PC-2000 dual-channel fiber optic spectrometer from Ocean Optics, Inc. was used to detect the optical signals from the sensor head, and its output fed to the flow rate measurement control system based on a multimode white light interferometric spectrum analyzer.

The analysis described in the previous section provides a clear guide to the design of the fiber optic sensor for flow detection. The fabrication technique was gradually improved through experience after making many sensor heads. Due to Invar's low coefficient of thermal expansion (CTE) (1.05×10^{-6}/ºC), which is much lower than most conventional metals and closer to fused silica [6], an Invar sheet from Electronic Space Products International, Inc was selected for the cantilever-beam and cut, polished and annealed. The inner diameter of the hollow fused quartz tubing was chosen to be 132mm, which limits the movement of the multimode fiber (125mm) to 5mm. PN-231 regular Nickel bellows from *Servometer, Inc*. were used for the packaging of the flow sensor. The size of the Invar cantilever beam was selected as 3mm × 30mm. Based on the working range and resolution of the multimode white light system [7], the thickness of the invar sheet, the gauge lengths and the original air-gaps of both fiber sensors were adjusted to maximize the visibility of both sensors through the complete measurement range. Also the gauge length was selected to be as small as possible to decrease the inherent thermal expansion. In fiber fabrication, the initial air gap between both fiber end-faces was adjusted to obtain the highest interference fringe visibility. The fabrication process is shown in Figure 9.3a and b; the photograph of the finished flow sensor is shown in Figure 9.3c; the sensor plugged into its fitting for testing or measurement is shown in Figure 9.3d. Both the lab-scale testing and field-testing have been performed to evaluate the prototype flow sensor system, as described in the following sections.

9.3 Lab-Scale Experiments and Results

Evaluation and testing of the flow sensors is necessary to improve the flow sensor design and fabrication. The lab-scale test system was set up as illustrated in Figure 9.4. This experimental set-up includes a FT-24NENW turbine flow meter, purchased from *Flow Technologies Inc.* For 1-1/2" pipe sizes, the custom ordered calibration flow rate range is from 1.6 to 90 GPM, the repeatability is ±0.05% of the full range, and the linearity is ± 0.5% of reading. A ¼ HP *Wayne* submersible utility pump was used to drive the water through the PVC pipes; with 1-1/2"pipe, the maximum flow rate should be 18.5GPM. A *DPF700* meter from *Omega, Inc* was ordered with a RS-232 option board to connect to a laboratory computer for preliminary flow rate testing. Both the fiber optic sensor and the thermometer were put into the testing pipes, and the pumped flow rate adjusted by changing the input of the electrical pump. Both the flow sensor output and the flow meter output were recorded for comparison. The testing system at CPT is shown in Figure 9.5.

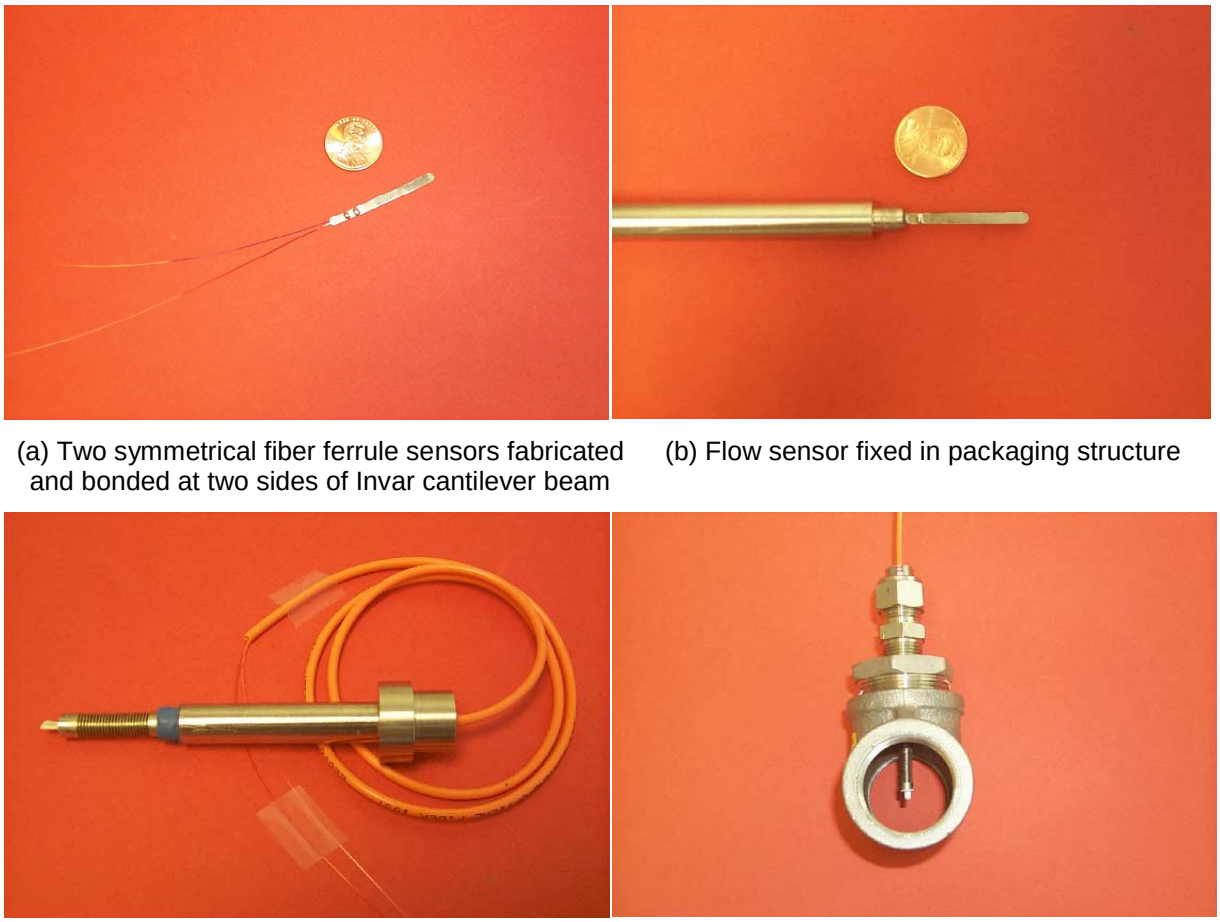

(a) Two symmetrical fiber ferrule sensors fabricated and bonded at two sides of Invar cantilever beam

(b) Flow sensor fixed in packaging structure

(c) Prototype fiber optic flow sensor

(d) Flow sensor fixed into T-fitting

Figure 9.3. Fabrication of flow sensor.

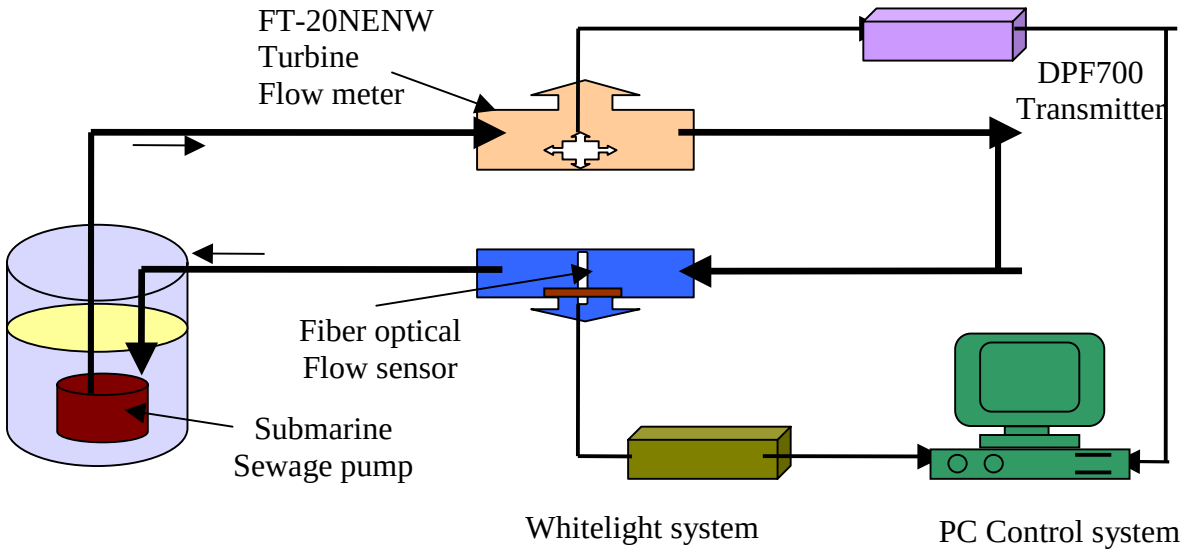

Figure 9.4. Lab-scale flow testing system setup.

(a) Lab-scale flow testing system loops

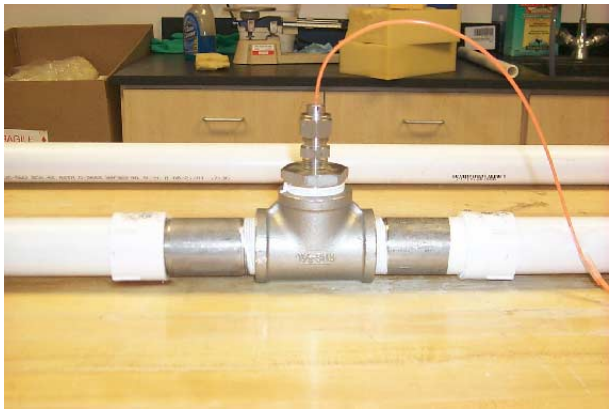

(b) Flow sensor deployed in testing

Figure 9.5. Flow sensor testing setup in Center for Photonics Technology, Virginia Tech.

Using this testing system, numerous experiments have been outperformed to evaluate the performance of the designed flow sensor system. The normal test temperature range was from 18~45°C with normal atmospheric pressure. The results shown below were obtained using the fiber optic flow sensor whose parameters are shown in Table 1.

Table 9.1. Parameters of fiber optic flow sensor used for lab scale testing.

Fiber type:	Multimode 50/125
Cantilever beam material:	Invar sheet
Cantilever beam size:	0.010"*1.5*0.13"
Original air gaps of two sensors:	9.211μm; 8.810μm
Original visibility of two sensors:	67%; 69%
Gauge length of two sensors:	1.8mm; 2 mm
Relative temperature coefficients:	0.9; 1
Sensor protection:	Flexible Ni-bellows

9.3.1 Sensor calibration

Sensor calibration is very important for sensor evaluation and application. It is usually conducted by applying known flow rates within its operating range to obtain the calibration curve, or one-to-one relationship between the original sensor output and the applied flow rate, which can be stored in the host computer and later used to convert sensor output to the flow rate reading. To ensure the calibration accuracy, the flow rate was held at each step for about three minutes before moving to the next step during the calibration process. By averaging the output of both the flow meter and flow sensor at each step, errors can be minimized. The original data is shown in Figure 9.6. Because the temperature effect coefficients (TEC) were determined by testing prior to sensor calibration (Table 9.1), Eq. (9-

1)~(9-3) were used to cancel the temperature effects. The compensated output is shown in Figure 9.6 and used to obtain the flow sensor calibration curve shown in Figure 9.7. In general, the calibration curve was obtained by taking the average of several consecutive sets of calibration data to further ensure the calibration accuracy and to generate the coefficients of calibration.

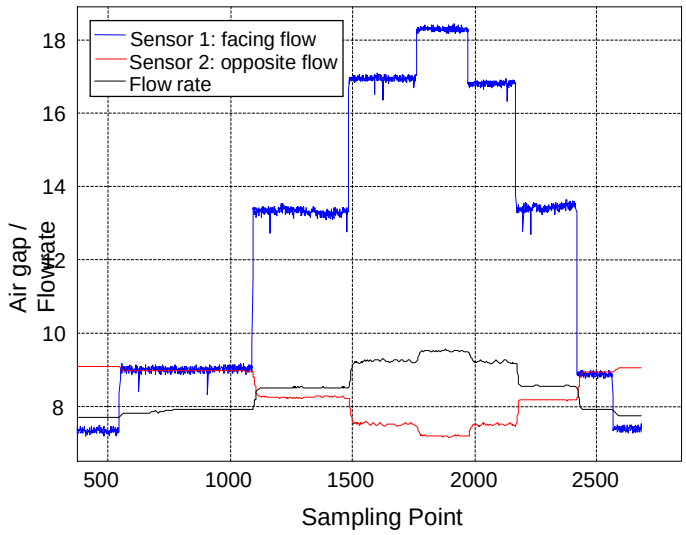

Figure 9.6. Relationship between flow rate and flow sensor air gaps.

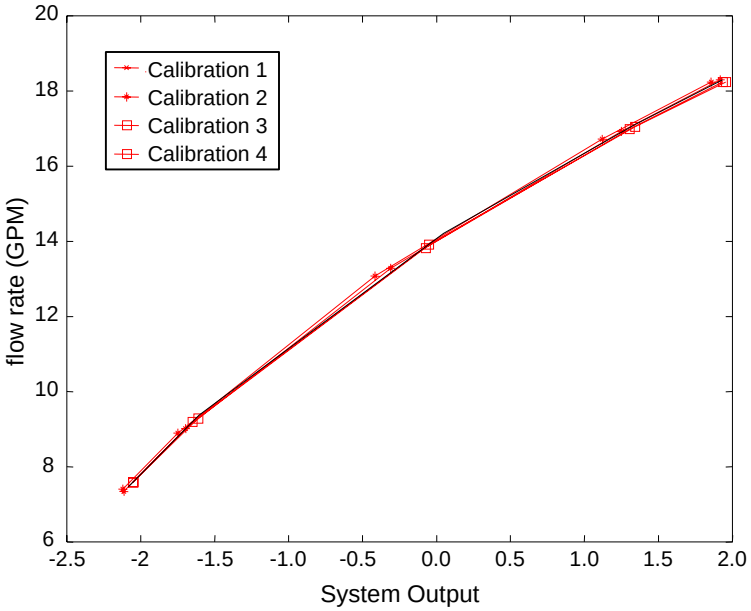

Figure 9.7. Flow sensor calibration curve.

9.3.2 Temperature compensation

Temperature dependence is critical for flow sensors used in oil field environment. It is a great challenge to design a flow sensor to have minimum (ideally zero) temperature dependence. With the self-compensation design as described in Section 2, it is possible, in theory, to have very small or even zero temperature sensitivity. Figure 9.8 shows the temperature independence characteristic of the flow sensor. Even though the environmental temperature changes from 23ºC (squares) to 45ºC (stars), the output of the fiber flow sensor matched the applied flow rate with high repeatability, indicating that this sensor design can compensate the temperature changes automatically, consistent with the theoretical analysis.

9.3.3 Measurement results

Using the calibration curve or coefficients, the fiber optic sensor was used for flow rate measurement and the results compared with the flow rate output from FT-24NENW flow meter in Figure 9.9.

9.3.4 Repeatability

Sensor repeatability can be determined by applying a preset flow rate repeatedly from one direction (increasing or decreasing). The largest difference in the sensor output readings can be used to specify the repeatability of the sensor. Under different water temperatures, four measurements up to the full operating range of the sensor were performed with the results shown in Figure 9.10a. For comparison purposes, the original calibration data is also shown. The deviation of the two measurements with respect to the calibration data is plotted in Figure 9.10b. The maximum deviation between the measured pressure and the calibrated pressure was within ±0.3GPM. The normalized repeatability of the sensor system with respect to its dynamic range was therefore ±1.62% of the full scale. This test also demonstrates that this sensor design can effectively compensate for temperature influences.

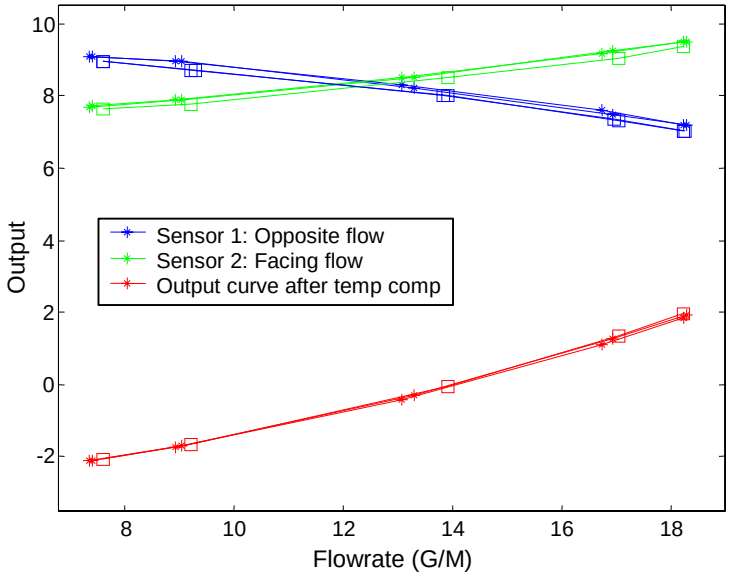

Figure 9.8. Fiber optic flow sensor self-compensation result.

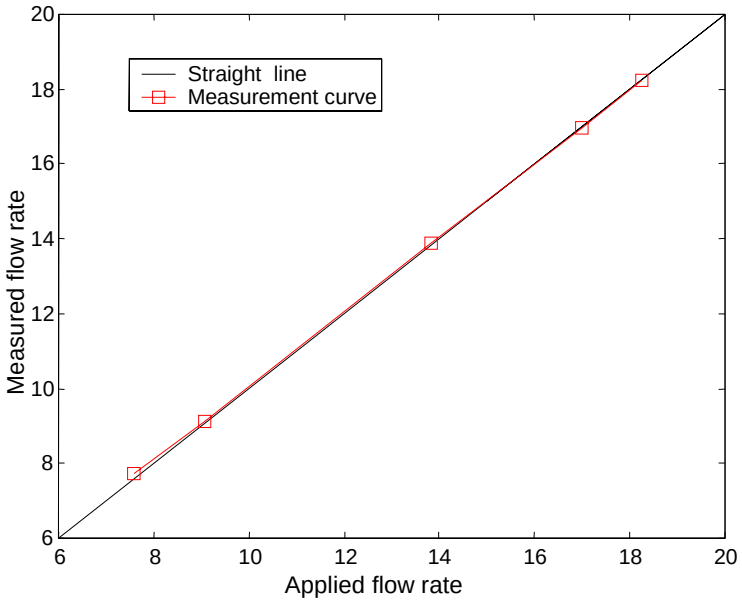

Figure 9.9. Flow sensor system calibration lines.

9.3.5 Dynamic flow measurements

To demonstrate the sensor's dynamic response, the calibrated flow sensor was tested under dynamic flow conditions. The reference flow signal was provided by the FT-24NENW Turbine flow meter. Comparison of the output of both the fiber optic flow sensor and flow meter shown in Figure 9.11 reveals that the fiber optic sensor matches the turbine flow meter very well.

9.3.6 Resolution of flow rate measurement

The resolution of a sensor system is usually interpreted as the standard deviation of a series of flow measurements. It is common to use twice the standard deviation as the direct measure of resolution. Evaluation of the flow sensor resolution was performed using a calibrated sensor. The sensor was placed in the testing pipe and the data from the test system was sampled at a rate of 60 samples per second for one minute, which should be sufficient compared to the system's frequency response of 10Hz. The flow rate measurement outputs within the one-minute sampling period are plotted in Figure 9.12. The standard deviation of the flow data within this time period was calculated to be σ=0.0097GPM. Therefore the resolution of the sensor system was estimated to be 2σ=0.0194GPM. The normalized resolution with respect to the dynamic range of the system was 0.11% of full scale.

9.3.7 Hysteresis of flow rate measurement

The hysteresis of the flow sensor can be measured by cycling the applied flow between the minimum and the maximum of the operating range in both increasing and decreasing directions. The hysteresis can be calculated as the largest difference between the output readings of the pressure cycles. Experiments were conducted to evaluate the actual hysteresis

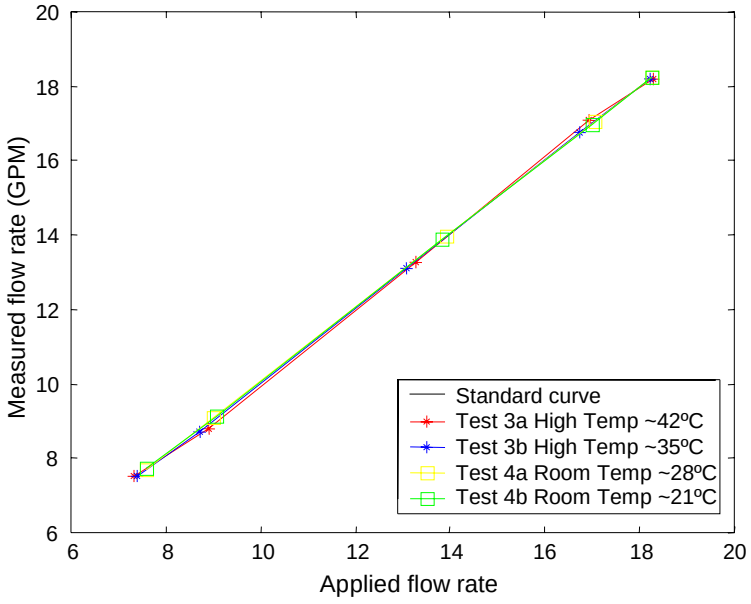

(a) Flow measurement repeatability results.

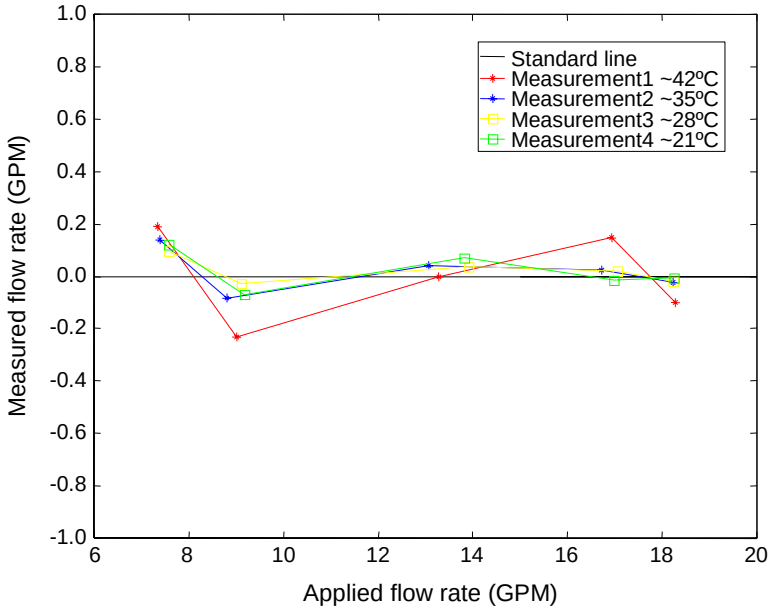

(b) Deviation of the measured flow with respect to the calibration data.

Figure 9.10. Flow measurement repeatability test results.

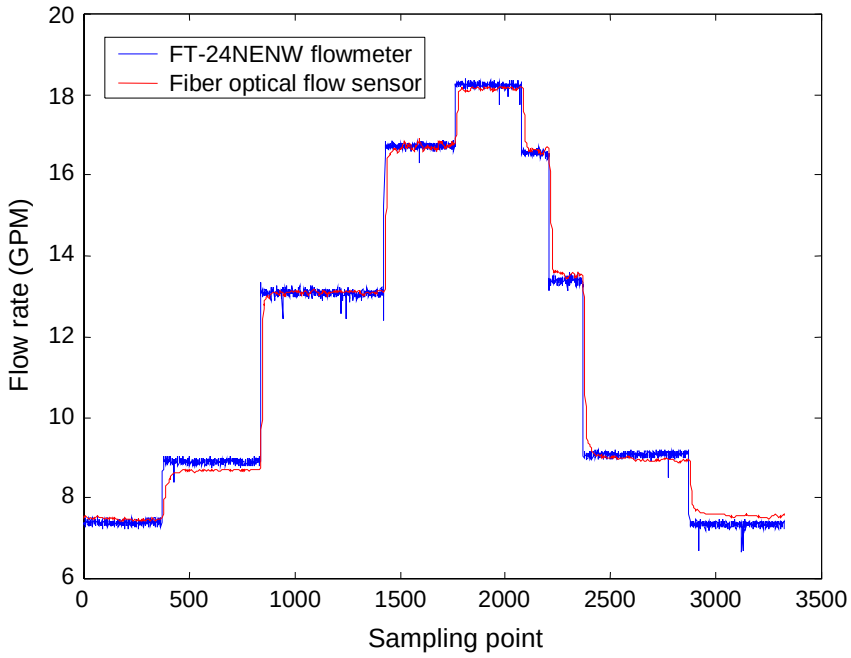

Figure 9.11. Dynamic response of flow sensor.

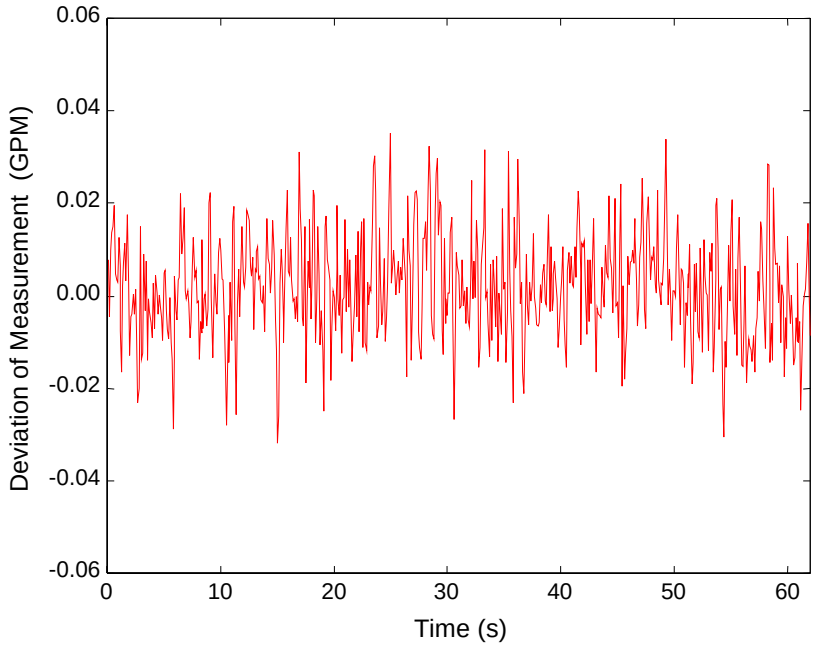

Figure 9.12. Resolution of flow sensor system.

of the flow sensor probe. The evaluation was conducted using the same flow testing system after the sensor system was calibrated. The applied flow was first increased to the maximum operating range of 18.5GPM, and then decreased after it was maintained at 18.5GPM for 30 minutes. The experimental results shown in Figure 9.13 demonstrate that the hysteresis of the full operating range is less than 1.35%.

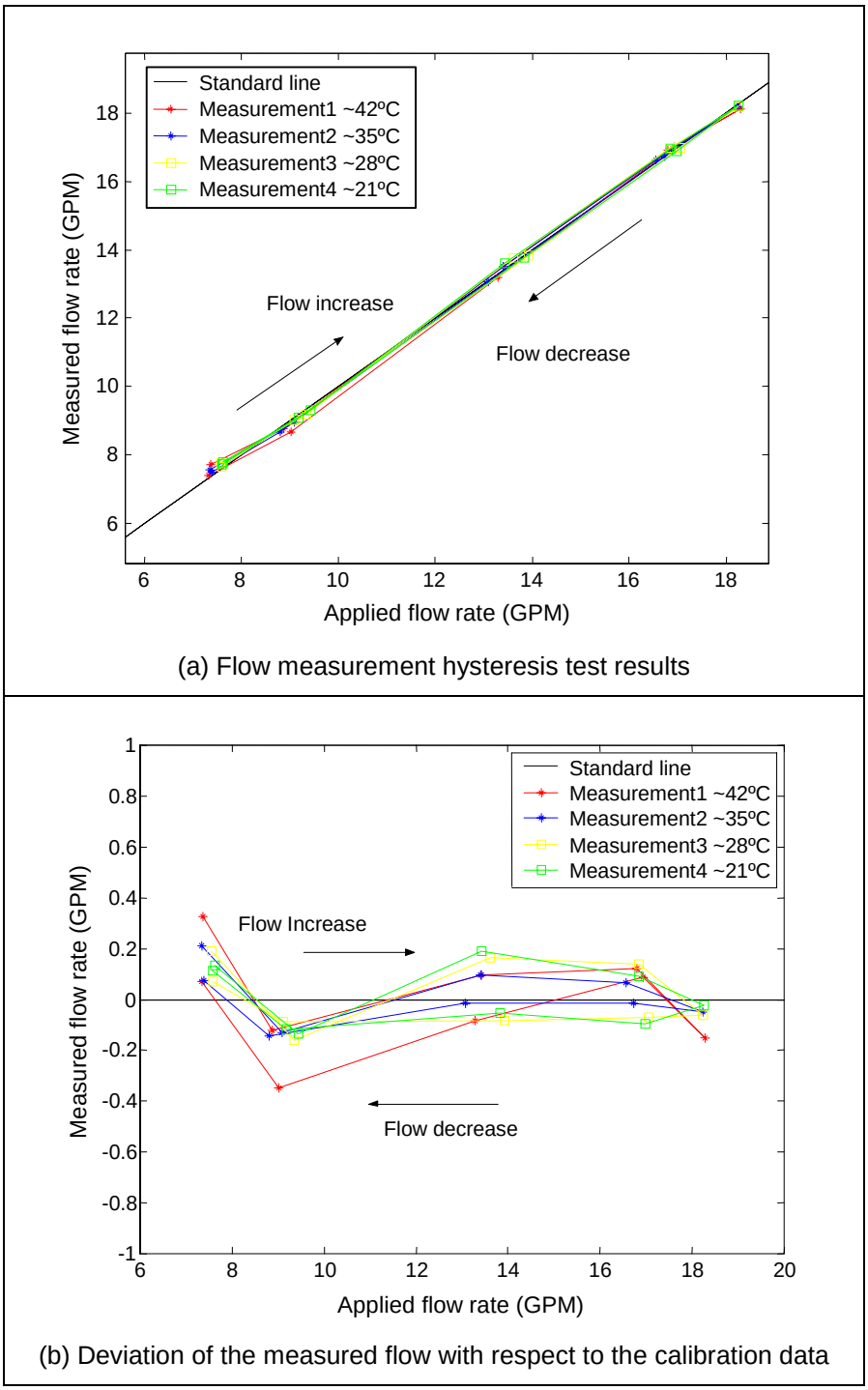

Figure 9.13. Hysteresis of flow sensor in lab-scale testing.

9.3.8 System stability test

The same flow sensor was also used to test the system stability. The sensor was kept in the flow-testing loop for 12 hours while the flow was maintained at 7.2GPM. The data acquisition system was programmed to sample the sensor's output every 10 seconds. The test results are shown in Figure 9.14. Processing the data revealed that the maximum peak-to-peak pressure variation within the 12-hour time period was 0.35 GPM. The data also showed that the output from FT-24NENW flow meter exhibited many discontinuities and fluctuations, which limited the evaluation of flow sensor performance. Thus we believe that the maximum variation was less than 1.89% of the full dynamic range.

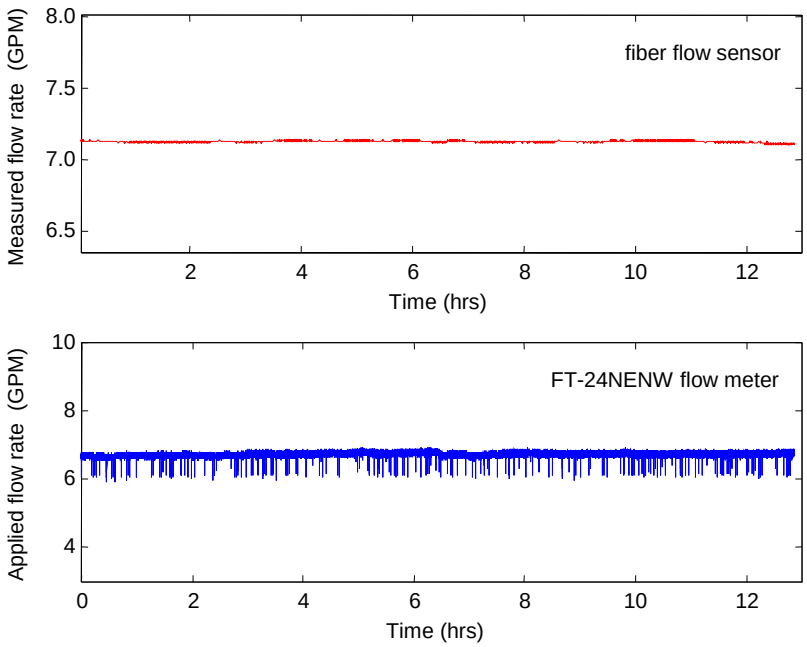

Figure 9.14. Flow sensor system stability test over 12 hours at 7.2 GPM.

10.0 Acoustic Sensors

Acoustic (or seismic) signals are another very useful piece of information in downhole oil recovery. An acoustic wave propagating in the oil reservoir can generate a pressure signal (generally small in amplitude) that can be detected using a fiber optic sensor with a high sensitivity to pressure fluctuations and a high frequency response. In this chapter, the design and implementation of the acoustic sensors is presented.

10.1 Principle of Operation

The basic principle and configuration of the diaphragm-based fiber optic acoustic sensor can be illustrated using Figure 10.1. The system consists of a sensor probe, a light source, an optoelectronic signal processing unit, and an optical fiber linking the sensor probe and the signal-processing unit. As shown in the enlarged view of the sensor head, the input fiber and the thin silica glass diaphragm are bonded together in a cylindrical silica glass tube to form a Fabry-Perot sensing element.

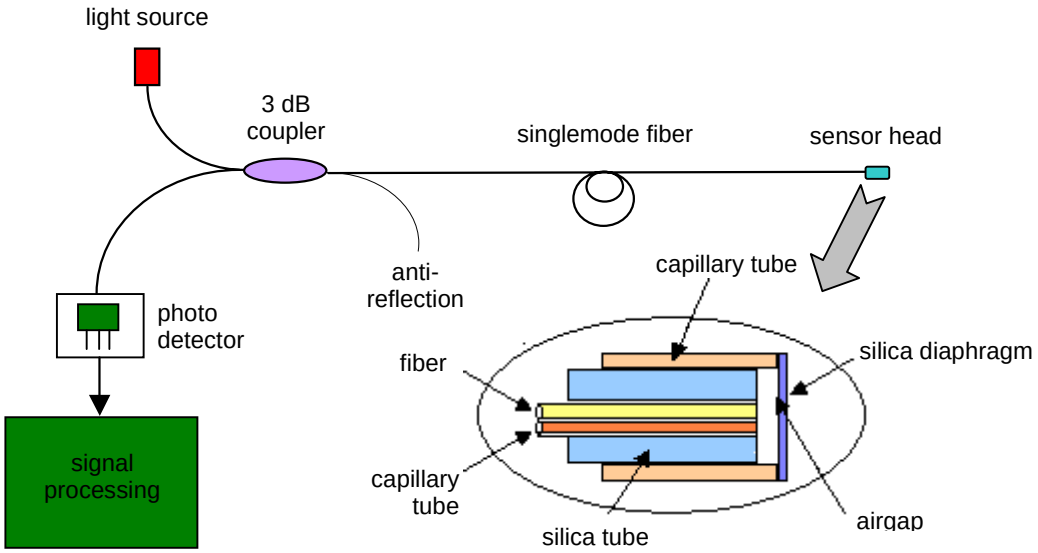

Figure 10.1. Illustration of the principle of the diaphragm-based fiber optic acoustic sensor.

The small pressure generated by an acoustic signal causes a deformation of the diaphragm and modulates the sealed air gap length. Similar to other interferometers, the acoustic fiber optic measurement exhibits very high sensitivity. As discussed previously, the measurement would suffer from the disadvantages of sensitivity reduction and fringe direction ambiguity when the sensor reaches peaks or valleys of the fringes. Therefore the dynamic range of the sensor is controlled through the sensor design and bonding technique used to fabricate the acoustic sensor so that the sensor operates only over the linear range of a half fringe,

corresponding to roughly a quarter fringe. As shown in Figure 10.2, the initial operating point is chosen to be at the center point of the interference fringe, and the thickness of the diaphragm is designed in such a manner that the imposed acoustic signal only deforms the thin diaphragm within the linear part of the sensor response curve. Therefore the sensitivity reduction and fringe direction ambiguity problems can be completely avoided.

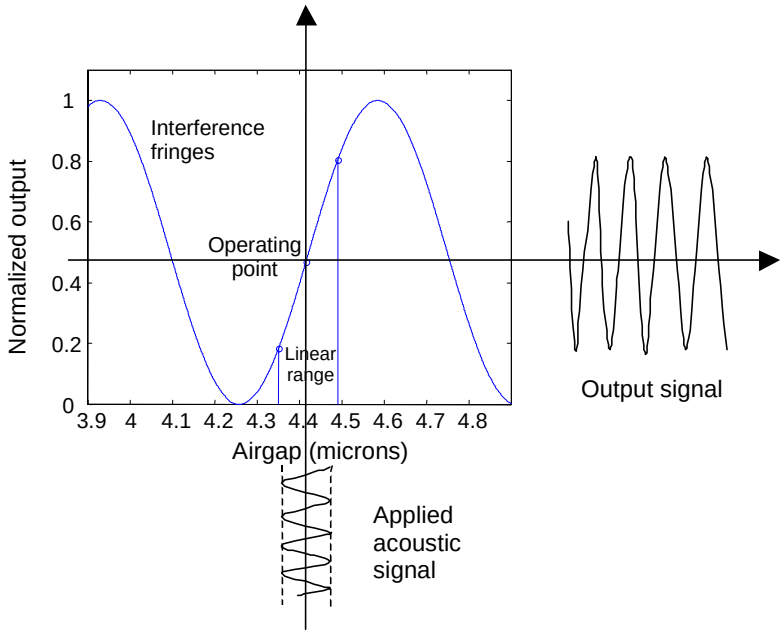

Figure 10.2. Illustration of a linear operating range of the sensor response curve.

It deserves special mention here that parallel to the fiber, a capillary tube placed through the inner hole of the ferrule is used as a pressure filter to transfer the pressure effect between the cavity and the outside. This acts as a mechanical high pass filter such that slowly varying pressure signals do not affect the diaphragm displacement. The reason is that the capillary tube is open to the outside environment. As the pressure outside the sensor increases, the pressure inside the sensor slowly equilibrates through the capillary tube. Because the inner diameter of the capillary tube is small, high frequency signals such as the acoustic signal have pressure cycle variations that are too fast for the capillary tube's small diameter allow equilibration. Therefore, the capillary tube "screens out" the slowly varying pressure cycles. This is particularly useful in the downhole environment where the pressures can become quite high and yet the acoustic signal pressure is so low.

10.2 Sensor Frequency Response and Sensitivity Design

We can use the structure shown in Figure 10.3 to model the acoustic sensor. The diaphragm vibrates in the presence of an acoustic wave as it imposes a dynamic pressure on the diaphragm. It is very important to design the sensor head to ensure high enough frequency response and sensitivity to achieve optimum detection of the acoustic signals.

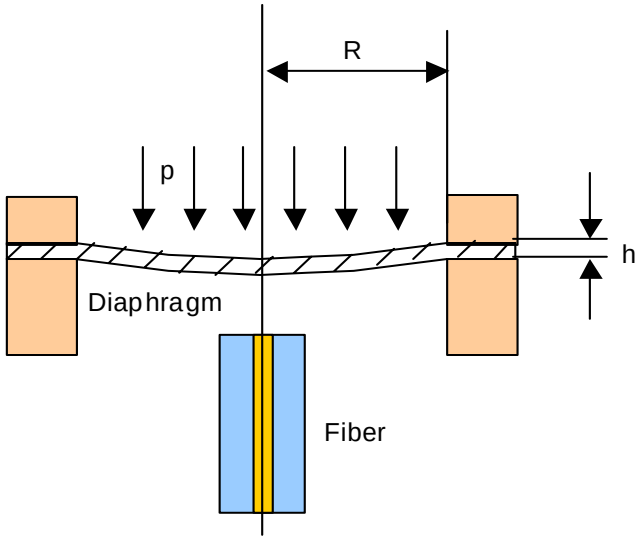

Figure 10.3. Structure model for diaphragm-based acoustic sensor.

The frequency response of the sensor is limited by the natural frequency (f_n) of the diaphragm. The natural frequency can be calculated by the following equation [8]:

$$f_n = \frac{\alpha}{2\pi R^2} \times \sqrt{\frac{Dg}{hw}}, \qquad \textbf{(10-1)}$$

where α is a constant related to the vibrating modes of the diaphragm, and takes a value of 10.21 for the fundamental mode; R is the effective radius defined by the inner diameter of the silica sensor glass tubing; h is the thickness of the diaphragm; g is the gravitational constant; w is the specific weight of the diaphragm material (for fused silica at 25 C°, 2.202×10^3 kg/m^3); and D is the flexural rigidity of the diaphragm defined by

$$f_n = \frac{\alpha}{2\pi R^2} \times \sqrt{\frac{Dg}{hw}}, \qquad \textbf{(10-2)}$$

where μ is the Poisson's ratio (μ = 0.17 for silica glass material at 25°C); E is the Young's modulus of the silica glass material (E = 73.73 GPa or 7.49×10^9 kg/m^2 at 25°C); The frequency response of the sensor can thus be calculated by combining Eq. (10-1) and (10-2) into

$$f_n = 2.749\times10^9 \frac{h}{R^2} \text{ (Hz)}, \qquad \textbf{(10-3)}$$

where h and R are in microns. As indicated by Eq. (10-3), the frequency response is proportional to the thickness of the diaphragm and inversely proportional to the square of the effective diaphragm radius. If we choose a diaphragm with an effective radius of R=1mm, we can plot the predicted frequency response of the sensor as a function of diaphragm thickness as shown in Figure 10.4. So for a 100 μm-thickness diaphragm, the theoretical natural frequency response in air should be 274.9kHz. So any acoustic signals under this frequency can be detected by this diaphragm-based sensor.

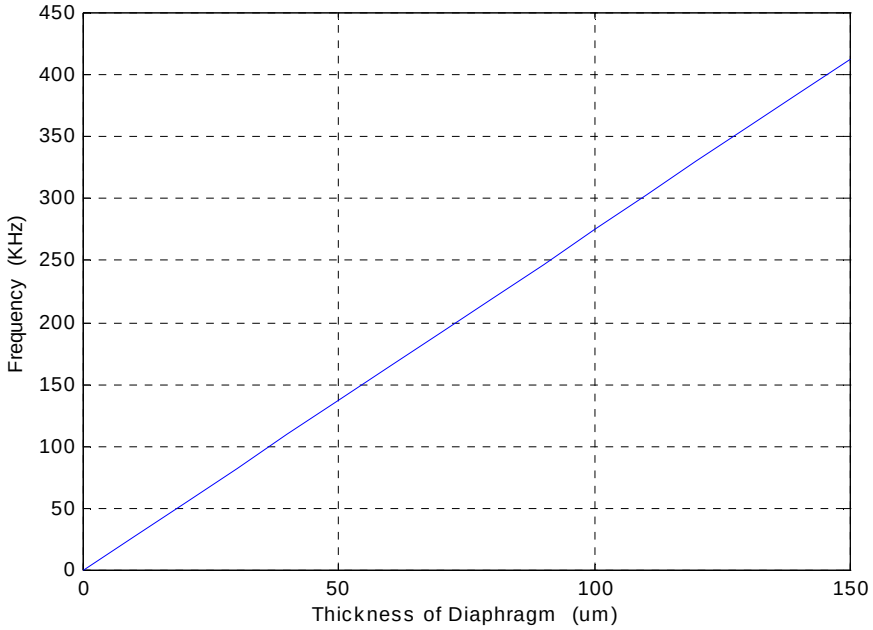

Figure 10.4. Predicted frequency response of the sensor at *R=1*mm.

The diaphragm will be deflected when there is a differential pressure p between the inside and outside of the sealed cavity. The out-of-plane deflection of the diaphragm y as a function of the pressure difference at any radial position r is given by [8]

$$y = \frac{3(1-\mu^2)p}{16Eh^3} \times (R^2 - r^2)^2 . \qquad \textbf{(10-4)}$$

In our sensor configuration, the fiber is positioned in the central part of the diaphragm so that only the center deflection y_0 is of interest, which is given by

$$y_0 = 1.71 \times 10^{-8} \frac{R^4}{h^3} p , \qquad \textbf{(10-5)}$$

where again, y_0, R and h are all in microns, and p is in pounds per square inch (*psia*). From the above equations, it is evident that the sensitivity of the sensor can be designed to fit different application requirements either by choosing diaphragm materials with different μ and E or by changing the geometric parameters of the sensor head with the desired effective diaphragm size R and thickness h. In general, a diaphragm with a larger radius and a smaller thickness will yield a higher sensitivity to the detection of the acoustic signals. However, as indicated above, the operating range of the acoustic sensor head needs to be limited within the linear range, which is a fraction of an interference fringe in order to avoid the sensitivity reduction and fringe direction ambiguity problems. This imposes a limitation on the thickness of the silica diaphragm. Figure 10.5 shows the sensor response with R=1mm, as predicted by Eq. (10-5). For a 100μm thick diaphragm, the theoretical pressure sensitivity in air should be 0.017um/psi.

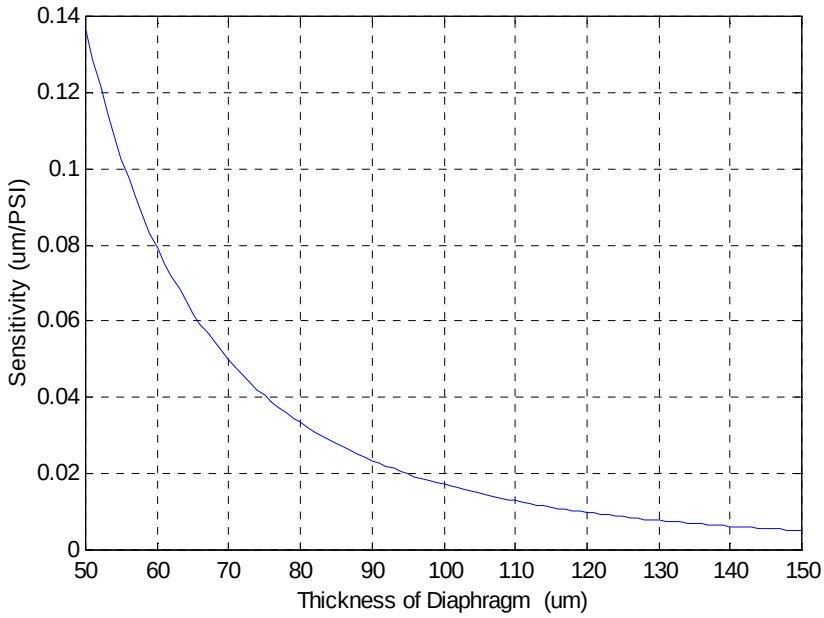

Figure 10.5. Theoretical sensor response (μm/ psi) versus diaphragm thickness at *R*= 1mm.

10.3 Acoustic Sensor Fabrication

As discussed in Chapter 7, the pressure sensor head is fabricated by bonding a silica fiber, ferrule, tube and diaphragm together to form an interferometer with a sealed cavity. To achieve high temperature stability, a uniformly strong bond is necessary among these four components. There are several challenging requirements in the acoustic sensor fabrication. First, the fabricated sensor should have an initial air gap allowing the sensor operating point to be located in the center of the linear part of an interference fringe. This requires precise air gap control and adjustment during the sensor fabrication. Second, the sensor operation requires a stable operating point to eliminate the sensitivity degradation and phase ambiguity problem. Therefore, the components used to make the acoustic sensor need to be made of the same or closely matched material so that the thermal stability of the sensor is ensured. Third, the sensor is intended to be used in the downhole environments; therefore for hydraulic deployment, the overall size of the sensor needs to be very small. To satisfy those special requirements, we investigated several sensor fabrication techniques including the epoxy-based sensor fabrication, the solder bonding method, and the controlled thermal bonding method. Although the first two methods appear to be relatively easy, the sensor performance doesn't satisfy the requirements. We therefore focused our research effort on the third method: controlled thermal bonding techniques

10.3.1 Epoxy-based sensor fabrication

The white light fiber interferometric system was used to monitor the change in air gap in the sensor head. Because the tunable laser is used as the light source, the original air gap of the sensor can be selected at any effective value to ensure that the sensor head will have sufficient visibility to detect the acoustic waves. The fabrication steps include 1) polish the

end of singlemode optical fiber, silica ferrule and silica tube separately; 2) place the diaphragm above the flat endface of the tube and bond them with Epoxy-907; 3) place the fiber and the capillary tube at the same time through the silica tube; ensure that the end faces of extend out of the ferrule, then bond them together; 4) when both are dry after the solidification time, place them into the silica tube, adjust the distance between the fiber's endface and diaphragm carefully to obtain high visibility, and bond the diaphragm when a suitable interference air gap is found using Epoxy-907. The air gap and visibility of the sensor head will change during the solidification, but usually by adjusting the laser wavelength of the tunable laser, a suitable air gap can still be found.

10.3.2 Direct thermal bonding method

The mechanism on which the direct thermal bonding method is based is similar to that of the SCIIB sensor bonding.. When using thermal bonding for sensor fabrication, it is very important to have precise temperature control. Temperatures that are too high could warp or melt the material and damage the structure of the components. On the other hand, temperatures that are too low could result in poor bond strengths.

Using methods similar to the SCIIB sensor fabrication, we use a CO_2 laser as the heating source to fabricate the acoustic sensor because of the small sensor size and the ability to focus the laser output to a small spot. Silica glass materials have very high absorption coefficient at the typical CO_2 laser wavelength (10.6 μm). The optical energy will be transferred to heat, and will raise the temperature, and will eventually reach the softening point of the glass material. The system setup is shown in Figure 10.6. The CO_2 laser, with a maximum output power of 25 W, was purchased from Synrad Inc. Precise control of the CO_2 laser power density (pulseduration and the pulse power) is achieved by a computer controlled D/A circuit and the laser control system. A computer controlled precision stage platform is also used to position the sensor head assembly with respect to the focused CO_2 laser beam.

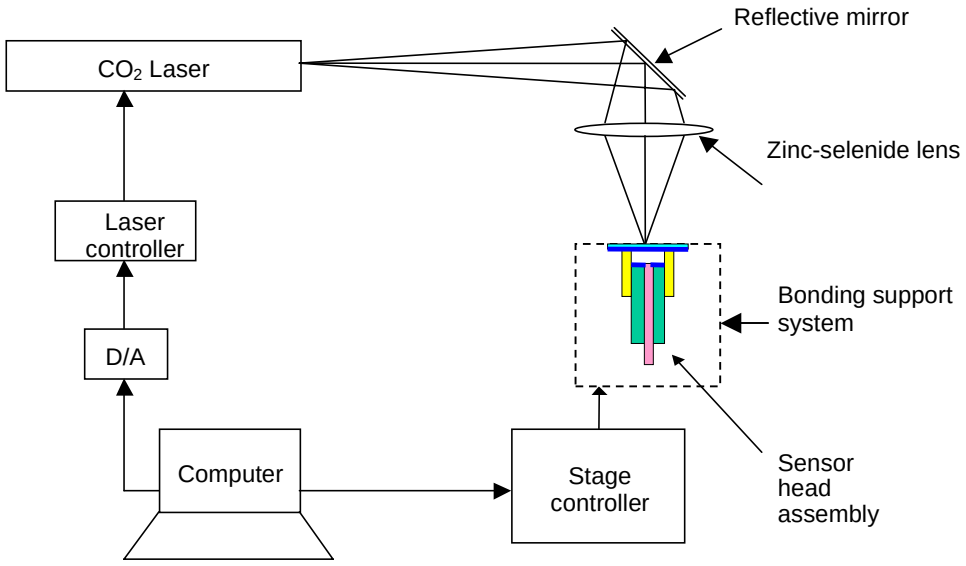

Figure 10.6. Direct thermal bonding diaphragm-based acoustic sensor fabrication system.

10.3.3 Intermediate layer thermal bonding

Previous experience with epoxy-based sensor and solder-based sensor fabrication suggested that a lower softening point material could be used between the two fused silica materials to achieve solid bonding. Borosilicate glass and soda lime glass have much lower softening points than the fused silica glass (1585°C), but higher than the operating temperature of all of the epoxies and most of the solders.

Based on this concept, an acoustic sensor fabrication system was designed using the intermediate layer method. The system configuration is shown in Figure 10.7. A furnace was used as the heating source. The sensor assembly, with the intermediate layer materials applied to the bonding region, was precisely positioned inside the furnace to allow uniform heating. A thermocouple was placed close to the sensor assembly so that the temperature could be precisely controlled and monitored during the sensor fabrication. The ferrule, fiber and the tube were bonded together by applying borosilicate powder. The bonding between the tube and the diaphragm was then achieved by using a special thin borosilicate fiber ring. The diaphragm was held before bonding by a vacuum tool. The holder for the ferrule and tube was made of fused silica glass, which has the same thermal expansion as the sensor components. After the sensor was bonded, it was necessary to anneal it for few hours to release the residual stress.

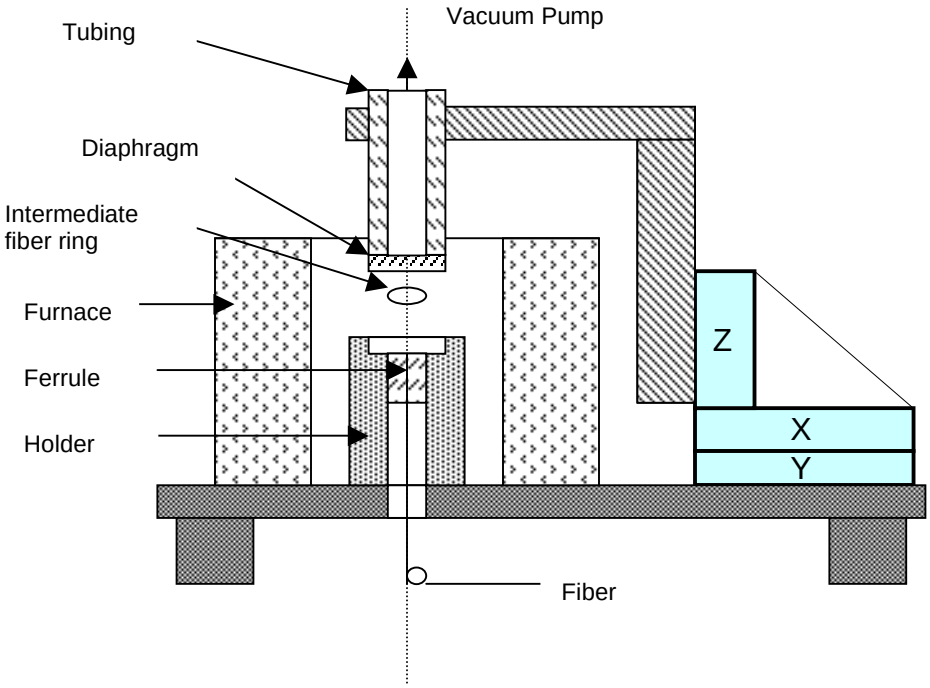

Figure 10.7. Acoustic sensor fabrication system using intermediate layer bonding method.

10.4 Acoustic Testing System

To evaluate the performance of the fabricated acoustic sensors, an acoustic test system was constructed (Figure 10.9). A WDU transducer was used to generate the ultrasonic signal by input from the pulse signal from a C-101-HV-2014 pulser. Also a WDU piezoelectric sensor was used as the standard to calibrate the fiber optic sensor. A 1221A preamplifier was used to amplify the detected acoustic signal from the WDU sensor. The WDU piezoelectric sensor and the fiber optic sensor were placed in a water tank to detect the acoustic signal from the WDU transducer. Amplified signals from both sensors are sent to the two channels of a Lecroy 505 digital storage oscilloscope so that by comparing these two outputs the fiber optic acoustic sensor could be calibrated. Figure 10.8 shows the experimental setup used for acoustic sensor testing.

10.5 Experimental Results

Using the testing system described above, the basic characteristics of the fiber optic acoustic sensors were evaluated. Data from a fiber optic acoustic sensor with a 1mm-diameter, 100μm-thick diaphragm is shown here. Driven by the pulse signal from C-101-HV-2014 pulser, the acoustic waves were generated and transferred to the sensors through water with fundamental frequency of f=130kHz. Figure 10.11 illustrates a series of detected signals from the fiber optic sensor and the WDU sensor. From the enlarged signal and FFT results in the bottom half of Figure 10.11, it is clear that the fiber optic acoustic sensor tracked the acoustic signals very well.

To determine the pressure sensitivity of the acoustic sensor, static water pressure was applied to the sensor head and the singlemode white light system was used to detect the air gap changes of the acoustic sensor. The relationship between the static pressure and the air gap is shown in Figure 10.10; the sensitivity is around 0.008nm/psi, which is near the theoretical value. So if we select the thin diaphragm, according to the Eq. 10-5, we can achieve very high sensitivity using this kind of acoustic sensor. These tests demonstrated that the fiber optic acoustic sensor could respond to the acoustic signal with high sensitivity in laboratory. The field test results are discussed in Chapter 13.

Figure 10.8. Photograph of acoustic testing system.

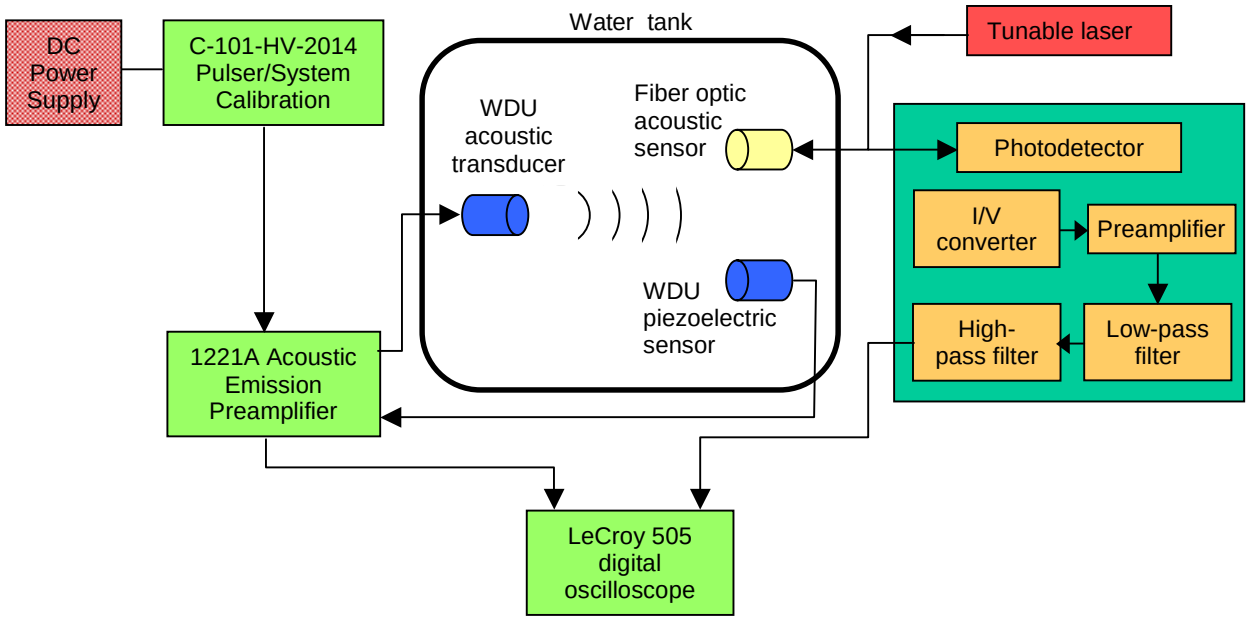

Figure 10.9. Acoustic sensor testing system configuration.

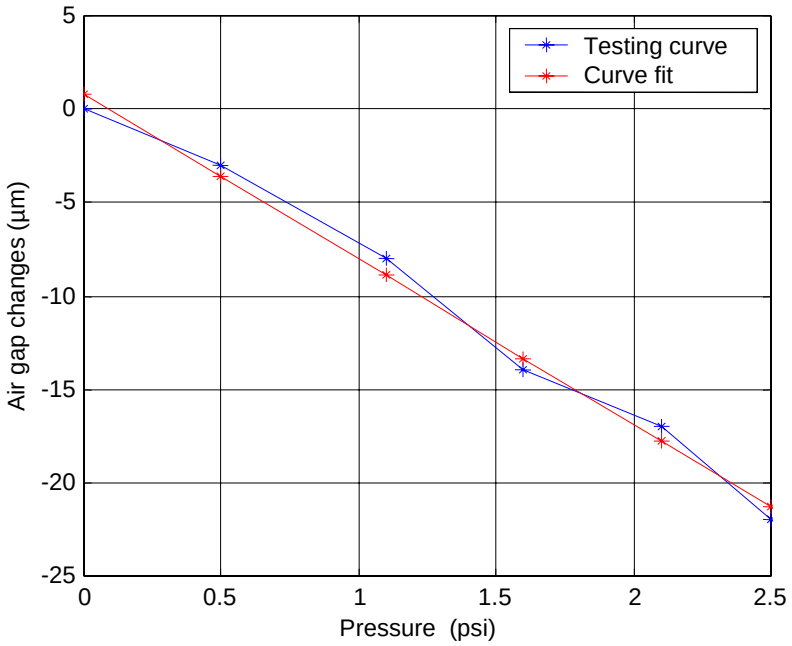

Figure 10.10. Pressure sensitivity of fiber optical acoustic sensor.

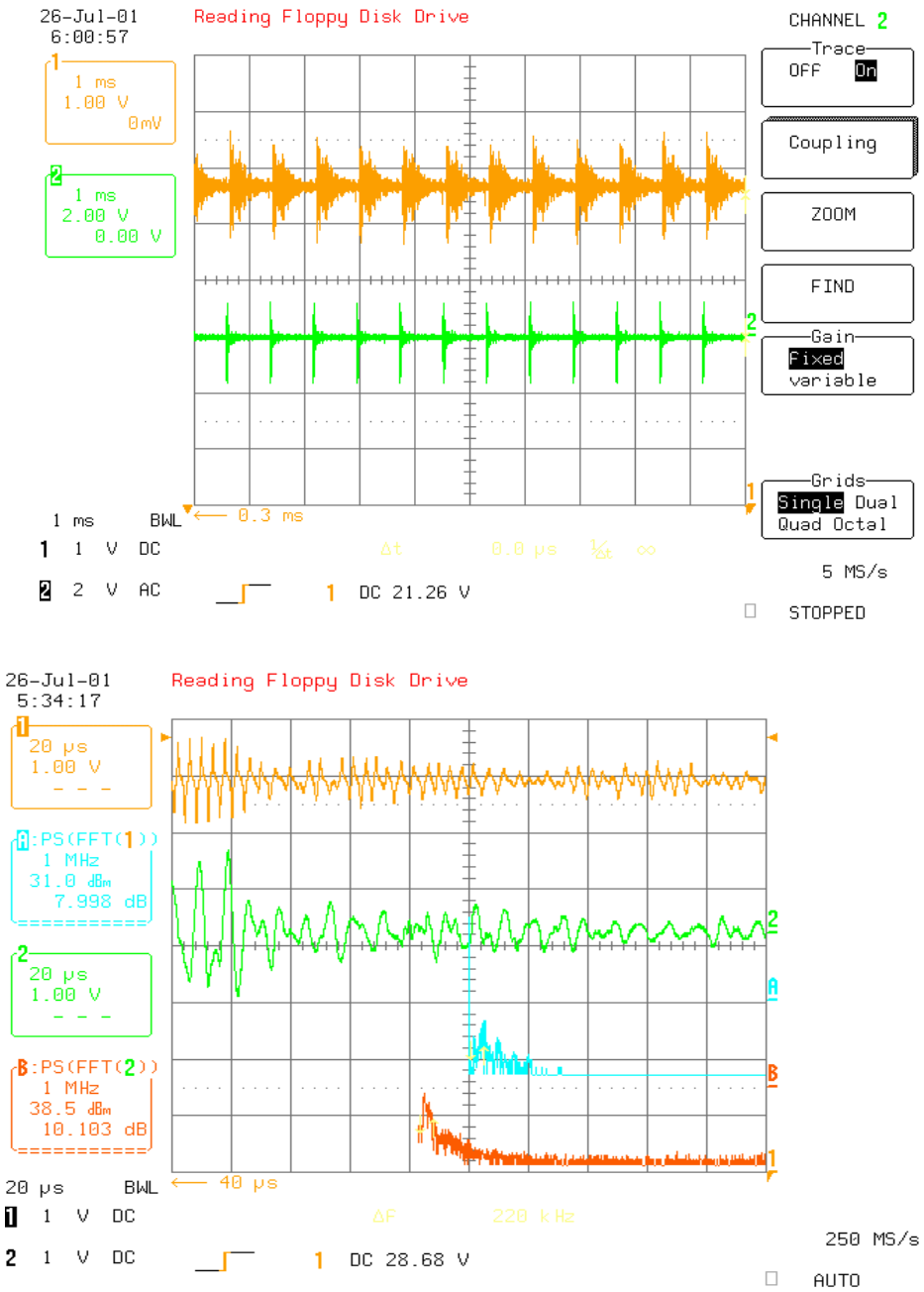

Figure 10.11. Comparison of acoustic signal from acoustic actuator (yellow) and acoustic sensor (green). The bottom graph is an enlargement of the acoustic signal from the LeCroy 505 oscilloscope.

11.0 Sensor Packaging Methods

The focus of this segment of the overall research project was aimed at development of suitable methods to protect the pressure and temperature sensor head from penetration by water and to improve the mechanical durability of the sensor head such that it would be able to survive the rigorous deployment process.

11.1 Packaging Requirements

While the method of protection selected had to be able to provide adequate protection from moisture penetration, at the same time, the protection could not be allowed to adversely affect the performance of the sensors. The requirements of the sensor packaging were:

1. Must provide adequate mechanical protection of the fiber sensor head and the connection between the sensor head and the transmission fiber
2. Must isolate the optical fiber sensor head from chemical corrosion and water penetration
3. For the pressure sensor, it must allow high pressure transduction fidelity
4. For the temperature sensor, it must isolate pressure while allowing high temperature transduction fidelity
5. The total finished size of the largest diameter of the protection package must be smaller than 1mm
6. The method selected must be simple and easy enough that it can be applied at the oil field site
7. For simplicity, it was desired that the method used to protect the splicing point of the optical fibers also be able to protect the sensor head rather than having two separate methods for each

A number of different methods were investigated to protect the sensor head, including laser ablation carbon coating with and without polyimide coatings, sputtering of gold thin films, additional outer glass tubings, and other methods of metallic coating. This chapter describes that effort, and the selected packaging method.

11.2 Determination of Minimum Bend Radius

In order to use optical fiber sensors for downhole oil exploration and recovery, it will be necessary for the fiber and sensor to bend around narrow passages within the deployment column. In some cases, the radius of curvature that the fiber optic cable and sensor assembly must traverse may be very small, possibly less than five or six inches. Therefore the minimum bend radius to which the fiber can be subjected without breaking or otherwise degrading is an important consideration in design of the overall system. In this segment of

the research, an experimental procedure and apparatus were developed to test the minimum bend radius that fibers treated under various conditions could survive.

In addition, it is anticipated that a protective coating may need to be applied to the fiber to prevent the penetration of water into the fiber. With this in mind, a theoretical analysis was undertaken to calculate the minimum bend radius as a function of coating thickness for several different potential coating materials in order to allow determination of the proper thickness more quickly than by trial and error.

11.2.1 Procedure for Minimum Bend Radius Testing

The apparatus shown in Figure 11.1 was constructed so that two parallel metal plates attached to a micrometer could be precisely positioned to hold a fiber at a fixed radius of curvature. On each of the two large, movable metal plates, two small ceramic plates were bonded to form a groove that was used to hold the fibers. These ceramic plates were bonded such that the distance between them was just slightly larger than the fiber diameter. In this way, the position of the fibers was fixed while the plates were brought closer together. The micrometer was calibrated to read zero when the two ceramic plates touched. The readings obtained from the micrometer represented the distance between the surfaces of the ceramic plates. The thickness of the ceramic plates was approximately the same thickness as the diameter of the optical fiber being tested. Therefore, the micrometer reading represented the separation distance between the inner fiber surfaces. The plates were moved at as close to a constant rate as possible during the first set of experiments. In the second set of experiments the plates were held at a constant separation distance and the time to failure was recorded.

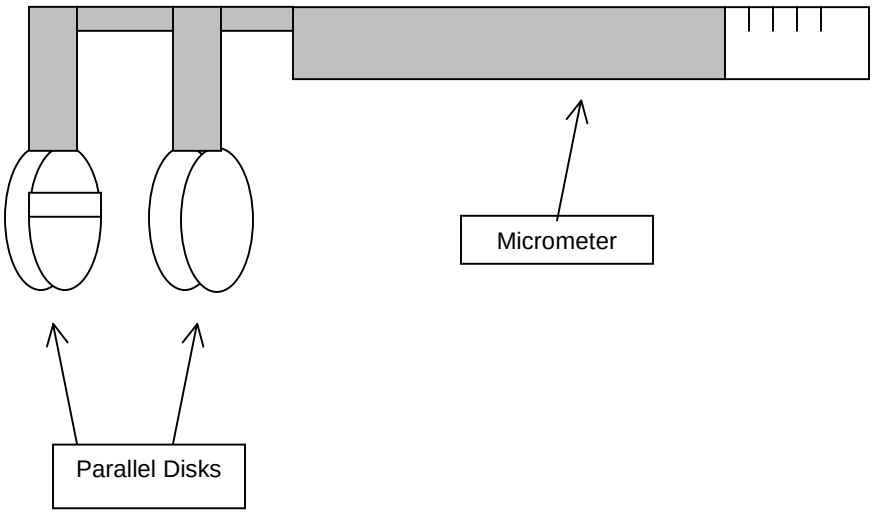

Figure 11.1. Apparatus used for minimum bend radius and time to failure testing.

Samples of singlemode fiber were cut into lengths approximately 25 cm long. The protective polyacrylate buffer (coating) was stripped from some of the fibers and left intact on others. The fibers were placed in a stainless steel tube. The tube was filled with water and the two ends of the tube were carefully sealed. The tubes were placed in an oven and heated to 200°C for specified lengths of time. The tubes were then cooled removed and opened. The water inside the tube was collected to ensure the tubes were properly sealed and the water was still present throughout the reaction time. In general, 15 fiber breaks were measured for each experimental condition. The data points shown in each of the figures that follow represent the average of the 15 measurements.

11.2.2 Minimum Bend Radius Results

Singlemode optical fiber with a cladding diameter of 125 microns was used as received for this experiment. In the first set of tests, the buffer was stripped with a razor blade. Testing of the minimum bend radius of these fibers showed that there was a large standard deviation. This was most likely due to the damage inflicted on the fiber by the razor blade. The procedure was changed to soaking the fiber in acetone to facilitate buffer removal. The acetone caused the buffer to swell and peel easily away from the fiber. The results for the minimum bend radius for the singlemode fiber showed that the fiber had a average minimum bend radius of 0.045" in with the buffer intact (as received) and 0.049" with the buffer removed by acetone.

The minimum bend diameter versus exposure time at 200°C is shown in Figure 11.2. The average minimum bend diameter for the fibers with the buffer on is approximately 0.08 in. and for the fibers with no buffer it is 0.22 in. The minimum bend diameter was the distance between the inner fiber surfaces when the fiber fractured. In both groups of fibers, the minimum bend diameter has no relation to the exposure time at 200°C. It appears that all the

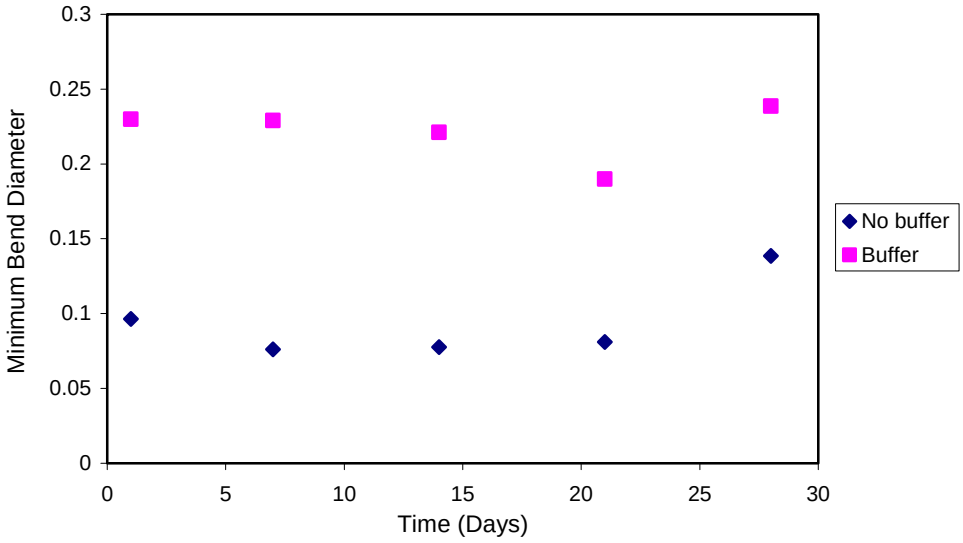

Figure 11.2. Minimum bend diameter versus exposure time at 200ºC.

degradation in the fiber occurs within the first day of exposure. After the first day of exposure, subsequent days of exposure do not affect the minimum bend diameter. It is not certain why the minimum bend diameter for the fibers with buffer shows a distinct difference from those exposed without the buffer. One likely explanation is that the buffer removal process damages the surface of the fibers. The failure of brittle ceramics is a statistical function of the probability of encountering a crack large enough produce failure at a given applied stress. The relation that governs brittle fracture in glass and ceramic materials is

$$\sigma_f = \frac{K_{IC}}{\sqrt{YC}}, \qquad \textbf{(11-1)}$$

where σ_f = the fracture stress, K_{IC} = fracture toughness of the material under mode I loading, Y = the crack geometry factor, and C = the crack size. As seen from this relationship, the stress required for fracture to occur in the glass fiber is a function of the size of the flaws that are present. Since glass materials (and ceramics in general) are much stronger in compression than tension, the fracture almost always originates on the tensile side of the fiber (when bent). Changing the flaw population distribution along the surface of the fiber changes the stress required to fracture the fiber and therefore will affect the minimum bend radius measured. Almost certainly, the fiber with the buffer removed undergoes much more damage than the fiber with the buffer in tact just from handling the fiber to cut and insert into the tubing and possibly from the tubing wall itself.

In order to investigate the effect of the rate of stress application on the failure bend diameter, an additional set of experiments were undertaken. The optical fibers were held at a fixed bend diameter and the time to failure measured. Figure 11.3 shows the time to failure for as-received polyacrylate-coated Corning SMF fiber versus bend diameter. The exponential relationship between the time to failure and the applied stress level indicates that the fiber is susceptible to stress corrosion cracking. This phenomenon, which is also referred to as fatigue in glasses, is a common occurrence. Normally, as described above, the fracture of the glass fiber occurs when the stress value reaches a critical limit dictated by the flaw population distribution. The crack propagation occurs at a velocity of approximately the speed of sound and appears for all practical purposes to occur instantaneously. If the stress is below the critical fracture stress, in certain circumstances the crack can grow at a sub-critical velocity. This is usually associated with the presence of water in the testing environment. The exact relationship between the sub-critical crack velocity and the applied stress is not known, and in some cases is assumed to be a power function. In other cases it is assumed to be exponential in nature. In this report we will assume that the relationship follows an exponential relationship. The details of how the water present in the environment assists the propagation of the crack are not completely understood. It is generally assumed that the water reacts at the crack tip in the presence of stress to break the Si-O bond. As the Si-O bonds are successively broken the crack elongates. The rate of the reaction of the water with the Si-O depends upon the value of the stress. At higher stress values, the crack propagates more quickly an therefore the time to failure is shorter. Conversely, at lower stress values the crack propagates more slowly and time required to reach the critical crack size for the given stress level is longer.

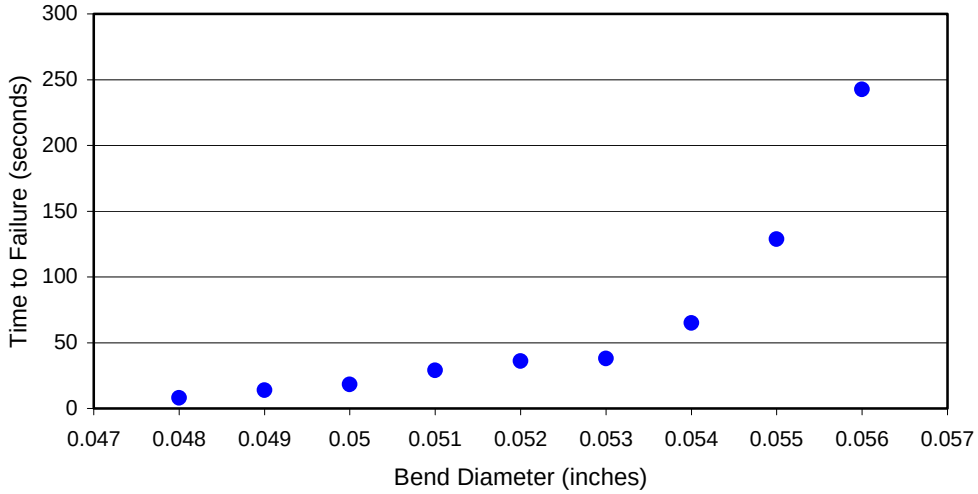

Figure 11.3. Time to failure versus bend diameter for Corning SMF.

Figure 11.4 shows the data from Figure 11.3 plotted with the y axis in log scale. The data appears linear when plotted in this semi-log plot. Since the diameter of the fiber is known and the radius to which the fiber is bent is known, the stress acting on the tensile surface of the fiber can be calculated. This has been done for each of the bend diameters in Figure 11.4 and the data re-plotted as a function of reciprocal stress in Figure 11.5. As shown in this figure, the log of the time to failure is directly proportional to the reciprocal stress applied to the fiber as is predicted by the theory. In the phenomenon of stress corrosion cracking of glass materials, water is known to play a key role in the process. It is believed that the water

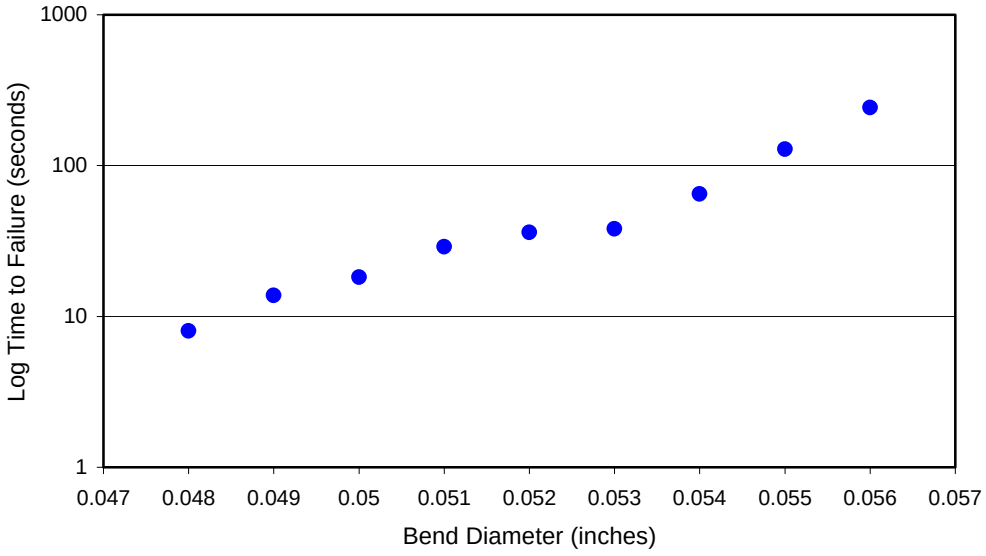

Figure 11.4. Time to failure versus bend diameter.

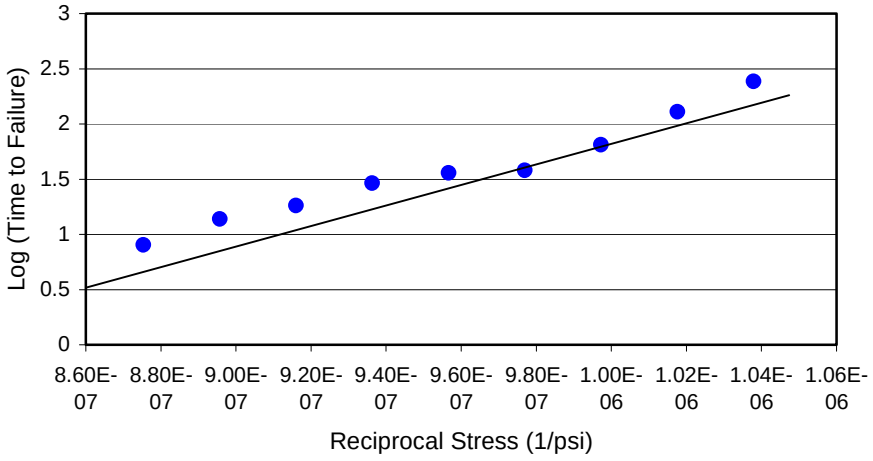

Figure 11.5. Time to failure versus reciprocal stress for Corning SMF.

lowers the energy required for crack propagation by breaking the Si-O (silicon-oxygen) bond as described above. This process is not completely understood. It might well be that water diffuses into the glass material at the crack tip due to the high values of stress in the crack tip vicinity. It is possible that it is this diffusion of water into the crack tip vicinity that lowers the overall fracture toughness of the material. In this model, fracture would occur when the fracture toughness reaches a low enough value.

In order to further investigate this phenomenon, as-received fibers were tested along with fibers soaked in water at room temperature for 30 minutes. These data are shown in Figure 11.6.

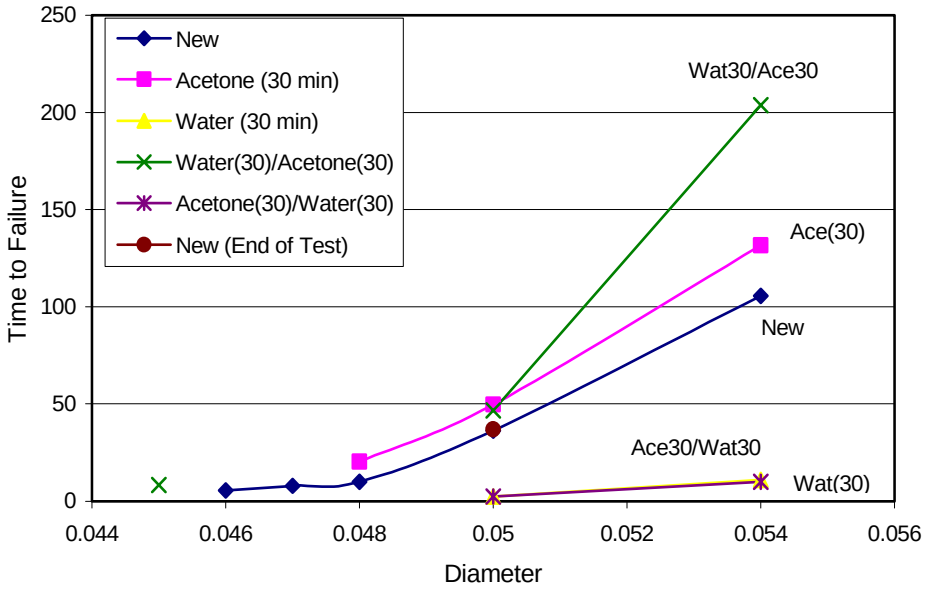

Figure 11.6. Average time to failure for optical fiber versus bend diameter.

After only 30 minutes of soaking, the fiber shows a significant reduction in the time to failure for the single mode fiber (SMF) with the buffer intact. Samples of the new singlemode fiber were also soaked in acetone for 30 minutes and an increase in the time to failure was observed. In order to investigate whether these processes were reversible, the SMF fibers were soaked in water for 30 minutes then in acetone for 30 minutes. The acetone soak completely negates the effect of the water soaking. Conversely, fibers soaked in acetone for 30 minutes then in water for 30 minutes show the water soaking completely negates the affect of the acetone soaking. All of these data are shown in Figure 11.6. These data clearly show that water has a detrimental effect on the time to failure of SMF fiber. The new unsoaked fiber that was tested had most likely absorbed water from the atmosphere. Removal of this water during the acetone soak is responsible for the increase in the time to failure of the fibers as compared to the "as-received" condition. The value for the fibers soaked in water for 30 minutes and then in acetone for thirty minutes held at a bend diameter of 0.054 inches is unusually high. It is suspected that the reason for this is solely due to measurement scatter. In that group of 15 fibers that were tested, one fiber exhibited a much longer time to failure than the other fibers in that group. If the reading for that fiber is eliminated, the data for that set would lie almost exactly on top of the data for the fibers soaked in acetone for 30 minutes (no water treatment).

In another set of experiments, samples of the SMF fiber were soaked in water for 24 hrs, then removed and allowed to stand in air for various periods of time before testing. The results are shown in Figure 11.7. After soaking in water for 24 hrs, the time to failure was very short (less than 1 second). As time progressed, however, the time to failure steadily increased until it reached the same level as that of the new fibers. This is most likely due to the loss of water from the fiber to the air. This result clearly shows that the process of degradation of the fiber due to exposure by water is completely reversible by allowing the fiber to lose the water by standing for a period of time in air. No permanent effects are observed due to the water treatment.

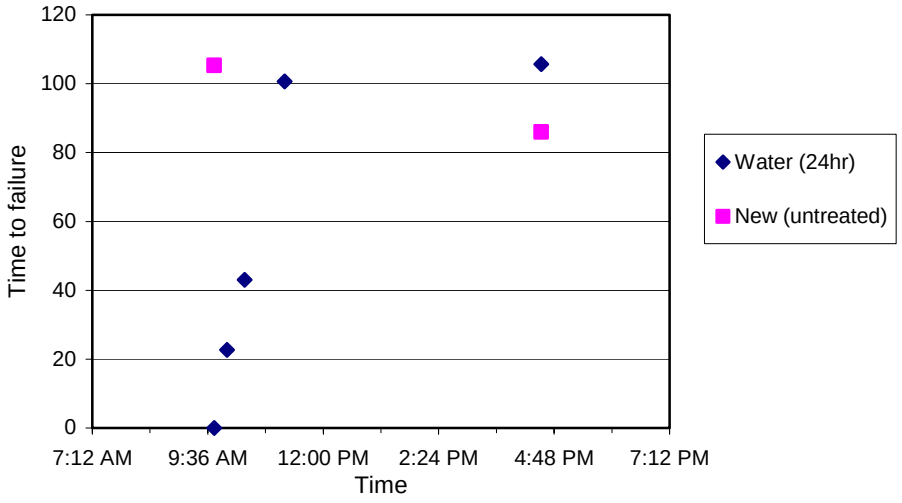

Figure 11.7. Time to failure versus time after exposure.

A theoretical treatment was undertaken to calculate the minimum bend radius as a function of coating thickness for several different materials. The data from these calculations is shown in Figure 11.8. The calculation is based on a 125 micron outer diameter optical fiber coated with various thickness and types of materials. The minimum bend radius was determined as that point at which 0.002% plastic strain would occur in the metal coating. From the curves, it can be seen that an upper limit of about 10 microns or so is about the maximum thickness the coating should be (depending of course upon the choice of material used).

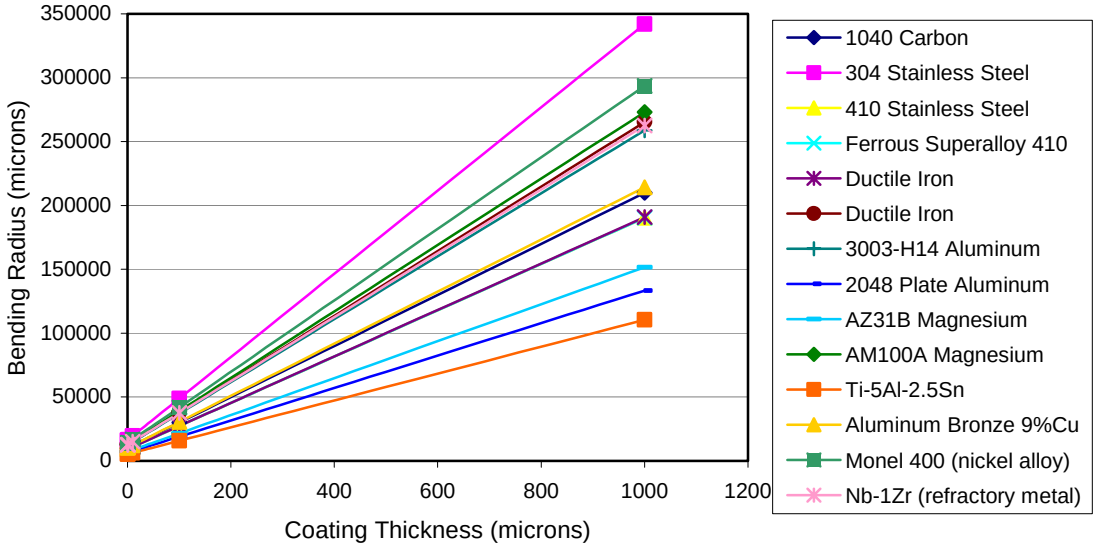

Figure 11.8. Calculated minimum bend radius versus coating thickness for various coating materials.

11.3 Water Effects at Elevated Temperature and Pressure

The goal of this segment of the research program was to evaluate the performance of the optical fiber that will be used to connect the sensor head to the outside world (above ground). Data from Chevron has indicated that penetration of water into optical fibers in the down-hole environment has proved to be detrimental to the life of the fiber. In order to protect the fiber from water, a series of experiments was performed to develop a suitable coating to protect the optical fiber. In order to test the effects of water at elevated temperature and pressure, a special apparatus was constructed as described in the experimental procedure section below. The fibers tested in these experiments were subjected to much higher temperatures than would normally be seen in the downhole environment (approximately 100% higher, 300°C test temperature as compared to 150°C expected maximum operating temperature). The effect of the increased testing temperature on the rate of diffusion of water into the silica fiber is expected to be exponential as described in the results and discussion section. Since the rate of penetration of water into the unprotected fibers was significant, several methods of protecting the fiber were tested in the experimental setup as well.

11.3.1 Experimental Procedure for Fiber Testing in Water at Elevated Temperature and Pressure

Two methods for protection of the optical fiber were selected for testing initially. These employed stainless steel needle tubing and carbon coating. In the case of stainless steel needle tubing, tubing approximately 508 micron OD and 292 micron ID was used. The polyacrylate-coated fiber was inserted into the stainless steel tubing which was filled with water. This fiber and tubing were inserted into another stainless steel tube approximately one quarter inch in diameter such that the needle tubing extended beyond the end of the tubing fittings. The fittings had been predrilled with a small hole just slightly larger than the diameter of the needle tubing. The needle tubing was sealed to the fitting using Miller-Stephenson 907 epoxy. This assembly was in turn inserted into a tube furnace heated at 300°C, such that the ends of the stainless steel tube, which were epoxied, stuck out of the ends of the furnace. The ends of the optical fibers were connected to a white light source and to an optical spectral analyzer respectively. Several other channels were prepared in the same way. In the second channel, a Spectran carbon/polyimide coated fiber was sealed in water in the stainless steel tubing. In the third channel, an as-received polyacrylate-coated multimode fiber without any additional protection was sealed. The fourth channel was used as a reference channel. A fiber was connected from the white light source to the optical spectrum analyzer directly without passing through the furnace. This was used as a reference to compensate for any changes in optical power from the white light source that might occur. All of the fibers were connected to the same white light source through a series of couplers such that once the connections were made they were not disturbed throughout the entire testing process. The pressure developed in the tubing can be determined from the steam tables. At 300°C the pressure inside the stainless steel tubing is 1440 psi.

11.3.2 Experimental Results – Optical Fiber Performance in Water at Elevated Temperature and Pressure

Figure 11.9 shows the absorption in decibels (dB) versus time in hours for the fibers immersed in water and heated to 300°C. As can be seen in this figure, the as-received fiber (without any protection) labeled "water" shows a relatively high absorption rate of water. In comparison, the carbon/polyimide coated fiber, labeled Spect 2, shows very low water absorption tendency. It must be pointed out that 300°C represents a much higher temperature than the fiber would normally experience in the downhole environment. Normally the fiber will experience temperatures less than 200°C. The penetration rate of water into the fiber is assumed to be diffusion controlled. Water at the surface of the fiber diffuses into the fiber due to the concentration difference between the surface and the interior. If the process is diffusion controlled, the flux of water into the fiber will be proportional to the diffusivity of water in the silica glass multiplied by the chemical potential gradient. If we let J= the flux of water, D= the diffusivity and $\nabla\mu$= the chemical potential gradient then

$$J = D\nabla\mu \,. \qquad \textbf{(11-2)}$$

The chemical potential is defined as the partial molar free energy

$$\mu = \frac{\partial G}{\partial n_i}, \tag{11-3}$$

where G= free energy of the system, and n_i = number of moles of component i. For diffusion only in one dimension, for example the x direction, assuming that the chemical potential gradient can be approximated by the concentration gradient of the diffusing species, the equation simplifies to

$$\mu = D\frac{\partial C_i}{\partial x}, \tag{11-4}$$

which is the familiar form of Fick's first law for diffusion.

Since diffusion is a thermally activated process, the diffusivity can be represented as

$$D = D_0 e^{-Q/RT}, \tag{11-5}$$

where Q= activation energy for the rate controlling process, R= the ideal gas constant, D_o= the pre-exponential term and T= the temperature. As seen from this relation, the diffusivity, and likewise the flux, will be exponentially dependent upon the temperature. Therefore, the penetration rate of water into the fiber at 300°C will be exponentially higher than the rate at 200°C. So the testing temperature of 300°C represents a significant accelerating factor in the testing.

The fiber within the needle tubing labeled as "W/T" (water with tubing) has shown no detectable change in the absorption due to water. This is a remarkably good result and shows the stainless steel needle tubing can provide excellent protection against water penetration.

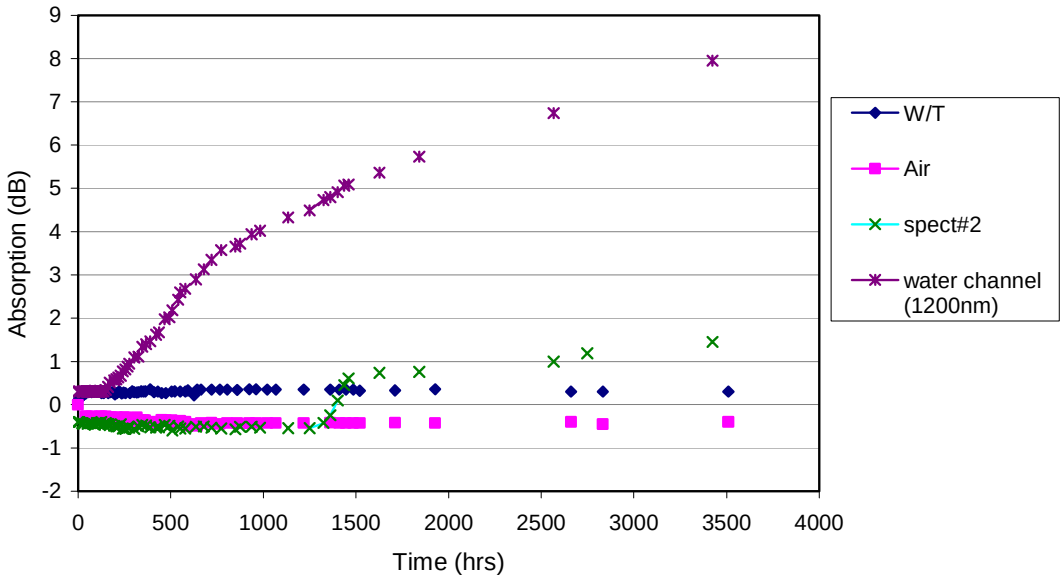

Figure 11.9. OH absorption versus time for fibers immersed in water at 200°C.

11.4 Carbon-Coated Fiber Development

Due to the outstanding results for protection against water penetration obtained for carbon coated and stainless steel needle tubing protected fibers, both metal coatings and carbon coatings were investigated to protect the sensor head. In this section, the results of the carbon coating development work will be presented. The coating method employed to deposit amorphous carbon onto the sensor head was laser ablation deposition. In this technique, a krypton-fluoride laser is directed through a series of mirrors and windows at a rotating carbon target in a vacuum chamber, which is pumped down to 10^{-6} torr. After stabilizing at this vacuum for a short period of time, oxygen is introduced into the chamber. The vacuum is stabilized at 10^{-4} torr. At this point the shutter to the laser beam is opened and the laser beam admitted to the target. A computer-controlled pulse firing sequence is initiated. The carbon is ablated from the surface with each pulse of the laser and deposits on the sample. The pulse count for samples coated to date has been 4000. After coating, the laser beam shutter is closed and the chamber is repressurized. The chamber cover is then opened and the samples removed.

Figure 11.10 shows an SEM micrograph of the fracture surface of a sensor coated using the laser ablation technique. As shown in this figure, the coating appears to be very uniformly distributed around the surface of the fused silica glass. It should be noted that the sample in this SEM micrograph is rotated about 10 degrees toward the viewer. The surface of the coating appears smooth and very uniform. The carbon coating thickness is approximately 1 micron. The fiber shown here is from the reflecting end of a sensor.

The entire sensor assembly was examined by optical microscopy as well. In transmitted light, the entire sensor system seemed uniformly coated. No pits, bubbles or obvious imperfections were observed. A Spectran carbon/polyimide coated fiber was used as the lead-in fiber in this sensor. The fiber was carbon-coated all over, except for the lead-in end, where the carbon coating was removed by soaking in hot sulfuric acid. After sensor bonding (fiber is bonded inside a fused silica tube), a short section of the fiber, which had been stripped, remained outside the tube. The laser ablation coating process not only coated the sensor head uniformly, but also coated the portion of the fiber that had been stripped during the sensor fabrication.

Experiments were also conducted to develop a method to overcoat the carbon-coated sensors with a polyimide coating. Several sensors were successfully coated with the polyimide material and cured.

11.5 Gold-Coated Fiber

This section describes the development of metallic coatings to protect the sensor head from penetration by water. Gold coatings were applied only to the sensor head and is believed to be approximately a few hundred nanometers thick based on previous experience with using the sputter coater to coat SEM samples. Figure 11.11 shows the results of the stability testing for a gold-coated sensor held at 205°C for two weeks in air. The standard deviation was calculated to be 0.0014.

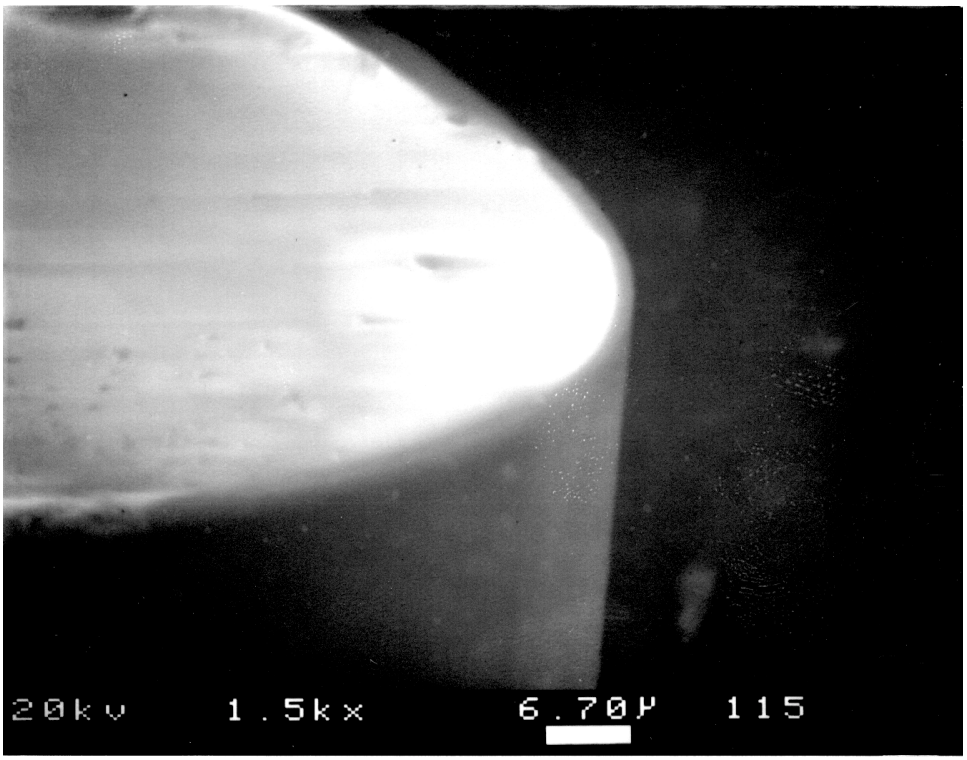

Figure 11.10. SEM micrograph of the fracture surface of an optical fiber coated with carbon by laser ablation

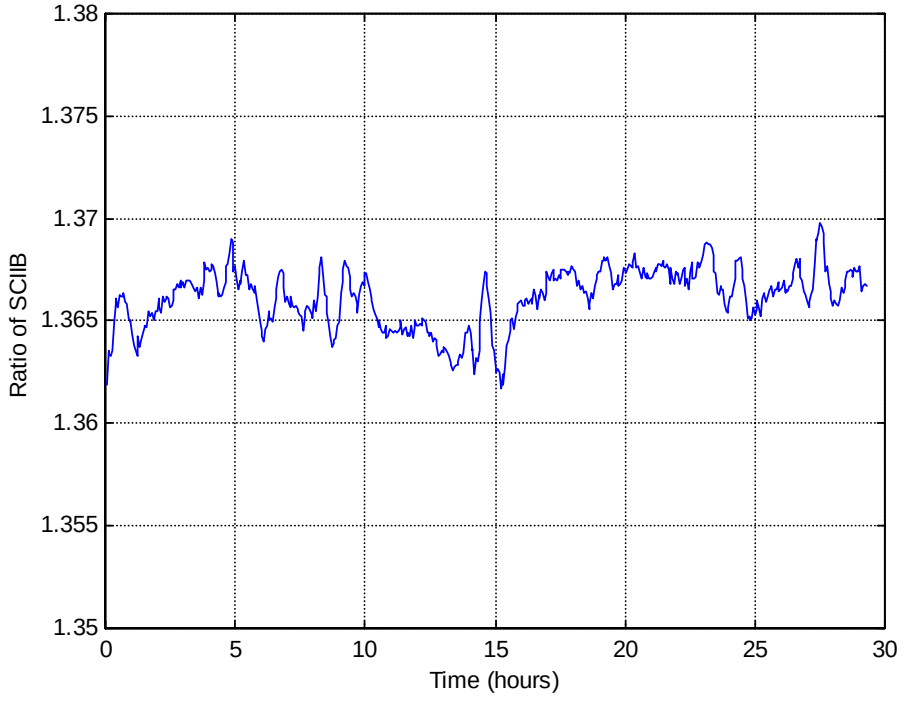

Figure 11.11. Results of stability testing of signal processing system – gold coated sensor held at 205°C.

In the downhole oil environment, the sensor will be subjected to simultaneous application of elevated temperature and pressure in an environment containing water. In order to evaluate the effects of such a combination of variables on the long-term stability of the sensor, a series of experiments was performed. In the first set of experiments an uncoated sensor was placed in the APP high-pressure calibration system. The system was heated to 200°C. The SCIIB output pressure as a function of the applied pressure was measured once per day. The results are shown in Figure 11.12 and Figure 11.13. As can be seen in this figure, the curve shifts as a function of exposure to the high temperature, high-pressure environment. The pressurizing fluid that was used in these experiments was water. It is believed that the shift in the curves represents the change in the physical dimensions of the sensor due to penetration of water molecules into the glass structure. The magnitude of the change from one day to the next day becomes smaller as time progresses. It is not certain whether the sensor is saturated with water, preventing further significant changes in sensor reading or whether the shift will progress.

The same experiment was repeated with a sensor coated with gold. The data obtained in this fashion is shown in Figure 11.14 and Figure 11.15. The gold-coated sensor exhibited a shift in the curve similar to the uncoated sensor, but larger in magnitude. The gold coating applied to the sensor did not adhere well. This is a common problem in the mirror industry. In order to allow the gold to stick to the substrate more strongly, a chromium layer was first applied to the glass before the gold is applied. In the sputtering system used in these experiments, the option to put down a layer of chromium before the gold was applied was not available. The new sputtering system acquired by CPT during this program does permit the deposition of chromium first followed by gold deposition.

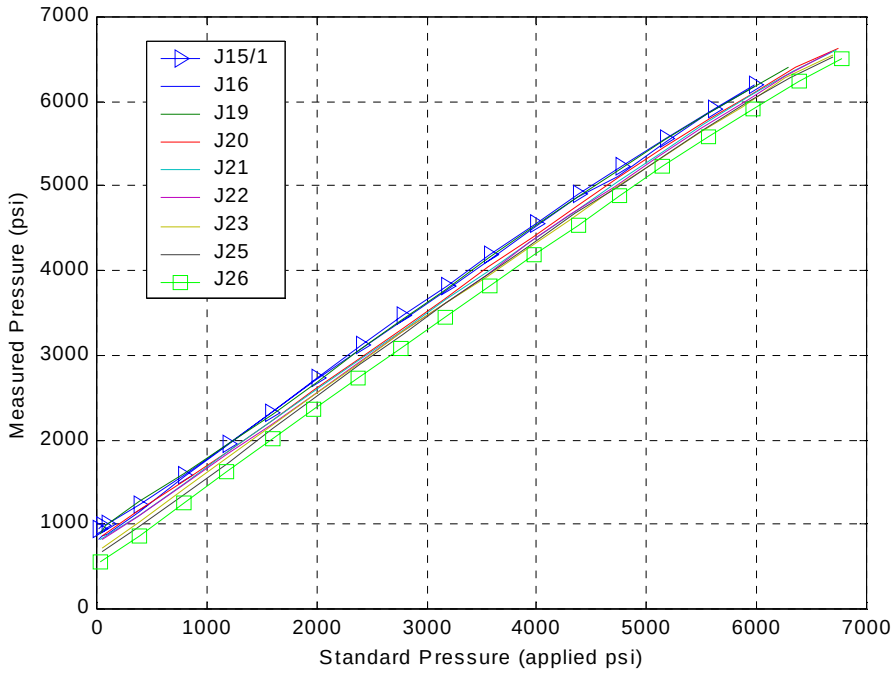

Figure 11.12. Measured pressure versus applied pressure as a function of exposure time for an uncoated sensor.

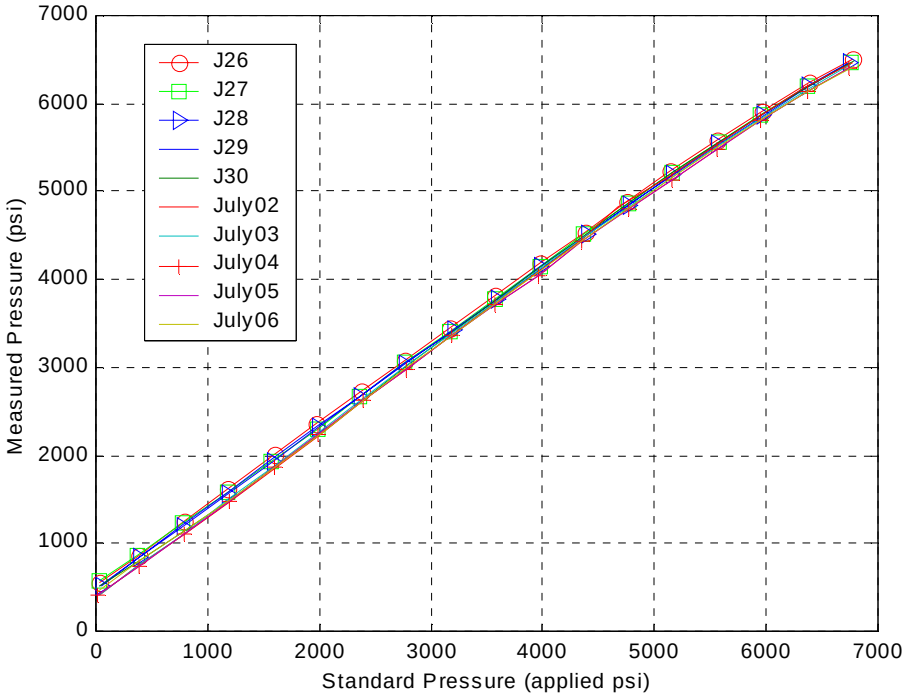

Figure 11.13. Measured pressure versus applied pressure as a function of exposure time for an uncoated sensor (continued).

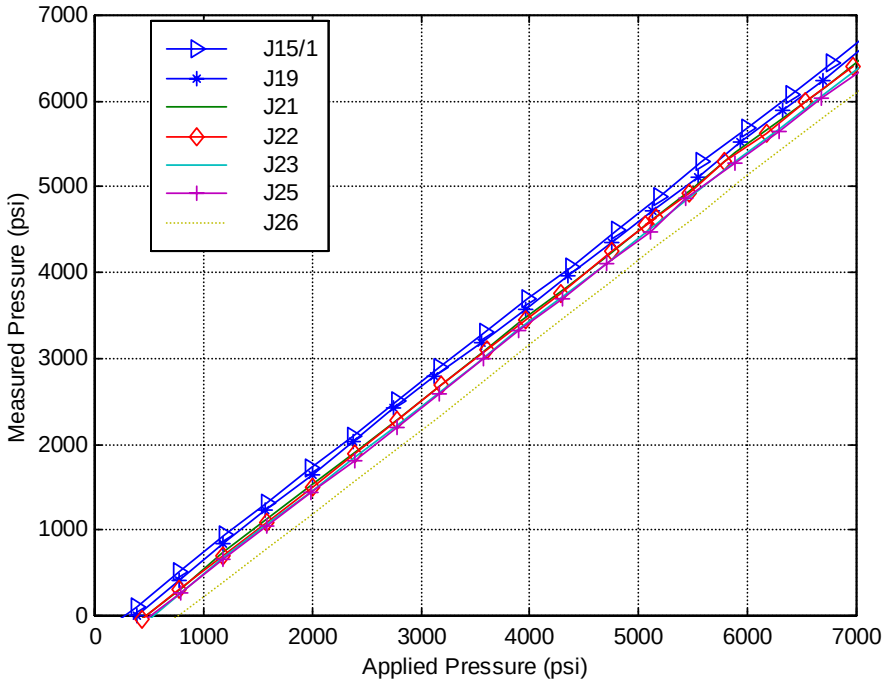

Figure 11.14. Measured pressure versus applied pressure as a function of exposure time for an gold coated sensor.

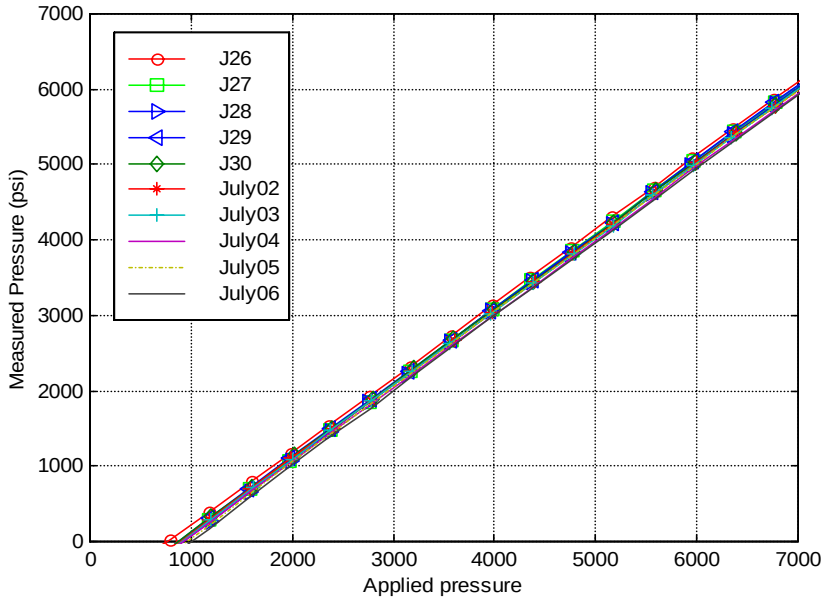

Figure 11.15. Measured pressure versus applied pressure as a function of exposure time for a gold-coated sensor.

Figure 11.16 shows the change in sensor output as a function of exposure time for both the gold-coated and uncoated sensor. The curves shown in this figure represent the variation between the pressure reading (in psi) as measured by the SCIIB system, at 3000 psi applied pressure, on the first day compared to the day being measured. For example, the pressure reading on day 5 from the SCIIB system at 3000 psi applied pressure minus the pressure reading from the SCIIB system on day 1 at 3000 psi applied pressure would become the value plotted for day 5. It can be seen from this figure that the readings for both the gold coated and the uncoated sensors show a positive trend. The magnitude of the slope for a gold-coated sensor is approximately twice the magnitude of the slope for the uncoated sensor. It is suspected that the increase in slope for both the gold-coated and uncoated sensor is due to penetration of water into the sensor.

Figure 11.17 through Figure 11.20 show a second set of data for the variation in calibration for a gold coated and an uncoated sensor. The data appear to be very consistent with the data shown in Figure 11.12 through Figure 11.15. The data for the pressure calibration variation versus number of days of exposure is shown in Figure 11.21 and shows a similar relation to that shown in Figure 11.16 for the previous set of data.

Figure 11.22 shows the variation in the SCIIB output ratio versus applied pressure for different states of polarization of the fiber pigtail. In this set of experiments, the fiber was rotated to various degrees while the readings were being acquired. The average system polarization error was calculated to be 1.12%. Figure 11.23 shows the variation in SCIIB output versus the applied pressure for different splicing losses. Initially, the system was spliced with a fusion splicer and the readings taken. The splice was then broken and respliced and the readings taken again. In each case the loss due to splicing as measured by the fusion splicer is noted on each curve on the graph.

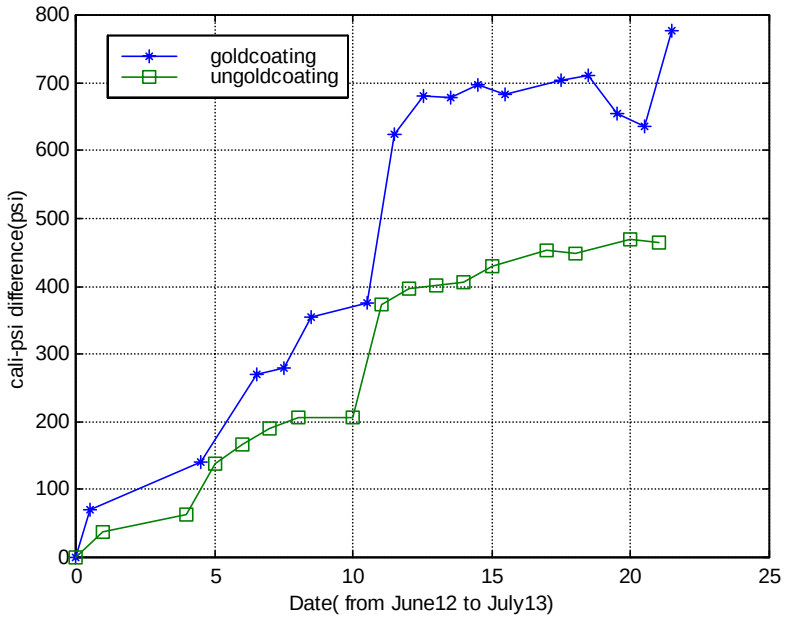

Figure 11.16. Pressure calibration difference between first and following days versus date for a gold coated and an uncoated sensor.

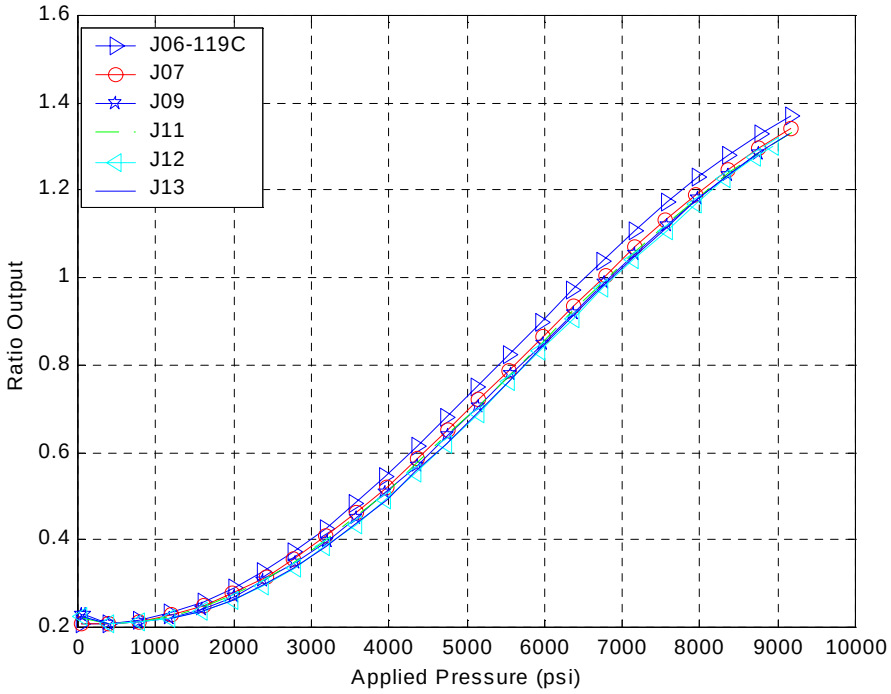

Figure 11.17. Measured pressure versus applied pressure as a function of exposure time for an uncoated sensor

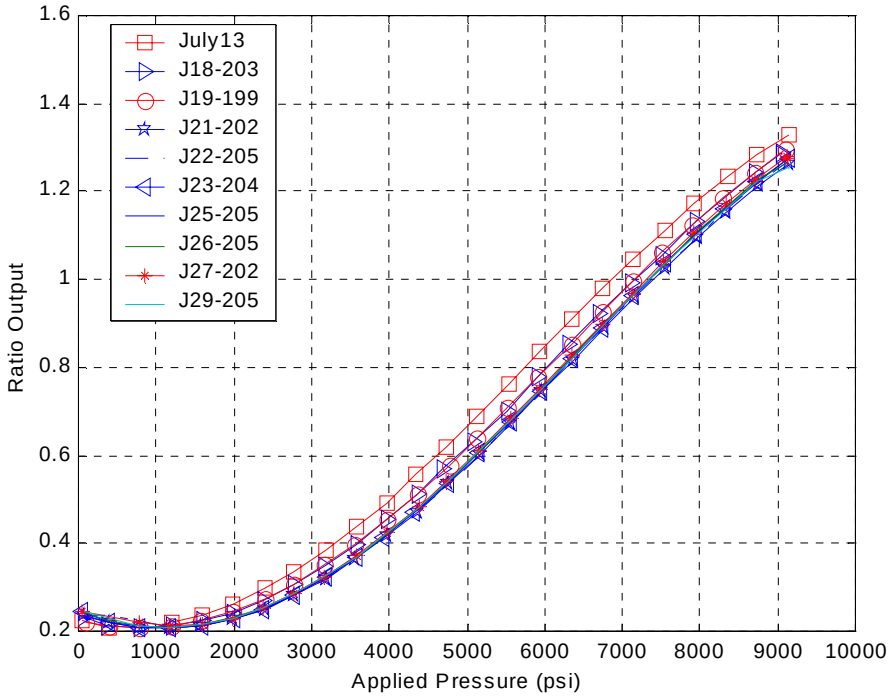

Figure 11.18. Measured pressure versus applied pressure as a function of exposure time for an uncoated sensor (continued).

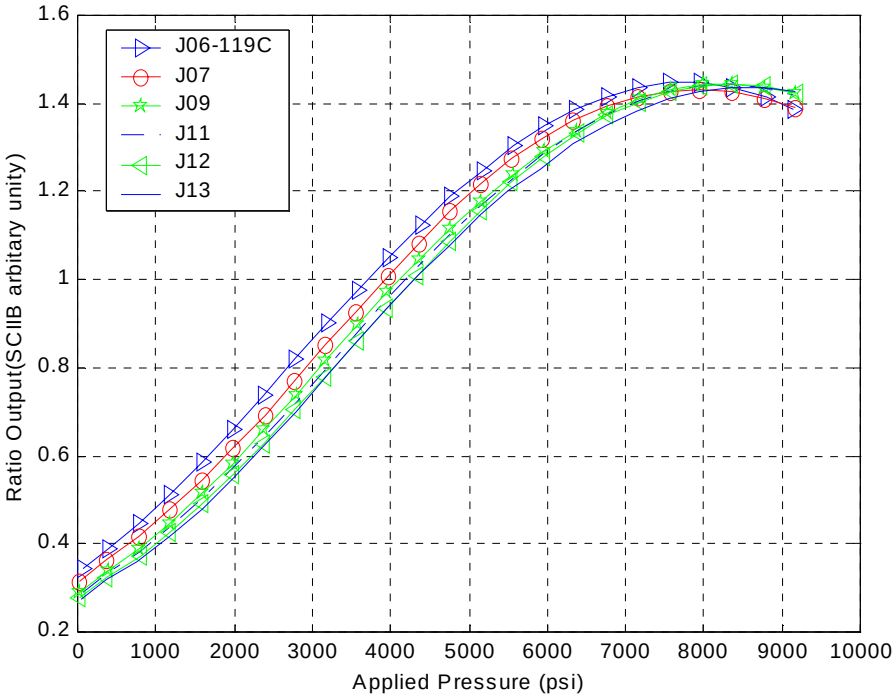

Figure 11.19. Measured pressure versus applied pressure as a function of exposure time for an uncoated sensor.

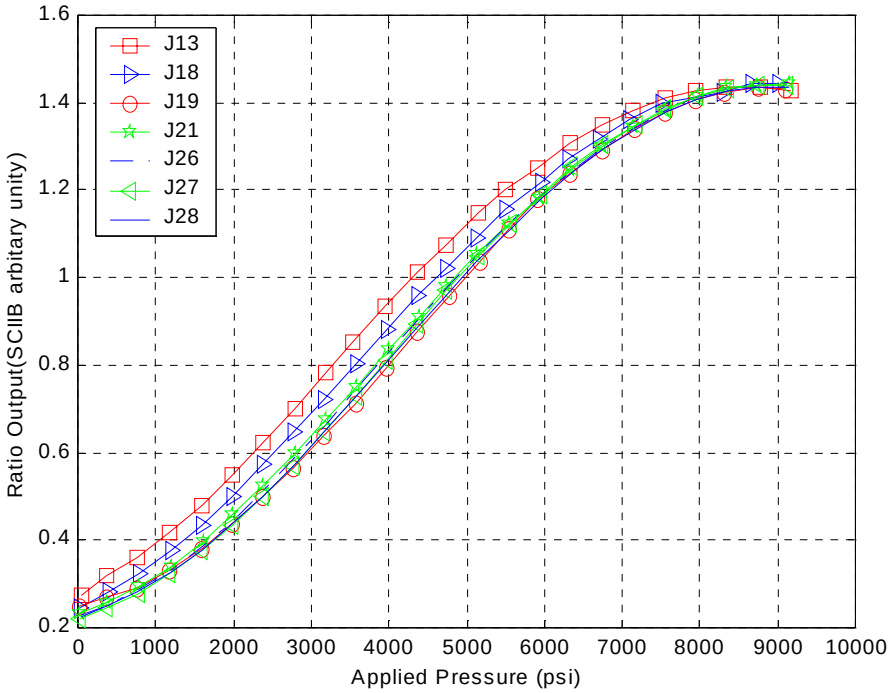

Figure 11.20. Measured pressure versus applied pressure as a function of exposure time for an uncoated sensor (continued).

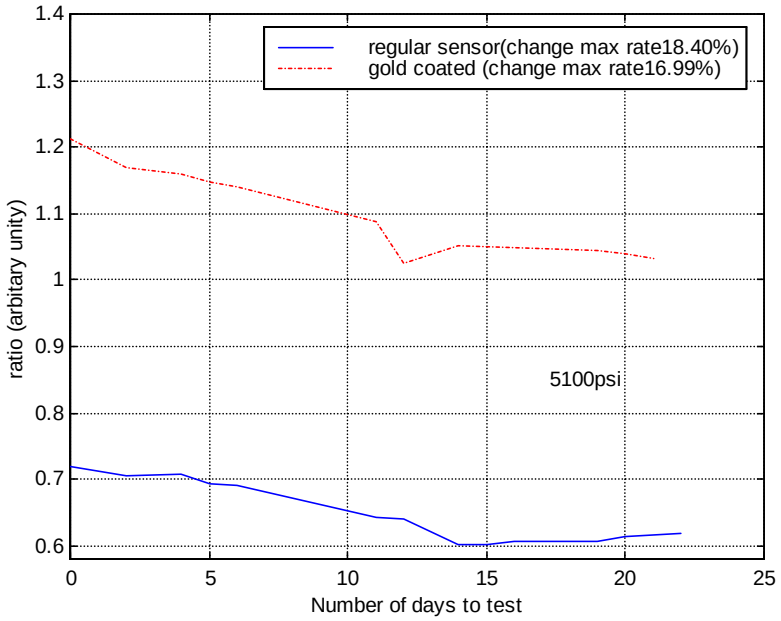

Figure 11.21. Pressure calibration difference between first and following days versus date for a gold coated and an uncoated sensor.

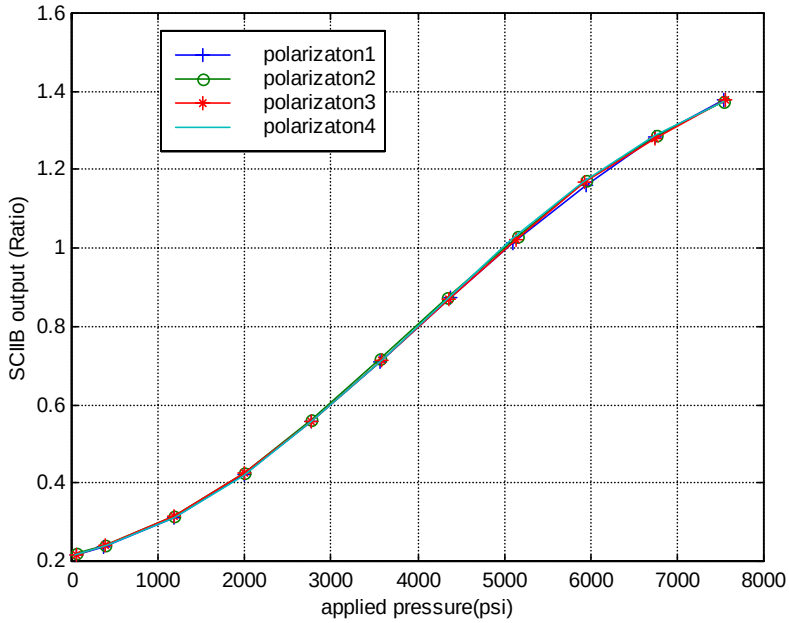

Figure 11.22. SCIIB output versus applied pressure and as a function of different fiber pigtail polarization states.

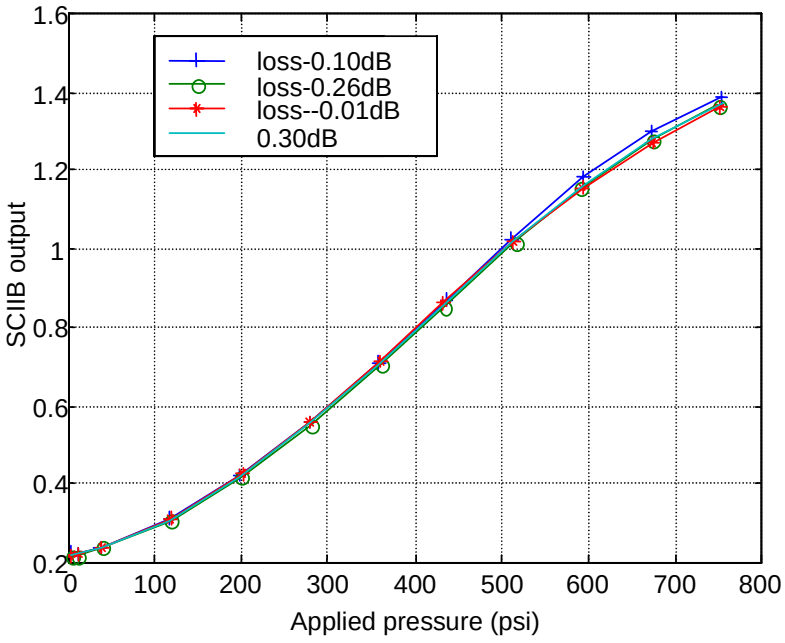

Figure 11.23. Effect of fusion splice loss on the SCIIB output.

In an attempt to improve the system stability, a second system was constructed. Calibration curve changes for this system for the fiber pigtail polarization state had an average polarization error of about 0.23%~0.787% as shown in Figure 11.24. Figure 11.25 shows the SCIIB output versus applied pressure for different splice losses for the improved system. The splice loss repeatability in the new system has dropped to approximately 0.5%

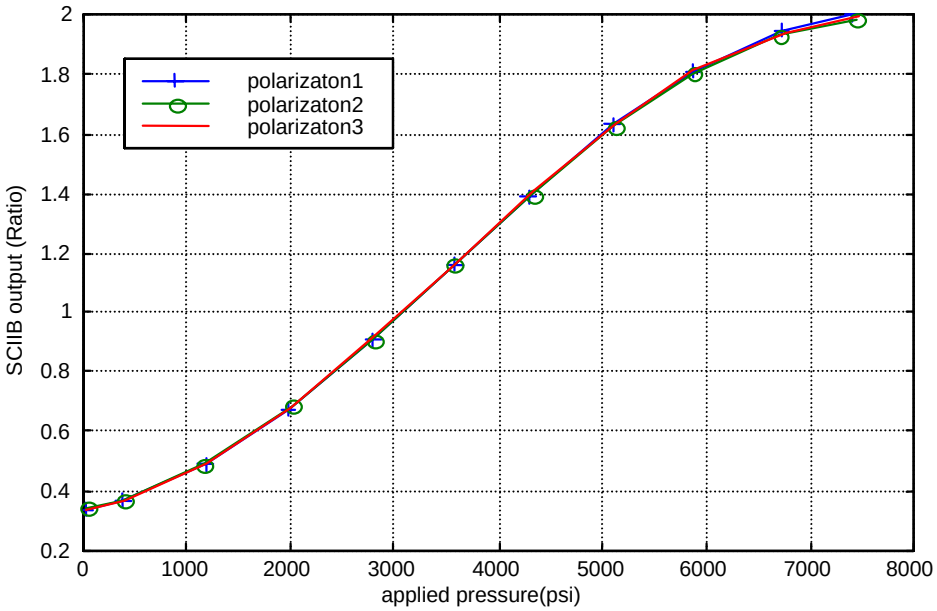

Figure 11.24. SCIIB output versus applied pressure and as a function of different fiber pigtail polarization states for improved system.

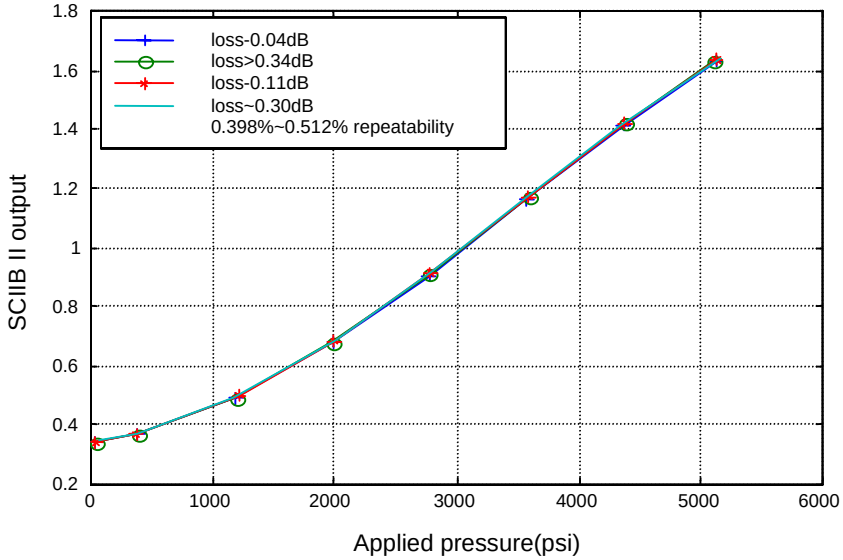

Figure 11.25. Effect of fusion splice loss on the SCIIB output for improved system.

11.6 Encapsulated Fiber

This method involves encapsulating the sensor head in a soft metallic material while simultaneously encapsulating the metal in an outer heat shrinkable tubing. The process required identification of suitable metallic and polymeric materials such that the melting temperature of the metallic material was in the same range as the consolidation temperature of the polymeric material.

11.6.1 Structure of the fiber sensor protection package:

The structure of the packaging system is shown schematically in Figure 11.26. The arrangement of the tubes can be performed quite easily be hand. In addition, no special microscopic equipment is necessary, so the process is very simple.

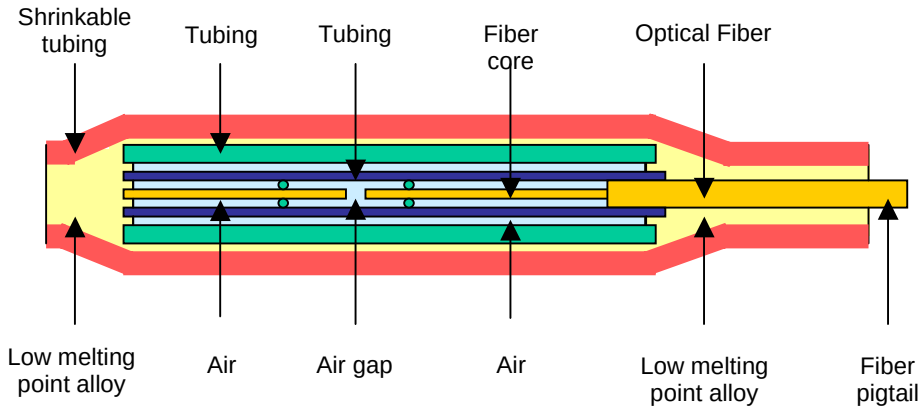

Figure 11.26. Schematic of the protection packaging assembly.

1. Materials:
   - Small tubing (silica glass tubing, stainless steel tubing, etc).
   - Heat shrinkable tubing
   - Low melting point metal or alloy

2. Structure: The sensor is positioned within the small outer tubing, of which, the diameter is only slightly larger than that of the sensor tubing. The small outer tubing is also a little bit longer than that of the sensor. The outermost part is the heat shrinkable tubing. Between the small outer tube which covers the sensor and the heat shrinkable tubing that covers the entire system, a low melting temperature metal is placed, which is used to isolate the sensor from moisture.

11.6.2 Packaging process

11.6.2.1 Material preparation:

1) Sensor preparation—It was important to ensure that the dimension of the sensor is small enough to allow proper packaging while still meeting the overall size requirements imposed on the sensor package by the deployment process.
2) Small tubing preparation—It was important to ensure that cutting of the tubing was performed evenly and control of the length was accomplished such that the outer glass tubing was slightly longer than that of the sensor head.
3) Shrinkable tubing preparation—It was important to control the length of this tubing such that it was a little longer than small outer tubing.
4) Low melting point metal preparation— Metal tubing was fabricated from metal sheets to aid in assembly of the components for bonding. As such, the metal tubing was cut slightly longer than the small outer tubing and shorter than the shrinkable tubing.

11.6.2.2 Fabrication Procedure:

1) Put the sensor into the small outer tubing.
2) Put the small outer tubing into low melting point metal tubing.
3) Put the metal tubing into the shrinkable tubing.
4) Carefully position the sensor and the tubing.
5) Heat them in a controlled way to make the shrinkable tubing shrink, while the metal is melted and flows out of the two ends of the shrinkable tubing.
6) The heating temperature, heating direction, and the amount of the metal is controlled.
7) For the pressure sensor, the metal contacts the two ends of the sensor. For the temperature sensor, at least one end of the sensor is free.
8) Final treatment: cut the excess part of the package and remove the excess metal on the ends of the packaged sensor.

This method proved to be extremely simple to employ in an oil field setting, was robust enough to be able to be applied reliably, and was found to be a very inexpensive solution. No special tools were required to perform the operation. The only tools used were a heat gun, small screwdriver, pliers and a ceramic plate to protect the surface below from heat. Extensive testing of the protected sensors was performed to ensure performance of the protection packing and to characterize the change in performance before protection versus after protection. Overall, the performance of the packaging method was found to be excellent.

12.0 Field Testing of Flow Sensor System

To demonstrate the feasibility of the developed flow sensor system, the prototype sensor system was field tested at the flow loops at the University of Tulsa from Aug 19, 2002~Aug 23, 2002. Two flow loops were involved in this field-tests; the detailed technical parameters and testing results are reported here.

12.1 Indoor Flow Testing

The indoor flow facility we used for flow testing is shown in Figure 12.1a. A variable frequency pump (0~1745RPM) from *Robins & Meyers, Inc* (Figure 12.1b) was used to pump the water into 1-1/2″ Schedule 40 flow loops, which combine many gauges including an adjustable pressure valve, pressure gauge from *Wika, Inc* and thermocouple from *Omega, Inc.* As shown in Figure 12.1(c), the flow sensor was deployed in the flow pipes using a 0.5~1.5inch NPT bushing through a 1.5inch NPT T-fitting. Figure 12.1(d) shows the flow sensor connected by a dual fiber cable to the rest of the fiber optic flow measurement system, which mainly includes a multimode fiber optic white light interferometric system. The output of white light system is shown as Figure 12.1(e), the flow rate measurement window is shown as Figure 12.1(f). The temperature of the flow loops during indoor testing was controlled by the air conditions and was stable at around 29ºC; the pressure in the flow pipes was controlled at around 5psi. The parameters of fiber optic flow sensor used in this indoor testing are listed in Table 12.1.

Table 12.1. Parameters of fiber optic flow sensor used for indoor flow testing in Tulsa.

Fiber type:	Multimode 50/125
Cantilever beam material:	Invar sheet
Cantilever beam size:	0.010"*1.5*0.13"
Original air gaps of two sensors:	10.46μm; 11.96μm
Original visibility of two sensors:	71%; 21%
Gauge length of two sensors:	2.2mm; 1.8mm
Relative temperature coefficients:	1; 0.85
Sensor protection:	Flexible Ni-bellows
Test conditions:	84~86ºF; 1~5psi

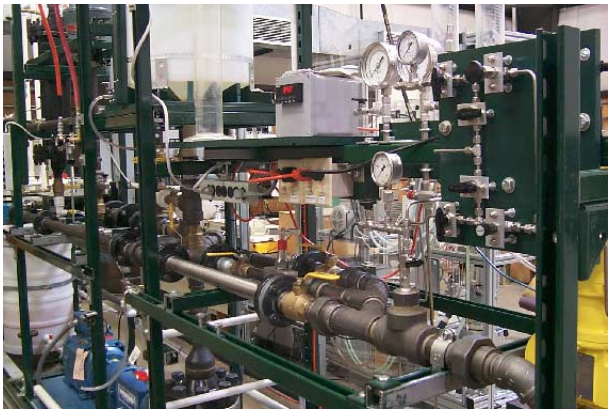

(a) Indoor flow test system in Tulsa University, OK

(b) Variable frequency pump

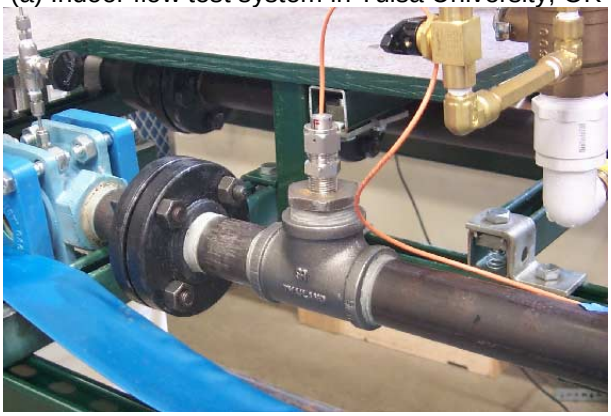

(c) Flow sensor in indoor flow loop

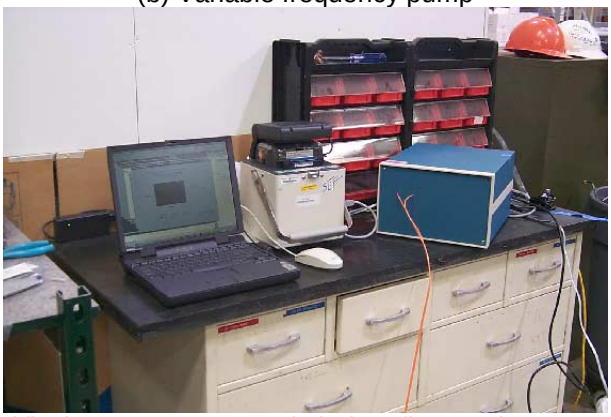

(d) Flow sensor system in indoor flow testing room

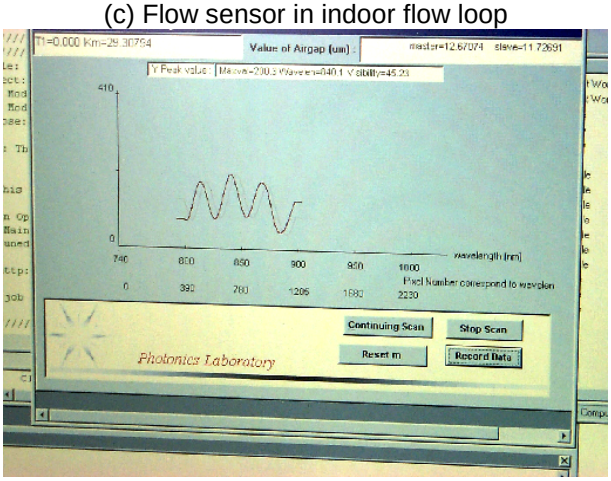

(e) Fiber optic white light system output window

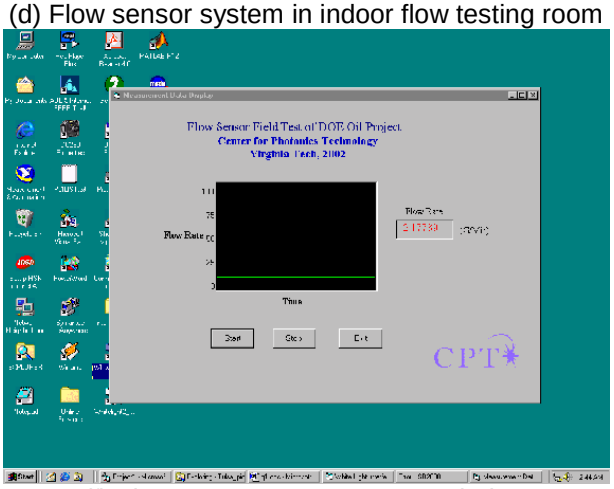

(f) Flow sensor system output window

Figure 12.1. Indoor flow testing system in University of Tulsa , OK.

Compared with the outdoor flow loops, the indoor flow testing facilities were at a very stable temperature and pressure. Due to some unexpected occurrences during shipping, when we arrived at the Tulsa testing field, only one channel of the white light system could be used for the indoor testing while we completed an urgent repair of the other channel. So for indoor testing, we used only one of the two sensors to measure the indoor loop flow rate.

12.1.1 Variable frequency pump calibration

The indoor flow testing system used a variable frequency pump from *Robins & Meyers, Inc* , which had an operating range from 0 to1745RPM, to drive water in the flow loop. Using the FT-NENW turbine flow meter, a calibration was performed first to convert the flow rate units from RPM to GPM; the calibration curve was shown in Figure 12.2.

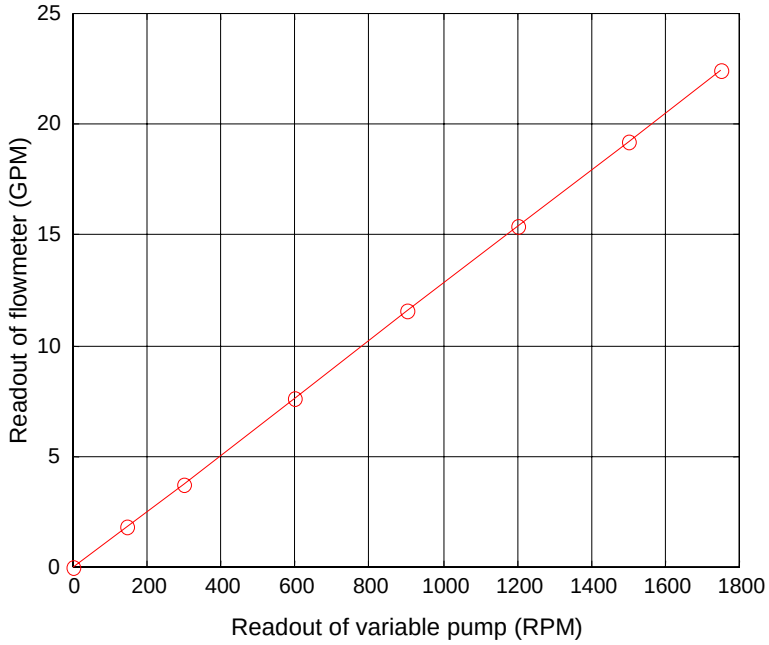

Figure 12.2. Variable frequency pump calibration curve using FT-24NENW flow meter.

12.1.2 Sensor calibration

Due to the difference in testing conditions between the indoor test loop and lab-scale testing, the sensor required recalibration prior to the testing in the outdoor system. The calibration curve of the fiber flow sensor using the output from a reference flow rate is shown in Figure 12.3.

12.1.3 Measurement results and repeatability

The real-time flow rate information was obtained through the calibrated relationship between the reference flow rate and the airgap change in the sensor head. Figure 12.5a shows the measurement results for repeatability testing. The flow sensor output is a linear function of the variable frequency pump rotational speed. A magnified view of the repeatability results is shown Figure 12.5b. For the full measurement range from 0 to 22.42 gallons per minute (GPM), the maximum deviation was ±0.26GPM, which is ±1.15% of full scale.

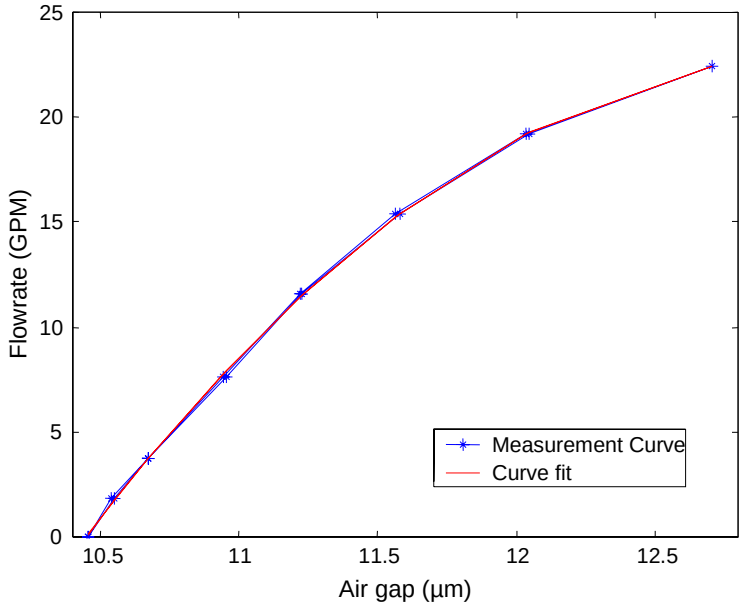

Figure 12.3. Flow sensor calibration curve for indoor flow testing in Tulsa, OK.

12.1.4 Resolution of indoor flow testing

For the indoor flow sensor system, 600 flow values were acquired in one minute with a sample frequency of 10 counts/second (Figure 12.4). The standard deviation of the flow data was σ=0.00123GPM; therefore, the resolution of the sensor system was estimated to be 2σ=0.0246GPM. The normalized resolution with respect to the dynamic range of the system was 0.11% of the full scale.

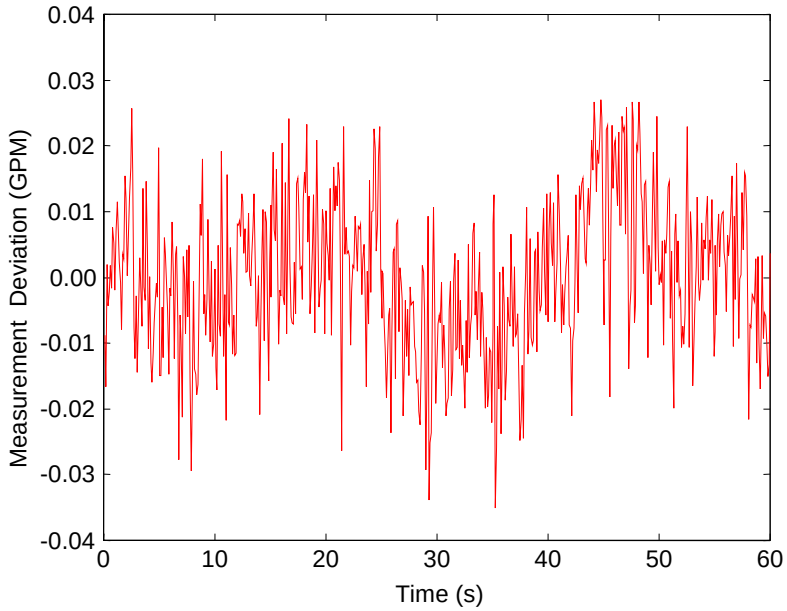

Figure 12.4. Resolution of flow sensor system, indoor flow testing.

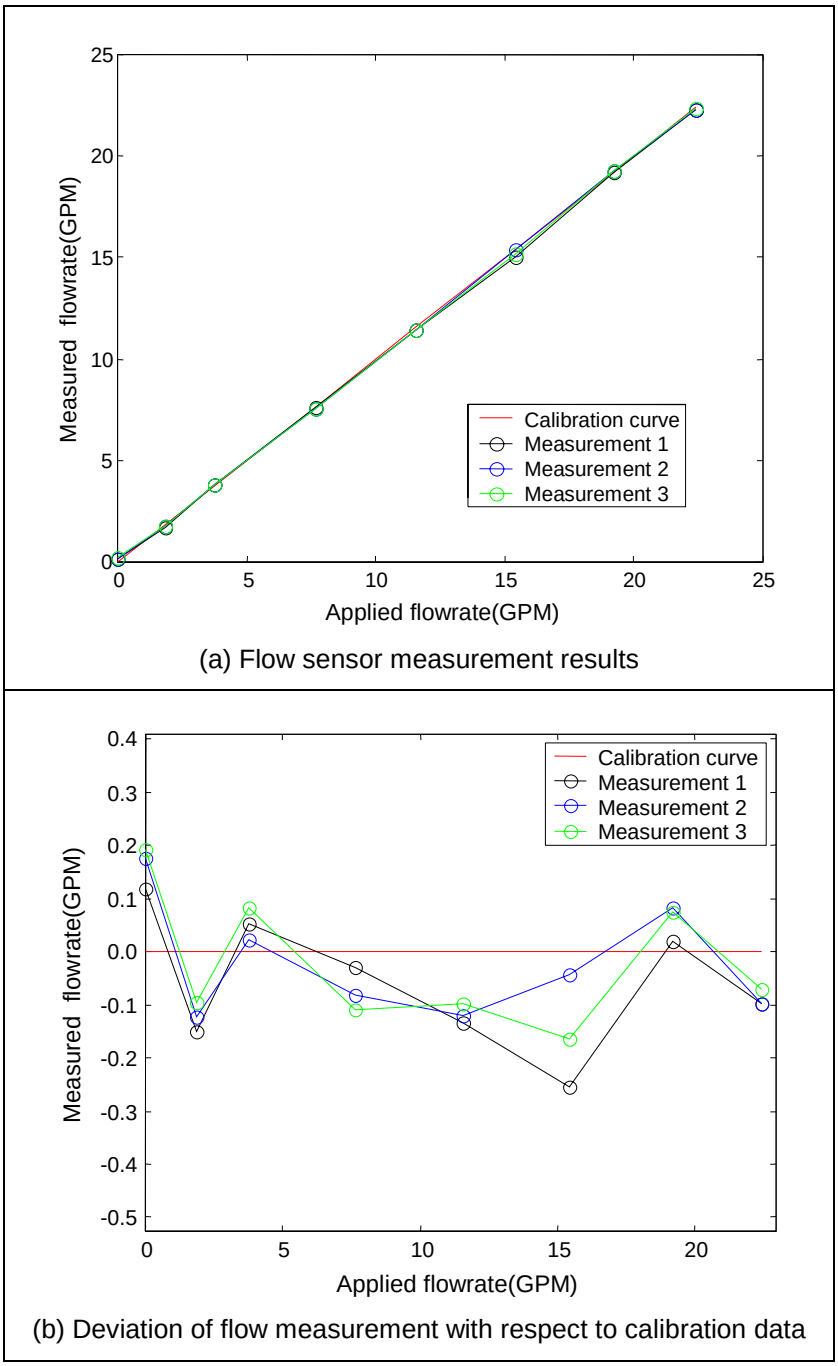

Figure 12.5. Measurement results from fiber flow sensor in indoor testing loop.

12.1.5 Hysteresis of flow sensor

The hysteresis characteristics of this sensor were also tested in the indoor flow loop (Figure 12.6a). No obvious hysteresis was observed for the measured range, as shown in the enlarged data in Figure 12.6b. The hysteresis of the full measurement range was measured to be 0.89% for the indoor flow tests.

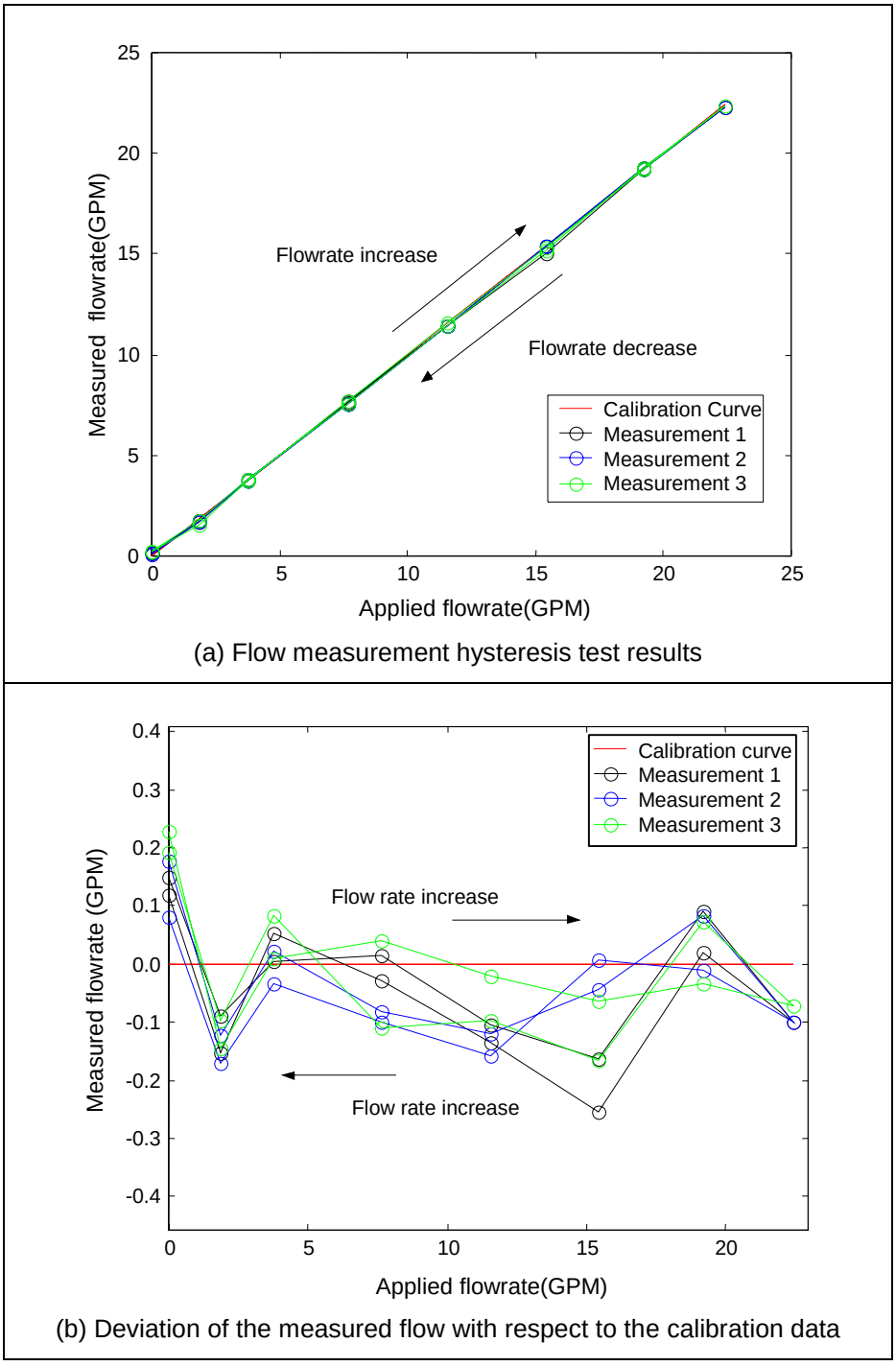

Figure 12.6. Flow sensor hysteresis measurement.

12.1.6 Stability testing

To further evaluate the sensor performance in the indoor flow loop, the stability of the designed sensor system was tested as shown in Figure 12.7. With the flow rate maintained at 4GPM for two hours, the output of the fiber optic flow sensing system was within 0.15GPM; the stability of the system was 0.67% of the full range.

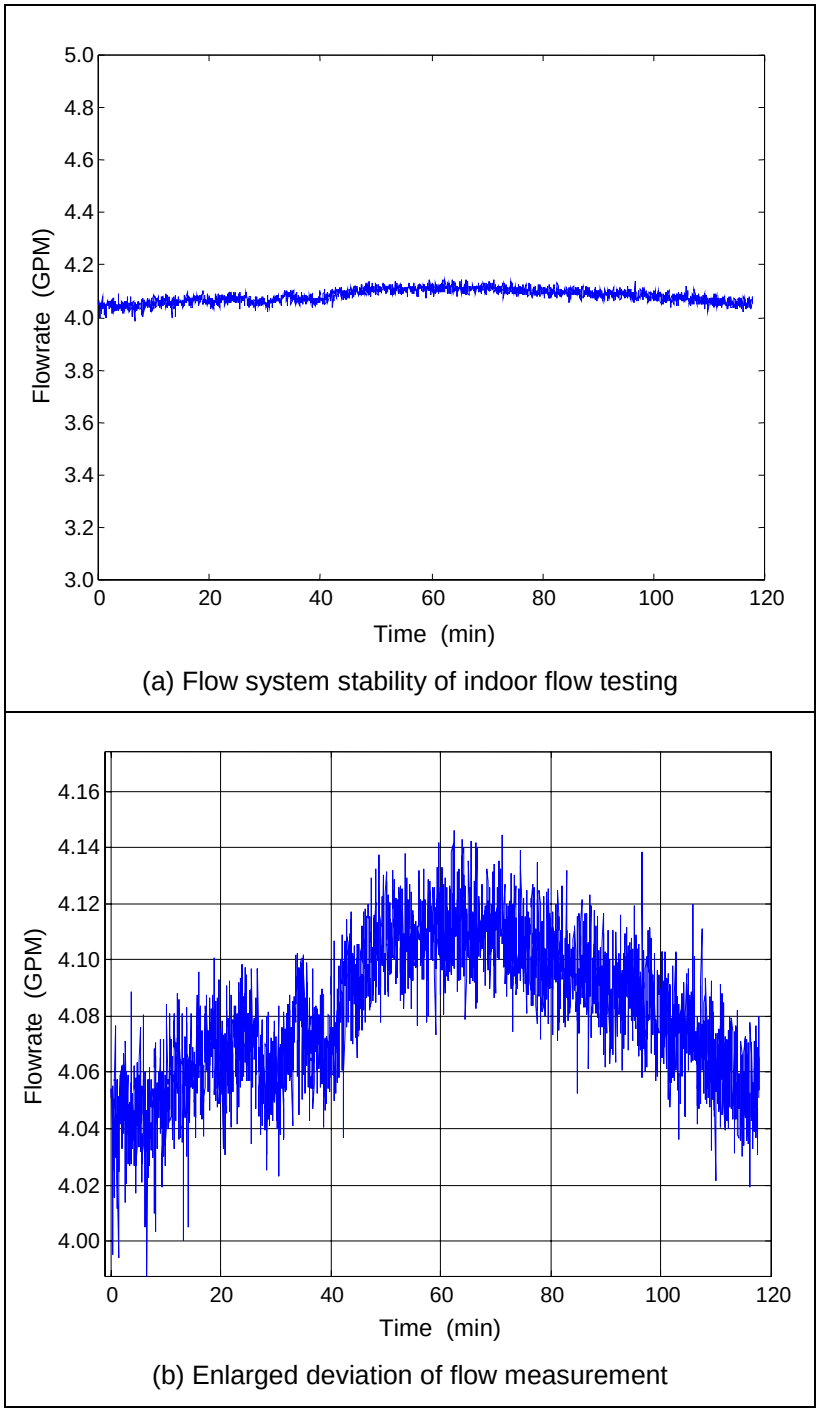

Figure 12.7. Flow system stability test over approximately 2 hours.

12.2 Outdoor Flow Loop Testing System and Results

The outdoor flow testing facility consisted of a simulated oil field flow environment combining pipes from 3 to 6 inches in diameter at various stages (Figure 12.8a). A variable frequency pump (Figure 12.8b)(0~2000GPM) from *Waukesha, Inc* was used for pumping water from the 3500-gallon tank shown in Figure 12.8c. The *Micro Motion* vibration flow meter shown in Figure 12.8d was used as the calibration. Many pressure and temperature gauges (Figure 12.8e) from *Rosemount Incare* were also distributed along the flow pipes to monitor the environmental conditions. The entire facility and gauges were controlled by the central computer in the control room. As shown in Figure 12.9, the fiber optic flow sensor was deployed in the outdoor 3-inch flow pipes using a 1.5 to 0.75inch NPT bushing through into a 0.75 inch welding port. The sensor probe was connected to the sensor system optoelectronic unit in the control room through a dual-core multimode fiber cable. The white light interferometer-based flow sensor control system is shown in Figure 12.10a and the flow rate measurement output window in Figure 12.10b. Using the *Micro Motion* flow meter as a reference, the sensor system was calibrated and tested with the water circulating in the flow loop at different flow rates. After spectrum detection and signal processing, the output flow rate data were digitized, displayed, and recorded.

Due to the complex structure of the outdoor flow testing system, for each testing step a minimum of 20 minutes was required to obtain a relatively stable flow rate. The flow meter and pump were designed for the flow rate range of 0~2000GPM, with ±0.2% accuracy of full range, around ±4GPM. So in the relatively low flow rate range of 0~64GPM, the accuracy of the reference flow meter was diminished. When the pump was set to a certain value, the flow rate fluctuated significantly, affecting the evaluation of the fiber optic sensor system's performance. The flow sensor was calibrated and tested based on the average outputs of the *Micro Motion* flow meter. The outdoor flow loop testing system experienced pressure fluctuations of around 9~66Psi, and temperature changes of approximately 26 to 37ºC. The flow sensor parameters for outdoor flow testing are listed in Table 12.2.

Table 12.2. Fiber optic flow sensor parameters for outdoor flow testing in Tulsa, OK.

Fiber type:	Multimode 50/125
Cantilever beam material:	Invar sheet
Cantilever beam size:	0.012" × 1.5" × 0.13"
Original air gaps of two sensors:	9.27μm; 9.61μm
Original visibility of two sensors:	52%; 29%
Gauge length of two sensors:	1.7mm; 178mm
Relative temperature coefficients:	1; 1
Sensor protection:	Flexible Ni-bellows
Test conditions:	84~86ºF; 1~5psi

(a) Outdoor flow testing loop

(b) Variable frequency pump (0~2000GPM)

(c) Water tank for outdoor flow testing loop

(d) Flow meter in outdoor flow loop

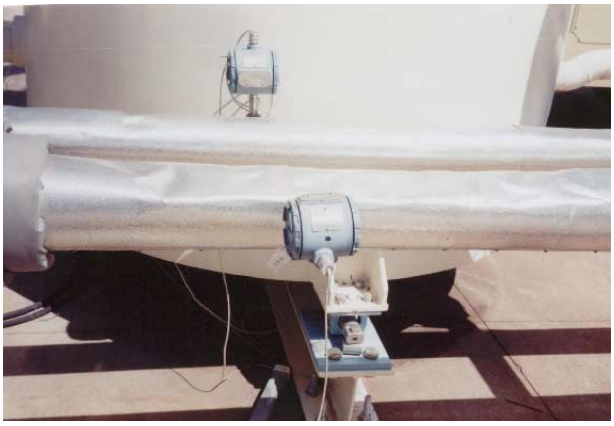

(e) Pressure and temperature gauge in outdoor flow loop

Figure 12.8. Outdoor flow testing facility in Tulsa University, OK.

Figure 12.9. Fiber optic flow sensor deployment in outdoor flow loops of Tulsa University, OK.

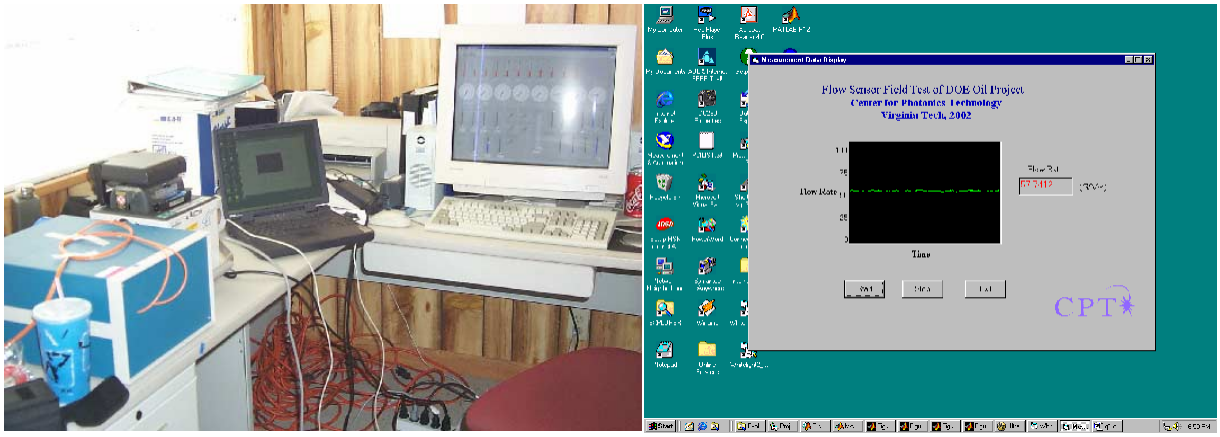

(a) Flow sensor measurement system in the control room of outdoor flow facility

(b) Output window of flow sensor

Figure 12.10. Fiber optic flow sensor control system for outdoor flow testing.

12.2.1 Calibration

Due to the difference in testing conditions (including pipe size, sensor deployment position and fluid characteristics) between the outdoor flow loop and lab-scale testing setup, the sensor required recalibration prior to testing in the outdoor system. Figure 12.11a shows the air-gaps of the two sensors and the output of the system with changes in the flow rate during the calibration. The calibration curve was generated as shown in Figure 12.11b, which provided the compensation coefficients used for the following measurement and evaluation.

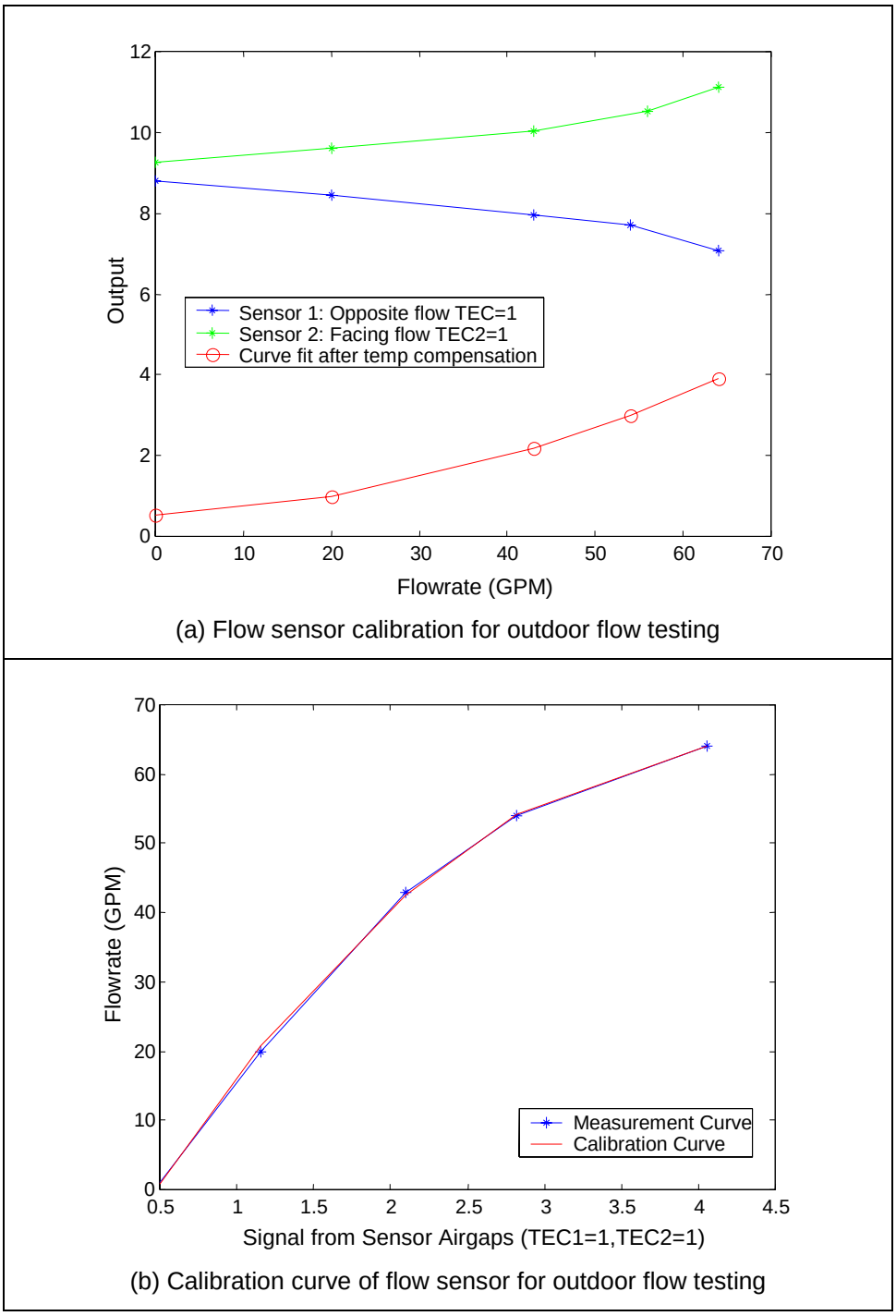

Figure 12.11. Flow sensor calibration for outdoor flow testing.

12.2.2 Stability

The stability of both *Micro Motion* flow meter and the fiber flow sensor are shown in Figure 12.12. Maintaining the variable frequency pump at 57GPM for 70 minutes, the maximum peak-to-peak fluctuation of the reference flow meter was 3.32GPM, which larger than that of the fiber optic flow sensor whose maximum fluctuation is 3.15GPM. Also the standard deviation of the reference flow meter was 0.61GPM, while of the fiber optic flow sensor was 0.42GPM. Relative to the *Micro Motion* flow meter, the mean deviation of fiber optic flow sensor was 0.9327GPM. Based on this data, we believed that the standard deviation of fiber flow sensor was less than 1GPM, and the stability of this sensor system was better than 1.56% for 0~64GPM full scale.

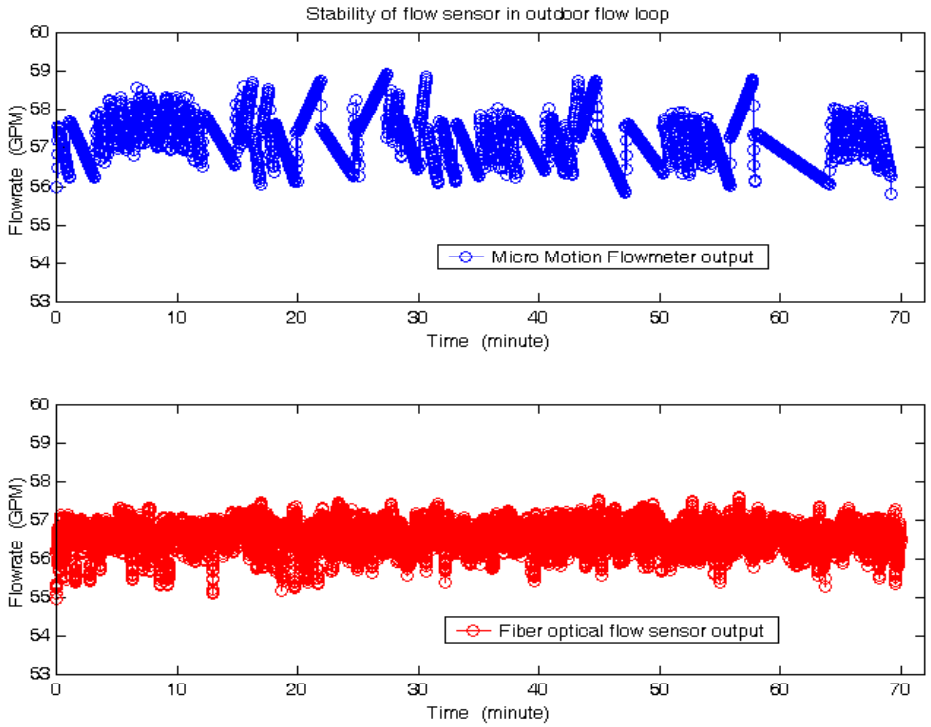

Figure 12.12. Flow sensor stability during outdoor flow testing.

12.2.3 Resolution

Using the same definition of resolution as described previously, the resolution of the fiber sensor system in the outdoor testing system is shown in Figure 12.13, and the calculated standard deviation from this data was σ=0.0083GPM. The resolution of the fiber optic sensor system was estimated to be 2σ=0.1664GPM. The normalized resolution for this sensor system was 0.26% of the full scale.

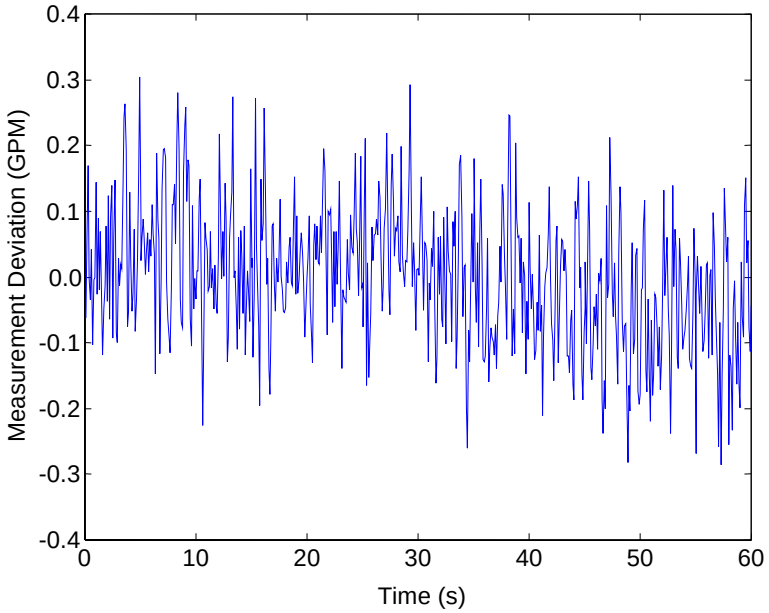

Figure 12.13. Resolution of fiber flow sensor during outdoor flow testing.

12.2.4 Repeatability

The flow rate in outdoor flow loop was measured based on above calibration curve and coefficients. Fig 28 shows the measurement results of flow rate measurements repeated three times. With respect to flow meter output, the deviation of these repeatability measurements were enlarged and shown in Fig 28(b). The maximum deviation was ±0.8GPM, which translates to ±1.25% of full scale.

12.2.5 Hysteresis

As shown in Figure 12.15, the hysteresis of the flow measurement was evaluated as 2.1% of full range during outdoor flow loop testing. Further improvement in sensor performance may be achieved by improving the sensor materials and fabrication techniques, the accuracy of the reference flow rate as well as the test system stability with respect to laminar flow generation.

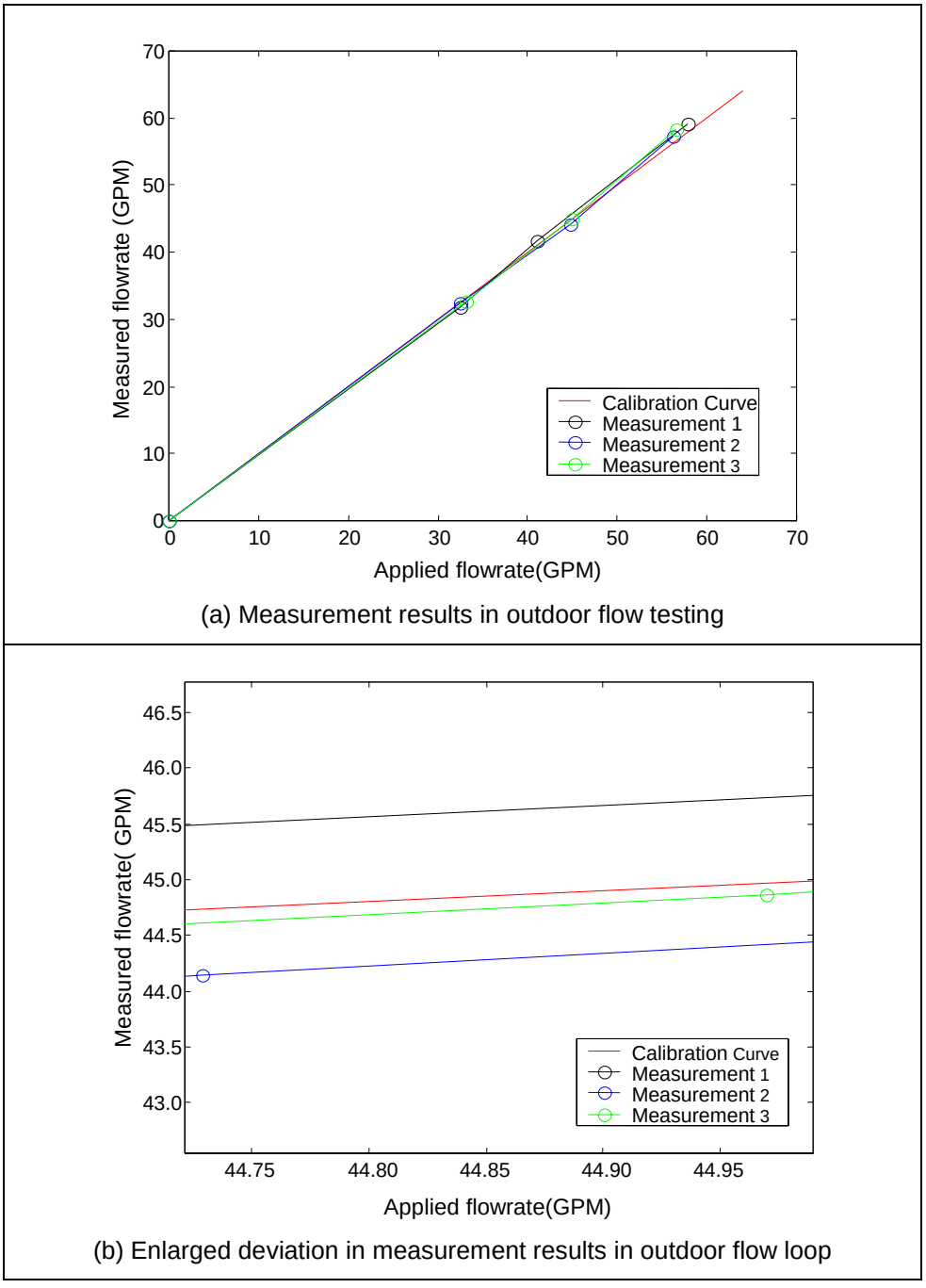

Figure 12.14. Measurement results and repeatability testing in outdoor flow testing.

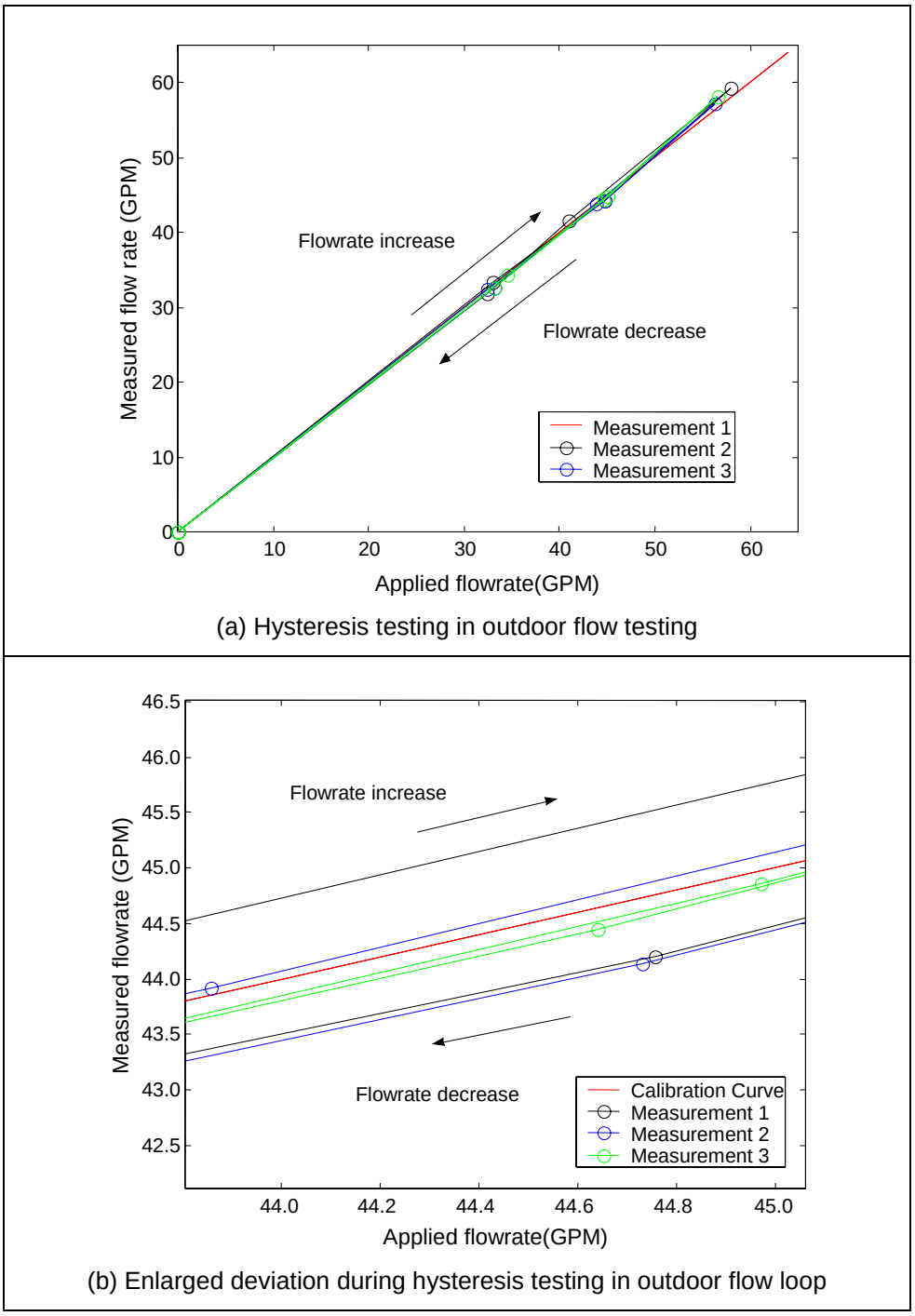

Figure 12.15. Hysteresis testing in outdoor flow testing.

Table 12.3 Summary of the performance evaluation results for fiber optic sensor systems.

	Repeatability	Hysteresis	Resolution	Stability
Lab-scale flow testing	±1.62%	1.35%	0.11%	<1.89% (~12hrs)
Indoor flow loop testing	±1.15%	0.89%	<0.11%	0.67% (~2hrs)
Outdoor flow loop testing	±1.25%	2.1%	0.26%	<1.56% (~70min)

Table 12.3 shows the overall summary performance of the fiber optic flow sensor testing for the both the laboratory testing and field testing.

13.0 Temperature and Pressure Sensor Field Testing

To evaluate the performance of the fiber optic sensor system in the oil site, a multimode white light sensor system was tested at the oil site of Chevron/Texaco Company (Coalinga CA).

13.1 First Coalinga Field Test

The main purpose of the first field test included verifying the deployability of the sensor head, testing the remote data access through the Internet, and evaluating the long term stability of the sensor head in the downhole environment.

13.1.1 Sensor deployment

A hydraulic optic fiber deployment system developed by the Chevron Company was used to deploy the pressure senor. The sensor head with connecting optical fiber was pumped down by utilizing hydraulic oil as the suspension media and force-imparting member. The sensor head moved down about 250m along the stainless steel pipe. The inner diameter of the metal pipe is smaller than 4mm, and there are several connectors along the pipe. Several times during the deployment of the sensor, the sensor apparently got stuck on something, and the sensor had to be drawn back a little by reversing the fluid flow direction and pushed forward again. The ability of the sensor to survive the rigors of the harsh deployment process is attributed to the improvements in mechanical durability of the sensor head. The position of the sensor head in the oil well was monitored by OTDR. After deployment, a pump was used to increase the pressure inside the testing pipe to about 3000psi, and then all valves were shut off to keep a constant pressure inside the pipe.

13.1.2 Remote access and control

13.1.2.1 Hardware configuration

The host computer that controlled the fiber sensor measurement was a Dell Latitude, P2-350 notebook with 128MB memory and 4.5GB hard disk. The Ethernet card was a SMC8040Tx 10/100 PC Card. The client computer was a PC desktop, P2-350 with 128MB memory, 6GB hard disk and a NE2000 compatible Ethernet card. This computer remotely controlled the host computer and obtained the measurement data through the internet.

13.1.2.2 Software configuration

The operating system was Windows 98 Second Edition. The remote control software was Symantec pcAnywhere 10.0, and the VPN service software was Nortel extranet access client V2.50.

13.1.2.3 Connection establishment

Host Computer:

In order for the notebook computer to log onto Chevron's intranet and obtain a static IP, the authorized user name and correct password was input when the computer enters Windows 98. The host computer must maintain the logon status.\

Client Computer:

On the client side, the computer is on the internet all the time through the Virginia Tech LAN. Each time the host computer was remotely controlled, the following steps were required:

(1) Run the extranet access client software; the window shown in Figure 13.1 will pop up. Then input the authorized user name and the pin plus passcode. The passcode is generated every 60 seconds by a security card.

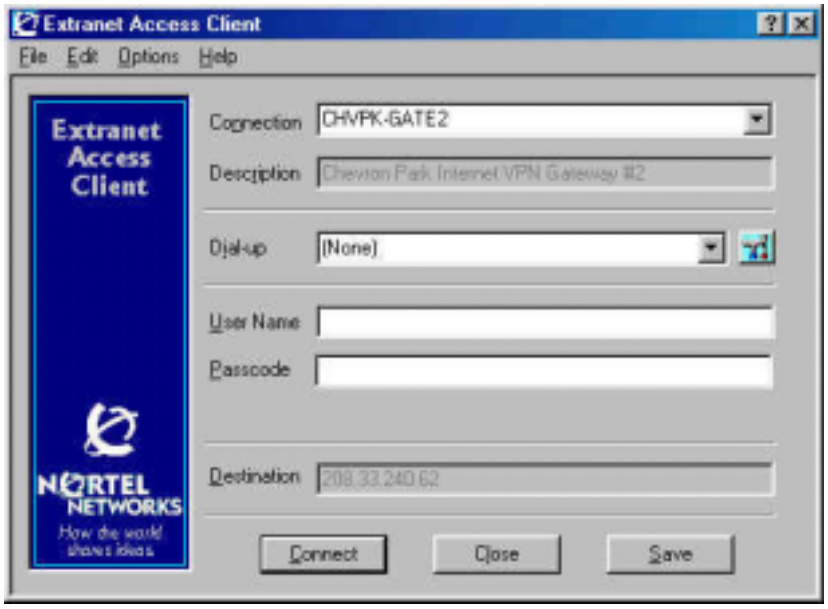

Figure 13.1. Nortel Extranet Access Client Software.

(2) Run 'pcAnywhere'and start the 'doe' task, which will try to connect to the host computer, when the host computer responds the window shown in Figure 13.2 will pop requesting the user name and password for secure connection.

When the above steps are performed successfully, the entire screen of the host computer will be displayed on the client computer. Then the host computer can be controlled using the client computer's mouse or keyboard.

Figure 13.2. pcAnywhere Manager Window.

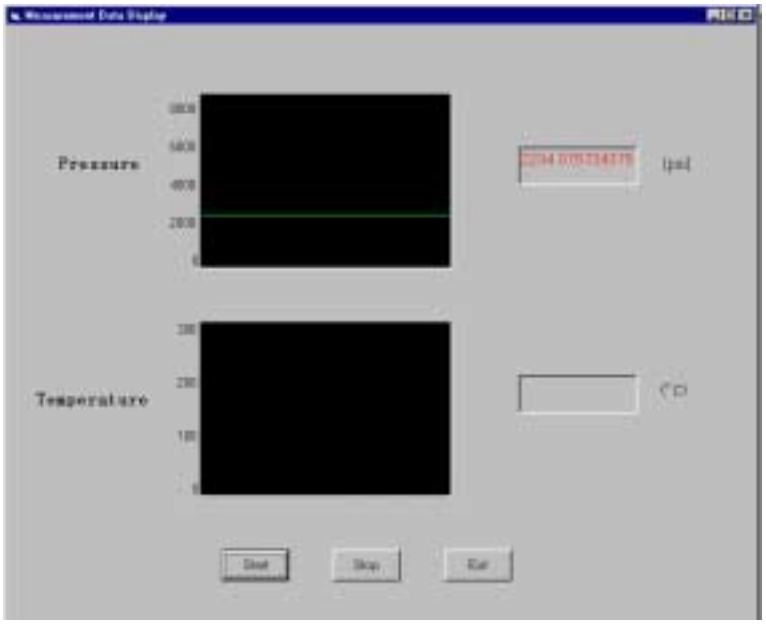

Figure 13.3. Pressure Measurement Window.

13.1.2.4 Data saving and remote access

The fiber sensor based measurement system measures the pressure in the oil well every minute and saves the data to the hard disk of the host computer. The software generates a new filename at time 00:00:00 every day so that one file will contain a single day's measurement data. The filename is the date, for example, '10-03-2001'. The data format is text, as follows:

Time		Pressure
10-03-2001	10:23:00	2290.3298
10-03-2001	10:24:00	2290.3021
……		

It is convenient to find a specific day's data by searching the filenames. Using one file for each day will not cause a huge size data file so that the download will be easy. For remote data access, we can use pcAnywhere's 'File Transfer' function: Run the file transfer function; a window will pop up showing the directory list of the host and the client computer separately in two subwindows. We can use a mouse to drag the file from the host window to the client window to finish the download.

13.1.2.5 Network security

The network security of the remote access is very important. The host computer cannot be accessed without running extranet access software first. The host computer is on Chevron's Intranet. Correct username and passcode are needed. The passcode consists of a PIN and Security Card Number, and the Security Card Number will change every 60 seconds and will be examined by the server of the Chevron's gateway. Also, pcAnywhere has its own network security: a username and password are needed to establish remote control. Therefore, the network security is very good.

13.1.3 Long-term stability

This system ran for more than three months in the downhole environment, and the computer was accessed remotely from Virginia Tech. The whole system functioned well during this period. Figure 13.4 shows the testing results for first 90 days.

The slow decrease in pressure was expected due to the leakage of the pressure system. A surface-mounted pressure sensor in-line with the fiber optic pressure sensor also shows the downward trend of the pressure with time. The magnitude of the drift downward for the surface mounted pressure sensor is much larger than for the subsurface fiber optic sensor.

13.2 Second Coalinga Field Test

After the successful achievement of the goals outlined for the first field test, the sensors were again deployed using a hydraulic optic fiber deployment system developed by the Chevron/Texaco Company and the position of the sensor head in the oil well monitored by OTDR. After deployment, a pump was used to increase the pressure inside the testing pipe to about 3000psi, and then all valves were shut off to maintain a constant pressure inside the pipe. As discussed previously, the sensor system was accessed remotely to control the host computer and obtain the measurement data. Data was saved to the hard disk of the host computer once per minute. The software generated a new filename at time 00:00:00 each day so that one file contained one day's measurement data. Figure 13.5 and Figure 13.6 show the testing results through the end of the fourth program year.

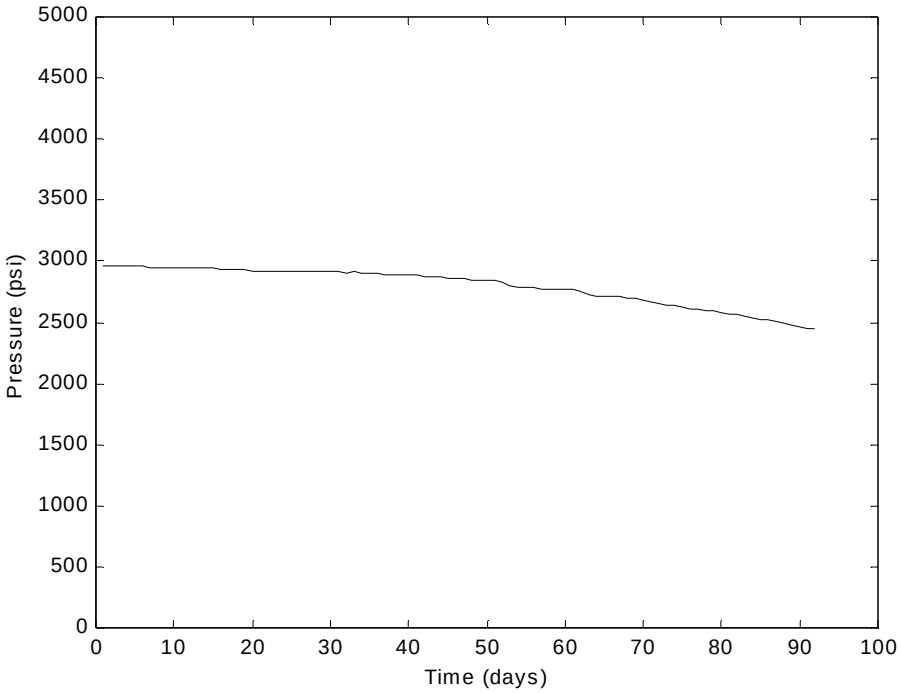

Figure 13.4. Ninety day testing result in oil site.

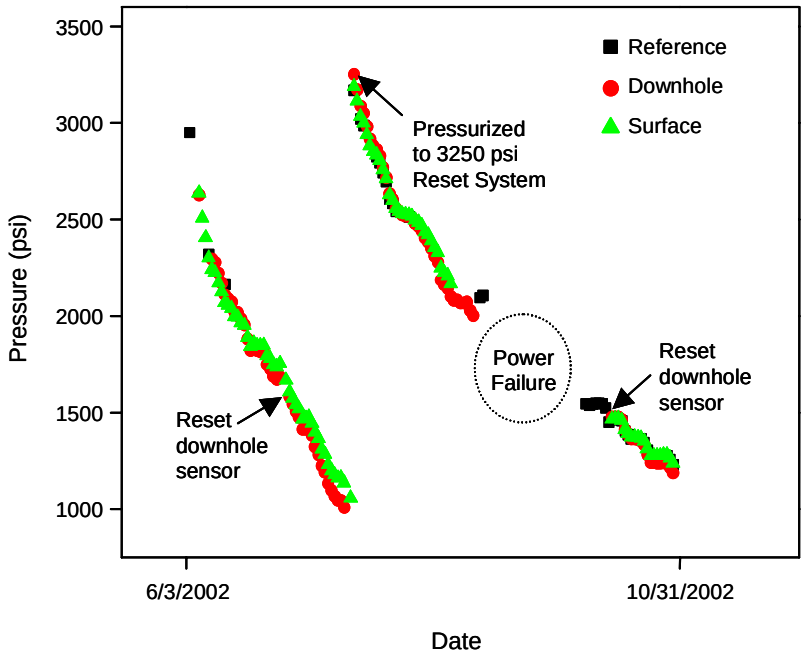

Figure 13.5. Pressure sensor output from 6/3/2002 - 10/31/2002.

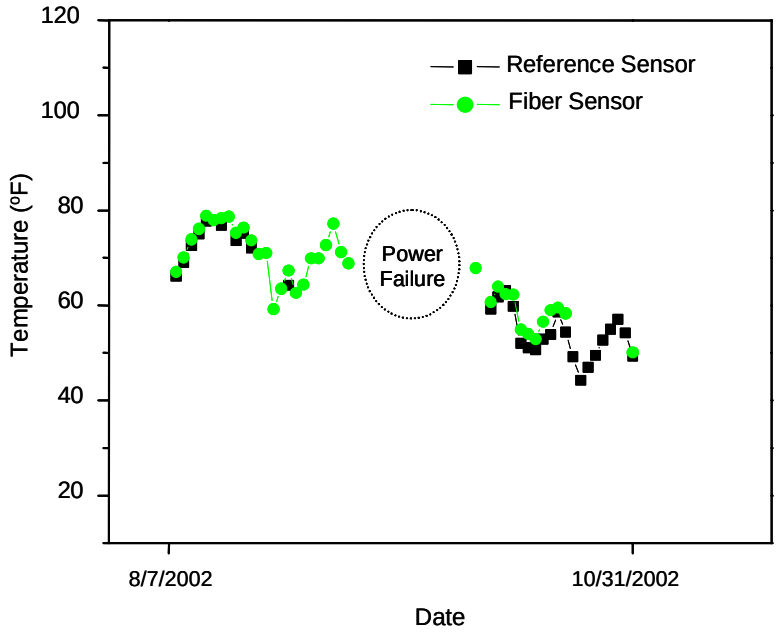

Figure 13.6. Temperature sensor output from 8/7/2002 – 10/31/2002.

14.0 Summary and Conclusions

This four and one half year program successfully developed optical fiber sensors for measurement of pressure, temperature, flow and acoustic waves, including three successful field tests in the oil fields of Chevron/Texaco in Coalinga, California and at the world class oil flow loop facilities at the University of Tulsa, in Tulsa, Oklahoma.

Successes demonstrated in this program include:

- Proven deployability of fiber optic sensors – no sensors have failed in any of the three field tests during deployment
- Pressure sensor resolution of 0.03psi, repeatability of 0.15% full scale and stability of 0.01%
- Flow sensor resolution of 0.26% and stability better than 1.56%
- Successfully completed two sets of field tests in the Chevron/Texaco's Coalinga, Ca oil fields
- Developed sensor and hermetic packaging that can be deployed through 0.25inch O.D., 0.125 inch I.D. high pressure steel tubing – packaged sensor is less than 1mm in diameter
- Developed remote monitoring and control systems so that all the computers in the field site at Coalinga, Ca could be monitored and controlled from virtually anywhere in the world through remote internet access
- Successfully developed and field tested flow sensors at the University of Tulsa's indoor and outdoor flow testing loops. The flow sensors preformed very well in both systems
- Successfully developed and tested acoustic sensors

In more detail, major research areas included design and fabrication of sensor probes, development of DSP-based signal processing techniques, construction of test systems, development and testing of strategies for the protection of optical fibers and sensors in the downhole environment, remote internet data access system to allow monitoring of the real time data from virtually anywhere in the world, evaluation of sensor performance in laboratory testing and improvement of the performance of the SCIIB optoelectronic signal conditioning system. A breakthrough in the signal demodulation method led to the development of the white light interferometer instrumentation system, which was ultimately shown to be the optimal system for high resolution, low speed applications, and was used in this project for pressure, temperature and flow measurements. Comprehensive testing was performed to systematically evaluate the performance of the fiber optic sensor systems in both laboratory and field environments.

Pressure and temperature sensors were successfully deployed using Chevron's hydraulic deployment method into a test well in Coalinga, California and the long-term stability of the

sensor head in the downhole environment verified. Hydraulic deployment added the additional constraint that the packaged sensors had to be less than 1mm in diameter to fit throught the hydraulic tubing. To ensure the durability of the sensor head such that it would be able to survive the rigorous deployment process, the sensor head was encapsulated in a soft metallic material while simultaneously encapsulating the metal in outer heat shrinkable tubing. This method proved to be extremely simple to employ in an oil field setting, was robust enough to be able to be applied reliably, and was found to be a very inexpensive solution. Extensive testing of the protected sensors verified the packaging performance.

A self-compensating fiber optic flow sensor based on a cantilever beam and fiber optic interferometer was designed and successfully tested in both laboratory and field tests. The extensive laboratory development work for the optical fiber sensors culminated in successful long term field demonstrations.

Every portion of the sensor systems from the sensor head to the protective packaging to the optoelectronic signal detection to the signal demodulation algorithm had to perform flawlessly in order for the field testing to be successful. The overall verification and culmination of the extensive development work in this project was manifested in the successful field testing results.

References

1. "Doing Business with DoE: Office of Fossil Energy - Gas and Oil Programs," DoE's Office of Gas and Petroleum Technology, Wsahington, DC (1994).
2. A. Wang, H. Xiao, J. Wang, Z. Wang, W. Zhao and R. G. May, Self-Calibrated Interferometric/Intensity-Based Optical Fiber Sensors,J. Lightwave Tech. 19 (10), 1495-1501 (2001).
3. G. P. Agrawal, Fiber-Optic Communication Systems, 2nd ed, John Wiley & Sons, New York (1997).
4. G. S. Brady, H. R. Clanser and J. A. Vaccari, in Materials Handbook, pp. 518, (1997).
5. N. P. Cheremisinoff, Applied fluid flow measurement - fundamentals and technology, M. Dekker, New York (1979).
6. N. P. Cheremisinoff and P. N. Cheremisinoff, Flow measurement for engineers and scientists., M. Dekker, New York (1988).
7. J. Dakin and B. Culshaw, Optical Fiber Sensors: Principles and Components, Artech House, Boston (1988).
8. M. di Giovanni, Flat and corrugated diaphragm design handbook,11, M. Dekker, New York (1982).

List of Acronyms and Abbreviations

A/D, analog to digital
APP, Advanced Pressure Products, Inc.
CCD, charge couple device
CPT, Center for Photonics Technology
CTE, coefficient of thermal expansion
EMI, electromagnetic interference
FWHM, full width half maximum
GRIN, graded index
LAN, local area network
LED, light emitting diode
MMF, multimode fiber
PC, personal computer
PZT, lead zirconium titanate
SCIIB, self-calibrated interferometric/intensity-based
SLED, superluminescent light emitting diode
SMF, singlemode fiber
SNR, signal to noise ratio
VTPL, Virginia Tech Photonics Laboratory (now Center for Photonics Technology)